DOCTORAL DISSERTATION

Future changes in atmospheric moisture and wind field using numerical simulations: Implications for moisture transport and wind energy

José Carlos Fernández Alvarez

2023
"International Mention"

Universidade Vigo

EIDO
Escola Internacional
de Doutoramento

Universidade Vigo

Escola Internacional de Doutoramento

José Carlos Fernández Alvarez

DOCTORAL DISSERTATION

Future changes in atmospheric moisture and wind field using numerical simulations: Implications for moisture transport and wind energy

Supervised by:
Luis GIMENO PRESA, PhD
Raquel Olalla NIETO MUÑIZ, PhD

2023

"International mention"

Escola Internacional de Doutoramento

Luis GIMENO PRESA, PhD and **Raquel Olalla NIETO MUÑIZ, PhD**

DECLARE that the present PhD Thesis, entitled **"Future changes in atmospheric moisture and wind field using numerical simulations: Implications for moisture transport and wind energy"**, submitted by José Carlos Fernández Alvarez to obtain the title of Doctor with "International Mention" by the Universidade de Vigo, was carried out under our supervision in the PhD Program "Auga, Sustentabilidade e Desenvolvemento", and it is presented under the modality of compendium of research articles.

Ourense, 22nd December, 2023

The supervisors:

Luis GIMENO PRESA, PhD **Raquel Olalla NIETO MUÑIZ, PhD**

Campus Universitario de Ourense, Universidade de Vigo
Departamento de Física Aplicada — Environmental Physics Laboratory (EPhysLab)
José Carlos FERNÁNDEZ ALVAREZ (jose.carlos.fernandez.alvarez@uvigo.es)

To my mother

For all the care, love, and dedication throughout my life.

Acknowledgements

During these three years, many people have contributed to develop the PhD thesis presented in this document. I would especially like to thank:

- My thesis directors **Raquel Nieto** and **Luis Gimeno**. Thank you very much for carefully guiding the thesis project, detailing each step and new ideas to develop. Also, thank you for your incredible patience in thoroughly reviewing the thesis and each article produced. Thank you so much.
- **Rogert:** Thank you for everything you did so that you could get here and then during the adaptation process in Ourense City. I will be grateful for my entire life.
- **Jorge Eiras:** Thank you very much for reviewing the articles in detail and giving me advice on how to be a better professional.
- **Albenis:** For being a friend and co-worker throughout this time and supporting me in any problem or need presenting.
- **Xurxo and Stephan:** Special thanks for your help, which was essential for my progress in very complicated topics of the thesis.
- **Ourense Friends:** To Jose Guerra, Migue, Alioth, and Luis Sotelo for the spectacular moments lived and shared that I will never forget. Many thanks, friends.
- **Claudia and José Alejandro:** For being the family we have in France and being aware of every problem we have. Thank you very much for the moments we enjoyed together.
- **Carlos Javier y Arlet:** For always being aware of the development of the thesis and living incredible moments together.
- To my co-workers **Milica, Coral, Marta, Patricia, Iago, and Angel**, thank you very much for the support provided during this period. In general, to the EPhysLab group for their collaboration at any time I need it.
- To the professors of the Department of Meteorology of the Higher Institute of Technologies and Applied Sciences of the University of Havana, Cuba for their concern about the progress of the thesis.
- To **Maykel, Abel, and Santana** for their unconditional support during this period and especially to Professor **Alfo** for always trusting me as a professional.

- To my wife **Gleisis**, who has supported me unconditionally and made me a better person. Thank you very much, my love.
- To my family, especially **MY MOTHER**, because they are always supporting me even though the distance is considerable.
- To Gleisis's family and especially to her mother for considering me a son to her. Thank you so much.

I'm sure I forgot very important people for a long time, to all of them **THANK YOU VERY MUCH**.

I would like to acknowledge the support from the Xunta de Galicia under Grant ED481A-2020/193. In addition, this work is supported by the SETESTRELO and EXMERISK projects (Grants PID2021-122314OB-I00 and TED2021-129152B-C43) funded by the Ministerio de Ciencia, Innovación y Universidades, and Agencia Estatal de Investigación, Spain. Partial support was also obtained from the Xunta de Galicia under Project ED431 C 2021/44 (Programa de Consolidación e Estructuración de Unidades de Investigació Competitivas (Grupos de Referencia Competitiva) and Consellería de Cultura, Educación e Universidade). In addition, it has been co-financed by the Fondo Social Europeo (F.S.E.). Finally, this work has been possible thanks to the computing resources and technical support provided by CESGA (Centro de Supercomputación de Galicia) and Red Española de Supercomputación (RES) (AECT-2022-3-0009 and DATA-2021-1-0005). Funding for open access charge: Universidade de Vigo/CISUG.

José Carlos FERNÁNDEZ ALVAREZ
jose.carlos.fernandez.alvarez@uvigo.es
Environmental Physics Laboratory (EPhysLab)
Universidade de Vigo
22nd December, 2023

Contents

Abstract

Since the end of the 19th century, human actions have impacted the atmosphere, oceans, and land, leading to global warming. Consequently, the global water cycle has undergone substantial widespread changes since the 20th century. A warmer climate increases the transport of water vapour into climate systems, affecting the frequency and intensity of hydrometeorological extreme events, such as heavy rainfall and droughts, in many regions. In addition, climate change is expected to affect the wind speed at a height of 10 m (V10), with significant geophysical and social impacts, such as affecting the feasibility of wind energy production, wave climate, storm surges, and onshore and offshore industries. Furthermore, modifications in the wind field influence variables such as soil humidity, evaporation, and water availability to determine arid and semi-arid conditions.

Owing to climate variability, significant decreases in water availability are expected in several areas. Given the fragility of water availability, there is a growing need to understand the changes induced by global warming to ensure a sufficient supply of water resources. It is important to determine the dependence between the moisture transport given by the moisture source-sink relationship and climate change, and how this influences continental precipitation for specific regions. In addition, changes in global atmospheric circulation may affect the behaviour of regional wind patterns and compromise wind energy production capacity. Future changes in the spatial and temporal distributions of V10 imply changes in the type of energy associated with this variable. Therefore, an analysis of future projections would improve the production capacity and energy efficiency with better planning and balancing of ideal regions for installation.

Currently, notable progress has been made in studies focusing on determining where precipitation originates and the moisture source-sink relationship, establishing climatology for most regions of the world. Many studies have provided detailed information on the role of synoptic-scale systems, particularly in Atmospheric Rivers (ARs). These meteorological systems are considered to be one of the main moisture transport mechanisms, along with low-level jet systems, tropical and extratropical cyclones, and monsoons. Specifically, most of them have focused on the intensity and frequency of ARs and, to a lesser extent, on the determination of the sources that cause the humidity they transport or their anomalous moisture uptake. However, few studies have analysed the moisture source-sink relationship in a future climate over long periods or for specific systems such as ARs.

The Lagrangian approach is a widely used methodology for studying the moisture source-sink relationship. Previous studies based on this approach have not aimed to quantify how climate change will influence the location and importance of moisture source regions, and how this will determine the transport of moisture to sinks (continental areas), and even fewer have used

high-resolution regional models. Moreover, regarding future changes in wind fields and related variables, numerous studies have been conducted in the Atlantic Ocean region using the Global Climate Models (GCMs) of the Coupled Model Intercomparison Project Phase 5 (CMIP5) and Phase 6 (CMIP6). However, the low resolution of the Global Climate Models used does not provide detailed information on climate change and its impacts in certain areas (regional scale), particularly where the weather and climate are not homogeneous.

Therefore, this thesis focuses on moisture transport and V10 by performing regional simulations at a higher spatial resolution, considering the North Atlantic as the study region. This spatial resolution increase will allow better reproduction of physical processes at higher spatial resolutions up to scales that allow the representation of convection (a few kilometres) essential for precipitation modelling. Furthermore, the results of this thesis are intended to provide more detail on the influence of climate change and its impact regionally and will allow decision-makers to take action on a given future climate signal or change. Specifically, a dynamic downscaling methodology which uses the advantages of the Eulerian mesoscale Weather Research and Forecasting (WRF) with an ARW dynamic kernel (WRF-ARW) and the Lagrangian dispersion model FLEXPART-WRF (regional model adapted from the FLEXible PARTicle dispersion model (FLEXPART) for WRF) was considered. Therefore, this study aimed to determine future changes in atmospheric moisture and wind fields using numerical simulations and analyse the implications for moisture transport and wind energy in the North Atlantic region.

To address the proposed overall objective, a dynamic downscaling methodology using reanalysis data was previously evaluated. This evaluation focuses on the representation of the moisture source-sink pattern using reanalysis data for several configurations of the dispersion models FLEXPARTv10.3 and FLEXPART-WRF for a specific period and over the North Atlantic Ocean region. Importantly, original and free software was developed to process the outputs of these models and obtain the necessary fields for the different studies. Next, the dynamically reduced dataset and the results of the FLEXPART-WRF dispersion model were used to determine future changes in the anomalous moisture uptake of the ARs reaching the Iberian Peninsula and in the strength and location of their moisture sources. Finally, future changes in V10 in the North Atlantic Ocean and how the modifications of the wind pattern influence offshore wind energy production were studied for three important subregions on each side of the basin: the Atlantic coast of the Iberian Peninsula, the United States East Coast, and the Caribbean Sea region.

The data used in this thesis come from different sources: reanalysis data from the European Centre for Medium-Range Weather Forecasts (ERA-Interim (ERA-I) and ERA5), climate outputs from the Community Earth System Model Version 2 (CESM2), and an ensemble of several climate models. These data were used as the initial and boundary conditions for the WRF-ARW model. The WRF-ARW outputs were used as inputs to the FLEXPART-WRF model. The Shared Socioeconomic Paths (SSPs) used in this study are the SSP2-4.5, SSP3-7.0, and SSP5-8.5 (representing an increase of 4.5 W/m^2, 7.0 W/m^2, 8.5 W/m^2, respectively). These scenarios present differences among themselves due to the level of radiative forcing projected at the end of the century, but at the same time, they show a wide spectrum of possibilities from a more positive scenario to the most extreme. A set of 30-year periods was used in the analysis of moisture transport: 2036–2065, mid-century (MC), 2071–2100, end-century (EC), and 1985–2014, historical reference period (HIST), using only the SSP5-8.5 scenario. For the analysis of the wind field and wind power density (WPD), the three SSPs were used but 5-year periods were considered: 2049–2053, mid-century (MC_5Y); 2096–2100, end-century (EC_5Y); and 2010–2014, historical period (HIST_5Y). Finally, the changes projected considering the differences in scenarios were determined as the difference in the expected pattern at MC and EC minus the HIST pattern.

A Lagrangian methodology that follows changes in specific humidity every 6 h was applied, considering the trajectories of the particles in the atmosphere. The residence time of water vapour in the atmosphere considered was 10 days to track the particles forward or backward in time. In the study of moisture transport, the North Atlantic and the Mediterranean Sea (NATL and, MED, respectively) were considered as moisture sources, even the Iberian Peninsula itself, to study the precedes of recycling, and the surrounding continental regions as their sinks. Moreover, to study the moisture associated with ARs, the anomalous moisture uptake over the ocean, specifically for landfalling ARs arriving on the Iberian Peninsula, was determined. Finally, to calculate WPD, the wind speed was extrapolated to a height of 120 m in a neutral atmosphere. They were extrapolated following a logarithmic wind profile, and the Atlantic coast of the Iberian Peninsula, the United States East Coast, and the Caribbean Sea region were considered the study regions.

A software is required to process the outputs of particle dispersion models. The TRansport Of water Vapor (TROVA) tool was implemented to facilitate the application of the different Lagrangian methodologies to the outputs of the FLEXPART and FLEXPART-WRF dispersion models. In addition, TROVA allows the consideration of several mesh resolutions for the input and output data and masks used for moisture transport studies. Therefore, it can be used for the outputs of these dispersion models forced by both ERA-I and ERA5 and allows the study of projected changes in the strength and location of moisture sources and sinks using climate model outputs from WRF simulations. Furthermore, TROVA has good computational efficiency owing to its development using parallel programming, which allows its use in supercomputers. Finally, it is a free software implemented in Fortran and Python and is available to the scientific community.

Once the software was developed, the evaluation of the moisture sources and sink patterns for the ERA5 data (at 1° and 0.5° of spatial resolution) was carried out using the FLEXPART model and the dynamic downscaling methodology explained above. It was obtained that the three configurations presented a correlation in the range of 0.4 to 0.6 using ERA5 for the representation of the moisture pattern that provides humidity on the Iberian Peninsula, compared to that of the control experiment, higher for FLEXPART outputs using ERA5 at 0.5° and lower for the configuration using FLEXPART-WRF and WRF-ARW outputs (FLEX-WRF). A few noticeable differences were observed for the configurations regarding the error, with the greater error observed in summer and the lowest in winter and autumn. Finally, FLEX-WRF provided a better representation of the moisture source pattern, with a predominance of mountainous orography during spring and summer. Notably, precipitation recycling processes are predominant during these seasons.

In the analysis of the Mediterranean Sea source moisture sinks, the three configurations showed low dispersion and high correlation values compared with the control experiment. A lower mean absolute error was obtained with respect to the values given for the IP. The mean square error increased in summer and decreased in autumn. Additionally, FLEX-WRF best represented the moisture sink pattern in regions of complex orography, with the best performance of all configurations. However, the contribution pattern associated with the Mediterranean Sea tended to be more constricted both in latitude and longitude, showing minor errors compared with the North Atlantic target region. For North Atlantic Ocean, the magnitudes of the absolute error and root mean square error showed values of up to 2.5 and 4.5 mm/day respectively. Furthermore, the correlations between the three configurations and the control experiment ranged from 0.4 and 0.7. The FLEX-WRF model showed little ability to determine the sink patterns associated with this source.

Once all the configurations were evaluated, future climate studies were conducted considering the same moisture sources and their associated sinks. Specifically, in the two future periods analysed, a general increase in humidity was projected to reach the surrounding continental areas of the North Atlantic Ocean and Mediterranean Sea. In the MC, a slight annual increase was observed in contributions from the North Atlantic Ocean basin and the western Mediterranean Sea. At end-century, a pattern was observed with values greater than the expected changes at MC. A significant increase in precipitation recycling processes is expected over the Iberian Peninsula during the winter months and varies annually from 2 % to 8 %. The results obtained regarding the increase in moisture contributions for the NATL and MED over the IP are compatible with the amplification of the Clausius–Clapeyron relationship. On the other hand, greater contributions from the Mediterranean Sea to continental precipitation were projected over the areas south of the Mediterranean Sea during both analysed periods. This contribution is expected to increase, being lower over the Iberian Peninsula mostly in summer, with maximum values at the end of the century. It is highlighted that the contribution in Eastern Europe will decrease, and for Western Europe, it is only appreciated in summer and spring. The NATL source will increase its contribution over the east coast of North America (mainly in winter and autumn), with notable values in the British Isles (mainly in winter), but it is expected to decrease latitudinally in the northern areas of western Europe, the Iberian Peninsula, and the west coast of Africa.

With regard to the ARs that move over the North Atlantic, a shift towards the north of the position was projected at EC and progressive strengthening throughout the century, showing the maximum distribution of vertically integrated water vapour transport (IVT) at 750 kg m^{-1} s^{-1}. Specifically, an increase in the advective dynamics of ARs is expected, particularly in landfalling ARs arriving over the Iberian Peninsula at EC. This behaviour is especially intense in the corridors that connect the Iberian Peninsula with its moisture sources. In general, a reinforcement of the anomalous moisture uptake was projected, and a shift of this amount towards southern latitudes is expected. The changes mentioned above were notable in winter (increases of 9 % and 24 % at MC and CE, respectively). Increases were projected in the winter, autumn, and annual seasons at MC located north of 20 °N and in the central North Atlantic; however, below 20 °N, it decreased slightly. At EC, the signal of the changes showed maximum values in winter, with anomalous moisture uptake being greater in regions of the central and western Atlantic, Caribbean Sea, and Gulf of Mexico. However, in autumn, the moisture sources are projected to be more remote, with an increase in anomalous moisture uptake around the Atlantic coast of the United States.

Finally, under SSP2-4.5 scenario, V10 decreased north of 30 °N in winter for MC_5Y and increased below 30 °N, except for the eastern region of the eastern Caribbean Sea. Decreases in V10 were simulated in spring, mostly in the North Atlantic Ocean, except the Caribbean Sea. Increases were projected for summer and autumn, except in the southern coastal region of the United States. Under SSP3-7.0 in winter, the tendency for wind speed to decrease was represented, with wind speed only increasing in two regions: the Iberian Peninsula and West African area. Increases were projected for summer and autumn in the Caribbean Sea, United States east coast, and Iberian Peninsula but the increases were minor compared with those obtained under SSP2-4.5. However, under SSP5-8.5, the maximum changes were projected for the winter season, showing a notable decrease over the Caribbean Sea around the African coast and in regions above 50 °N. In addition, the North Atlantic Ocean region increased during summer and autumn. Finally, the observed changes at EC_5Y were slightly different to those for MC_5Y under SSP2-4.5 and SSP3-7.0, but more pronounced under SSP5-8.5 scenario.

Under SSP2-4.5 the WPD decreased in winter over the west coast of the Iberian Peninsula, showing maximum decreases in the northern part. In spring, increases were projected mostly on the west coast of the Iberian Peninsula. Increases in WPD were expected around the coasts of the Iberian Peninsula in summer, mainly along the coast of Galicia and northern Portugal. When under SSP3-7.0, a WPD increase is expected in winter, with notable values in northern Galicia, whereas for spring, a remarkable decrease is expected along the Iberian Peninsula west coast. Increases in WPD are expected over the northwest Iberian Peninsula during summer and autumn. Under SSP5-8.5, the most marked difference was the expected increase over the northern region of the Iberian Peninsula during autumn. However, at the end of the century, notable changes were simulated over the same region mentioned but extended up to 40 °N. These changes were apparent in winter under all three SSPs but were more notable with SSP5-8.5.

For the United States east coast subregion, under SSP2-4.5, a winter WPD decrease was predicted for latitudes above 35 °N, showing maximum values around the coasts of the states of Maine, Massachusetts, New Hampshire, and New Jersey. During summer, increases in WPD were mainly observed around the coasts of North Carolina, South Carolina, and Virginia. Under SSP3-7.0, WPD decreased in winter; however, increases were simulated in autumn, with an increase on the east coast of the northernmost states of the United States. Under SSP5-8.5, the pattern was the opposite, showing increases below 40 °N and decreases above 40 °N in winter. For EC_5Y, in summer, WPD decreased under SSP3-7.0 but increased under SSP5-8.5.

Under SSP2-4.5 for MC_5Y in the dry season, the WPD pattern was reinforced in the Caribbean Sea subregion, mainly for the Venezuelan Basin, compared to the historical period. In the wet season, in the Colombia and Venezuela Basins, WPD increased around the southern and northern coasts of La Española and in the eastern region of Cuba. However, under SSP3-7.0, WPD decreased over most of the Caribbean Sea during the dry season, with increases in the Colombian Basin. This behaviour differed during the wet season, with increases around the coasts of Colombia and Venezuela. The changes predicted under SSP5-8.5 at MC were similar to those under SSP3-7.0 but differed from those under SSP2-4.5, projecting a considerable increase for the entire region this last scenario. At the end of the century, a decrease was simulated over the Yucatán and Colombia basins under the three SSPs during the dry season, with a small increase in the Venezuela Basin. During the wet season, there was a marked increase in WPD in the Caribbean Sea, except for the Yucatán Basin.

From the results obtained, it can be concluded that the TROVA software allows the study of the moisture source-sink relationship in current and future climates. The FLEXPARTv10.3 dispersion model fed with the last reanalysis data from the European Center for Medium-Range Weather Forecasts (ECMWF) ERA5 showed the moisture source and sink regions as the FLEXPARTv9.0 version running with the old ERA-Interim dataset. Additionally, the FLEXPART version for the dynamically downscaled ERA5 data using WRF can represent similar moisture sources and sinks with better regional resolution. Finally, this dynamic downscaling methodology contributes to the study of moisture sources and sinks in future climates, considering data from climate change models that consider different scenarios of warming and Shared Socioeconomic Pathways at a higher spatial resolution, which is one of the main demands of The Intergovernmental Panel on Climate Change to improve both global and regional simulations.

Resumo

É inevitable que a actividade humana teña influído no quecemento da atmosfera, océanos e continentes desde o inicio da Época Industrial. Como consecuencia deste quecemento, o ciclo global da auga experimentou cambios substanciais e xeneralizados desde mediados do século XX. Un clima máis cálido aumenta o contido de vapor de auga na atmosfera e, polo tanto, intensifícase o transporte do mesmo desde as rexións evaporativas ata as áreas onde ocorre a precipitación. Como resultado, en moitas rexións do planeta, os fenómenos meteorolóxicos e climáticos extremos (como precipitacións intensas e secas) están a cambiar en frecuencia e intensidade. Ademais, e en relación con esta intensificación da rama atmosférica, agárdase que o cambio climático tamén afecte a outras variables como á velocidade do vento, especialmente na superficie. Estes cambios no vento superficial implica importantes impactos xeofísicos, como cambios na humidade do chan, evaporación e recursos hídricos, influíndo na evolución das contornas áridas e semiáridas, e tamén socioeconómicos, xa que compromete, por exemplo, a viabilidade das operacións e investimentos no eido da enerxía eólica (tanto *onshore como offshore*).

Baixo o escenario de cambio climático, espéranse diminucións significativas na dispoñibilidade de auga en diferentes áreas do planeta. Esta fraxilidade crecente nos recursos hídricos provoca unha necesidade de comprender en profundidade os cambios inducidos polo quecemento global e así poder garantir un subministro suficiente de auga se se toman medidas adecuadas. Polo cal, é crucial coñecer que dependencia existe entre o transporte de humidade, dado pola relación fonte-sumidoiro de humidade, e o cambio climático, así como determinar como esta relación inflúe na precipitación continental para rexións específicas. Ademais, como xa se apuntou, os cambios na circulación atmosférica global poden afectar ao comportamento dos patróns eólicos rexionais, e a capacidade de produción de enerxía eólica poderíase ver comprometida nun futuro. Os cambios futuros na distribución espacial e temporal do vento a 10 m implicarían cambios na produción enerxética asociada. Polo tanto, unha análise de proxeccións futuras mellloraría a capacidade de produción e a eficiencia enerxética para unha mellor planificación das rexións ideais para a instalación dos polos eólicos.

Actualmente téñense logrado avances notables nos estudos enfocados a determinar onde se orixinan as precipitacións e cal é a relación fonte-sumidoiro de humidade, establecendo climatoloxías para a maioría das rexións do mundo. Moitos estudos centráronse en caracterizar o papel desempeñado polos mecanismos de transporte de humidade na atmosfera, por exemplo desde as rexións tropicais ou subtropicais ata latitudes máis altas. En particular, nos últimos anos, e en referencia a estes mecanismos, os estudos sobre Ríos Atmosféricos (ARs) foron abundantes. Estes sistemas meteorolóxicos considéranse un dos principais mecanismos de

transporte de humidade global xunto cos sistemas de chorro de baixos niveis, ciclóns tropicais e extratropicales, e mais os monzóns. En concreto, a maioría dos estudos enfocáronse en analizar a intensidade e frecuencia dos ARs, en menor medida na determinación das fontes de humidade que contribúen á humidade transportada, e moito menos na análise de proxeccións para clima futuro que estuden a relación fonte-sumidoiro de humidade durante períodos longos.

O enfoque lagrangiano é unha metodoloxía amplamente utilizada durante as últimas décadas para investigar a relación fonte-sumidoiro de humidade. Estudos previos baseados neste enfoque non tiñan ata o día de hoxe cuantificado como o cambio climático influirá na importancia das rexións fontes, como se modificará o transporte da humidade cara aos seus sumidoiros (áreas continentais), e menos aínda realizado esta análise mediante o uso de modelos rexionais de alta resolución espacial. Por outra banda, con respecto aos cambios do campo do vento e as súas variables derivadas no futuro, téñense levado a cabo numerosos estudos na rexión do océano Atlántico utilizando modelos climáticos globais (GCMs) das fases diferentes fases do Proxecto de Intercomparación de Modelos Acoplados (CMIP). Con todo, a súa baixa resolución inicial dificulta a obtención de información máis precisa sobre o impacto do cambio climático a escala rexional, principalmente en rexións onde o tempo e o clima non sexan moi homoxéneos.

Por tanto, esta tese céntrase no estudo e análise do transporte de humidade e a velocidade do vento a 10 m mediante a realización de simulacións rexionais de alta resolución espacial na rexión do Atlántico Norte para cubrir parte das brechas que seguen existindo actualmente nestes ámbitos do coñecemento. Isto permitirá ter ferramentas melloradas para a xestión dos tomadores de decisións e actuar da maneira máis eficaz ante un determinado sinal de cambio climático futuro e así poder minimizar os seus efectos.

Para abordar o obxectivo xeral proposto, realízase en primeiro lugar a necesaria rexionalización a alta resolución sobre o Atlántico Norte das variables meteorolóxicas implicadas no estudo mediante unha redución dinámica usando o modelo eureliano de mesoescala *Weather Research and Forecasting* (WRF) con núcleo dinámico ARW (WRF-ARW). Realizouse a avaliación desta rexionalización comparando con datos das reanálises ERA-Interim (ERA-I) e ERA5 do Centro Europeo de Prognósticos Meteorolóxicos a Prazo Medio (ECMWF). Esta avaliación estivo maioritariamente centrada na representación da relación fonte-sumidoiro de humidade en rexións concretas do océano Atlántico Norte para un período dun ano. Especificamente, utilizáronse diferentes configuracións e versións do modelo de dispersión de partículas lagranxiano Flexible PARTicle (FLEXPART), en concreto FLEXPARTv10.3 e FLEXPART-WRF (versión adaptada para o uso de datos procedentes do WRF). Para o procesamento das saídas destes modelos, desenvolveuse un novo software libre con grande eficiencia computacional. Posteriormente, utilizouse o conxunto de datos obtidos da redución dinámica con WRF para determinar cambios futuros na absorción anómala de humidade asociada aos ARs que chegan á Península Ibérica (PI) e na intensidade e posición das súas fontes de humidade. Tamén, desde un enfoque máis climatolóxico, analizáronse os cambios futuros nas fontes e nos seus sumidoiros de humidade na rexión de interese. Finalmente, estudáronse os cambios futuros para a velocidade do vento a 10 m e como as futuras variacións do patrón de vento inflúen na produción de enerxía eólica mariña. O estudo centrouse en tres subrexións importantes a ambos lados da conca do Atlántico Norte: a costa atlántica de Península Ibérica, a costa este dos EE.UU. e a rexión do Mar Caribe.

Os datos utilizados nesta tese proveñen de diferentes fontes: datos da reanálise do Centro Europeo de Prognósticos Meteorolóxicos a Medio Prazo (ERA-I e ERA5), resultados climáticos do *Community Earth System Model Version 2* (CESM2), e un conxunto (*ensemble*) de varios modelos climáticos considerados no último informe do Panel Intergobernamental sobre Cambio Climático (IPCC). Estes datos utilizáronse como condicións iniciais e de fronteira para forzar o modelo WRF-ARW e así obter as saídas rexionais a maior resolución espacial sobre a rexión do Atlántico Norte. As saídas de WRF-ARW utilizáronse logo como datos de entrada para o modelo FLEXPART-WRF. Como proxeccións de clima futuro utilizáronse os escenarios SSP2-4.5, SSP3-7.0 e SSP5-8.5, que representan un aumento de 4.5 W/m^2, 7.0 W/m^2 e 8.5 W/m^2 respectivamente (SSPs: Traxectorias Socioeconómicas Compartidas, das súas siglas en inglés). Estes escenarios presentan diferenzas entre si debidas a distintos niveis de forzamento radiativo proxectado cara finais de século, pero ao mesmo tempo mostran un amplo espectro de posibilidades de desenvolvemento socioeconómico desde un escenario máis positivo ata o máis extremo e negativo. Para as análises do transporte de humidade utilizouse un período longo de 30 anos: 2036-2065 para mediados de século (MC), 2071-2100 para finais de século (EC) e 1985-2014 como período de referencia histórico (HIST), utilizando unicamente o escenario SSP5-8.5. Para a análise do campo eólico e a densidade de potencia eólica (WPD) utilizáronse os tres SSPs, pero considerando períodos máis curtos de 5 anos: 2049-2053 para mediados de século (MC_5E), 2096-2100 para finais de século (EC_5E) e 2010-2014 para o período histórico (HIST_5E). Os cambios proxectados no futuro calculáronse como a diferenza do patrón esperado nos períodos MC e EC menos o patrón HIST.

Para a determinación do patrón de fontes e sumidoiros de humidade aplicouse unha metodoloxía lagranxiana amplamente utilizada nas últimas décadas, que consiste en seguir e computar os cambios de humidade específica ao longo das traxectorias das partículas nas que o volume da atmosfera é dividida. O modelo lagranxiano utilizado foi FLEXPART nas súas diferentes versións. As partículas son seguidas cada 6h durante un período de 10 días -tempo de residencia do vapor de auga na atmosfera-, ben cara atrás no tempo (para determinar as fontes de humidade dunha rexión) ou cara a adiante (para localizar sumidoiros). Neste estudo de transporte de humidade (para presente e futuro) consideráronse como fontes de humidade oceánicas o Atlántico Norte (NATL) e o Mar Mediterráneo (MED), e a propia Península Ibérica (para poder estudar procesos de reciclaxe de precipitación), e como os seus sumidoiros as rexións continentais circundantes, sobre as que se computou a humidade dispoñible para precipitar que a elas chega. Para o estudo dos cambios futuros nas fontes de humidade que contribúen á humidade transportada polos ARs, consideráronse para realizar a climatoloxía “control” en tempo histórico aqueles eventos que chegaron á Península Ibérica (LARs, polas súas siglas en inglés). Como variable para analizar estes cambios usouse a absorción anómala de humidade (AMU, polas súas siglas en inglés; diferenza entre as fontes de humidade climatolóxicas para unha rexión e as fontes para os días de LARs). O cálculo da AMU realizouse tanto para o período histórico como para mediados e finais do século, co fin de comparalos e determinar os cambios proxectados.

Para facilitar o post-procesamento das saídas das diferentes versións do modelo FLEXPART (FLEXPART e FLEXPART-WRF) implementouse unha nova ferramenta de software: TROVA (*TRansport Of water Vapor*), que facilita a aplicación de diferentes metodoloxías lagranxianas ás saídas dos modelos de dispersión. Ademais, TROVA permite considerar varias resolucións horizontais tanto para datos de entrada como de saída, e para as diferentes máscaras utilizadas como fontes de humidade (ben sexa nas análises cara a adiante no tempo como para cara atrás). Por tanto, TROVA pódese utilizar para procesar as saídas destes modelos de dispersión forzados tanto por ERA-I, ERA5, ou as simulacións rexionais de WRF forzado previamente con saídas de diferentes modelos climáticos. Esta versatilidade permite posteriormente o estudo de climatoloxías de fontes e sumidoiros de humidade, e os cambios proxectados en intensidade e localización das mesmas. Outra das vantaxes de TROVA é que ten unha alta eficiencia computacional debido á súa implementación con programación paralela, o que permite o seu uso en supercomputadores. Ademais, trátase dun software libre implementado en Fortran e Python dispoñible para toda a comunidade científica.

Unha vez desenvolto o software, realízase unha avaliación en período histórico dos campos espaciais do patrón de fontes de humidade asociado ás fontes seleccionadas neste estudo -NATL, MED e PI-, e tamén do patrón obtido nos sumidoiros para as fontes oceánicas. Nesta avaliación considéranse os resultados das saídas do modelo FLEXPARTv10.3 usando datos ERA5 a resolución de 1° e 0.5° e os campos obtidos con FLEXPART-WRF forzado cos datos rexionais de WRF a 0.18° (FLEX-WRF) inicializado con ERA5. A avaliación realízase utilizando como experimento de control FLEXPARTv9.0 forzado con ERA-I a 1°. En xeral, para as fontes de humidade obtívose que a correlación entre as diferentes configuracións variou desde 0.4 a 0.6, sendo a mellor para os campos de ERA5 a ambas resolucións. Observáronse poucas diferenzas notables nas configuracións en canto ao erro absoluto medio e a raíz do erro cuadrático medio, observándose estacionalmente o rendemento máis baixo no verán e o mellor no inverno e outono. Finalmente, observouse que os resultados obtidos con FLEX-WRF representan un mellor patrón espacial naqueles sumidoiros con orografía complexa, sobre todo durante primavera e verán, estacións de particular interese xa que é cando predominan os procesos de reciclaxe de precipitación.

En particular, para a análise dos sumidoiros de humidade asociada á fonte do Mar Mediterráneo (MED), as tres configuracións avaliadas respecto ao experimento control mostraron baixa dispersión espacial e, por tanto, valores altos de correlación. Ademais, obtivéronse valores do erro absoluto medio menores respecto a os obtidos na avaliación das fontes de humidade comentada anteriormente e o erro cuadrático medio foi maior, cun aumento no verán e unha diminución no outono. Ademais, FLEX-WRF foi a mellor configuración na representación do patrón de sumidoiros de humidade en rexións onde predomina a orografía complexa (principalmente en Europa central). Doutra banda, para NATL a magnitude do erro absoluto e a raíz do erro cuadrático medios foron superiores aos mostrados polo patrón de contribución de MED, debido a que este patrón é máis extenso tanto en latitude como en lonxitude, o que dificulta a súa mellor representación e esaxera as diferenzas entre os valores simulados e o experimento de control. Ademais, obtívose que a correlación para as tres configuracións oscilou entre 0.4 e 0.7 respecto ao experimento de control. Finalmente, a configuración FLEX-WRF mostra a menor habilidade para representar o patrón de sumidoiro asociado coa fonte NATL.

Unha vez avaliadas todas as configuracións, realizouse o estudo dos cambios futuros en intensidade e posición das fontes de humidade e os seus sumidoiros asociados. En concreto, proxectouse un aumento xeneralizado da humidade que alcanzará as zonas continentais circundantes procedente tanto do océano Atlántico Norte como do mar Mediterráneo. No período de mediados de século (MC), obsérvase un lixeiro aumento anual nas contribucións desde a conca do océano Atlántico Norte e do Mar Mediterráneo occidental. Para finais de século (EC) obsérvase un patrón con maiores valores respecto a os cambios esperados para MC. Ademais, espérase un aumento nos procesos de reciclaxe de precipitación na PI durante os meses de inverno e anualmente para MC e EC (relativamente superior neste último período), oscilando entre un 2 % e 8 %. Os resultados obtidos en relación ao aumento nas contribucións de humidade desde NATL e MED sobre a PI para finais de século son consistentes coa expectativa dun aumento da capacidade de almacenamento de auga da atmosfera compatible coa formulación de Clausius-Clapeyron. Doutra banda, proxéctanse contribucións maiores da fonte MED á precipitación continental nas zonas situadas ao sur do Mar Mediterráneo, tanto para MC como EC. Esta contribución tamén aumentará, aínda que en menor medida, sobre a PI, principalmente na tempada de verán, sendo maior para EC. A súa contribución sobre Europa do Leste diminuirá e para Europa occidental só se aprecia nas estacións de verán e primavera. A fonte NATL aumentará a súa contribución sobre a costa leste de América do Norte (principalmente no inverno e outono) e sobre as Illas Británicas maiormente no inverno, pero obsérvase unha diminución nas zonas do norte de Europa occidental, PI e na costa occidental de África.

En canto aos ARs que se desprazan sobre o Atlántico Norte, proxéctase un desprazamento latitudinal da súa posición para EC e un fortalecemento progresivo na súa intensidade ao longo do século. En concreto, espérase un aumento da dinámica advectiva destes sistemas, especialmente notable para os ARs que chegan á PI. Este comportamento é especialmente intenso nos corredores que conectan a Península Ibérica coas súas fontes de humidade. Doutra banda, en termos xerais, proxéctase un aumento da AMU, moi notable no inverno con aumentos do 9 % e 24 % para MC e EC, respectivamente. Ademais, obsérvase un desprazamento latitudinal cara ao Norte desta variable para o futuro, proxectándose aumentos xeneralizados para todo o ano, e en particular no inverno e outono para MC por encima dos 20 °N no Atlántico Norte central;

por baixo de 20 °N esta diminuirá lixeiramente. Para EC, o sinal dos cambios mostra valores máximos no inverno, sendo a AMU maior en rexións do Atlántico central e occidental, o Mar Caribe e o Golfo de México. Prevese que no outono as fontes de humidade sexan máis remotas cara ao oeste, feito asociado a un aumento da AMU desde a costa atlántica dos Estados Unidos.

Para pechar os estudos desta tese analizáronse os cambios futuros para a velocidade do vento a 10 m (V10) na rexión do Atlántico Norte. Concretamente, estudáronse as proxeccións de V10 considerando os escenarios SSP2-4.5, SSP3-7.0 e SSP5-8.5 para dous períodos de 5 anos para MC e EC. Os resultados mostran para SSP2-4.5 unha diminución de V10 no período MC_5E ao norte de 30 °N para o inverno e un aumento por baixo de 30 °N, excepto para a rexión oriental do Mar Caribe. Ademais, espérase unha diminución xeneralizada na primavera principalmente no océano Atlántico Norte, con excepción do Mar Caribe, pero proxéctanse aumentos para o verán e outono, exceptuando a rexión costeira sur de Estados Unidos. Para SSP3-7.0, no inverno continua a tendencia á diminución de V10, pero con dúas rexións onde aumenta: a Península Ibérica e África occidental. Ademais, espéranse aumentos para o verán e o outono no Mar Caribe, a costa este de EE. UU. e a PI, pero relativamente menores en comparación cos obtidos usando SSP2-4.5. Con todo, para SSP5-8.5, os cambios maiores proxéctanse para o inverno, observándose unha diminución notable sobre o Mar Caribe, preto da costa africana e en rexións por encima dos 50 °N. Ademais, a rexión do océano Atlántico Norte mostrará un incremento de V10 no verán e outono. Para EC_5E considerando SSP2-4.5 e SSP3-7.0 obsérvanse aumentos en comparación con MC_5E, sendo maiores baixo o escenario SSP5-8.5.

Finalmente, para determinar se os cambios de V10 afectan á densidade de enerxía eólica (WPD), e polo tanto á capacidade futura de xerar enerxía renovable eólica offshore, realízase un estudo desta variable en tres rexións de interese a ambos os dous lados da conca do océano Atlántico Norte: a costa atlántica da Península Ibérica (PI), a costa Este de Estados Unidos (US) e a rexión do Mar Caribe (CS). Para o cálculo da WPD emprégase unha extrapolación da velocidade do vento a unha altura de 120 m considerando unha atmosfera con estabilidade neutra e perfil logarítmico do vento. Os resultados mostran diferenzas entre os escenarios e as rexións de estudo. Así, para o escenario SSP2-4.5 en MC_5E espérase para a costa oeste da PI unha diminución de WPD en inverno, observándose os maiores cambios canto máis ao norte, e un aumento na primavera e verán, máis notable nesta última estación en rexións como a costa de Galicia e norte de Portugal. Baixo o escenario SSP3-7.0 proxéctase un aumento de WPD no inverno, con valores destacados no norte de Galicia, e unha diminución notable na primavera ao longo de toda a costa oeste da PI. En verán e outono, espéranse aumentos no noroeste da PI. Para SSP5-8.5 e MC_5E é destacable o aumento na rexión norte da PI no outono. Con todo, para EC_5E no inverno espéranse aumentos notables ao noroeste da PI, estendéndose ata os 40 °N. No verán proxéctanse aumentos considerables en toda a costa atlántica da PI considerando todos SSPs, pero máis salientables para SSP5-8.5.

Para a rexión da costa leste de EE.UU., utilizando SSP2-4.5 para MC_5E, proxéctase unha diminución de WPD no inverno para latitudes superiores a 35 °N, mostrando valores máximos ao redor das costas dos estados de Maine, Massachusetts, New Hampshire e New Xersei. Durante o verán proxéctanse aumentos na costa de Carolina do Norte, Carolina do Sur e Virxinia. Baixo o escenario SSP3-7.0, espérase que WPD diminúa no inverno, sendo contrario o comportamento no outono, proxectándose un aumento na costa dos estados máis ao norte. Considerando SSP5-8.5, no inverno espérase un patrón diferente, mostrando aumentos por baixo de 40 °N e diminucións por riba de 40 °N. Para EC_5E destaca a diminución baixo o escenario SSP3-7.0 e o aumento no verán para SSP5-8.5.

Na rexión do Mar Caribe, considerando SSP2-4.5 para MC_5E na tempada seca espérase un fortalecemento de WPD principalmente para a conca de Venezuela comparado co período histórico. Para a tempada húmida, obsérvase un incremento en rexións da conca de Colombia e Venezuela, ao redor das costas sur e norte da Española, e na rexión oriental de Cuba. Considerando SSP3-7.0, para a estación seca obsérvase unha diminución na maior parte do Mar Caribe, mostrándose aumentos na conca de Colombia. Ademais, espérase un comportamento diferente na tempada húmida, onde se proxecta un aumento nas costas de Colombia e Venezuela. Finalmente, utilizando SSP5-8.5 os cambios para MC son similares aos mostrados para SSP3-7.0, pero diferentes respecto ao escenario SSP2-4.5, xa que se proxecta un aumento considerable para toda a rexión estudada. Para EC, agárdase unha diminución de WPD para a estación seca nas concas de Iucatán e Colombia utilizando todos os SSPs, cun lixeiro aumento na conca de Venezuela. Para a tempada húmida, obsérvase un aumento destacable no Mar Caribe, exceptuando no Iucatán.

Dos resultados obtidos pódese concluír que o software TROVA permite estudar a relación fonte-sumidoiro de humidade para o clima actual e futuro. O modelo de dispersión FLEXPARTv10.3 forzado coa reanálise ERA5 (última versión do ECMWF), nunca utilizado anteriormente, con diferentes resolucións espaciais, mostra adecuadamente as rexións de fontes e sumidoiros de humidade comparado coa versión FLEXPARTv9.0 executado con datos ERA-I. Ademais, a versión de FLEXPART forzado con datos obtidos a partir dunha redución dinámica usando WRF e a reanálise ERA5 representa de forma similar as fontes e sumidoiros de humidade, pero cunha mellor resolución espacial. Finalmente, esta metodoloxía de redución de escala dinámica permite o estudo de fontes e sumidoiros de humidade en clima futuro a unha maior resolución espacial, xa que rexionaliza datos de diferentes modelos climáticos globais con diferentes escenarios de forzamento radiativo como condicións iniciais e de fronteira. Este derradeiro punto é unha das principais demandas do último informe do IPCC para poder mellorar as simulacións do comportamento da humidade e o seu transporte.

List of Figures

List of Tables

List of Acronyms

- **NATL:** North Atlantic Ocean source
- **MED:** Mediterranean Sea source
- **IP:** Iberian Peninsula
- **IPCC:** Intergovernmental Panel on Climate Change
- **V10:** Wind speed at 10 m
- **CC:** Clausius–Clapeyron
- **IVT:** Vertically integrated water vapour transport
- **SST:** Sea surface temperature
- **E:** Evaporation
- **P:** Precipitation
- **ARs:** Atmospheric rivers
- **LLJs:** Low-level jet systems
- **IWV:** Total vertically integrated water vapor flux
- **WCB:** Warm conveyor belt
- **TMEs:** tropical moisture export
- **US:** United States
- **CS:** Caribbean Sea
- **GCMs:** Global climate models
- **CMIP6:** Coupled Model Intercomparison Project Phase 6
- **CMIP5:** Coupled Model Intercomparison Project Phase 5
- **ScenarioMIP:** Scenario Model Intercomparison Project
- **SSPs:** hared socioeconomic pathways
- **RCMs:** Regional climate models
- **WRF:** Weather Research and Forecasting
- **FLEXPART-WRF:** FLEXible PARTicle dispersion model version for WRF
- **FLEXPART:** FLEXible PARTicle dispersion model
- **LARs:** Landfalling ARs arriving in the Iberian Peninsula
- **TROVA:** TRansport Of water Vapor
- **ERA-I:** ERA-Interim reanalysis data
- **ECMWF** European Center for Medium-Range Weather Forecasts
- **CESM2:** Community Earth System Model Version 2

- **ESGF2:** Earth System Grid Federation
- **CMIP6-ENS:** Bias-corrected CMIP6 global database
- **AMU:** Anomalous moisture uptake
- **IPART:** Image-Processing-based Atmospheric River Tracking
- **WPD:** Wind power density
- **Z500:** Geopotential height at 500 hPa
- **PRPs:** Precipitation recycling processes

1

Introduction

The importance of climate change on the development of society is an indisputable reality, as highlighted in the sixth report of the Intergovernmental Panel on Climate Change (IPCC, 2021). Climate change has been studied in detail with regard to variables such as precipitation, temperature (and its extremes), sea level rise, Arctic sea ice, and atmospheric circulation changes (Ramanathan and Feng, 2008; Xu and Ramanathan, 2017; Steffen et al., 2018). However, some variables related to the atmospheric branch of the hydrological cycle, such as moisture transport associated with extreme precipitation events and wind speed (for instance, the wind speed at a height of 10 m (V10), which is important for renewable energies) must be studied in greater depth.

In addition, many of the consequences or implications of these variables are related to processes or mechanisms that, according to the IPCC, need to be improved on a regional scale. Recent evidence modelling shows that there are increases in precipitation extremes which show limitations owing to the dependence of this variable on microphysical processes (Singh and O'Gorman, 2014; Sandvik et al., 2018). Furthermore, these extremes, on an instantaneous scale, are sensitive to these processes; however, on a daily scale, they depend on the degree of convective agg irrigation (Bao and Sherwood, 2019). Therefore, regional-scale studies that represent regional processes and their influence on dynamics are important for understanding how regional precipitation and hydrology will change in the face of climate change (Allan et al., 2020).

Near-surface wind speed plays a crucial role in climate system physics, which could have an important impact on socioeconomic and environmental factors (Roderick et al., 2007), including evapotranspiration and precipitation (McVicar et al., 2012), damage associated with wind speed, such as tornadoes and significant sea level rise (He et al., 2021), air quality (Wu et al., 2020), and the wind energy industry (Carvalho et al., 2017; Santos et al., 2018).

This thesis focuses on the moisture transport and wind speed at the surface using high-resolution regional simulations. This allows an increase in the reproduction of physical processes at higher spatial resolutions up to scales that allow convection (a few kilometres). The results of this study will demonstrate in more detail the influence of climate change and its regional impact and will inform decision-makers. For instance, the most immediate impact of extreme precipitation is the potential for flooding, which increases the risk of landslides (IPCC, 2021). Extreme rainfall can also decrease water quality, affecting human health, aquatic ecosystems, and fishing operations (EPCC, 2023).

1.1 The hydrological cycle and its importance

The atmosphere retains a small amount of the total water available on Earth. They play a crucial role in linking the reservoirs of oceans, lakes, soils, continental and sea ice, and rivers through moisture transport, evapotranspiration, and precipitation. While water vapour represents only approximately 0.25 % of the atmospheric mass (Seidel, 2002; Trenberth and Smith, 2005; Quante and Matthias, 2006; Wallace and Hobbs, 2006), it has a significant influence on global climate and weather patterns (Held and Soden, 2000). In addition, the hydrological cycle involves moisture evaporation in one region and precipitation in another, as determined by the atmospheric, oceanic, and hydrological transport of water (Gimeno et al., 2012). In oceanic areas, the evaporation rate is greater than the precipitation rate; therefore, the oceans represent a net moisture source. This moisture is displaced by transport from the atmosphere to continental regions. However, continents, where precipitation is predominant, act as moisture sinks. Surface water reaches rivers, groundwater, and other bodies and is transported to the ocean, closing the hydrological cycle. A schematic representation of this cycle is shown in Figure 1.1 (Allan et al., 2020).

Therefore, the hydrological cycle can be summarised as a series of stages in which water changes in a closed cycle, circulating between different subsystems before returning to its initial stage (Peixoto and Oort, 1992; Palazzi and Provenzale, 2016). Moreover, the hydrological cycle determines an annual evaporation rate of approximately half a million km^3 of water, 86 % of which originates in the oceans and, to a lesser extent, continents (Quante and Matthias, 2006). In addition, 90 % of the water evaporates in the ocean and precipitates back into the ocean. However, the remainder is continuously transported and precipitated. Of this precipitation, two-thirds is obtained on the continents through a process called precipitation recycling and the rest enters the ocean directly (Trenberth and Dai, 2007; Van der Ent and Savenije, 2011).

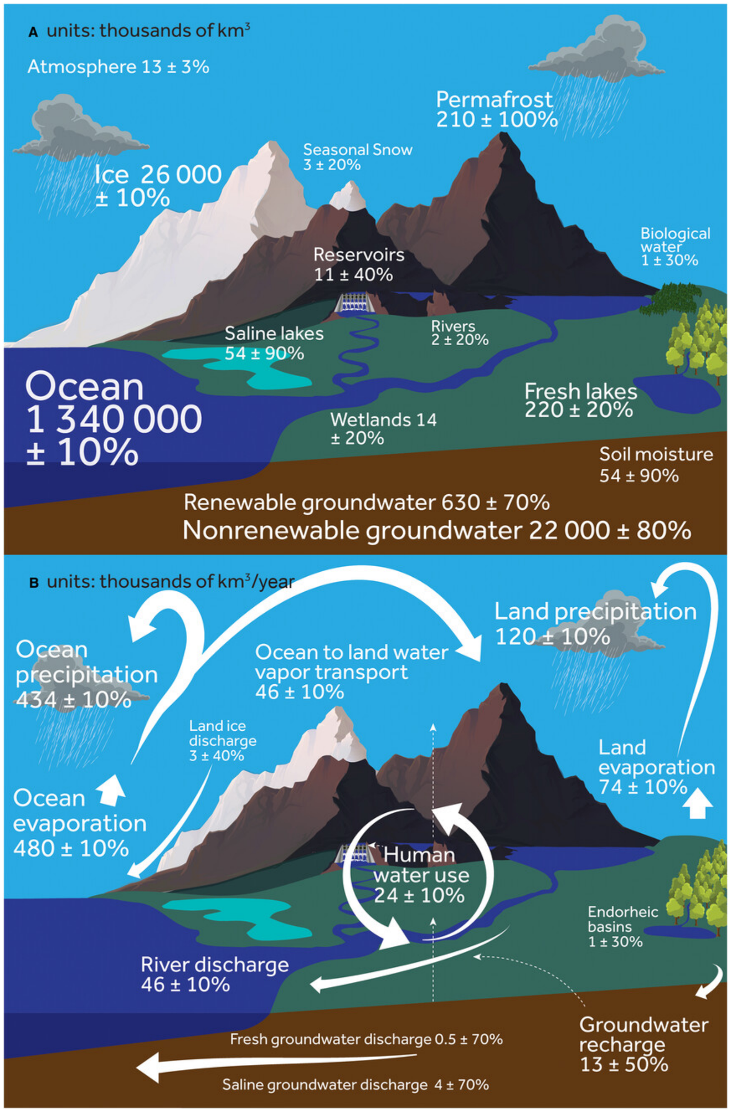

Figure 1.1: Representation of the global water cycle: (a) stores (in thousands of km^3) and (b) flows (thousands of km^3 per year). Taken from Allan et al. (2020).

Therefore, the details of the mechanisms and processes that govern the evaporation of water from oceans and the atmospheric transport of moisture are important questions in atmospheric sciences (Gimeno, 2013). Many studies have investigated the atmospheric components of the hydrological cycle to identify moisture sources and sinks and their relationship with precipitation over continents. Therefore, a study of the changes in moisture transport and its associated sources and sinks would provide detailed information on the effects of climate change on hydrological cycles (Gimeno et al., 2012).

1.2 Changes in the hydrological cycle: climate change influences

Under the influence of climate change, modifications to the hydrological cycle, both in nature and intensity over time, constitute a major challenge facing humanity. It is expected that if there is no reduction in greenhouse gas and CO_2 emissions, the mean temperature increase will exceed 2 °C in the 21st century (IPCC, 2021). As a thermodynamic response, it is expected that for every 1 °C increase in mean temperature, the water vapour available in the atmosphere will increase by 7 % (Trenberth et al., 2003; O'Gorman and Muller, 2010) considering the Clausius–Clapeyron relationship (Wentz and Schabel, 2000). This will in turn lead to other notable modifications in global moisture transport; global annual average evaporation will increase (Held and Soden, 2006), causing changes in evaporation rates in different oceans (Yu, 2007). These factors will lead to an increase in vertically integrated water vapour transport (IVT) (Espinoza et al., 2018; Sousa et al., 2020). According to Huang et al. (2020), these changes will predominate in mid-latitude circulation. Additionally, heavy precipitation and its frequency will intensify as the atmosphere increases in temperature (Min et al., 2011; Pall et al., 2011; O'Gorman, 2015; Fischer and Knutti, 2016; Neelin et al., 2017).

Moreover, increases in moisture near surface levels provide a reference for extreme precipitation increases influenced by microphysical and dynamic processes (O'Gorman, 2015; Pendergrass et al., 2016; Pfahl et al., 2017), which in turn are spatially and temporally dependent (Pendergrass, 2018). Therefore, streamflow, flooding, and their responses to precipitation in the context of climate change are complex, and an exact relationship that represents the hazard of flooding versus monthly precipitation has not yet been determined (Stephens et al., 2015; Emerton et al., 2017). Nieto et al. (2014) proposed that changes in certain hotspot moisture source regions are related to the expected increase in the intensity of extreme precipitation and drought events (Donat et al., 2016, 2019), possibly with a magnitude significantly different from current events during the 21st century (Giorgi, 2019).

A generalised *"dry gets drier and wet gets wetter"* mechanism was projected, in which higher precipitation is reinforced by higher gross moisture stratification (Chen et al., 2019). Finally, the availability of water resources (Cosgrove and Loucks, 2015) exhibits marked latitudinal and regional differences (Madakumbura et al., 2019). This is of great global importance as the global population is continually increasing and consumption patterns are changing, while humanity has not developed the tools necessary for the future management and planning of water resources (Dubois et al., 2011; Ritchie and Roser, 2019).

Furthermore, modifications in atmospheric circulation patterns are expected with a warmer atmosphere, which determines modifications in the atmospheric water equilibrium both globally and regionally (Allan et al., 2020). Globally, climate change is expected to weaken and expand the tropical circulation with the latitudinal displacement of dry tropical regions and mid-latitude jets (Collins et al., 2013). Modifications in land use and irrigation determine responses at a local scale that generate changes in atmospheric circulation due to differences in the balance of energy and humidity of the surface (Wey et al., 2015; de Vrese et al., 2016; Wang-Erlandsson et al., 2018). This indirectly responds to an increase in radiative forcing (Samset et al., 2016, 2018) and spatial changes in precipitation (Bony et al., 2013; Richardson et al., 2016).

Specifically, changes in global atmospheric circulation have a lower occurrence probability than thermodynamic drivers. The weaker Walker circulation is an example of these changes under a changing climate (Sohn et al., 2013; DiNezio et al., 2018). Monsoon thermodynamic amplification is projected to be the opposite of the decrease in tropical circulation; however, a decrease in monsoon precipitation is expected because of a possible decrease in aerosol emissions (Christensen et al., 2013; Endo et al., 2018). Furthermore, a southward shift of the Intertropical Convergence Zone was observed due to the cooling of the Northern Hemisphere, which caused a drought in the Sahel in 1980 (Hwang et al., 2013; Undorf et al., 2018). However, a limited role has been determined for warming increases in the Arctic (Cohen et al., 2014; Dai and Song, 2020) and sea ice decreases in determining changes in weather patterns in mid-latitudes that can generate floods or droughts.

The North Atlantic is an interesting region given its atmospheric and oceanic variability, which determines the weather and climate conditions of the surrounding continental regions (Woollings et al., 2010). Several studies have demonstrated changes in prevailing climate systems in the North Atlantic. For example, in the period 2005–2016, a jet stream speed increase prevailed in the winter season; however, in summer, it shifted towards the south owing to a weakening of the North Atlantic Oscillation (Robson et al., 2018). In addition, it is projected that with an increase in radiative forcing, the winter North Atlantic storm track will intensify and extend towards the east (Ulbrich et al., 2008). Furthermore, the sea surface temperature (SST) in the subpolar gyre is cooling, unlike the general pattern of global warming (Rahmstorf et al., 2015). Additionally, increases in the zonal flow regime in winter and an increase in the anticyclonic circulation to the west of the United Kingdom in summer have been reported (Rousi et al., 2021). These changes can influence floods and droughts in Europe. Additionally, a sharp decrease in the frequency of the Scandinavian blockade was observed. Finally, according to the latest IPCC report (IPCC, 2021), the Atlantic meridional circulation is projected to weaken throughout the 21st century under all climate change scenarios. If these projections are true, notable changes in the regional climate patterns and water cycle are expected. In addition, a shift of tropical rains towards the south is projected, with a possible weakening of the African and Asian monsoons, contrary to the strengthening of the southern monsoon and a latitudinal shift of the storm track in the North Atlantic, leading to a drier Europe (Roberts et al., 2012; Orme et al., 2017).

1.3 Moisture sources and sinks

Moisture source and sink studies are essential for continuing hydrological cycle studies at different time scales. This makes it easier to determine source-sink relationships at regional and global scales and the crucial mechanisms that transport moisture (Gimeno et al., 2020). This source-sink relationship implies evaporation and precipitation processes. Evaporation is the process by which water molecules transform into a gaseous state (water vapour). Subsequently, this water vapour remains in the atmosphere for approximately 10 days before condensing and reaching the surface in the form of precipitation (Van Der Ent and Tuinenburg, 2017; Gimeno et al., 2021). Therefore, the predominance of evaporation or precipitation in certain regions determines the presence of moisture sources or sinks.

Moisture sources are defined as regions where evaporation (E) dominates precipitation (P) ($\mathrm{E} - \mathrm{P} > 0$) and moisture sinks as regions where precipitation prevails over evaporation ($\mathrm{P} - \mathrm{E} > 0$), with a net moisture loss (e.g., Stohl and James, 2004, 2005; Gimeno et al., 2010b; AM, 2023). On a global scale, the regions of maximum divergence of the vertically integrated moisture flux correspond to moisture source regions (Trenberth and Guillemot, 1998) and they can be defined as threshold-based; for instance, 750 mm/yr for oceanic sources and 500 mm/yr for land sources, as in Gimeno et al. (2010a). The main moisture sources are located in oceanic subtropical areas, inner continental seas, and major river basins, such as the Amazon and Congo rivers (Harrison et al., 2016). In contrast, the most extended sink regions, which can be considered large moisture sinks, are located in the Intertropical Convergence Zone (Waliser and Graham, 1993; Schneider et al., 2014) and other secondary regions in mid-latitudes, mainly in winter, associated with storm trajectories (Gimeno et al., 2012; Hawcroft et al., 2012; Papritz et al., 2014; Nieto et al., 2019; Papritz et al., 2021).

Gimeno et al. (2010a) showed that, in general, moisture source regions play an asymmetric role in precipitation generation, especially over land. These authors emphasised that some landmasses receive moisture from one or more global sources belonging to a specific hemisphere. Furthermore, continental areas that receive moisture contributions from a single source may be more affected by climate change than regions that receive moisture contributions from multiple sources (Gimeno et al., 2012). In the Northern Hemisphere, there is a hot-spot area, the Iberian Peninsula, that is positioned in a previlegious latitude (Giorgi, 2006; Diffenbaugh et al., 2007; Diffenbaugh and Giorgi, 2012; Masson-Delmotte et al., 2022) that receives moisture from two major global moisture sources: the North Atlantic Ocean and Mediterranean Sea. These moisture sources and the Iberian Peninsula sink area are located in the North Atlantic, which is the region of interest in this thesis (see Data and Methodology).

Specifically, the North Atlantic is classified as the main source of precipitation on a global scale because of its moisture contribution to precipitation in different regions on both sides of the Northern Hemisphere. Its moisture contribution is notable in eastern North America, Central America, and northern South America, mainly during summer. However, in winter, its influence increases in Europe, northern Africa, and central South America (Gimeno et al., 2010a). The Mediterranean Sea is a very important moisture source for the surrounding continental regions. In winter, it contributes to the humidity that causes precipitation in areas located mainly in northeastern Europe; however, in summer, it contributes in all directions, extending to northern Europe, northeastern Africa, and the Middle East (Gimeno et al., 2010b; Nieto et al., 2010). The Iberian Peninsula is a sink for these two large oceanic sources, but at the same time, it is considered a moisture source because it presents in the central and eastern regions the process of so-called precipitation recycling (Rios-Entenza et al., 2014; Rios-Entenza and Miguez-Macho, 2014).

Over the last few decades, multiple methodologies have been used to determine moisture sources and sinks. A review of them, as well as their use, advantages, and disadvantages, was presented by Gimeno et al. (2012). These methodologies include analytical or box models, Lagrangian and Eulerian numerical models and physical moisture tracers. Specifically, analytical or box models are simple tools for studying the vertically integrated water vapour balance considering a series of assumptions. For example, these studies considered negligible changes in atmospheric water storage or well-mixed atmospheres. Their approximations indicate that they are less complex models owing to their implementation and because they require fewer computational resources. However, they present limitations in the analysis of physical phenomena related to moisture transport. In addition, the Lagrangian and Eulerian numerical models allow for a deeper study because they consider tracers that include many physical processes during the residence time of water vapour in the atmosphere. Winschall et al. (2014) proposed a comparison between Eulerian and Lagrangian models, concluding that Lagrangian models are more acceptable for climatological analysis because of their computational efficiency. The Eulerian approach is more suitable for case studies, although it requires predefined moisture sources because it includes processes such as precipitation, evaporation, and turbulent mixing. Finally, the ideal method for evaluation is the use of physical tracers which analyse hydrogen and oxygen isotope concentrations in precipitation and water vapour (Gimeno et al., 2020).

1.4 Atmospheric rivers (ARs): a major moisture transport mechanism

Low-level jet systems (LLJs) and atmospheric rivers (ARs) play essential roles in global atmospheric moisture transport. According to Gimeno et al. (2016), LLJs are important mechanisms in (sub)tropical regions, whereas ARs are crucial in extratropical regions. ARs have been well described on both global and regional scales in investigations focusing on climatological characteristics (Waliser et al., 2012; Rutz et al., 2014; Ralph et al., 2013b; Maclennan et al., 2023), and on moisture transport (Ramos et al., 2018; Vázquez et al., 2018; Algarra et al., 2020). LLJs have been analysed and characterised in different regions, focusing on moisture transport (Stensrud, 1996; Marengo et al., 2004; Algarra et al., 2019). A more detailed study of both mechanisms and their associated moisture transport will provide a greater perspective on future changes and physical support that contribute to climate projections (Gimeno et al., 2010a, 2012).

However, moisture transport mechanisms such as monsoons (Dominguez et al., 2008) and tropical cyclones (Pérez-Alarcón et al., 2022), which contribute significantly to the precipitation that reaches certain regions of the planet, should not be ignored. For instance, monsoons have been studied in North America (Higgins et al., 2004), Asia, Australia, and New Zealand (Smith et al., 2008; Pope et al., 2009), Pérez-Alarcón et al. (2022, 2023) analysed tropical cyclones for different basins, focusing on their moisture sources.

The present study focuses on ARs, as these systems occur and impact the North Atlantic region. ARs were defined by international experts during an International ARs Workshop as "*a long (>* 2000 *km), narrow, and transient corridor of strong horizontal water vapour transport from the subtropics to mid-latitudes (Zhu and Newell, 1998), that is typically associated with a low-level jet stream ahead of the cold front of an extratropical cyclone*" (AMS, 2022). This definition was accepted by the American Meteorological Society and incorporated into the glossary of meteorological terms. ARs are associated with almost all (~ 90 %) of the total vertically integrated water vapour flux (IWV) in mid-latitude regions and at the same time are simultaneously related to the warm conveyor belt (WCB) to the mid-latitude cyclone pre-cold-frontal region. It is generally accepted that more than 90 % of the total IWV at mid-latitudes is carried by these structures. Moreover, ARs are often associated with the pre-cold frontal regions of extratropical cyclones in the warm conveyor belt (Carlson, 1990; Madonna et al., 2014; Binder et al., 2016; Wandel et al., 2021; Joos et al., 2023). These mechanisms present a region with high specific humidity at low levels, along with a vertical distribution of equivalent potential temperature and strong winds at low levels (Ralph et al., 2004, 2005, 2018), showing low-level sinking ahead of the AR. In addition, the relationship between warm conveyor belts and tropical moisture export to understand ARs was highlighted by Dettinger et al. (2015). Figure 1.2 shows in detail the structure and characteristics of AR in detail.

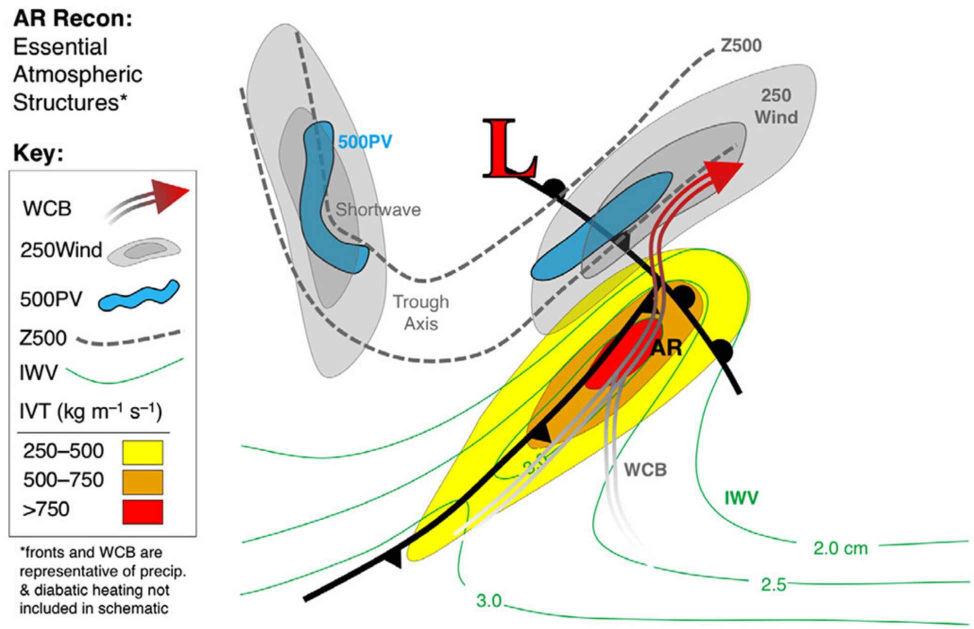

Figure 1.2: Schematic of atmospheric structures essential for AR recognition. Taken from Wilson et al. (2022).

Additionally, the moisture origin of an AR occurs in two ways (Bao et al., 2006): the local convergence of moisture associated with the extratropical cyclone cold front and tropical moisture transport towards the poles. According to Matrosov (2013), three precipitation regimes associated with AR predominate with a similar average frequency: i) "cold" rain given by ice precipitation observed in higher latitudes, ii) "warm" rain, with a predominance of a certain amount of ice precipitation above the freezing point, and iii) a "mix" of both precipitation regimes.

AR can be detected using the following approaches: i) integrated water vapour from satellite measurements, reanalysis data, or model outputs (Ralph et al., 2004; Dettinger et al., 2011; Ralph et al., 2013a; Guan and Waliser, 2015; Collow et al., 2022). Specifically, the IWV criteria are based on the amount, length, and width parameters of the IWV pattern, e.g., areas with IWV $>$ 2 cm, IWV $<$ 1000 km, and IWV $>$ 2000 km. ii) Determining IVT from 1000 to 300 hPa from reanalysis or atmospheric models (Zhu and Newell, 1998) considering thresholds in IVT to define an AR (IVT250, this threshold determines that an AR exists in a continuous region greater than or equal to 2000 km in length with IVT $\geq$ 250 kg m^{-1} s^{-1}). iii) Considering filters for filamentous moisture structures without considering the thresholds for the IVT or IWV fields. These methods perform spatiotemporal "spikiness" filtering on the variables mentioned above, showing a lower sensitivity to parameter selection.

In extratropical regions in both hemispheres, ARs are crucial for moisture transport (Gimeno et al., 2014; Guan and Waliser, 2015). Moreover, ARs provide a large amount of water vapour, causing intense rainfall that occasionally triggers disastrous floods, landslides, and destruction of different ecosystems. However, in some desert regions, such as California and Arizona in the United States and Baja California in Mexico, they are important for providing precipitation (Cavazos and Rivas, 2004; Dettinger et al., 2015; Rivera et al., 2014). The occurrence of ARs is prominent in other regions. For example, southern Africa is affected by the occurrence of ARs, which feed into the flood regions in South Africa (Ramos et al., 2017; Blamey et al., 2018). They are also found in colder regions, such as Antarctica, where the contribution of AR snowfall was up to 30 % from 2010 to 2019 but increase in the period from 2015 to 2019 (Li et al., 2023).

Furthermore, the moisture sources of ARs that affect the Arctic have been characterised (Vázquez et al., 2018). Case studies of AR associated with a cutoff and the extratropical transition of a tropical cyclone were conducted in Australia (Qi et al., 1999) and New Zealand (Sinclair, 1993). Specifically, in Australia, ARs contribute 20–35 % of the annual rainfall in southeastern Australia and 10–20 % in southwestern Australia (ARIA, 2023). In South America, ARs determine strong transport from the Pacific, causing winter orographic precipitation over the central region of Chile (Viale and Nuñez, 2011), with maximum rainfall recorded at mountaintops (Falvey and Garreaud, 2007).

In southern Europe, ARs determine 20–30 % of the total precipitation, particularly in the autumn and winter months, and ARs determine day numbers with annual maximum rainfall for the Western European region (Eiras-Barca et al., 2021). This behaviour has been highlighted in the coastal regions of Western Europe (Lavers and Villarini, 2013). Eiras-Barca et al. (2018) showed that although most flood events in the NW Iberian Peninsula are not caused by AR, they are generally responsible for extreme coastal cases. Ralph et al. (2019) proposed a scale of 1–5 (beneficial-hazardous) to characterise the impacts of ARs on the west coast of the United States. This scale was adopted by Eiras-Barca et al. (2021) and applied to the shores of Europe. They found that the most frequent ARs in Europe were of categories 1–2, determining the highest percentage of precipitation, with little association with extreme precipitation events. Although ARs of categories 3–5 events are less probable, they generate a minor contribution to annual precipitation and are associated with extreme rainfall.

ARs are also not exempt from the effects of climate change. With increasing temperature, the humidity in the atmosphere will increase. This was demonstrated by the Clausius-Clapeyron relationship of 7 % K^{-1}, which is projected for the future climate. Therefore, in contexts where the atmosphere is more humid, ARs are projected to transport greater amounts of moisture (Lavers et al., 2013). Additionally, an increase in extreme precipitation events related to ARs is projected (e.g., Lavers and Villarini, 2015; Espinoza et al., 2018). Therefore, numerous studies have projected that in a more humid atmosphere, the moisture flux will increase and, consequently, ARs will increase in intensity and frequency (Ramos et al., 2016; Espinoza et al., 2018; Kamae et al., 2019). In addition, ARs present a generalized significant increase in anomalous moisture uptake (AMU) (Algarra et al., 2020). These changes in the wind field (Zhang et al., 2019; Sousa et al., 2020) have a notable impact on society and different ecosystems.

1.5 Changes in the wind field: Implications for wind energy

The wind speed at a height of 10 m (V10) is an important field for analysis in a changing climate because modifications in V10 significantly influence social and environmental development (Pryor et al., 2006). Specifically, V10 strengthening can aggravate moisture and heat fluxes at the air-sea interface (Renault et al., 2017) or increase soil erosion, causing dust storms (Alizadeh-Choobari et al., 2014; Wang et al., 2017). The influence of changes in V10 on atmospheric variables has been documented. For example, Donohue et al. (2010); Niyogi et al. (2011) and McMahon et al. (2013) found that changes in V10 influence evaporation and, therefore, the hydrocarbon cycle in different regions. Furthermore, Liu et al. (2014) demonstrated that decreases in V10 led to a decrease in the expansion of drought areas in China. Araghi et al. (2022) showed that changes in V10 modified the total evapotranspiration, aboveground biomass, and efficiency in the use of water resources and crops. Finally, Jeong et al. (2020) demonstrated that V10 could determine variations in precipitation regimes. Therefore, modifications of V10 should be considered in studies of the impacts of changing climates, with an emphasis on regions with drought occurrence.

On the other hand, renewable energy sources are an ideal way to decarbonise the economy and reduce greenhouse gas emissions. Currently, onshore and offshore wind power stand out in the context of renewable energy. Both are obtained by taking advantage of the wind speed. The first is generated when wind turbines are physically located over land and therefore generate electricity from the wind; however, the second is when the turbines are above water (generally oceans) and are used for the same objective. Specifically, it is known that offshore wind energy is a highly developed energy source with projections to increase its growth in the future associated with technological development in this sector. However, possible changes in V10 owing to climate change should be considered as these changes can impact the production of offshore wind energy. Several authors have shown that a 1–5 % decrease in wind speed can lead to 1.7–8.6 % losses in wind energy generation (Jacobson and Kaufman, 2006; He et al., 2010). Therefore, offshore wind energy is sensitive to climate change. Thus, in this thesis, we focus on V10, which is related to offshore wind energy production.

In addition, regions on both sides of the North Atlantic (Europe and the United States East Coast) have shown an evolution in offshore wind energy studies, highlighting that it is a region with great availability of offshore wind resources. The North Sea has the highest density of offshore wind farms in the world. With the United Kingdom, Belgium, the Netherlands, and Germany all showing notable advances in their installed offshore wind capacity in recent years

(GWEC, 2020). Increases in offshore wind farm density are expected in different regions of the North Atlantic Ocean as the technology of this wind farm type develops (IREA, 2019; GWEC, 2021). This increase has been demonstrated by installation off of the Iberian Peninsula's west coast, which is a suitable region for offshore wind farms (Salvador et al., 2018; Costoya et al., 2020b). According to several authors (e.g., Costoya et al., 2020a; deCastro et al., 2019), the exploitation of offshore wind resources should increase along the eastern coast of the United States. Finally, changes in offshore wind energy production in the Caribbean Sea region may be of great economic interest. Specifically, this region is composed of islands with separate electrical systems. Therefore, this type of energy can improve energy production.

Finally, global climate models (GCMs) have been used to analyse future wind changes and their implications for wind energy in future climates considering different climate change scenarios (Stocker, 2013). Currently, GCM outputs corresponding to the 6th phase of the Coupled Model Intercomparison Project (CMIP6) are available (Eyring et al., 2016). Additionally, the Scenario Model Intercomparison Project (ScenarioMIP) (O'Neill et al., 2016) provides scientists with future projections with different scenarios considering the levels of greenhouse gas emissions and land modification due to land use and vegetation cover (O'Neill et al., 2017). According to Riahi et al. (2017), updated scenarios are obtained using evaluated models and subsequently forced with different updated paths of social development, commonly known as Shared Socioeconomic Pathways (SSPs) (Riahi et al., 2017). These SSPs and CMIP6 are considered the basis for obtaining IPCC climate change projections (IPCC, 2021).

1.6 Scope of this thesis

Global warming intensifies the variables of the different subsystems that constitute the climate system. In addition, will intensify or modify atmospheric circulation and key aspects of the hydrological cycle and related variables (with higher evaporation and precipitation rates), such as the amount of moisture transported in the atmosphere or wind field. These changes could compromise water resource availability and the capacity for wind energy production in future climates.

Given the fragility of water resources, there is a growing need to understand the changes caused by global warming to ensure sufficient supply of water resources. It is important to determine the dependence between the moisture transport given by the moisture source-sink relationship and climate change, and how this influences continental precipitation for specific regions (Gimeno et al., 2020). Furthermore, variations in the spatial and temporal distribution of V10 (Pryor et al., 2005) imply changes in the energies dependent on this variable, specifically near the surface. Therefore, the analysis of future projections can improve the production capacity and energy efficiency by allowing better planning and determining the most ideal regions for technology installation, such as offshore wind farms. Moreover, the study of these modifications will provide detailed information to decision-makers on future changes associated with offshore wind energy production (Murcia et al., 2015).

Currently, notable advances have been made in studies focused on determining where precipitation originates and the moisture source-sink relationship, establishing a climatology for most regions of the world (Gimeno et al., 2012, 2020) using current climate data (e.g., reanalysis data). In addition, many studies have analysed ARs, focusing on moisture transport, characteristics, and intensity (e.g., Dettinger et al., 2015; Ralph et al., 2017; Eiras-Barca et al., 2017). Most studies have focused on the intensity and frequency and, to a lesser extent, the determination of the sources that originate from the moisture they transport or the AMU from the ARs (Algarra et al., 2020). However, few studies have analysed future changes in the source-sink relationship over long periods or for specific events, such as ARs. In addition, specific studies that considered the Lagrangian methodology did not consider how climate change, using climatic scenarios proposed by the IPCC, will influence changes in the location and intensity of the source regions of moisture and the transport from those regions to continental regions.

Regarding future changes in the wind field and wind energy density, numerous studies have been published in the North Atlantic region considering GCMs belonging to the Coupled Model Intercomparison Project Phase 5 (CMIP5) and Phase 6 (CMIP6) (Fernández-Alvarez et al., 2023a). However, the low resolution of the GCM does not show detailed signals of climate change and its effects in a specific region (regional scale), mainly where weather and climate are not homogeneous. To achieve this, sophisticated numerical models are required for climate simulations and projections at sufficiently high resolutions to achieve adequate mitigation and future adaptation to climate change. Current regional climate models can generate future projections with a higher resolution than those currently available for CMIP6. These regional models are forced by the latest generation of the CMIP6 GCMs. This methodology mentioned above is referred to in the literature as dynamic downscaling, which is used to represent physical-dynamic processes on a regional scale and thus obtain a greater understanding of future changes in V10 and their implications for wind energy generation.

Currently, there have been few studies on future changes in the locations of moisture sources and sinks on a regional or global scale. Furthermore, these changes may modify the most active spatial regions for AR occurrence. In addition, it is necessary to continue detailing changes in the wind field at a higher resolution because of its economic importance in the production of renewable energy. Therefore, a dynamic downscaling methodology was proposed using the Eulerian mesoscale regional model (Weather Research and Forecasting (WRF) with ARW dynamic core (WRF-ARW)) and a Lagrangian dispersion model (FLEXible PARTicle dispersion model version for WRF (FLEXPART-WRF, regional version)). Specifically, this thesis aims to determine future changes in atmospheric moisture and wind fields using numerical simulations and analyse the implications for moisture transport and wind energy. This study focused on the North Atlantic region (see the Data and Methodology section).

2

Objectives

This section proposed the objectives for the development of this thesis. The overall objective of this thesis was to **determine the future changes in atmospheric moisture and wind field using numerical simulations and the implications for moisture transport and wind energy in the North Atlantic.**

This thesis focused on i) determining future changes in atmospheric moisture by studying changes in the intensity and position of moisture sources and sinks in the defined domain (see the Methodology section) using a Lagrangian dispersion model, FLEXPART-WRF. For this, a dynamic downscaling methodology was evaluated using reanalysis data. Different configurations of the FLEXPART (FLEXible PARTicle dispersion model) and FLEXPART-WRF models were considered to determine their ability to represent the patterns of both moisture sources and sinks. This evaluation focused on a specific period in the North Atlantic region and most of Europe. ii) Determining future changes in the AMU for landfalling ARs (LARs) arriving on the Iberian Peninsula and in the intensity and position of its main moisture sources. The downscaled dataset and outputs from the Lagrangian model (FLEXPART-WRF) were used for this. iii) Analyzing future changes in V10 in the North Atlantic Ocean and how its modifications would imply changes in the availability of offshore wind energy resources for three subregions of wind and economic interest (the United States East Coast, western Iberian Peninsula, and the Caribbean Sea). It should be noted that to postprocess the outputs of the Lagrangian model, a new free software that is available online was developed.

2.1 Specific objectives

Specific objectives were proposed for the development of this thesis:

1- Develop software for post-processing the outputs from global or regional runnings of the FLEXPART or FLEXPART-WRF Lagrangian dispersion model

To develop this thesis, a post-processing tool for the results was required that allows for the use of different methodologies. In addition, this tool must allow for the use of the outputs of the FLEXPART model in its different versions, global and regional (from FLEXPART-WRF), and any spatial resolution of input and output data. Therefore, these issues were addressed in the software TRansport Of water VApor (TROVA). This objective was achieved in the article: *"TROVA: TRansport Of water Vapor"* (Fernández-Alvarez et al., 2022) published in *SoftwareX* journal.

2- Compare the representation of moisture sources and sinks for ERA5 reanalysis data with different configurations of lagrangian models

Most published research on moisture sources and sinks comes from studies using ERA-Interim reanalysis data (ERA-I) from the European Center for Medium-Range Weather Forecasts (ECMWF) from 1979 to 2009. ERA-I data have spatial (1°) and temporal (6 h) resolution but are not available from 1 June 2023. In addition, the ERA5 reanalysis covers the period from 1950 to the present. The ERA5 data have higher spatial (0.25°, 0.5°, and 1°) and temporal (1 h) resolutions, presenting improvements in very important variables of the hydrological cycle, such as precipitation, evaporation, sea surface temperature, and sea ice. Therefore, these advantages could indicate a better representation of the moisture source-sink relationship; however, this has to be evaluated with respect to the ERA-I reanalysis associated with these improvements, mainly due to changes in the vertical and horizontal resolutions. This evaluation is necessary to use the moisture sources or sinks found using ERA5 as a standard for comparison when considering outputs with climate models. Furthermore, to study local transport with a greater representation of physical processes at smaller scales, it is necessary to increase spatial resolution. This was achieved using a forced model with outputs from a mesoscale regional climate model (e.g., WRF-ARW). This methodology was used to study extreme precipitation events in the Mediterranean region. However, it is essential to compare the ability of this methodology to reproduce moisture source and sink regions. Furthermore, the ability of forced Lagrangian models using ERA5 data to represent moisture sources and sinks has not yet been evaluated. This objective was addressed in the article: *"Comparison of Moisture Sources and Sinks Estimated with Different Versions of FLEXPART and FLEXPART-WRF Models Forced with ECMWF Reanalysis Data"* (Fernández-Alvarez et al., 2023d) published in *Journal of Hydrometeorology* journal.

3- Analyse future changes for atmospheric moisture sources and sinks in the North Atlantic and their implications for moisture transport

In the context of climate change, it is important to determine the dependence between moisture transport given by the moisture source-sink relationship and climate change, and its role in continental precipitation for specific regions. Currently, in the literature consulted, no analysis has considered Lagrangian methodology and climate change to determine future changes in the location and intensity of moisture source regions and their transport to continental regions. In this study, the climatic outputs of CMIP6 were considered for a scenario with a radiative forcing of 8.5 W/m^2 in 2100. This objective was addressed in an article focused on the moisture sources and sinks located in the North Atlantic: *"Projected changes in atmospheric moisture transport contributions associated with climate warming in the North Atlantic"* (Fernández-Alvarez et al., 2023b) published in *Nature Communications* journal.

4- Study the future changes of the moisture source associated with Atmospheric Rivers in the North Atlantic region under climate scenarios

Several investigations have projected that there will be a more humid atmosphere and, therefore, an increase in the moisture flux. In this context, ARs are expected to increase in frequency and strength, resulting in more extreme precipitation events. However, future changes in the location of moisture sources that could alter the most frequent regions of ARs have not yet been sufficiently discussed. This objective was addressed in an article focused on moisture sources feeding the LARs arriving at the Iberian Peninsula: *"Changes in Moisture Sources of Atmospheric Rivers Landfalling the Iberian Peninsula With WRF-FLEXPART"* (Fernández-Alvarez et al., 2023c) published in *Journal of Geophysical Research: Atmospheres.*

5- Evaluate future changes for wind and offshore wind energy in the North Atlantic region

Using GCMs, possible modifications to V10 and their future impacts on wind energy production at global or regional scales have been analysed. Previous studies using GCMs have focused on the same area of interest as in this thesis, the North Atlantic region. However, GCMs have a low resolution, making it impossible to represent more detailed physical mechanisms and processes in regions where climate change could have a notable impact. Then, to avoid this limitation, Regional Climate Models (RCMs) forced with the outputs of GCMs were used, which have many advantages, such as more precise numerical models that allow future projections with the best resolutions to achieve mitigation and adaptation to the climate. Specifically, the WRF-ARW model can perform dynamic downscaling using GCM CMIP6 as initial and boundary conditions. This objective was addressed in the article *"Dynamic downscaling of wind speed over the North Atlantic Ocean using CMIP6 projections: Implications for offshore wind power density"* (Fernández-Alvarez et al., 2023a) published in *Energy Reports.*

3

Data and Methodology

3.1 Data used

The data considered in this study included reanalysis data, outputs from a climate model (Community Earth System Model Version 2, CESM2), and an ensemble of several climate models. A summary of their primary characteristics is provided in Table 3.1. A more detailed explanation is provided in the following subsections.

3.1.1 ECMWF data reanalysis

ERA5 and ERA-I reanalysis data were used as the initial and boundary conditions for the WRF-ARW plus FLEXPART-WRF (Brioude et al., 2013), and global FLEXPART (Stohl, 1998; Stohl and Thomson, 1999; Stohl and James, 2005) models. Simulations were carried out using these data and the models were used to study moisture sources and sinks. In addition, they were considered reference data for the evaluation of the configurations used in this thesis, as explained in Section 3.2. The used variables were the total precipitation, evaporation, components of the vertical integral of the water vapour transport, vertical integral of the divergence of the moisture flux, specific humidity at 850 hPa, evaporation, moisture budget, geopotential height at 500 hPa, and wind components at 10 m.

The reanalysis used in scientific research offer several advantages. These data provided information on more than a hundred variables. They are global and have spatial and temporal resolutions suitable for many climatological analyses. In addition, they are available for long periods, covering three or more decades. With advances in data assimilation, millions of observations have been incorporated, improving the quality of data and, in turn, allowing an improvement in model biases. These data are easily available and simple to process. However, they have limitations. First, the data depend on the location, time scale, and variable analysed. For example, variables involved in the hydrological cycle must be considered cautiously. Furthermore, combining or assimilating both observed and simulated data can lead to spurious variations and trends in reanalysis.

This thesis evaluates the ability to reproduce the moisture sources and sinks of the Lagrangian models FLEXPART and FLEXPART-WRF using the ERA5 reanalysis as the initial and boundary conditions (see Chapter 2). Therefore, its advantages over its predecessor (ERA-I) should be mentioned. ERA5 (Hersbach et al., 2020) is the latest version of the global reanalysis of the ECMWF. The number of observations assimilated by ERA5 increased considerably, reaching approximately 24 million per day in 2019. In addition, from 1979 to 2019, 94.6 billion four-dimensional (4D-Var) observations were assimilated, 65 million for ocean waves, and one billion corresponding to surface air temperature and relative humidity. ERA5 has spatial resolutions of 0.25°, 0.5°, and 1° (Hersbach and D., 2016) and a temporal of $\sim$ 1 h. In addition, the latest version had a horizontal resolution of 31 km and 137 vertical levels (1000–0.01 hPa). In contrast, the global reanalysis ERA-I (Dee et al., 2011) has a temporal resolution of 6 h and spatial resolution of 1° at 60 vertical levels from 1000 to 0.1 hPa. A comparison of the distribution of the vertical levels can be found on the following websites: https://confluence.ecmwf.int/display/UDOC/L60+model+level+definitions and https://confluence.ecmwf.int/display/UDOC/L137+model+level+definitions.

Furthermore, ERA5 has considerably improved the previous version available (i.e., ERA-I) in the representation of physical mechanisms (Hersbach et al., 2020). For instance, the new reanalysis has improved warm rain and ice phase processes, ice supersaturation (microphysics parameterisation), the representation of mixed-phase clouds, and forecast variables for precipitation, rain, and snow. In addition, ERA5 revises the entrainment and coupling with large-scale (convection parameterisation). These improvements have enabled better reproduction of precipitation in tropical and extratropical oceanic regions. ERA5 and ERA-I reanalysis data can be downloaded from the websites: https://cds.climate.copernicus.eu/cdsapp#!/dataset/reanalysis-era5-single-levels-monthly-means?tab=form and https://apps.ecmwf.int/datasets/data/interim-full-daily/levtype=sfc/.

3.1.2 CESM2 model data

To study changes in moisture sources and sinks in future climates, CESM2 outputs (Danabasoglu et al., 2020) were considered. The CESM2 includes the physics of the atmosphere, oceans, ice, and other climate system components. For this thesis, the CESM2 data were downloaded at 0.9 x 1.25 ($\sim$ 1°, 288x192 lon/lat, 32 vertical levels until 2.25 mb) spatial resolution. The variables downloaded from CESM2: 3D-variables (6 h): specific air humidity (hus), air temperature (ta), meridional wind (va), and zonal wind (ua). Also, the 2D-variables (daily) included near-surface specific humidity (huss), total water content of the soil layer (mrsol), near-surface air temperature (tass), sea surface temperature (tos), soil temperature (tsl), and land or sea ice temperature (tslsi). The static variables were the surface altitude (orog) and percentage of grid cells occupied by land (including lakes) (sftlf).

The CESM2 model outputs were processed using a code developed in NCAR Command Language (NCL) and Fortran (Bruyère et al., 2015) to create intermediate files in binary format to force WRF-ARW. In addition, CESM2 (26 vertical levels) allows its use because it has the necessary variables to establish the initial and boundary conditions required by WRF-ARW and at a better spatial resolution than others moldels available in CMIP6.

The selection of this model was based on the criteria explained below. Structures such as jet streams, storm tracks, global divergent circulation, and North Atlantic oscillations were compared by (Simpson et al., 2020). According to the evaluation conducted by the authors, the CESM2 model was within the group of CMIP models that best represented these variables. In addition, the precipitation in CESM2-based sub-seasonal forecast systems is similar to that obtained with the NOAA CFSv2 model and slightly lower than that provided by the ECMWF model (Richter et al., 2022). In addition, the North Atlantic Oscillation structure in winter and summer was relatively well represented in CESM2, with small minor biases, similar to other models (Simpson et al., 2020). This implies an adequate representation of the associated precipitation anomalies over the Mediterranean region (Bladé et al., 2012). According to these authors, many models present inadequacies in their representation, showing very weak changes in precipitation mainly to the east. Moreover, CESM2 provides a velocity potential representation of the upper troposphere in both summer and winter. This element is closely related to tropical precipitation, presenting improvements in precipitation in regions such as the Indian Ocean, East Asia, tropical Atlantic, and Amazon (Simpson et al., 2020). CESM2 has been used to study the effects of sea surface temperature on future changes in ARs (McClenny et al., 2020; McClenny, 2021). Finally, Shen et al. (2022) determined that CESM2 has adequate representation skills for past global terrestrial near-surface wind speeds ($\sim$ 10 m above the ground).

The Shared Socioeconomic Pathways (O'Neill et al., 2016) used in this thesis were SSP2-4.5, SSP3-7.0, and SSP5-8.5. SSP2-4.5 corresponds to the mean level of radiative forcing (4.5 W/m^2 for 2100), in which the environmental systems will degregate but with advances in the use of resources and energy (Riahi et al., 2017). SSP3-7.0 corresponds to a radiative forcing of 7.0 W/m^2 in 2100, representing the medium to high end of the range of radiative forcing. This scenario proposes considerable changes in land use with a decrease in global forest cover. Finally, SSP5-8.5 is the most extreme scenario, based on the continued use of fossil fuels, with a radiative forcing of 8.5 W/m^2 by 2100. Finally, the CESM2 data were obtained from the Earth System Grid Federation (ESGF2) https://esgf-node.llnl.gov/search/cmip6/.

3.1.3 Bias-corrected CMIP6 global database (CMIP6-ENS)

A bias-corrected CMIP6 global dataset (Xu et al., 2021) was used to evaluate the forced WRF-ARW simulations using CESM2 outputs. This analysis was necessary to determine whether the results obtained with CESM2 were dependent on the level of warming of the model at the end of the century. In this case, the CESM2 model has an increase with respect to the pre-industrial period of ~ 4 °C for the period 2060–2079 (Seneviratne and Hauser, 2020). These data were selected for this comparison because they represent an ensemble of climate models. This enables the average of these to smooth out the pattern and is less dependent on the level of warming in a given model.

The bias-corrected CMIP6 global dataset (Xu et al., 2021) was based on 18 models from the CMIP6 and ERA5 datasets. Xu et al. (2021) showed a nonlinear trend with respect to the average of all their studied climate models. In addition, the mean climate and interannual variance were obtained based on the ERA5 reanalysis. According to the authors, this bias-corrected database provides high-quality boundary and initial conditions for regional simulations (e.g., with WRF-ARW), allowing reliable climate projections to be obtained at a regional scale in fields such as atmospheric environment, hydrology, agriculture, and wind energy. The dataset spans the historical period of 1979–2014 (HIST) and future scenarios (SSP2-4.5 and SSP5-8.5) for 2015–2100. The dataset has a spatial resolution of 1.25°x1.25° and a temporal resolution of 6 h. These data are of better quality than the individual models in the representation of mean climatology, interannual variation, and extreme events. The database was obtained from `https://www.scidb.cn/en/detail?dataSetId=791587189614968832`. Developers of this database have the necessary code to create intermediate files to force WRF-ARW. This data can be downloaded from the same repository.

Table 3.1: Summary of the databases used. The spatial (°) and temporal resolution (h), vertical atmospheric levels, the top-pressure level (hPa), and number of points for each database are shown.

Data	Spatial resolutions	Temporal resolutions	Vertical levels	Pressure top
ERA5	0.25° (1440x721)	1, 3 and 6	137	0.01
ERA-I	1° (181x360)	6	60	0.1
CESM2	1° (288x192)	6	32	2.25
CMIP6-ENS	1.25° (288x145)	6	14	50

3.2 Methodology

3.2.1 Experimental setup for the configurations of the different FLEXPART model versions

The objective of this thesis was to determine future changes in moisture sources and sinks and, in turn, changes in the V10 wind in the North Atlantic region. To achieve this, the future climate was simulated using a regional FLEXPART model, that is, the FLEXPART-WRF model. However, the input data for FLEXPART-WRF must be compatible with the configuration of the model that is suitable for the WRF-ARW outputs. Therefore, the data must have had previous dynamic downscaling with WRF-ARW, both the ERA5 reanalysis and the climatic outputs of CESM2. Moreover, in climatic studies which present projections, an evaluation of the configuration of the model used for a historical period of 30 years is necessary (see Section 3.2.6). ERA5 data were used in this thesis because it is the latest reanalysis of the ECMWF available and has been updated to date.

Moreover, it is important to remember that, to date, no studies have used the ERA5 reanalysis and it is necessary to make a comparison for a known period of ERA-I. Therefore, 2014 was considered as the control year to evaluate the reproduction of the moisture sources and sinks of this reanalysis. Specifically, simulations with ERA5 and downscaling of ERA5 as input data for the global and regional FLEXPART models were compared with the forced FLEXPART representation with ERA-I. In addition, experiments were conducted at different spatial resolutions. Next, we explain in detail how the comparison was carried out using the ERA5 reanalysis, the configurations used, and how the climate simulations were carried out using CESM2.

For this purpose, the results of the FLEXPARTv9.0 Lagrangian model forced by the reanalysis data of ERA-I (Dee et al., 2011) with $\sim 1^\circ$ of horizontal resolution and 61 vertical levels were used as "control values" (hereafter named FLEX-ERA-I.1, the control experiment). In this control experiment, two million particles were released into the atmosphere and distributed uniformly. The ERA-I meteorological fields were updated every 6 h in the global domain. This configuration has been used in numerous investigations to determine moisture sources and sinks on a global or regional scale (Gimeno et al., 2020). According to its developers, FLEXPARTv9.0 only works with ERA-I; however, currently, the reanalysis available in the ECMWF Integrated Forecast System is ERA5 because ERA-I (has not been available since 1 June 2023). Therefore, it is necessary to use a more updated version of the FLEXPART model, version 10.3 (Pisso et al., 2019), that allows the use of ERA5 as a forcer. According to Pisso et al. (2019), the actual version shows improvements compared to the previous v9.0. Improvements in the physics and parameterisation of different versions of the FLEXPART model were presented by Pisso et al. (2019).

The Lagrangian model FLEXPARTv10.3 presents improvements, for example, in the convective atmospheric boundary layer, includes a new scheme that uses biased turbulence statistics. In addition, they incorporated improvements in the wet deposition of aerosols (Grythe et al., 2017), detailing the sizes of these particles, types of precipitation, and differentiating between in-cloud and below-cloud scavenging activities. Finally, FLEXPARTv10.3 uses 3D cloud water fields for a detailed representation in the vertical direction. A summary of the configurations used for the evaluation is presented in Table 3.2. This table shows the model versions, input and output data features, and the particles into which the atmosphere was divided with each model, among the other elements considered in the comparison.

The FLEXPARTv10.3 model was forced with the ERA5 reanalysis at 0.5° and 1° spatial resolution and a temporal resolution of 6 h. Both resolutions were used for two purposes: 1) the configuration with 1° (herein FLEX-ERA5.1) was used as a direct comparison with the control experiment used, which was FLEXPARTv9.0 forced with ERA-I, and 2) the configuration at 0.5° (herein FLEX-ERA5.05) was used to increase the spatial resolution (double compared to the version with 1°) and better represent the physical processes. Both experiments showed considerable improvements in the vertical resolution associated with ERA5 compared with ERA-I.

Considering that the study region included the North Atlantic, dynamic downscaling was performed using the WRF-ARWv3.8.1 model (Skamarock et al., 2008). The proposed methodology allows for a more accurate representation of physical processes at the grid scale as a sub-grid with domains and regions centred on the areas of interest. This model was used to simulate forced meteorological conditions using initial conditions from reanalyses or climate models on a regional scale. Figure 3.1 represents the regional domain of the study, 115 °W–42 °E and 19 °S–59 °N. The WRF-ARW outputs had a $\sim 0.18°$ horizontal spatial resolution and were saved every 6 h. Additionally, the WRF-ARW outputs had 40 vertical levels and 480 x 800 nodes in the output grid. The parameterisation schemes used were evaluated for the region by Insua-Costa and Miguez-Macho (2018) and Insua-Costa et al. (2019).

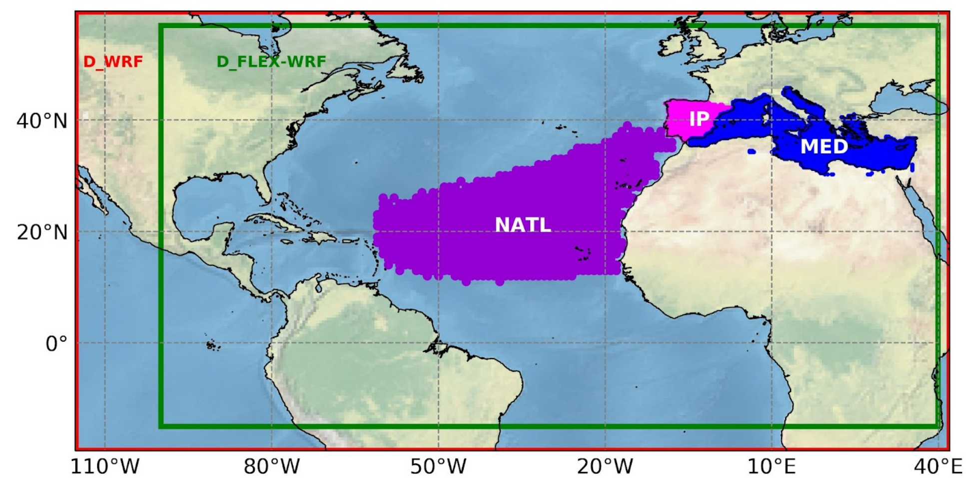

Figure 3.1: Domains used for the WRF-ARW (red) and FLEXPART-WRF (green) models. The target regions for moisture sources are the Mediterranean Sea (MED, blue), the North Atlantic moisture source (NATL, dark violet), and the Iberian Peninsula (IP, pink) as a moisture sink.

Next, the outputs of the WRF-ARW model were used to execute the appropriate version of FLEXPART for WRF its version v3.3.2 (Brioude et al., 2013). The domain considered was smaller than that shown in Figure 3.1 for the WRF-ARW model. Its spatial resolution was 0.18° and it had 400x777 grid points. The FLEXPART-WRF configuration considers the Hanna turbulence parameterisation scheme (Hanna, 1982) and uses an activated convection scheme. The atmosphere was divided into 2 million particles, guaranteeing a homogeneous distribution of the atmospheric mass throughout the vertical column. The model was run in its forward in time mode for the simulated periods. In addition, the domain-filling option was considered for the runs of FLEXPART-WRF. According to Stohl and James (2004), this option allows the atmosphere to contain particles of equal mass during simulations. This experiment was named FLEX-WRF.

These configurations shown above were used all in the present climate. Therefore, once the reproduction of moisture sources and sinks was evaluated, the dynamic downscaling methodology with WRF-ARW plus FLEXPART-WRF was used forced with CESM2 under SSP5-8.5 for future climatic studies of moisture transport. Thirty years of simulations were considered and were split into three periods: mid-century (MC; 2036–2065), end-century (EC; 2071–2100), and HIST (1985–2014). For the analysis of the wind field and wind energy density, a dynamic downscaling methodology was used considering three SSPs (SSP2-4.5, SSP3-7.0, and SSP5-8.5). In this case, the periods mid-21st century (MC_5Y: 2049–2053) and the end-21st century (EC_5Y: 2096–2100) are used (HIST_5Y: 2010–2014). Finally, future changes were determined as the difference between the E-P pattern for 30 years obtained at MC, EC, and HIST. Similarly, the analysis for V10 or wind power density (WPD) was conducted, but considering periods of five years.

Table 3.2: Configurations used for evaluation. Summary of models and input databases used for different experiments. For each experiment, the input and output model data characteristics, resolution, number (in millions) of particles released, vertical atmospheric levels, upper-pressure level (hPa), and number of levels up to 50 hPa (LN50hPa) are listed.

Experiment name	Model	Input data database	Input (output) resolution	Vertical levels	Pressure top (LN50hPa)	Number of particles/domain
FLEX-ERA-I.1	FLEX-PARTv9	ERA-I	1.0°(1.0°)	60	0.1(21)	2/global
FLEX-ERA5.05	FLEX-PARTv10.3	ERA5	0.5°(0.5°)	137	0.01(48)	30/global
FLEX-ERA5.1	FLEX-PARTv10.3	ERA5	1.0°(1.0°)	137	0.01(48)	9/global
FLEX-WRF	FLEXPART-WRFv3.3.2	WRF-ERA5	0.18°(0.18°)	40	50(40)	2/regional

3.2.2 Sources and sinks used for moisture transport analysis

To study moisture transport in present and future climates, the North Atlantic and Mediterranean Sea moisture sources were selected, and the Iberian Peninsula was used as a sink (Figure 3.1). As mentioned previously, the North Atlantic and Mediterranean Sea (more details in the Introduction) are two of the main global oceanic sources that contribute moisture to continental precipitation (Gimeno et al., 2010a). According to Gimeno et al. (2010a), the areas with the greatest moisture contribution from the North Atlantic are North America, Central America, northern and central South America, Europe, and northern Africa. Furthermore, Nieto et al. (2010) determined that the Mediterranean Sea contributes considerably to the surrounding areas in terms of the moisture contribution to continental precipitation. A strategic region (mid-latitude hotspot) due to the contribution of more than one moisture source is the Iberian Peninsula (Gimeno et al., 2012). This moisture sink is one of the areas with the highest frequency of ARs in the North Atlantic, along with the British Isles (e.g., Algarra et al., 2020). Therefore, the extended North Atlantic region selected for this thesis is optimal for conducting this type of analysis because its climate is dependent on the moisture contribution from North Atlantic and Mediterranean Sea sources and is affected by heavy recycling processes (Gimeno et al., 2010b; Nieto et al., 2010) and ARs.

In addition, the NATL source definition (violet mask in Figure 3.1) was not arbitrary but was chosen according to Gimeno et al. (2010a), including a 750 mm/yr threshold for the annual mean vertically integrated moisture flux divergence field. For the Mediterranean Sea source (blue mask in Figure 3.1), the area was defined by the geographic limits of the basin. Both masks have been used in the literature, particularly the North Atlantic, introduced by Gimeno et al. (2010a), and the Mediterranean Sea, introduced by Nieto et al. (2010).

3.2.3 Identification of the moisture source and sinks

Moisture sources and sinks were estimated using the Lagrangian methodology. This consisted of quantifying the changes in the specific humidity q for each particle into which the atmosphere was divided for the dispersion model. This analysis was performed for each trajectory at time (t every 6 h). According to Stohl and James (2005) these changes can be calculated as:

$$e - p = m(\frac{dq}{dt}) \tag{3.1}$$

where m is the mass of the particle and the increase or decrease in the water vapour content in the trajectory of each particle is given by the terms e-p. This analysis was performed for each particle and the total surface freshwater flux was calculated as the sum of the contributions of all particles in a grid of area A at time t. The previous description is summarised by the following equation:

$$E - P = \frac{\sum_{i=1}^{n}(e-p)_k}{A} \tag{3.2}$$

where E is evaporation, P is precipitation, and N is the total number of particles found in the grid. In this thesis, the residence time of water vapour in the atmosphere was considered to be 10 days, which is the time at which the particles were followed (Numaguti, 1999; Van Der Ent and Tuinenburg, 2017; Gimeno et al., 2021). The final result of E-P is the integrated calculation from days 1 to 10.

According to the literature, forward or backward in time tracking can be performed on moisture particles over time in a specific target region, allowing moisture sources and sinks to be identified (Stohl and James, 2004, 2005). Specifically, a moisture source (sink) is defined as a region where evaporation (precipitation) predominates over precipitation (evaporation); therefore, there is a moisture gain (loss). These moisture sources ($\mathrm{E} - \mathrm{P} > 0$) (sinks, $\mathrm{P} - \mathrm{E} > 0$) were determined by backward (forward) experiments in the time mode. Finally, to study the moisture associated with ARs, this thesis focused on AMU over the ocean (Algarra et al., 2020), specifically on ARs that make LARs. Specifically, AMU was determined as the difference between the $\mathrm{E} - \mathrm{P} > 0$ pattern for each day with the occurrence of LAR and the climatological pattern of $\mathrm{E} - \mathrm{P} > 0$ in the 30 years considering the occurrence or absence of LAR. The analysis was performed for each grid point. In addition to representing the centroid of the area where the AMU associated with the ARs occurred, the weighted centroid method was used, as described by Nishikawa (2020):

$$lat_c, lon_c = \frac{\sum_{i=1}^{N} w_k(lat_k, lon_k)}{\sum_{i=1}^{N} w_k} \tag{3.3}$$

where N is the number of grid points where the AMU occurs and w is the weighted vector.

$$w = \frac{AMU}{max(AMU)} \tag{3.4}$$

3.2.4 Detection of Atmospheric Rivers

An the Image-Processing-based Atmospheric River Tracking (IPART) method (Xu et al., 2020) was used to detect AR occurrences from the outputs of the WRF-ARW model. The detection algorithm is based on thresholds at the spatiotemporal scale of ARs and is independent of the IVT thresholds. According to Xu et al. (2020), this approach is suitable for studies that consider climate change.

The IVT field was calculated using the following equations:

$$IVT = \sqrt{u_q^2 + v_q^2} \tag{3.5}$$

$$u_q = \frac{1}{g} \int_{ps}^{p} uqdp \tag{3.6}$$

$$v_q = \frac{1}{g} \int_{ps}^{p} vqdp \tag{3.7}$$

where g is gravitational acceleration, q is specific humidity, ps is surface pressure, p is maximum pressure, and u and v are the zonal and meridional wind components (Lavers et al., 2012).

This method was based on image processing using a reconstruction technique (Vincent, 1993). Specifically, IPART subtracts a "dilation grayscale reconstruction" image from the initial image. This image corresponds to positive IVT values. After this difference, an anomalous image is obtained, in which possible ARs are searched. Finally, the nonzero regions show the regions with potential ARs. More details on this method can be found in an article published by Xu et al. (2021).

3.2.5 Wind energy density determination

The wind power density (WPD) was considered when offshore wind energy was studied based on wind speed. The WPD was calculated considering V10. Moreover, the WPD (W/m^2) indicates the available energy that a wind turbine can convert to wind energy in a certain region. Generally, WPD is used to compare the wind potential in different regions using the wind field (Akdağ and Dinler, 2009). This value was determined using the following equation. In this equation, the air density is considered $\rho = 1.225$ kg/m^3, (Ulazia et al., 2019) and the wind speed is denoted by v (m/s).

$$WPD = \frac{1}{2}\rho v^3 \tag{3.8}$$

To calculate the WPD, the wind speed at the height of the wind turbines (approximately 120 m) was required. To fulfil this requirement, a logarithmic profile was used, considering an atmosphere with neutral stability (Swart, 2009). The physical formulations used were as follows:

$$u_z = u_{zm} \cdot \left(\frac{ln \frac{h}{z_0}}{ln \frac{h_m}{z_0}} \right) \tag{3.9}$$

where u_{zm} is V10 (m/s), $h_m = 10\ m$ is the height for the wind speed, u_z (m/s) is the wind speed extrapolated to 120 m and $z_0 = 1.52 \cdot 10^{-4}$ is the local roughness length. This methodology has been used by Yamada and Mellor (1975) and Carreno-Madinabeitia et al. (2021).

Three areas on the eastern and western boundaries of the North Atlantic Ocean were analysed. Figure 3.2 shows the areas considered for the analysis of V10 (full area) and the WPD: Atlantic coast of the Iberian Peninsula (red box), east coast of the United States (green box), and Caribbean Sea region (yellow box).

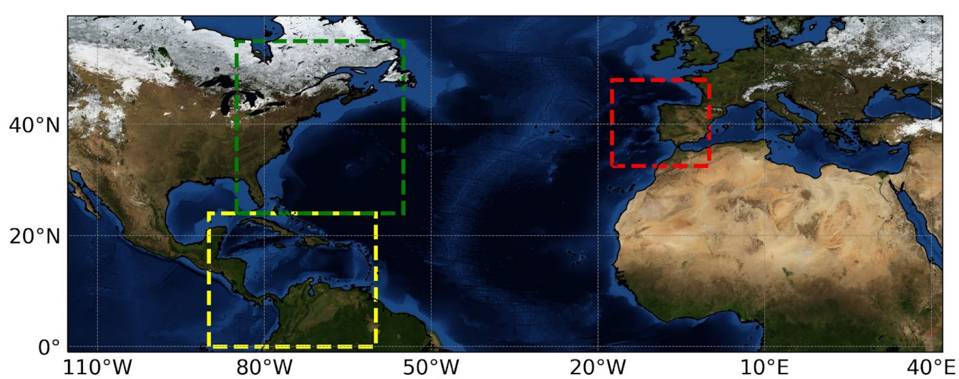

Figure 3.2: Areas considered for the analysis of wind speed at 10 m (full area) and the WPD in the North Atlantic Ocean, the Atlantic coast of the IP (red box), the East coast of the United States (US, green box), and the Caribbean Sea region (CS, yellow box).

3.2.6 Statistical evaluation of the configurations

For the wind and moisture sources and sinks analyses, the boreal winter (January-March, JFM), spring (April to June, AMJ), summer (July-September, JAS), autumn (October-December, OND) and annual (January-December, ANNUAL) periods were used. The selection of these periods was mainly based on the ability to use all the years simulated for the HIST, MC, and EC. Similar periods to study the moisture sources associated with the Iberian Peninsula were used by Gimeno et al. (2010b), allowing direct comparison between the results. Table 3.3 shows the statistics used to evaluate the configurations considering moisture transport or the wind field. In these statistics, the values for the simulated and observed variables are represented by x_i and y_i, respectively, and n is the number of values and their mean values are represented by $\overline{x}$ and $\overline{y}$. In addition, the coefficient of determination (R^2) and coefficient of variation (VAR) were used to determine the relationship between the mean of the variable and its variability.

Table 3.3: Statistics are used for the evaluation of the configurations considering the moisture transport or the wind field. Taken from Brown et al. (2013).

Statistics	Equation
Absolute error (MAE)	$\frac{\sum_{i=1}^{n}\lvert x_i - y_i\rvert}{n}$
Root mean square error (RMSE)	$\sqrt{\frac{\sum_{i=1}^{n}(x_i - y_i)^2}{n}}$
Pearson's correlation (R)	$\frac{\sum_{i=1}^{n}(x_i-\overline{x})(y_i-\overline{y})}{\sqrt{\sum_{i=1}^{n}(x_i-\overline{x})^2}\sqrt{\sum_{i=1}^{n}(y_i-\overline{y})^2}}$
Bias (B)	$\frac{\sum_{i=1}^{n}(x_i - y_i)}{n}$
Standard deviation (STD)	$\sqrt{\frac{1}{n-1}\sum_{i=1}^{n}(x_i-\overline{x})^2}$

4

Set of publications

This section shows the **5** publications that form the results of this research. The first presents the development of the software: TRansport Of water VApour (TROVA), which is necessary to process the FLEXPART and FLEXPART-WRF dispersion model outputs to obtain the moisture source and sink regions. The second article focuses on the evaluation of the ERA5 reanalysis to deduce moisture sources and sinks. The third analyses future changes in moisture sources and sinks in the North Atlantic region. The fourth focuses on the ARs, both in terms of intensity and moisture transport, associated with these events in future climates. The fifth focuses on the future projections of wind and wind power density in the North Atlantic.

Table 4.1 presents a description of the following elements for each article published in this thesis: title, author, year of publication, and journal. The articles were ordered coherently, complying with the objectives outlined in Chapter 2. Appendix A presents the complementary materials used in each study.

The first article is *"TROVA: TRansport Of water Vapor"* by **Fernández-Alvarez, J. C.**; Pérez-Alarcón, A.; Nieto, R.; Gimeno, L. (Fernández-Alvarez et al., 2022). This paper presents the TROVA software. This was implemented in Python and Fortran to analyse moisture sources and sinks. This tool allows the selection of the main Lagrangian methodologies reported in scientific research. This software uses the outputs of the Lagrangian FLEXible PARTicle dispersion model and its regional version, FLEXPART-WRF, considering different spatial resolutions.

Using TROVA, the results published in the paper were obtained: *"Comparison of Moisture Sources and Sinks Estimated with Different Versions of FLEXPART and FLEXPART-WRF Models Forced with ECMWF Reanalysis Data"* by **Fernández-Alvarez, J. C.**; Vázquez, M.; Pérez-Alarcón, A.; Nieto, R.; Gimeno, L. (Fernández-Alvarez et al., 2023d). This study compared the ability of the FLEXPART Lagrangian models and their regional versions to show the patterns of moisture sources and sinks. Different configurations with different resolutions were used, and ERA5 was considered for the initial and boundary conditions. The study period was the year 2014 and considered the North Atlantic and Mediterranean Sea as moisture sources and the Iberian Peninsula as a moisture sink. The results with FLEXPARTv9.0 fed with ERA-Interim were used as "control values".

From the results of the two previous articles, the future climate simulations were obtained and published in *"Projected changes in atmospheric moisture transport contributions associated with climate warming in the North Atlantic"* by **Fernández-Alvarez J. C.**; Pérez-Alarcón A.; Eiras-Barca, J., Rahimi S.; Nieto R.; Gimeno L. (Fernández-Alvarez et al., 2023b). This study simulated changes in moisture sinks associated with North Atlantic and Mediterranean Sea sources under the SSP5-8.5 scenario at MC and EC. Furthermore, the Iberian Peninsula was considered a moisture sink for both sources and an important region because of its location.

After analysing how the sources that provide humidity to the Iberian Peninsula will change in the future climate, the changes in the position and intensity of LARs arriving at the Iberian Peninsula and their associated moisture sources were projected and published in *"Changes in Moisture Sources of Atmospheric Rivers Landfalling the Iberian Peninsula With WRF-FLEXPART"* by **Fernández-Alvarez, J. C.**; Pérez-Alarcón, A.; Eiras-Barca, J.; Ramos, A.M.; Rahimi-Esfarjani, S.; Nieto, R.; Gimeno, L (Fernández-Alvarez et al., 2023c). This study considered the use of the WRF regional model and its outputs to force the FLEXPART-WRF model. The representation of climatic variables in present climate was evaluated by considering the ERA5 reanalysis. However, to determine future changes during the 21st century, the CESM2 model of CMIP6 was used as a forcer.

The fifth paper entitled *"Dynamic downscaling of wind speed over the North Atlantic Ocean using CMIP6 projections: Implications for offshore wind power density"* was published in 2023 by **Fernández-Alvarez, J. C.**; Costoya, X.; Perez-Alarcon, A.; Rahimi, S., Nieto, R.; Gimeno, L. (Fernández-Alvarez et al., 2023a). This article presents an analysis of the wind speed at a height of 10 m (V10) in the North Atlantic Ocean using the WRF-ARW model and the GCM CESM2 as forcers. Previously, the wind speed pattern at 10 m was compared with the ERA5 data. In addition, future changes in the WPD in three regions with wind potential were analysed: the United States (US) East Coast, western Iberian Peninsula, and Caribbean Sea.

4.1 List of publications

Table 4.1: Set of publications.

Title	Authors	Year	Journal
TROVA: TRansport Of water VApor	**Fernández-Alvarez, J. C.**; Pérez-Alarcón, A.; Nieto, R.; Gimeno, L.	2022	SoftwareX
Comparison of moisture sources and sinks estimated with different versions of FLEXPART and FLEXPART-WRF models forced with ECMWF reanalysis data.	**Fernández-Alvarez, J. C.**; Vázquez, M.; Pérez-Alarcón, A.; Nieto, R.; Gimeno, L.	2023	Journal of Hydrometeorology
Projected changes in atmospheric moisture transport contributions associated with climate warming in the North Atlantic	**Fernández-Alvarez, J. C.**; Pérez-Alarcón A.; Eiras-Barca, J., Rahimi S.; Nieto R.; Gimeno L.	2023	Nature Communications
Changes in moisture sources of atmospheric rivers landfalling the Iberian Peninsula with WRF-Flexpart.	**Fernández-Alvarez, J. C.**; Pérez-Alarcón, A.; Eiras-Barca, J.; Ramos, A. M.; Rahimi-Esfarjani, S.; Nieto, R.; Gimeno, L.	2023	Journal of Geophysical Research: Atmospheres
Dynamic downscaling of wind speed over the North Atlantic Ocean using CMIP6 projections: Implications for offshore wind power density.	**Fernández-Alvarez, J. C.**; Costoya, X.; Pérez-Alarcón, A.; Rahimi, S., Nieto, R.; Gimeno, L	2023	Energy Reports

4.2 TROVA: TRansport Of water VApor

Fernández-Alvarez, J. C., Pérez-Alarcón, A., Nieto, R., & Gimeno, L. (2022). TROVA: TRansport Of water VApor. *SoftwareX*, 20, 101228.

Table 4.2: Detailed description of the journal where the first article was published. The data is updated from 2022 according to the Web of Science (JCR). **IF**: impact factor.

Journal	Description	Journal metrics
SoftwareX	**Publisher**: Elsevier, **Scope**: SoftwareX publishes software articles with impacts on current research practices emphasizing software developers as responsible for this impact.	**IF:** 3.4, 5-year **IF**: 3.3, **Ranking**: 36 out of 131 in Computer Science, Software Engineering (**Q2**)

SoftwareX 20 (2022) 101228

Contents lists available at ScienceDirect

SoftwareX

journal homepage: www.elsevier.com/locate/softx

Original software publication

TROVA: TRansport Of water VApor

José C. Fernández-Alvarez [a,b,*], Albenis Pérez-Alarcón [a,b], Raquel Nieto [a], Luis Gimeno [a]

[a] Centro de Investigación Mariña, Universidade de Vigo, Environmental Physics Laboratory (EPhysLab), Campus As Lagoas s/n, Ourense, 32004, Spain
[b] Departamento de Meteorología, Instituto Superior de Tecnologías y Ciencias Aplicadas, Universidad de La Habana, La Habana, Cuba

ARTICLE INFO

Article history:
Received 28 April 2022
Received in revised form 27 July 2022
Accepted 6 October 2022

Keywords:
Moisture sources
Precipitation
Python
FLEXPART
FLEXPART-WRF
Evaporation

ABSTRACT

The TRansport Of water VApor (TROVA) software, developed in Python and Fortran for the study of moisture sources and sinks, is presented here. TROVA includes the main Lagrangian methodologies established in the literature, using outputs from the global FLEXible PARTicle dispersion model and the regional FLEXPART-WRF model at different spatial resolutions. TROVA will benefit users investigating the physics of the atmosphere and fields associated with this branch in the study of current and future changes in source–sink moisture relationships and their link with mean and extreme precipitation.

Code metadata

Current code version	*1.0*
Permanent link to the code/repository used for this code version	https://github.com/ElsevierSoftwareX/SOFTX-D-22-00100
Permanent link to reproducible capsule	https://github.com/tramo-ephyslab/TROVA-master/blob/main/Inputs/
Legal code license	*GNU General Public License (GPL)*
Code versioning system used	*Git*
Software code languages, tools, and services used	*Python, Fortran, and MPI*
Compilation requirements, operating environments, and dependencies	*Linux operating system*
If available, link to the developer documentation/manual	
Email support for questions	l.gimeno@uvigo.es

Software metadata

Current software version	1.0
Permanent link to executables of this version	https://github.com/tramo-ephyslab/TROVA-master
Legal Software License	GNU General Public License (GPL)
Computing platforms/Operating Systems	Python, Fortran and MPI/Linux
Installation requirements & dependencies	Python3, numpy1.16+, mpi4py3+, scipy1.2+
If available, link to user manual - if formally published include a reference to the publication in the reference list	
Support email for question	l.gimeno@uvigo.es

1. Motivation and significance

There is considerable research interest in the meteorology and hydrology communities on understanding the origin of moisture and precipitation that occurs over a given region, due to the dependence of life on water resources [1]. There are different

* Corresponding author at: Centro de Investigación Mariña, Universidade de Vigo, Environmental Physics Laboratory (EPhysLab), Campus As Lagoas s/n, Ourense, 32004, Spain.
E-mail address: jose.carlos.fernandez.alvarez@uvigo.es (José C. Fernández-Alvarez).

https://doi.org/10.1016/j.softx.2022.101228

approaches to studying moisture transport, for example, several authors have implemented classical Eulerian [2], Lagrangian [3,4], and stable isotope approaches [5], as well as new sophisticated and robust methods such as Eulerian mesoscale tracer tools [6]. However, the Lagrangian approach has advantages over other methods as it provides details regarding the origin of the air mass and the mechanism of moisture fluctuations (increases and decreases) in the particles along the trajectories affecting the moisture in the target region [7]. Recently, the accuracy and robustness of this approach have facilitated the assessment of the average values for moisture sources in various climatic regions [7]. The original Lagrangian method developed by Stohl and James [4] facilitated the determination of the moisture source of precipitation over a given area and the sinks associated with a given moisture source; a more sophisticated method based on the previously cited study [4] was developed by Sodemann et al. [8] to determine specific moisture sources. Then, these methodologies were modified to obtain finer results but with the disadvantage of being more computationally expensive and requiring a larger volume of data. For example, Sun and Wang [9] introduced areal source receptor attribution to the methodology of Stohl and James [4], and Keune et al. [10] presented a unified framework to estimate the origins of atmospheric moisture (and heat) as a derivation of Sodemann et al. [8], including the possibility of performing bias correction based on source–receptor relationships.

In general, all these methods calculate the difference of Evaporation (E) and Precipitation (E) (E-P) to quantify the transport based on particle trajectories. In these analyses, a moisture source and sink are considered when E-P < 0 and E-P > 0, respectively. This E-P computation can be applied to the outputs of Lagrangian particle dispersion models, such as those from the FLEXible PARTicle dispersion model (FLEXPART [11–14], its regional version FLEXPART-WRF [15], or by using the online trajectory module (version 1.0) for the model COSMO [16], or to trajectories from the LAGRANTO model [17]. These models are normally forced with reanalysis data, such as ERA-Interim (ERA-I, [18]), ERA5 [19] or earlier versions, or the outputs of a regional model such as Weather Research and Forecasting System (WRF-ARW) [20] forced with different reanalysis or climatic data or using COSMO model outputs [21].

The values of E and P for a vertical air column are determined from humidity changes in water vapor particles that crossed the column along their trajectories over a predefined time period [22]. The trajectories are obtained from outputs of the dispersion models mentioned above, and the usual time to track them is around 8–10 days, the mean atmospheric water vapor residence time (WVRT) [23,24]. However, calculating the E-P field representation from the outputs of these models is very cumbersome, both in the post-processing phase and in application of the aforementioned methodologies. This is due to the large volume of data under consideration, which depends on the number of particles analyzed, number of days to track them, and the spatial and vertical resolutions.

Currently, some tools based on the methodology of Sodemann et al. [8], such as WaterSip [25], identify moisture sources based on a considerable number of thresholds applied to particle behavior along their trajectories, or the adaptation thereto as Heat And MoiSture Tracking (HAMSTER) framework, [10], which applies a bias-corrected source–receptor by adjustment of certain meteorological fields. However, the current online-version of HAMSTER only supports grids of one degree for the whole run configuration (for defining the target region (mask), the reference data (FLEXPART forced with ERA-I), and outputs).

Here, we present a software that facilitates the use of the methodologies of Stohl and James [4] and Sodemann et al. [8] using FLEXPART and FLEXPART-WRF outputs, with the possibility of considering different grid resolutions for both input and output data and masks used for the moisture sources or sinks: the TRansport Of water VApor (TROVA) software. In addition, the versatility of TROVA for use with different types of numerical outputs from FLEXPART or FLEXPART-WRF will be useful for studies on future changes associated with moisture sources and sinks using outputs from these forced models under future climate scenarios. TROVA has already been used to study moisture sources and sinks with different approaches. Specifically, using the methodology of Stohl and James [4], numerous publications have been made in several regions worldwide, some of them could be consulted at https://ephyslab.uvigo.es/moisturetransport/index.php/Publications. However, recent research, based on the study by Sodemann et al. [8], has been conducted using this tool to determine moisture sources for precipitation associated with major hurricanes in the North Atlantic basin [26,27]. Examples for moisture sources and sinks are presented in Section 3.

2. Software

2.1. Software architecture

TROVA is a software with the main algorithm written in Python, using libraries such as numpy, netCDF4, scipy, mpi4py, and other basic python libraries [28] (https://github.com/tramo-ephyslab/TROVA-master). However, the calculations of greater time and computational requirements are carried out with functions developed in Fortran, improving the efficiency of the tool. This software was developed and tested on the Linux operating system, and we believe that it is fully compatible with any system supporting Python 3. In addition, it has been used in high performance computing CESGA (Centro de Supercomputación de Galicia) with different core numbers (https://github.com/tramo-ephyslab/TROVA-master/tree/main/run_example_HPC). Finally, a configuration input file is used that allows the user to modify fields depending on the problem to be solved, without modifying the tool itself. TROVA outputs correspond to the E-P field for each day analyzed and its integrated sum for these days (output file in NetCDF, ASCII, and npy format). In addition, it saves the humidity changes for all particles in the analyzed time interval.

For a more detailed understanding of TROVA, Fig. 1 presents a flowchart explaining the general algorithm of the software. The first step to be performed is the configuration of the input file where the parameters of the run are set. The second step is to run the model forward or backward in time to determine the moisture sources or sinks, respectively. The tracking mode is defined in the input file. In the third step, the files needed to track the particles should be indicated, and then the calculations of the moisture changes of the particles are performed using the functions developed in Fortran. This will allow for greater computational efficiency and decrease the execution time. The fourth step is the calculation of the E-P field, from the Stohl and James (2005) equation, on the user-defined output grid. Finally, TROVA saves the outputs in the user-defined format, which can be NetCDF, ASCII, and npy.

2.2. Software functionalities

TROVA allows the study of moisture sources and sinks based on calculation of the E-P fields, using the main methodologies of Stohl and James [4] and Sodemann et al. [8]. In addition, TROVA provides the advantage of using different numerical outputs from FLEXPART and FLEXPART-WRF at different spatial resolutions, ensuring better representation of the E-P field to be obtained. The Table 1 shows a comparison of the TROVA with WaterSip and HAMSTER in which the main differences/advantages can be observed.

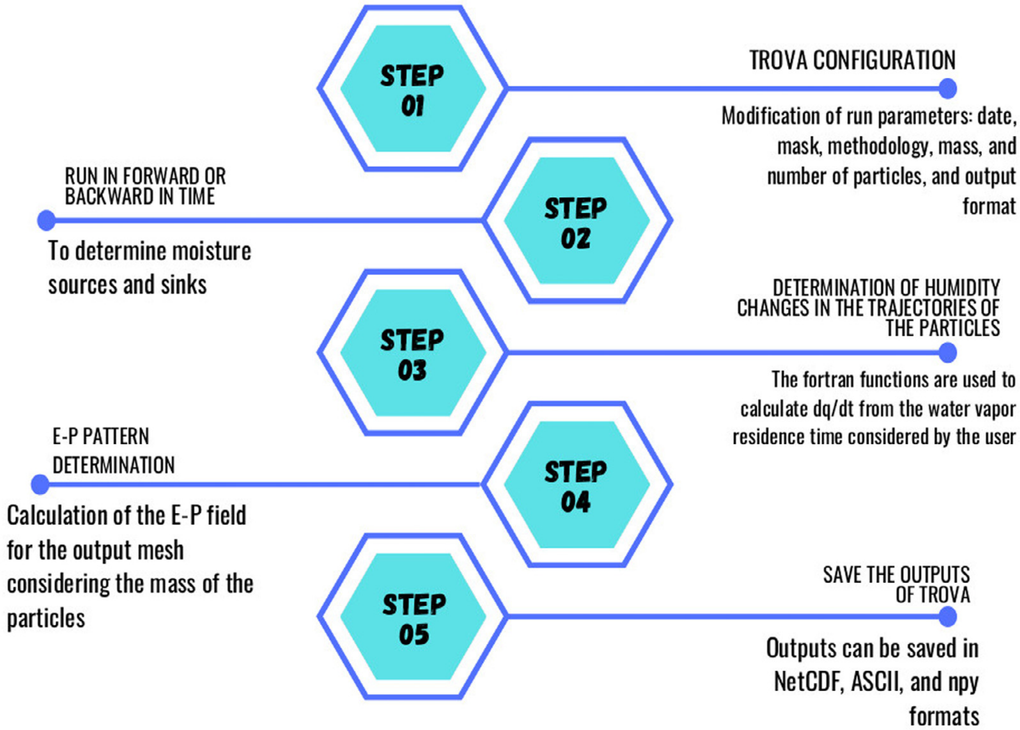

Fig. 1. Flowchart the TROVA software structure/processes.

Table 1
TROVA comparison with WaterSip [25] and HAMSTER [10]. Main differences/advantages.

Comparison parameters	Softwares		
	TROVA	WaterSip	HAMSTER
Input data	Outputs of the FLEXPART and FLEXPART-WRF models forced with reanalysis (ERA-Interim and ERA5) or climatic scenarios	Outputs of the FLEXPART and Lagranto models forced with ERA-Interim	Outputs of the FLEXPART model forced with ERA-Interim
Input data spatial resolution	Several (e.g. 1°, 0.5°, 0.25°, and 0.18°)	1°	1°
Output data spatial resolution	Several (e.g. 1°, 0.5°, 0.25°, and 0.18°)	1°	1°
Lagrangian methodologies implemented	Stohl and James [4] and Sodemann et al. [8]	Sodemann et al. [8]	Sodemann et al. [8] including the possibility of performing bias correction based on source–receptor relationships
Use for related studies with future changes in moisture sources and sinks	Yes	No	No
Parallelization	Yes	Yes	No
Adapted for High-performance computing	Yes	Yes	No

2.3. Software validation

TROVA software has been validated by Perez-Alarcon et al. [26, 27] in the analysis of tropical cyclone moisture sources for the North Atlantic basin using the methodology of Sodemann et al. [8]. In these studies, the outputs of FLEXPART with ERA-I (∼1° of spatial resolution) were used as input data. Currently, a TROVA evaluation has been carried out using the methodology of Stohl and James [4] for studies of the sources that contribute to humidity on the Iberian Peninsula and for sinks associated with the sources of the North Atlantic Ocean and the Mediterranean Sea [29]. In this study, FLEXPART is used with ERA5 (∼0.5° and 1°) and ERA-I (∼1°) and FLEXPART-WRF is forced with outputs of the WRF model (forced with ERA5 at 0.25°) at a resolution of 0.18°.

3. Illustrative examples

To demonstrate the use of TROVA software, several examples of its application for two target regions (masks, Fig. 2b–f) in the North Atlantic Ocean are presented. In addition, some examples to determine moisture sources and sinks for these case studies are shown. It is important to note that different outputs of FLEXPART forced with reanalysis data from ERA-I, ERA5, and FLEXPART-WRF (also forced with ERA5) were used. We also present results using different spatial resolutions (1°, 0.5°, and 0.18°, respectively) for these input data to showcase TROVA's ability. The data available for testing with TROVA is available at the link: https://doi.org/10.5281/zenodo.6490365.

Fig. 2b-c represents the moisture sources associated with a tropical cyclone (red circle in Fig. 2a) using the methodology of Sodemann et al. [8] for October 17, 2014, at 18 UTC. These

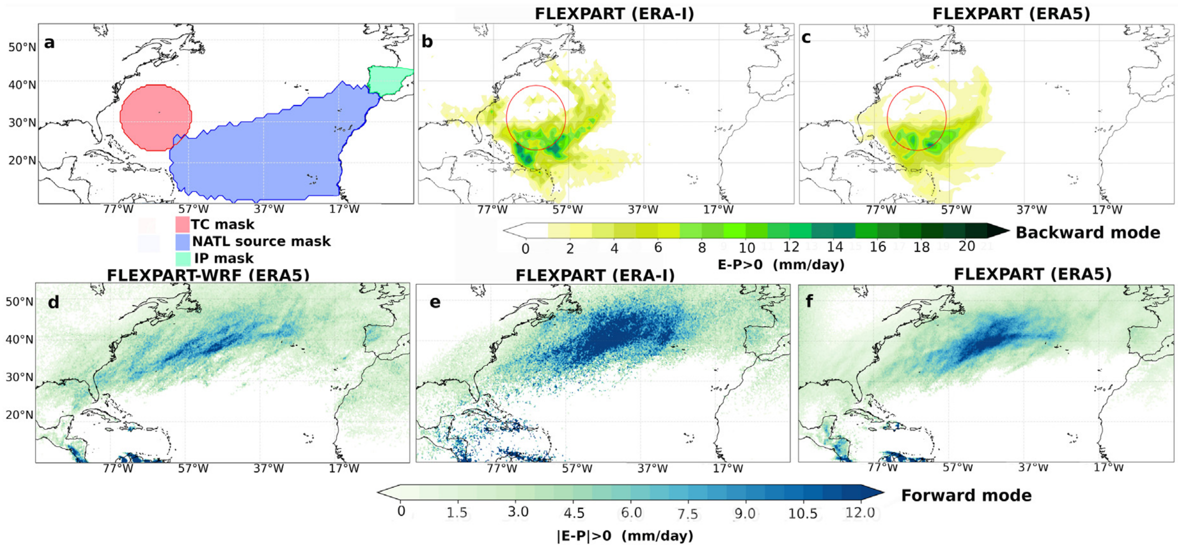

Fig. 2. Pattern representation of moisture sources and sinks associated with a TC and NATL. The patterns correspond to numerical outputs of the dispersion models: FLEXPART (∼0.5°) [c, f], FLEXPART (1°) [b, e] and FLEXPART-WRF (∼0.18°) [d]. ERA5 and ERA-I are the reanalyses used for forcing. The masks for the TC and NATL-source are represented in pink and blue, respectively [a].

results have been published by Perez-Alarcon et al. [26,27] for case studies or climatological analyses of all tropical cyclones (TCs) in the North Atlantic basin. In addition, Fig. 2d–f shows the moisture sinks associated with a target position over the North Atlantic Ocean, the so-called NATL moisture source (blue area in Fig. 2a), for the period from January to March 2014 (boreal winter). In this case, the methodology of Stohl and James [4] was used. These results show similarity with the pattern found by Gimeno et al. [22].

In these two examples, two types of masks have been used, one that is mobile for tracking a TC (regional), changing position as the TC moves (in this case only one position is shown) and another fixed for the NATL (global), allowing correct representation of the pattern to be achieved in each example. The WVRT for these examples was considered as 10 days. The number of days considered in the TROVA runs is an adjustable parameter, depending on the number of days used for the residence of the water vapor. This facilitates the use of optimal integration times determined by Nieto et al. [30] globally and thus provides a better representation in the pattern of moisture sources. It is necessary to clarify that the differences in the patterns for the same case study are related to differences in input data. These differences are associated with the differences in the configurations of FLEXPART and FLEXPART-WRF models and not related to the TROVA software.

3.1. Sensitivity analysis of TROVA

Below is a sensitivity analysis of the software in which the input data corresponding to FLEXPART-WRF with a spatial resolution of ∼0.2° was considered constant, but the spatial resolution of the TROVA output mesh was varied to analyze the sensitivity of this software for different resolutions in the representation of the E-P pattern. The period considered corresponds to the months of January to March 2014 (boreal winter). It is important to note that different FLEXPART or FLEXPART-WRF input data were not considered for this analysis (as shown in Fig. 2), since these data present differences related to the configuration of each model, which influences the representation of the moisture budget. Therefore, differences in the E-P pattern cannot be directly associated with TROVA.

Table 2 shows the calculated statistics in the representation of the moisture sources contributing to the precipitation in the Iberian Peninsula (IP, in Fig. 2a) in winter. In general, it is observed a smoothing of the E-P pattern as the spatial resolution of the output grid decreases, as shown by the mean, the extreme values, and the standard deviation. This result is related to the method of calculating the humidity changes (dq/dt, [4]) at the nodes of the output grid; for each point of the grid, when the resolution is low, many particles showing dq/dt<0 or dq/dt>0 are added and a smoothing of the final dq/dt value is obtained. However, when a higher resolution is considered, the sum of dq/dt values at the nodes considers fewer particles, and the pattern shows higher values. This does not imply errors in TROVA, simply that the user must know the resolution at which he/she wishes to work and thus obtain a more homogeneous pattern or one with greater variation.

To corroborate the above, we analyzed the changes in the structure of the E-P pattern that can be observed for the different gridded resolutions. For this, the Structural Similarity Index (SSIM, Wang et al. [31]) was used. The SSIM is perfect when the value is 1 and shows the greatest difference when it approaches -1. For this analysis, the images in Fig. 3 of the moisture sources for 0.2, 0.25, 0.5, and 1 degrees of spatial resolution were used. Fig. 3a is considered as the reference image as it has input data at ∼0.2° , therefore its representation should be the most perfect. In general, it is verified that there is a smoothing of the pattern as the spatial resolution decreases, but the structure is shown to be very similar between all resolutions, as shown by a SSMI with values $\geq$ 0.85. Therefore, it is suggested to use a resolution for TROVA very similar to that of the FLEXPART-WRF or FLEXPART input data.

4. Impact

The moisture transport from ocean sources to the continents forms the link between evaporation from the ocean and precipitation over the continents, thus establishing the moisture source–sink relationship [32]. In the context of climate change, a change in moisture transport is associated with the moisture increase derived from the increment of temperature [33, 34]. Therefore, the study of moisture transport is crucial for a better understanding of the observed changes and those derived

Table 2
Statigraphs used in the comparison.

Resolution	Statigraphs (mm/day)				Structural similarity
	Mean	Maximum	Minimum	Standard deviation	SSIM
0.2°	0.12	2.00	0.0	0.15	–
0.25°	0.10	1.85	0.0	0.13	0.86
0.5°	0.08	1.25	0.0	0.11	0.85
1.0°	0.07	1.10	0.0	0.10	0.86

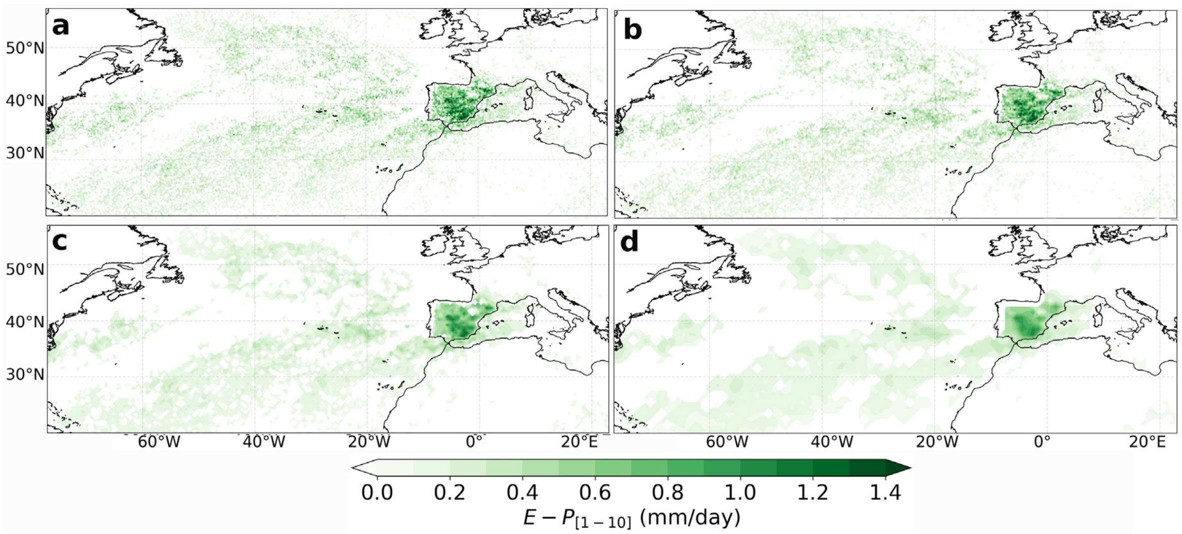

Fig. 3. Moisture sources pattern (E-P>0) that contributed to precipitation over the Iberian Peninsula (IP) calculated from TROVA using different spatial resolutions: (a) 0.2, (b) 0.25, (c) 0.5 and (d) 1 degrees.

from projections of future climate data [1,32]. Therefore, it is important to have a set of tools for Lagrangian post-processing of different model outputs. Specifically, TROVA enables the user community to post-process these model outputs in present and future times to understand changes in the hydrological cycle. In addition, TROVA allows for the two main Lagrangian methodologies established in literature to be integrated into a single tool, thus facilitating comparison of the results obtained and proposing more conclusive results for the scientific community.

5. Conclusions

In this study, TROVA software is presented with its use in the analysis and modeling of atmospheric moisture transport. We anticipate that TROVA will benefit a wide range of users of this scientific field and help understand future changes in the hydrological cycle, thus predicting changes in precipitation over certain regions. In addition, the software will enable the study of future changes in moisture sources and sinks for climatological analysis, specific local events, extremes, or meteorological phenomena.

CRediT authorship contribution statement

José C. Fernández-Alvarez: Conceptualization, Methodology, Software, Writing – original draft, Writing – review & editing, Data curation, Formal analysis. **Albenis Pérez-Alarcón:** Data curation, Software, Methodology, Formal analysis. **Raquel Nieto:** Conceptualization, Writing – review & editing, Investigation, Supervision. **Luis Gimeno:** Conceptualization, Writing – review & editing, Investigation, Supervision.

Declaration of competing interest

The authors declare that they have no known competing financial interests or personal relationships that could have appeared to influence the work reported in this paper.

Data availability

Data will be made available on request.

Acknowledgments

J.C.F-A acknowledge the support from the Xunta de Galicia (Galician Regional Government) under the grants no. ED481A-2020/193. A.P-A acknowledges a PhD grant from the University of Vigo. This work is supported by the SETESTRELO project (PID2021-122314OB-I00) funded by the Ministerio de Ciencia, Innovación y Universidades, Spain. Partial support was also obtained from the Xunta de Galicia under the project "Programa de Consolidación e Estructuración de Unidades de Investigación Competitivas (Grupos de Referencia Competitiva)" (ED431C 2021/44). In addition, this work has been possible thanks to the computing resources and technical support provided by CESGA (Centro de Supercomputación de Galicia).

Appendix A. Supplementary data

Supplementary material related to this article can be found online at https://doi.org/10.1016/j.softx.2022.101228.

References

[1] Gimeno L, Stohl A, Trigo RM, Dominguez F, Yoshimura K, Yu L, et al. Oceanic and terrestrial sources of continental precipitation. Rev Geophys 2012;50:RG4003. http://dx.doi.org/10.1029/2012RG000389.

[2] Van der Ent RJ, Savenije HHG. Length and time scales of atmospheric moisture recycling. Atmos Chem Phys 2011;11:1853–63. http://dx.doi.org/10.5194/acp-11-1853-2011.

[3] Stohl A, James PA. Lagrangian analysis of the atmospheric branch of the global water cycle. Part I: Method description, validation, and demonstration for the 2002 flooding in central Europe. J Hydrometeorol 2004;5:656–78. http://dx.doi.org/10.1175/1525-7541(2004)005%3C0656:ALAOTA%3E2.0.CO;2.

[4] Stohl A, James PA. A Lagrangian analysis of the atmospheric branch of the global water cycle: Part II: Earth's river catchments ocean basins, and moisture transports between them. J Hydrometeorol 2005;6:961–84. http://dx.doi.org/10.1175/JHM470.1.
[5] Dansgaard W. Stable isotopes in precipitation. Tellus 1964;16:436–68. http://dx.doi.org/10.3402/tellusa.v16i4.8993.
[6] Insua-Costa D, Miguez-Macho G. A new moisture tagging capability in the weather research and forecasting model: Formulation, validation and application to the 2014 Great Lake-effect snowstorm. Earth Syst Dynam 2018;9:167–85. http://dx.doi.org/10.5194/esd-9-167-2018.
[7] Gimeno L7, et al. Recent progress on the sources of continental precipitation as revealed by moisture transport analysis. Earth Sci Rev 2020;201:103070. http://dx.doi.org/10.1016/j.earscirev.2019.103070.
[8] Sodemann H, Schwierz C, Wernli H. Interannual variability of greenland winter precipitation sources: Lagrangian moisture diagnostic and North Atlantic oscillation influence. J Geophys Res-Atmos 2008;113:D03107. http://dx.doi.org/10.1029/2007JD008503.
[9] Sun B, Wang H. Moisture sources of semiarid grassland in China using the Lagrangian particle model FLEXPART. J Clim 2014;27:2457–74. http://dx.doi.org/10.1175/JCLI-D-13-00517.1.
[10] Keune J, Schumacher DL, Miralles DG. A unified framework to estimate the origins of atmospheric moisture and heat using Lagrangian models. Geosci Model Dev 2022;15:1875–98. http://dx.doi.org/10.5194/gmd-15-1875-2022.
[11] Stohl A, Hittenberger M, Wotawa G. Validation of the Lagrangian particle dispersion model FLEXPART against large scale tracer experiment data. Atmos Environ 1998;24:4245–64. http://dx.doi.org/10.1016/S1352-2310(98)00184-8.
[12] Stohl A, Forster C, Frank A, Seibert P, Wotawa G. The Lagrangian particle dispersion model FLEXPART version 6.2. Atmos Chem Phys 2005;5:2461–74, https://www.atmos-chem-phys.org/acp/5/2461/.
[13] Stohl A, et al. The Lagrangian particle dispersion model FLEXPART version 9.3. 2016, https://www.flexpart.eu/export/496c6079149f12fbb3e7ecf1f351470794679655/flexpart.git/doc/latex-manual/flexpart9.3.pdf. [Accessed 31 March 2022].
[14] Piso I, et al. The Lagrangian particle dispersion model FLEXPART version 10.3. Geosci Model Dev Discuss 2019. http://dx.doi.org/10.5194/gmd-2018-333.
[15] Brioude J, et al. The Lagrangian particle dispersion model FLEXPART-WRF version 3.1. Geosci Model Dev 2013;6:1889–904. http://dx.doi.org/10.5194/gmd-6-1889-2013.
[16] Miltenberger AK, Pfahl S, Wernli H. An online trajectory module (version 1.0) for the nonhydrostatic numerical weather prediction model COSMO. Geosci Model Dev 2013;6:1989–2004. http://dx.doi.org/10.5194/gmd-6-1989-2013.
[17] Sprenger M, Wernli H. The LAGRANTO Lagrangian analysis tool - version 2.0. Geosci Model Dev 2015;8:2569–86. http://dx.doi.org/10.5194/gmd-8-2569-2015.
[18] Dee DP, et al. The ERA-interim reanalysis: Configuration and performance of the data assimilation system. Q J R Meteorol Soc 2011;137:553–97. http://dx.doi.org/10.1002/qj.828.
[19] Hersbach H, et al. The ERA5 global reanalysis. Q J R Meteorol Soc 2020;146:1999–2049. http://dx.doi.org/10.1002/qj.3803.
[20] Skamarock W, et al. A description of the advanced research WRF version 3. Technical report, 2008, p. 113. http://dx.doi.org/10.5065/D6DZ069T.
[21] Baldauf M, Seifert A, Foerstner J, Majewski D, Raschendorfer M, Reinhardt T. Operational convective-scale numerical weather prediction with the COSMO-model: Description and sensitivities. Mon Weather Rev 2011;139:3887–905. http://dx.doi.org/10.1175/MWR-D-10-05013.1.
[22] Gimeno L, Nieto R, Trigo R, Vicente-Serrano SM, López-Moreno JI. Where does the Iberian Peninsula moisture comme from? An answer based on a Lagrangian approach. J Hydrometeorol 2010;11:336–421. http://dx.doi.org/10.1175/2009JHM1182.
[23] van der Ent RJ, Tuinenburg OA. The residence time of water in the atmosphere revisited. Hydrol Earth Syst Sci 2017;21:779–90. http://dx.doi.org/10.5194/hess-21-779-2017.
[24] Gimeno L. The residence time of water vapour in the atmosphere. Nat. Rev. Earth Environ. 2021;2:558–69. http://dx.doi.org/10.1038/s43017-021-00181-9.
[25] Fremme A, Sodemann H. The role of land and ocean evaporation on the variability of precipitation in the Yangtze River valley. Hydrol. Earth Syst. Sci. 2019;23:2525–40. http://dx.doi.org/10.5194/hess-23-2525-2019.
[26] Pérez-Alarcón A, Coll-Hidalgo P, Fernández-Alvarez JC, Sorí R, Nieto R, Gimeno L. Moisture sources for precipitation associated with major hurricanes during 2017 in the North Atlantic basin. J Geophys Res-Atmos 2022;127. http://dx.doi.org/10.1029/2021JD035554, e2021JD035554.
[27] Pérez-Alarcón A, Sorí R, Fernández-Alvarez JC, Nieto R, Gimeno L. Where does the moisture for North Atlantic tropical cyclones come from? J Hydrometeorol 2022;23:457–72. http://dx.doi.org/10.1175/JHM-D-21-0117.1.
[28] Anaconda Documentation. https://docs.anaconda.com. [Accessed 22 March 2022].
[29] Fernandez-Alvarez JC, Vazquez M, Pérez-Alarcón A, Nieto R, Gimeno L. Assessment of moisture sources and sinks estimated with different versions of FLEXPART and FLEXPART-WRF models forced with ECMWF reanalysis data. J Hydrometeorol 2022. (Unpublished results).
[30] Nieto R, Gimeno L. Addendum: A database of optimal integration times for Lagrangian studies of atmospheric moisture sources and sinks. Sci Data 2021;8:130. http://dx.doi.org/10.1038/s41597-021-00902-1.
[31] Wang Z, Bovik AC, Sheikh HR, Simoncelli EP. Image quality assessment: From error visibility to structural similarity. IEEE Trans Image Process 2004;13:600–12. http://dx.doi.org/10.1109/TIP.2003.819861.
[32] Gimeno L. Oceanic sources of continental precipitation. Water Resour Res 2014;50:3647–9. http://dx.doi.org/10.1002/2014WR015477.
[33] Bao J, Sherwood SC, Alexander LV, Evans JP. Future increases in extreme precipitation exceed observed scaling rates. Nat Clim Chang 2017;7:128–32. http://dx.doi.org/10.1038/nclimate3201.
[34] Prein AF, et al. Increased rainfall volume from future convective storms in the US. Nat Clim Chang 2017;7:880–4. http://dx.doi.org/10.1038/s41558-017-0007-7.

4.3 Comparison of moisture sources and sinks estimated with different versions of FLEXPART and FLEXPART-WRF models forced with ECMWF reanalysis data

Fernández-Alvarez, J. C., Vázquez, M., Pérez-Alarcón, A., Nieto, R., & Gimeno, L. (2023). Comparison of moisture sources and sinks estimated with different versions of FLEXPART and FLEXPART-WRF models forced with ECMWF reanalysis data. *Journal of Hydrometeorology*, 24(2), 221-239. **@ American Meteorological Society. Used with permission.**

Table 4.3: Detailed description of the journal where the second article was published. The data is updated from 2022 according to the Web of Science (JCR). **IF**: impact factor.

Journal	Description	Journal metrics
Journal of Hydrometeorology	**Publisher**: American Meteorological Society, **Scope**: This journal considers research that includes results from numerical modelling, and observed or predicted data for the flows and storage of water and energy. In addition, it includes those related to interactions with the boundary layer or processes associated with radiation or precipitation.	**IF:** 3.8, 5-year **IF**: 4.4, **Ranking**: 38 out of 109 in Meteorology & Atmospheric Sciences (**Q2**)

Comparison of Moisture Sources and Sinks Estimated with Different Versions of FLEXPART and FLEXPART-WRF Models Forced with ECMWF Reanalysis Data

JOSÉ C. FERNÁNDEZ-ALVAREZ,[a,b] MARTA VÁZQUEZ,[a] ALBENIS PÉREZ-ALARCÓN,[a,b] RAQUEL NIETO,[a] AND LUIS GIMENO[a]

[a] *Centro de Investigación Mariña, Universidade de Vigo, Environmental Physics Laboratory (EPhysLab), Ourense, Spain*
[b] *Departamento de Meteorología, Instituto Superior de Tecnologías y Ciencias Aplicadas, Universidad de La Habana, Havana, Cuba*

(Manuscript received 4 February 2022, in final form 27 October 2022)

ABSTRACT: Moisture transport and changes in the source–sink relationship play a vital role in the atmospheric branch of the hydrological cycle. Lagrangian approaches have emerged as the dominant tool to account for estimations of moisture sources and sinks; those that use the FLEXPART model fed by ERA-Interim reanalysis are most commonly used. With the release of the higher spatial resolution ERA5, it is crucial to compare the representation of moisture sources and sinks using the FLEXPART Lagrangian model with different resolutions in the input data, as well as its version for WRF-ARW input data, the FLEXPART-WRF. In this study, we compare this model for 2014 and moisture sources for the Iberian Peninsula and moisture sinks of North Atlantic and Mediterranean. For comparison criteria, we considered FLEXPARTv9.0 outputs forced by ERA-Interim reanalysis as "control" values. It is concluded that FLEXPARTv10.3 forced with ERA5 data at various horizontal resolutions (0.5° and 1°) represents moisture source and sink zones as represented forced by ERA-Interim (1°). In addition, the version fed with the dynamic downscaling WRF-ARW outputs (~20 km), previously forced with ERA5, also represents these patterns accurately, allowing this tool to be used in future investigations at higher resolutions and for regional domains.

SIGNIFICANCE STATEMENT: The FLEXPART dispersion model forced with ERA5 reanalysis data at various resolutions represents moisture source and sink zones compared to when it is forced by ERA-Interim. When the Weather Research and Forecasting Model is used to dynamically downscale ERA5, FLEXPART-WRF can also represent moisture sources and sinks, allowing this tool to be used in future investigations requiring higher resolution and regional domains and on regions with a predominance of complex orography due to its ability to represent local moisture transport.

KEYWORDS: Moisture/moisture budget; Mesoscale models; Model comparison; Reanalysis data; Regional models

1. Introduction

Currently, for the fields of hydrology, climatology, and meteorology, it is necessary to understand the origin of humidity and precipitation that occurs over a given region, especially on continents, in which water resources play a vital role (Randhir 2012). Considering that approximately 90% of the water in the atmosphere comes from evaporation over the oceans, lakes, and other open water bodies, its atmospheric transport plays an important role in the precipitation component of the hydrological cycle, allowing redistribution of water toward the land (Quante and Mathias 2006). Therefore, to understand moisture transport processes, it is necessary to know how water vapor is distributed in the atmosphere, considering its concentration is highly variable in space and time (Gimeno et al. 2010a). In this sense, the moisture transport and changes in the source–sink relationship can play a critical role in the hydrological cycle, allowing for the analysis of variations in the relative importance of oceanic sources versus terrestrial sources in continental precipitation at a large scale (Gimeno et al. 2012). On the other hand, in the context of climate change, it is important to study future changes associated in the source–sink relationship and how it may influence continental precipitation.

Different methods have been developed to identify atmospheric moisture sources and their related sinks; they can be classified into numerical water vapor tracers, analytical models, and physical water vapor tracers using isotopes. Gimeno et al. (2012, 2020) demonstrated their validity, specific uses, advantages, and disadvantages. Various studies on moisture source–sink assessments have been conducted at global scales. In the last decades, several authors have investigated moisture transport in different regions. A complete summary of the studies is shown in Gimeno et al. (2020), including investigations related to extreme events such as droughts or floods and meteorological or circulation systems. Additionally, numerical methods have been increasingly used. Such methods can be classified into Eulerian and Lagrangian; the former deals with the water balance at fixed locations as time varies, while the latter is based on studying the water vapor budget of air parcels as they travel either forward or backward in time and space (Stohl and James 2005). The Lagrangian Flexible Particle

Supplemental information related to this paper is available at the Journals Online website: https://doi.org/10.1175/JHM-D-22-0018.s1.

Corresponding author: José C. Fernández-Alvarez, jose.carlos.fernandez.alvarez@uvigo.es

DOI: 10.1175/JHM-D-22-0018.1

(FLEXPART) dispersion model (Stohl and James 2004), in its several versions, has been widely used in many studies to determine moisture sources and sinks usually fed with the three-dimensional (3D) ERA-Interim global atmospheric reanalysis data (ERA-I; Dee et al. 2011) from the European Centre for Medium-Range Weather Forecasts (ECMWF), covering the period from January 1979 to August 2019 with a 1° horizontal spatial resolution. However, this reanalysis has been superseded by the ERA5 reanalysis (Hersbach et al. 2020).

A current challenge for the coming years in the atmospheric moisture transport field requires advances in the evaluation of the moisture sources, which has been limited mainly due to the grid scale of the model results (Gimeno et al. 2020). These advances allow for a better understanding of the role of moisture transport in precipitation distribution. As such, the new ERA5 reanalysis data have a higher spatial (0.25°, 0.5°, and 1°) and temporal resolution (1 h), including an improved representation of the troposphere, a better global balance of precipitation and evaporation, and more consistent coverage of sea surface temperature and sea ice (Hersbach et al. 2020). In addition, this dataset covers a longer period, from 1950 to the present, with daily updates being available 5 days behind real time. These improvements may better represent the source–sink relationships involved in the atmospheric branch of the hydrological cycle; however, it is necessary to compare this fact with respect to the previous reanalysis products such as ERA-I. Furthermore, at the time of submission of this work, no studies have compared moisture sources and sinks using ERA5 data to feed any version of the FLEXPART model to our best knowledge.

If the further representation of the physical processes involved in moisture transport at a regional scale is required, it is necessary to increase the resolution of the computational domain. These more detailed results can be achieved feeding the Lagrangian model with a dynamic mesoscale model for a regional domain. Recently, the use of the FLEXPART model adapted for input data from the Weather Research and Forecasting (WRF) Model (Brioude et al. 2013) but forced with National Centers for Environmental Prediction (NCEP) reanalysis data (Kalnay et al. 1996) was used to analyze the moisture sources associated with a rainfall event using backward trajectories over Japan in July 2020 (Zhao et al. 2021). Furthermore, Cloux et al. (2021) found that this model performed well in identifying local and mid-distance sources involved in extreme precipitation events in the Mediterranean area but performing simulations with WRF outputs forced by ERA-I that is no longer updated. Both studies are highly local and focused on the effects of the precipitation associated with meteorological systems. However, it is still necessary to evaluate the ability of this model to represent large-scale sources and sinks of moisture.

Therefore, the objective of this investigation was to compare the representation of moisture sources and sinks for ERA5 reanalysis data with different configurations of the Lagrangian models FLEXPART and FLEXPART-WRF for 2014, carried out for the North Atlantic region and most of Europe, taking into account that the version of WRF used is optimized for the Iberian Peninsula (IP) (Insua-Costa and Miguez-Macho 2018; Insua-Costa et al. 2019), and the analyzed region includes two of the main global oceanic moisture sources, the Mediterranean Sea (MED) and the North Atlantic Ocean (NATL) (Gimeno et al. 2010a).

2. Materials and methods

a. *Configurations and data used to force the different FLEXPART model versions*

The outputs of the FLEXPARTv9.0 Lagrangian model (Stohl 1998; Stohl and Thomson 1999; Stohl et al. 2005) forced by ERA-I reanalysis data (Dee et al. 2011) from the ECMWF with a 1° horizontal resolution and 61 vertical levels (herein, FLEX-ERA-I.1) are considered as our "control" values. The simulation was carried out for a global domain, tracking every 6 h forward in time 2.0 million air parcels (or particles) into which the atmosphere is evenly divided. This number of particles is chosen to have at least one particle at each point of the grid and most vertical levels. This configuration is the same as the one widely used in previous research to represent the behavior of moisture sources and sinks at global or regional scales (Gimeno et al. 2020, and references therein). This FLEXPART version (v9.0) allows working with input data from the ECMWF Integrated Forecast System, such as ERA-I, but does not allow the newest ERA5 (Hersbach et al. 2020). Pisso et al. (2019) described the physical characteristics, parameterizations, and improvements of the different FLEXPART models over time. FLEXPARTv9.0 includes a global land-use inventory, allowing accurate dry deposition calculations everywhere on the globe, distinguishing between in-cloud and below-cloud scavenging for washout, relying on simple diagnostics for clouds based on gridscale relative humidity. The physics of the FLEXPARTv9.0 model is described by the zero-acceleration scheme and a set of parameterizations. For instance, Hanna's (1982) parameterization scheme is used for wind fluctuations, the frictional velocity is computed using surface stresses, and sensible heat fluxes is considered in the boundary layer parameterization. Meanwhile, the profile method (Berkowickz and Prahm 1982) is applied in the absence of frictional velocity information. Turbulent motion is parameterized considering a Markov process based on the Langevin equation (Thomson 1987). Emanuel and Živković-Rothman's (1999) one-dimensional convection model is used as a convection scheme. Radioactive decay and dry and wet deposition are also considered in the physics of the model.

The latest version of this Lagrangian model, FLEXPARTv10.3, was updated to run with the ERA5 dataset (among other changes), which is particularly important given that ERA-I has no longer been updated since August 2019. The new version of this Lagrangian model (Pisso et al. 2019) presents modifications with respect to the previous v9.0. A new scheme applying more realistic skewed rather than Gaussian turbulence statistics in the convective atmospheric boundary layer has been incorporated. Furthermore, the wet deposition scheme for aerosols was revised (Grythe et al. 2017), introducing dependencies on aerosol size and precipitation type (rain or snow) and distinguishing between

TABLE 1. Main changes in ERA5 vs ERA-I improving the wet and dry biases (from Hersbach et al. 2020).

Elements	ERA5 main changes
Microphysics parameterization	Improvements for warm-rain processes and ice-phase processes and ice supersaturation.
Large-scale cloud and precipitation scheme	Improved representation of mixed-phase clouds and prognostic variables for precipitating rain and snow.
Convection parameterization	Revision of the entrainment and the coupling with the large-scale (a large redistribution of rainfall from the Hadley cell to the Walker cell).
Assimilated data	Increased from ~0.75 million per day on average in 1979 to around 21 million per day by July 2018.

in-cloud and below-cloud scavenging. Moreover, the model reads 3D cloud water fields from meteorological input files.

Considering that this work compares the ability of the new FLEXPARTv10.3 to reproduce moisture sources and sinks forced by several horizontal resolutions of the new ERA5, it is necessary to highlight some improvements of ERA5 with respect to ERA-I, which are considerable in the troposphere (Hersbach et al. 2020); these include changes in the physical parameterizations of subgrid-scale processes and the formulation of the organized deep entrainment in the convection parameterization scheme (Bechtold et al. 2008); the moisture-convergence-based entrainment formulation was replaced with environmental relative-humidity-dependent entrainment. A complete evaluation of the ERA5 reanalysis is presented by Hersbach et al. (2020). According to Hersbach et al. (2020), the improvements in precipitation field occur both over the extratropical regions, tropical oceanic zones [where correlations were already quite high in ERA-I compared to the Tropical Rainfall Measuring Mission (TRMM/3B43)], and over the tropical landmasses, where ERA-I showed particularly low correlations). Moreover, global correlations with data from the Global Precipitation Climatology Centre (GPCP) at a 2.5° resolution (from 1979 to 2018) are also improved with ERA5 (77% versus 67% for ERA-I). In addition, ERA5 provides data with a higher vertical resolution, with 137 vertical hybrid sigma/pressure levels from 1013.25 to 0.01 hPa; ERA-I only has 61. Moreover, ERA5 provides a larger set of different horizontal spatial resolutions (Hersbach and Dee 2016), including 0.25°, 0.5°, and 1°. The main changes in ERA5 compared to ERA-I that can improve the wet and dry biases (Hersbach et al. 2020) are shown in Table 1.

Here, the FLEXPARTv10.3 model has been fed every 6 h with two datasets of ERA5 reanalysis data at different resolutions: first, for a direct comparison with our control experiment, with ERA5 at 1° (hereafter named as FLEX-ERA5.1), and then, to increase the resolution of the Lagrangian outputs, with ERA5 at 0.5° (herein denoted as FLEX-ERA5.05). It should be noted that vertical resolution improved using ERA5 compared to ERA-I, and consequently the FLEX-ERA5.1 and FLEX-ERA5.05 versus the control experiment FLEX-ERA-I.1.

The FLEXPART model needs to maintain the atmospheric mass (one particle per vertical level is required) during the simulation; this must be considered in terms of the number of particles to be simulated. As ERA5 has a higher vertical resolution than ERA-I (more than double, 137 versus 61 levels), therefore the parcels in which the atmosphere is divided must be greater than in the FLEX-ERA-I.1 control simulation. Therefore, for the FLEX-ERA5.1 experiment, the atmosphere is homogeneously divided and evenly distributed into approximately 9 million particles, and 30 million for FLEX-ERA5.05. It is important to note that the data download time becomes slower as the horizontal and vertical resolution increases and that the run time also increases as a function of the number of particles into which the atmosphere is divided, which is why the global experiment with ERA5 at 0.25° is not operational. The best ratio between time, computational power, and capacity for storing the model outputs is decisive when deciding on the experiments to be performed.

Although the experiments explained above have been run on a global scale, it is possible to obtain resolution gains and improve the physical characterizations of the results by using input data on a regional scale. With this aim, a dynamic downscaling was carried out using the WRF-ARWv3.8.1 model (Skamarock et al. 2008) forced every 6 h with ERA5 reanalysis data at 0.25° in latitude and longitude. Figure 1a shows the regional domain for the study, 115°W–42°E and 19°S–59°N. WRF outputs were downscaled to 0.18° of the horizontal spatial resolution and saved every 6 h. A spinup was carried out for a month before the beginning of the study period. These simulations were carried out in two intervals using the restart mode of the WRF-ARW. We used the WSM6 microphysics scheme (Hong and Lim 2006), the Yonsei University PBL scheme (Hong et al. 2006), the revised MM5 surface layer scheme (Jimenez et al. 2012), the United Noah Land Surface Model (Tewari et al. 2004), the RRTMG shortwave and longwave schemes (Iacono et al. 2008), and the Kain–Fritsch ensemble cumulus scheme (Kain 2004). Spectral nudging of waves longer than 1000 km was activated to avoid distortion of the large-scale circulation within the regional model domain due to the interaction between the model's solution and the lateral boundary conditions (Miguez-Macho et al. 2004). The selection criteria for these parameterizations are based on the fact that they have been evaluated in several investigations for the region (e.g., Insua-Costa and Miguez-Macho 2018; Insua-Costa et al. 2019).

The regional WRF-ARW outputs using ERA5 (herein WRF-ERA5) were used to run the appropriated version of FLEXPART adapted for WRF in its v3.3.2 version (Brioude et al. 2013). WRF-ERA5 outputs have 40 vertical levels in sigma coordinates from the surface to approximately 50 hPa (pressure top to use in the model) and 480 × 780 grid nodes (~0.18°). The FLEXPART-WRF used these 40 levels reducing the computational cost maintaining the atmosphere properties since the primary changes in humidity occur down the

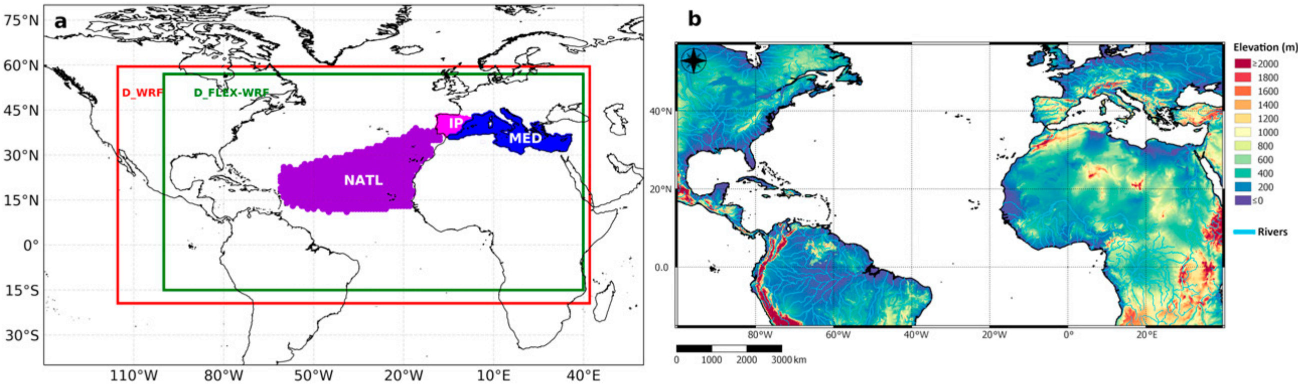

FIG. 1. (a) Domains for WRF-ERA5 (red) and FLEX-WRF (green) simulations. The individual target regions under the study are colored: the Mediterranean Sea (MED) is shown in blue, the Iberian Peninsula (IP) in pink, and the North Atlantic Ocean (NATL) in dark purple. (b) Orography of the region, where the WRF simulations are performed, was taken from the HydroSHEDS project (Lehner et al. 2008).

tropopause. The simulated area has 400 × 777 grid points (smaller in size than WRF outputs), where the particles are released. In addition, for FLEXPART-WRF, we used Hanna's scheme for turbulence parameterization (Hanna 1982), with a convection scheme activated. In this simulation, to maintain the distribution of atmospheric mass, the atmosphere was homogeneously divided into 2 million air parcels (or particles), which were subsequently moved forward in time by the model along the whole study period. The outputs from this experiment are denoted as FLEX-WRF in the text. Table 2 summarizes the FLEXPART versions of the model, input and output data characteristics, the particles moved by the model, vertical atmospheric levels, pressure top, and number of levels up to 50 hPa (NL50 hPa).

b. *Moisture sources and sinks used for the comparison*

The selection criteria for the study regions were based on two reasons: first, that the North Atlantic and European areas encompass two of the main global oceanic moisture sources, the NATL and the MED (as defined in Gimeno et al. 2012), and second, due to the availability of a correctly regionalized WRF-ARW Model for the IP (Insua-Costa and Miguez-Macho 2018; Insua-Costa et al. 2019), an area located between these both sources and a sink of moisture from both in different seasonal periods (Gimeno et al. 2010a,b). Focusing on these three areas (included in Fig. 1a), we have compared the ability of the new FLEXPARTv10.3 fed with ERA5 and the FLEXPART-WRFv3.3.2 configurations to represent the atmospheric moisture sources and sinks.

The NATL source is considered a dominant oceanic source that contributes moisture to continental precipitation at both sides of the basin, from North to South America, and over Europe and northern Africa (Gimeno et al. 2010a). The importance of this source has been well documented in several previous analyses, e.g., for Central America (Durán-Quesada et al. 2010), South America (Drumond et al. 2008), or Europe (Gimeno et al. 2010b). Moreover, the NATL contributes to the North and South American monsoon systems, as well as to the Atlantic intertropical convergence zone (ITCZ) (Castillo et al. 2014; Drumond et al. 2011a). According to Gimeno et al. (2010a), the moisture provided from NATL to be transported in the atmosphere increases during winter and decreases strongly in summer, although it does not show many variations in its size and position throughout the year. Many authors have identified the NATL as an important moisture source for Europe, mainly in autumn and winter, as well as in summer months with less influence (e.g., Sodemann and Stohl 2013; Gómez-Hernández et al. 2013). In addition, it has also been found that moisture transport toward Europe from the North Atlantic is strongly influenced by the cyclonic activity and atmospheric rivers (Lavers and Villarini 2013).

The MED, positioned at the border between the tropical climate zone and the midlatitude climate belt, presents a large meridional gradient. Its particular geography, a completely

TABLE 2. Summary of the models and input database used for the different experiments. Characteristics of the input and output model data, resolution, number (in millions) of released particles, vertical atmospheric levels, the top pressure level, and number of levels up to 50 hPa are listed for each experiment.

Experiment name	Model	Input database	Input data resolution	Output resolution	No. of particles/ domain	Vertical levels	Pressure top (hPa)	NL50 hPa
FLEX-ERA-I.1	FLEXPARTv9	ERA-I	1.0°	1.0°	2 million/global	61	0.1	21
FLEX-ERA5.05	FLEXPARTv10.3	ERA5	0.5°	0.5°	30 million/global	137	0.01	48
FLEX-ERA5.1	FLEXPARTv10.3	ERA5	1.0°	1.0°	9 million/global	137	0.01	48
WRF-ERA5	WRF-ARWv3.8.1	ERA5	0.25°	0.18°	—	40	50	—
FLEX-WRF	FLEXPART-WRFv3.3.2	WRF-ERA5	0.18°	0.18°	2 million/regional	40	50	40

closed basin connected to the Atlantic Ocean through the narrow Gibraltar Strait, high mountain ridges surrounding it (its Alps reach 4800 m), islands, peninsulas, and many regional seas and basins, determines a complicated land–sea distribution pattern with a large spatial variability of sea and atmospheric circulation with many subregional and mesoscale features (Lionello et al. 2006). MED plays an important role in the study area in terms of atmospheric moisture transport for precipitation. During boreal summer (when its contribution is higher), it provides moisture to its surroundings, reaching all directions, extending into northern Europe, northeast Africa, and the Middle East. During autumn and winter, its contribution as a moisture supplier for continental areas is reduced, similar to the IP (Gimeno et al. 2010a). The significance of the MED as a moisture source lies in the fact that, for some regions adjacent to it, it is the single major oceanic source of moisture for precipitation (Schicker et al. 2010; Nieto et al. 2010; Drumond et al. 2011b; Gómez-Hernández et al. 2013).

The IP is in southwestern Europe, surrounded by the Mediterranean Sea to the east and the Atlantic Ocean to the west. The precipitation regime in the north and west of the IP is strongly affected by the mean annual cycle of the Atlantic storm track and its variability, whereas in the interior and east of the IP, large-scale synoptic systems share importance with convective precipitation (Trigo et al. 1999, 2000). The main moisture sources that affect the IP are the tropical–subtropical region of North Atlantic Ocean and Mediterranean Sea (a more local source). In addition, the recycling process is a characteristic of the IP, predominantly in the east and center of the region and less relevant in the west and north (Gimeno et al. 2010a; Rios-Entenza and Miguez-Macho 2014; Rios-Entenza et al. 2014).

The period selected for the comparative analysis was 2014. We studied the averaged conditions throughout this year. Despite the short temporal time frame, this can be considered a standard year because the major modes of variability over the region did not show extremes in their phases, such as the North Atlantic Oscillation or El Niño–Southern Oscillation.

c. *Identification of the source and sinks of moisture*

The particles modeled from the different versions of FLEXPART can be followed backward or forward in time along their trajectories to identify moisture sources and sinks, respectively. For that purpose, the particles over a selected region were followed normally for 10 days, which is considered the average residence time of water vapor in the atmosphere (Numaguti 1999; van der Ent and Tuinenburg 2017).

For each particle, the moisture variation along each trajectory every 6 h was computed as

$$(e - p) = m\left(\frac{dq}{dt}\right) \tag{1}$$

where e is the evaporation from the environment, p the precipitation, m the mass of the parcel, and q the specific humidity. Once the individual $(e - p)$ computations for all the parcels were computed for all the trajectories, the total surface freshwater flux at each grid cell $(E - P)$ was computed by adding the contribution by all parcels residing over a gridded area (A) at a specific time. The total budget is computed as

$$(E - P) = \frac{\sum_{k=1}^{N}(e - p)}{A}, \tag{2}$$

where E represents total evaporation, P total precipitation, and N is the total number of particles over A.

It is necessary to consider that the moisture sources for a region are defined as those areas where evaporation dominated over precipitation (i.e., $E - P > 0$) when the backward in time is performed. Otherwise, to find the moisture sinks of air masses leaving a region, it is necessary to detect where they show a net loss of moisture, that is, where precipitation dominates over evaporation, $(E - P) < 0$. For a better representation and interpretation of $(E - P)$ field in the case of sinks (precipitation), it is multiplied by -1 to represent positive rainfall values on the maps, and we will refer to it along the manuscript hereafter as $(P - E) > 0$.

Considering the methodology presented above, in the interval of the 10 days of the trajectories there are 40 values of $(e - p)$, four values every 6 h for each day and particle. For the calculation of the daily pattern $(E - P)_{[d]}$ [d = 1–10 days] according to Eq. (2), the changes in specific humidity (q) are considered along these four values during one day for each particle [Eq. (1)], and the final daily $(e - p)$ value is assigned to the last geographical position of the particle. This ensures that all contributing particles in a given area are taken into account. Subsequently, the sum of the daily values is divided by the area of the considered grid. The pattern integrated for the 10 days, $(E - P)_{[1–10]}$, is the sum of $(E - P)_{[d]}$ from days 1 to 10. As $(E - P)_{[1–10]}$ pattern is determined for the 365 days of the year 2014, the annual and seasonal $(E - P)_{[1–10]}$ patterns could be calculated as means of convenient periods [the whole year, or January–March (JFM), April–June (AMJ), July–September (JAS), and October–December (OND)]. Both methodologies (back and forward performances) and $(E - P)$ field representation, for individual days and/or integrated along the whole trajectories, have been used in numerous studies (e.g., Castillo et al. 2014; Drumond et al. 2008; Nieto et al. 2006; Vázquez et al. 2020).

In this work we compare (i) the moisture sources for a target region, the IP, and (ii) the sinks of moisture for the NATL and MED basin sources. Therefore, backward and forward modes were used, respectively.

d. *Comparison methodology*

The annual and seasonal comparison (increases/decreases) between the dataset obtained in this work was carried out using the ERA-I dataset and derived fields as the control and for 2014. The boreal seasonal periods were selected as in Gimeno et al. (2010b): winter (JFM), spring (AMJ), summer (JAS), and autumn (OND).

First, we compare differences in the integrated water vapor transport [IVT, see Eq. (3)] fields among ERA5, WRF-ERA5, and the control ERA-I datasets. This was done to determine if the WRF Model correctly represents the variables involved in the moisture transport, as the specific humidity and the zonal and meridional wind. The IVT was calculated as

$$\mathrm{IVT} = \sqrt{u_q^2 + v_q^2}, \tag{3}$$

$$u_q = \frac{1}{g}\int_{\mathrm{ps}}^{p} uq\,dp, \tag{4}$$

$$v_q = \frac{1}{g}\int_{\mathrm{ps}}^{p} vq\,dp, \tag{5}$$

where g is the gravitational acceleration, q is the specific humidity, ps is the surface pressure, p pressure on the top, and u and v are the zonal and meridional wind, respectively (Lavers et al. 2012; Zhang et al. 2019). The pressure levels used for IVT calculation were from 1000 to 300 hPa (Ramos et al. 2018).

Later, we compare the differences in the moisture fields (sources and sinks) obtained from the different FLEXPART models used in this work. The comparison was made for the $(E - P)$ field integrated during the 10 days [denoted as $(E - P)_{[1\text{–}10]}$], and on individual days (d): 1, 3, 5, and 10 [denoted as $(E - P)_{[d]}$]. In addition, to analyze whether the representation of moisture sources and sinks are correct, the divergence of the IVT (DIVT) was also checked.

The statistics used (Brown et al. 2013) were the mean absolute error (MAE), root-mean-square error (RMSE), Pearson's correlation (R), bias (B), and standard deviation (STD).

The MAE [Eq. (6)] measures how far two variables or fields are; the closer values are to zero, the more accurate the simulation will be:

$$\mathrm{MAE} = \frac{\sum_{i=1}^{n}|x_i - y_i|}{n}. \tag{6}$$

The RMSE [Eq. (7)] can quantify the magnitude of the deviation of the simulated values concerning the control; when the value of RMSE is equal 0 the simulation is considered perfect:

$$\mathrm{RMSE} = \frac{\sqrt{\sum_{i=1}^{n}(x_i - y_i)^2}}{n}. \tag{7}$$

In Eqs. (6) and (7) [and in Eqs. (8)–(10)], x_i represents the fields from FLEX-ERA5.05, FLEX-ERA5.1, and FLEX-WRF and y_i the control values from FLEX-ERA-I.1; n is the number of points.

The R is an index that measures the degree of covariation between different linearly related variables [Eq. (8), where $\overline{x}_i$ and $\overline{y}_i$ are the mean values of x_i and y_i]. The correlation between two variables X and Y is positive; when one of them increases, the other increases. The closer to one is the value of the correlation coefficient, the more similar the behavior between both variables:

$$R = \frac{\sum_{i=1}^{n}(x_i - \overline{x}_i)(y_i - \overline{y}_i)}{\sqrt{\sum_{i=1}^{n}(x_i - \overline{x}_i)^2(y_i - \overline{y}_i)^2}}. \tag{8}$$

The B [Eq. (9)] provides the difference between a field of values and the control one; the closer the B values are to zero, the more accurate the simulation. The $B < 0$ values indicate a decrease with respect to the control, while $B > 0$ indicates an increase:

$$B = \frac{\sum_{i=1}^{n}(x_i - y_i)}{n}. \tag{9}$$

The STD [Eq. (10)] provides a variability measure in the same units as the quantity being characterized:

$$\mathrm{STD} = \sqrt{\frac{1}{1-n}\sum_{i=1}^{n}(x_i - \overline{x}_i)^2}. \tag{10}$$

Finally, the coefficient of determination (R^2) is used to eliminate a possible exaggeration of the similarities between different sets of results shown by Pearson's coefficient. In addition, the coefficient of variation (VAR = STD/mean) was used to analyze the relationship between the size of the mean and the variability of the variable. It is important to note that when the mean is very close to zero when calculating STD/mean, the value increases, losing the meaning of the coefficient of variation, and therefore it does not necessarily imply a large dispersion of data.

3. Results

The results of the comparison of each configuration with respect to FLEX-ERA-I.1 will be presented following the conceptual diagram in Fig. 2. Initially, the variables involved in moisture transport were analyzed [precipitation (P), evaporation (E), total column water (TCW), IVT, and specific humidity at 850 hPa (q850)]. Later the patterns for moisture sources and sinks ($E - P$ fields) were compared for each target region considered in the study. After that, an analysis of the representativeness of each configuration were carried out using Taylor diagrams. In addition, the MAE and RMSE were determined to know the approximate errors that are made in the use of each configuration in the representation of the patterns of sources and sinks with respect to the control values. Finally, and taking into account the results obtained in the previous steps, the conclusions that make up this analysis are drawn.

a. *Comparison of fields related to moisture transport*

Figure 3 shows the IVT fields from the WRF-ERA5 (at 0.18°), ERA5 (at 0.25°), and ERA-I (control values, at 1°) datasets. The results for ERA5 and WRF-ERA5 match with ERA-I, showing similar areas of maxima and minima values; they accurately represent the known movement of the North Atlantic anticyclone to

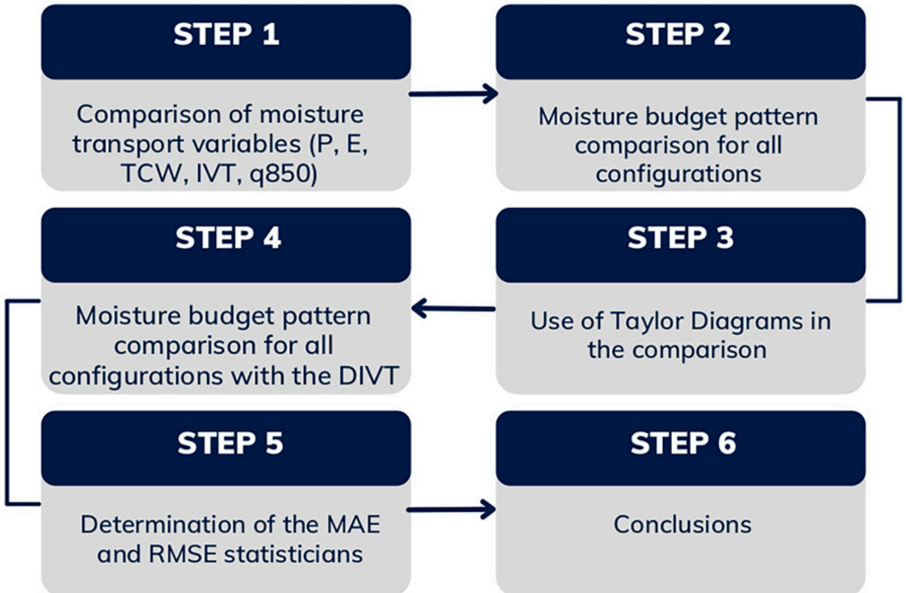

FIG. 2. Conceptual diagram used in the research.

the west in summer or eastward in autumn, and the IVT maximum toward Europe during winter coming from the NATL source (Gimeno et al. 2010b). In addition, the ITCZ was also captured as an area of IVT maxima during all seasons that influence Central America, the Caribbean Sea, and South America.

The higher resolution of WRF-ERA5 and ERA5 captured greater details about the IVT field over areas with significant moisture transport, for instance over the east coast of South America in the Amazon and over the North Atlantic at 30°N. However, WRF-ERA5 increases the IVT (comparing with ERA-I) over certain areas with complex orography (e.g., the Andes, the Rocky Mountains, and southeast of the African continent) and at the edges of the domain. Similar to Rahimi et al. (2022), it seems that WRF simulates a higher IVT than ERA5 in both the ERA5- and global climate models–driven experiments. This could be related to the conditions provided by the WRF Model for the simulations that generate certain uncertainties (Warner et al. 1997); in this case, using local parameterizations and to the initial and boundary conditions, respectively. Visual analysis of the IVT field shows that both products match for the region and therefore allow their use as forcers for the FLEXPARTv10.3 and FLEX-WRF models.

On the other hand, a comparison of the fields related to the water cycle (P, E, IVT, TCW, and q850) from ERA5 and ERA-I reanalyses was carried out, and a Student's t test was used to determine the areas where exits significant differences (at significance level of 5%). Changes and improvement of the ERA5 reanalysis over the areas that act as moisture sources or sinks for our target areas (all north to 10°N) are the key to achieve the better source–sink relationship. The ERA5 total precipitation (P) pattern shows a decrease in the tropical region and intertropical convergence zone and a relative increase for the midlatitude regions (especially in winter and spring) compared with ERA-I (Fig. S1 in the online supplemental material). These results are due to the fact that ERA-I overestimates (underestimates) deep convection and moisture flux convergence over the tropics (midlatitudes), leading to excessive (less) precipitation (Nogueira 2020). Both cases are significantly improved in ERA5, because of better parameterizations and its higher resolution (see Table 2). Significant differences (at 95%) appear over the Caribbean Sea and tropical region; however, in midlatitudes no significant changes are observed. The evaporation (E) field comparison shows a general increase for ERA5, but not significant, and a significant decrease over the western middle Atlantic Ocean basin in summer and autumn (Fig. S2). It is notable that the Mediterranean Sea and North Atlantic regions show an increase from 1 to 2 mm day^{-1}. Nogueira (2020) showed that surface evaporation is slightly higher in ERA5 compared to ERA-I, showing a behavior inversely proportional to precipitation. The total column water ($E - P$) corresponding to ERA5 with respect to ERA-I shows a general decrease throughout the domain, except for the mountainous regions of the Andes Mountains with statistically significant differences (Fig. S3). Notable decreases are observed in the Mediterranean Sea and the North Atlantic, mainly in the seasons of spring, summer and autumn (statistically significant at 95%). In general, the IVT calculated from ERA5 presents lower values than from ERAI; however, areas of increase are observed near the coasts of Africa and over the continent for the winter and annual periods (Fig. S4). In addition, the specific humidity field at 850 hPa presents lower values for ERA5 than for ERA-I, but with the greatest differences over the tropical regions of the Northern Hemisphere and over the South Atlantic (Fig. S5). Maximum differences stand out near the east coast of South America and west of Africa around 10°S. Nogueira (2020) showed that, overall, ERA5 improved the representation of moisture sink/source patterns, primarily over tropical oceans.

b. Representation of the moisture sources for the IP

In this section, the sources of moisture for the IP [$(E - P)_{[1\text{–}10]} > 0$ fields], from the FLEX-WRF, FLEX-ERA5.05, and

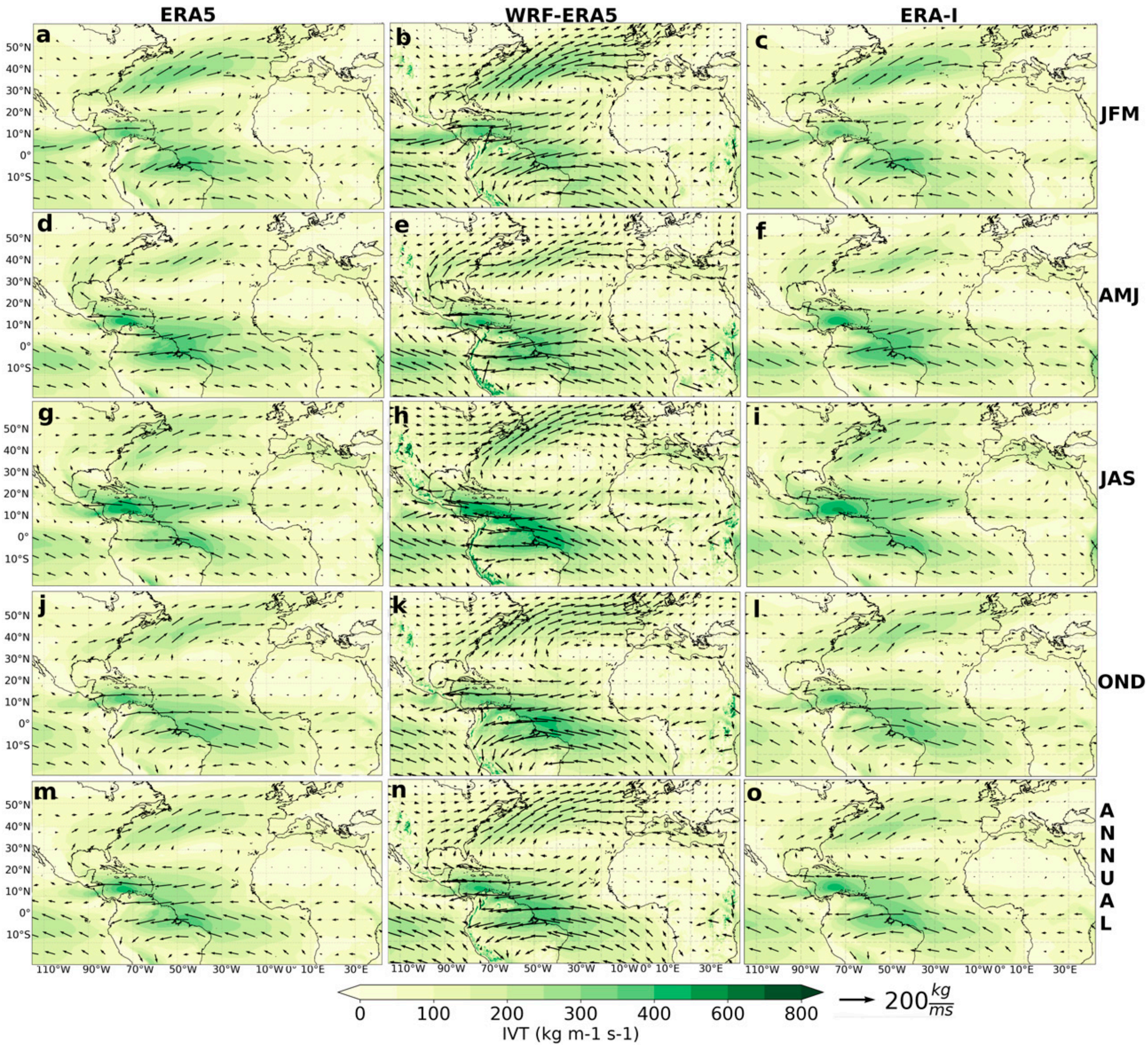

FIG. 3. Annual and seasonal IVT module (colors; kg m^{-1} s^{-1}) and direction (arrows; kg m^{-1} s^{-1}) for ERA5, WRF-ERA5, and ERA-I for 2014 at 0.25°, 0.18°, and 1° resolutions, respectively. The fields displayed correspond to (a)–(c) winter (JFM), (d)–(f) spring (AMJ), (g)–(i) summer (JAS), (j)–(l) autumn (OND), and (m)–(o) annual.

FLEX-ERA5.1 models were compared with those from FLEX-ERA-I.1 (the control) to demonstrate that the different configurations forced with ERA5 represent the moisture sources and results using the ERA-I reanalysis found by previous research as in Gimeno et al. (2010a).

Figure 4 represents the moisture sources for the IP determined from the outputs of each FLEXPART model in the study (first to fourth columns). The fifth column represents the IVT (arrows) and its divergence (colored areas), computed using the ERA-I dataset. In general, there is suitable correspondence between the source zones and areas of IVT divergence. To check the robustness of the results, different statistical parameters were calculated to compare the different configurations with the control experiment. The STD, correlation coefficient, and B are plotted in Fig. 5 for each season, while Fig. 6 shows the MAE and RMSE.

In winter (JFM), the main source of moisture for the IP, the NATL (Gimeno et al. 2010b), is well represented by all the configurations; in general, they all represented a similar spatial pattern over the North Atlantic Ocean and the IP surroundings; the recycling process over the IP was also captured. The small STD confirmed this ($<$0.2 mm day^{-1}) and R values ranging 0.45–0.5 (Fig. 5a). The B showed a general decrease, with values of 0.07, 0.09, and 0.11 for the FLEX-ERA5.1, FLEX-WRF, and FLEX-ERA5.05 experiments, respectively (see Fig. 5a). FLEX-ERA5.1 showed the lowest MAE, with similarly higher values for the other two experiments FLEX-ERA5.05 and FLEX-WRF (Fig. 6a). The RMSE (Fig. 6b)

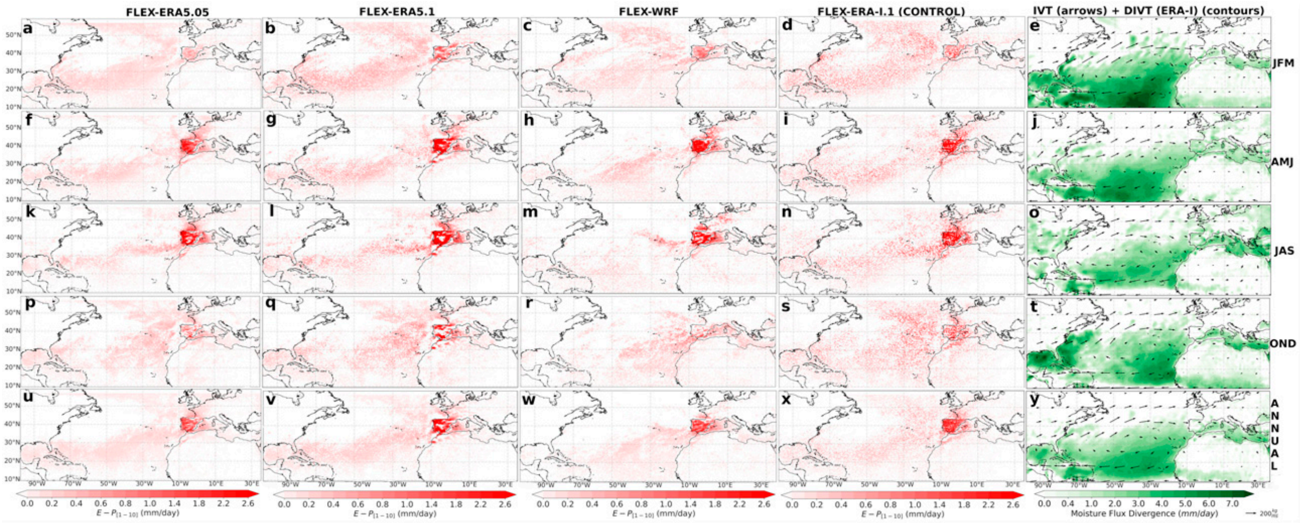

FIG. 4. Moisture sources patterns [$(E - P)_{[1\text{–}10]} > 0$; mm day^{-1}] for the IP from the Lagrangian outputs of FLEX-ERA5.05, FLEX-ERA5.1, FLEX-WRF, and FLEX-ERA-I.1. The right column represents the IVT field (arrows; kg m^{-1} s^{-1}) and its divergence (contours; mm day^{-1}) from ERA-I at 1°. The fields displayed correspond to (a)–(e) JFM, (f)–(j) AMJ, (k)–(o) JAS, (p)–(t) OND, and (u)–(y) annual.

showed values ~0.2 mm day^{-1} for FLEX-WRF and FLEX-ERA5.1 but slightly higher for FLEX-ERA5.05. The RSME weighs the maximum errors and, therefore, indicates the largest errors for each configuration. The higher RMSE values observed in FLEX-ERA5.05 can be related to the smoother pattern over the Atlantic corridor (see Fig. 4).

In spring (AMJ), there is suitable agreement in the pattern of the three configurations under study (Figs. 4f–i), as shown by high R (around 0.7) and STD values (around 0.2–0.4 mm day^{-1}) in Fig. 5b. The lowest STD was obtained for FLEX-ERA5.05 and the highest for FLEX-ERA5.1. Again, the B indicates a decrease of the sources compared to the control values for the three

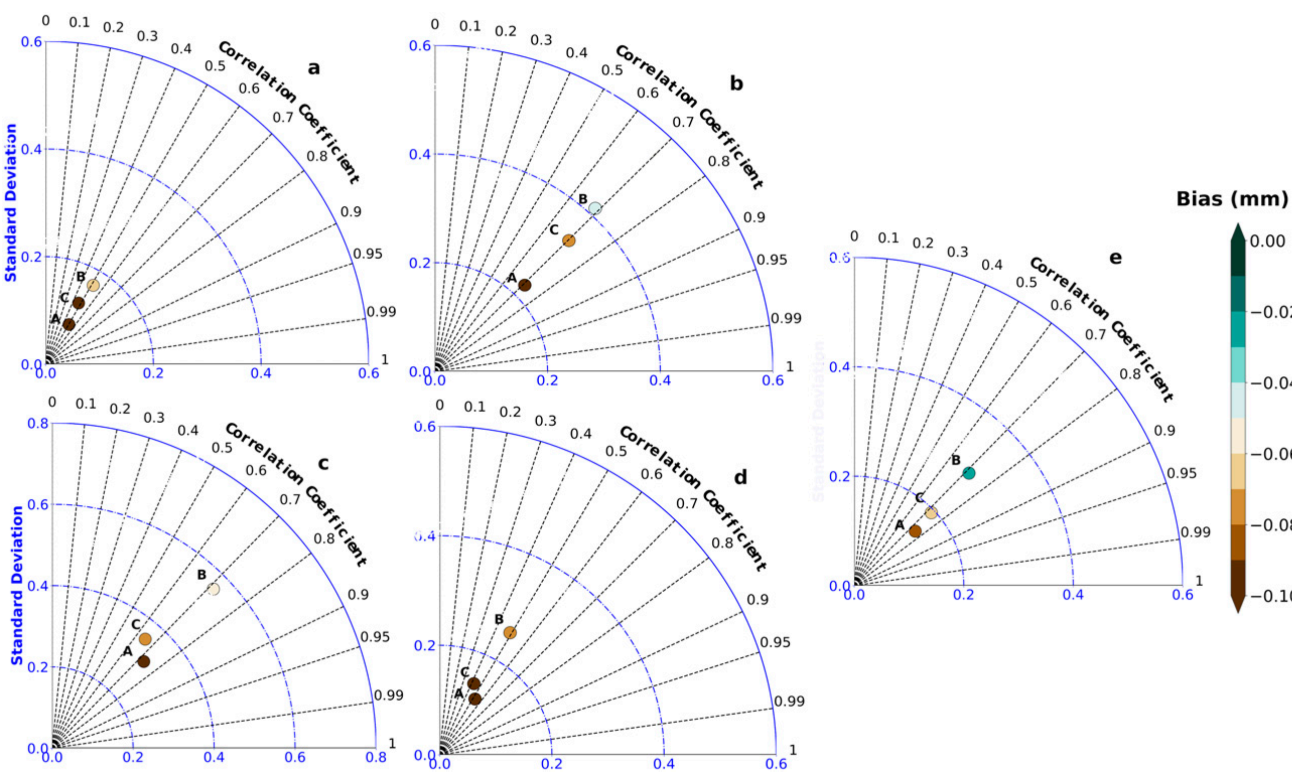

FIG. 5. Taylor diagrams to compare the $(E - P)_{[1\text{–}10]} > 0$ fields of FLEX-ERA5.05, FLEX-ERA5.1, and FLEX-WRF with respect to the control field FLEX-ERA-I for the moisture sources for the IP in terms of B, correlation coefficient, and STD. (a) JFM, (b) AMJ, (c) JAS, (d) OND, and (e) annual. The letters A, B, and C correspond to the configurations FLEX-ERA5.05, FLEX-ERA5.1, and FLEX-WRF, respectively.

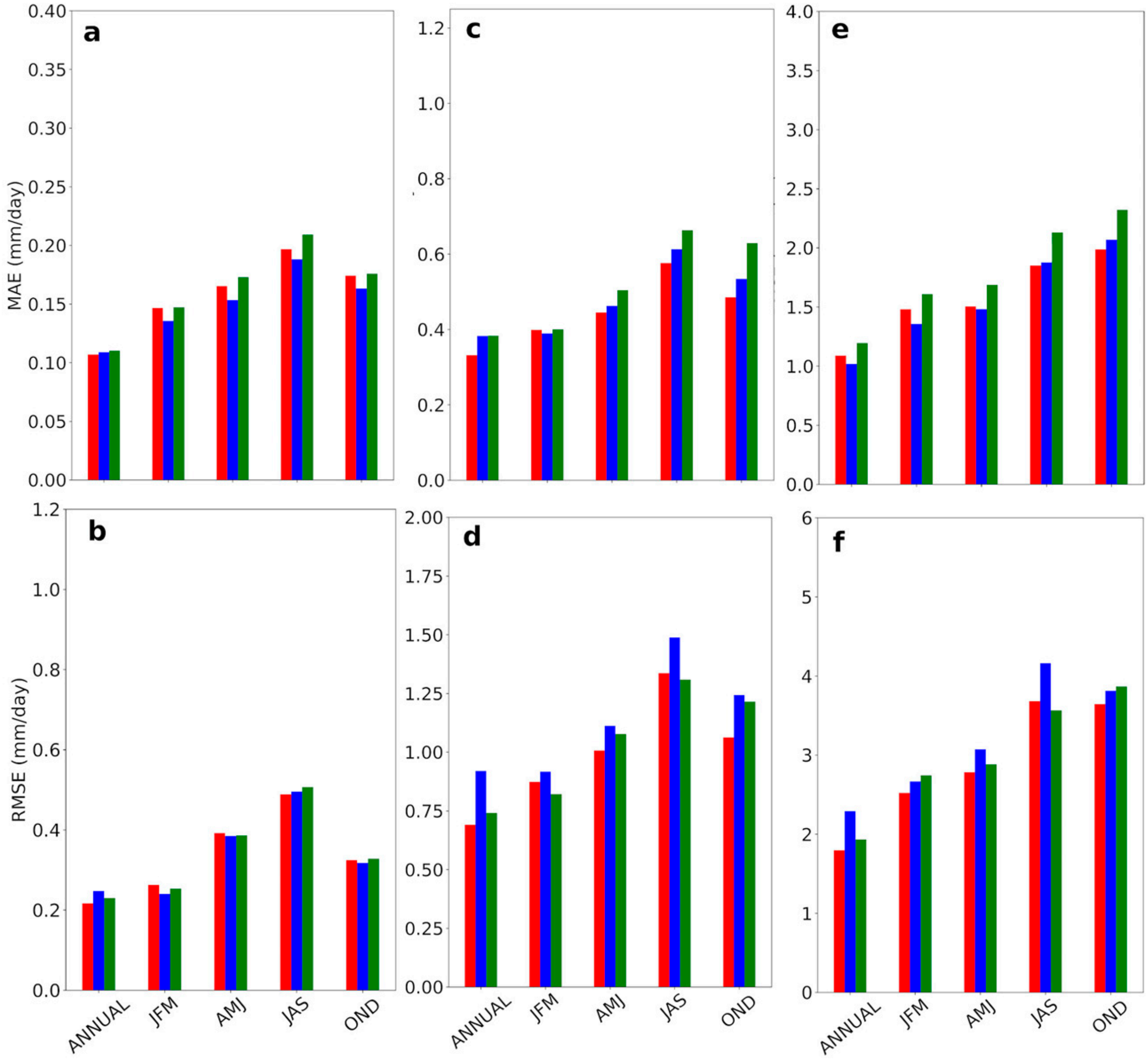

FIG. 6. MAE and RMSE for the moisture sources patterns of FLEX-ERA5.05, FLEX-ERA5.1, FLEX-WRF, and FLEX-ERA-I for the (a),(b) IP, (c),(d) MED, and (e),(f) NATL. The red, blue, and green bars correspond to FLEX-ERA5.05, FLEX-ERA5.1, and FLEX-WRF, respectively.

configurations. However, B differs between them, showing the lowest values for FLEX-ERA5.1 (~0.02 mm day^{-1}) followed by FLEX-WRF ~0.06 mm day^{-1} and FLEX-ERA5.05 with ~0.08 mm day^{-1}. Regarding the MAE, FLEX-ERA5.1 showed a lower value than the remaining configurations, followed by FLEX-ERA5.05 and FLEX-WRF, which showed very little difference. RMSE differs in this order (see Figs. 6a,b): the highest value was found for FLEX-ERA5.05 (~0.4 mm day^{-1}) but with similar values for FLEX-ERA5.1 and FLEX-WRF close to 0.38 mm day^{-1}.

In summer (JAS), the patterns are quite similar, but the moisture values seemed smaller in the case of FLEX-WRF (Figs. 4k–n). The best results compared to the control was obtained with FLEX-ERA5.05 with an R value of ~0.73 and the lowest STD of ~0.46 mm day^{-1} (Fig. 5c). Although FLEX-ERA5.1 presented an R value of ~0.7, a higher STD conditioned it than FLEX-ERA5.05, unlike FLEX-WRF with an STD < 0.2 mm day^{-1} but with a relatively lower R (~0.65) than the other configurations. The B showed similar behavior as in winter, indicating a marked decrease for FLEX-ERA5.05 and FLEX-WRF but slightly lower for FLEX-ERA5.1. As seen in Figs. 6a and 6b, the maximum seasonal MAE and RMSE occurred in this season for all the configurations. FLEX-WRF showed the lowest MAE with ~0.2 mm day^{-1}, while FLEX-ERA5.05 and FLEX-ERA5.1 had higher values (~1.99 and ~1.88 mm day^{-1}, respectively). On the other hand, RMSE showed similar values, with the lowest achieved for FLEX-ERA5.05 (~0.48 mm day^{-1}) and slightly higher values for FLEX-WRF and FLEX-ERA5.1 (~0.5 mm day^{-1}).

In autumn (OND), the values of the pattern showed differences over the IP (recycling processes), mainly for FLEX-ERA5.1 (Figs. 4p–s). Regarding the statistics, the lowest STD values were for FLEX-ERA5.05 and FLEX-WRF, showing similar values of ~0.1 mm day^{-1}; FLEX-ERA5.1 was slightly higher with ~0.26 mm day^{-1}. The *B* always showed a decrease, reaching its maximum for FLEX-ERA5.05; a pattern for which a slightly smoother field can be observed compared to the control configuration of FLEX-ERA-I.1. The lowest MAE was found for FLEX-ERA5.1 (~0.16 mm day^{-1}), although very similar to the other configurations. Regarding the RMSE, the values are the same for FLEX-WRF and FLEX-ERA5.1 (~0.3 mm day^{-1}) and slightly higher for FLEX-ERA5.05.

Annually the pattern was well represented for all the experiments (Figs. 4u–x), as shown in the correlation values of 0.7–0.8 for all configurations (Fig. 5e) and the low STD values for FLEX-ERA5.05 and FLEX-WRF (<0.2 mm day^{-1}). The *B* was in the range of 0.02–0.06 mm day^{-1}, showing a slight decrease compared to the control pattern. The MAE was around 0.1 mm day^{-1} for all configurations, but the RMSE showed the lowest value for FLEX-ERA5.05 (~0.21 mm day^{-1}), higher for FLEX-WRF (~0.23 mm day^{-1}) and FLEX-ERA5.1 (~0.25 mm day^{-1}).

In addition to the described results, the behavior of the models was also evaluated for some specific days of moisture transport to ensure that the fields were correctly represented in individual days (*d*). Figures S6–S9 show the $(E - P)_{[d]} > 0$ values for days 1, 3, 5, and 10 backward in time, and Figs. S10–S13 show the Taylor diagrams. In general, the *R* values ranged from values between 0.6 and 0.7 on day 1 backward, reaching ~0.8 in some season values, with a decrease from day 1 to day 10 when *R* showed a range of 0.2–0.4. Decreases predominated for all configurations, showing a higher dispersion of values for FLEX-ERA5.1. In terms of correlations, FLEX-WRF has lower values. Finally, the MAE tends to have higher values the longer the time backward, especially for FLEX-ERA5.05 and FLEX-WRF showing maxima on days 3 and 5; however, the RSME shows its maximum on day 1, decreasing toward day 10 (Fig. S14).

Another test was done to check the ability of each FLEXPART configuration to adequately represent $(E - P)_{[d]} > 0$ values over the two areas defined by Gimeno et al. (2010b) as main moisture sources for the IP: the tropical-subtropical North Atlantic (TSNA) and the Mediterranean basin (IPM) (see Fig. S35). The temporal evolution of the contribution from both sources was quantified as in Nieto et al. (2006) and Gimeno et al. (2010a). Figure S15 shows the time series of $(E - P)_{[d]} > 0$ values over TSNA and IPM accounted for FLEX-ERA5.05 (red line), FLEX-ERA5.1 (blue line), FLEX-WRF (green line), and FLEX-ERA-I.1 (orange line). For winter and both sources (Figs. S33a,b), all configurations followed the control behavior, the maximum values were accounted for around days 4–7, and the minimum appeared on day 1. However, for TSNA the lowest contributions were obtained for FLEX-WRF and FLEX-ERA5.05 from day 2 to 10, and the highest for FLEX-ERA5.1. Between days 1 and 2, there was a slight increase for FLEX-WRF. For the IPM source from day 1 to 3, FLEX-ERA5.05 decreased the values. For spring, the TSNA series showed very similar values from days 7 to 1, reaching a higher convergence between the three configurations for day 4. For IPM all configurations reached their maximum for day 1, showing the highest decrease for FLEX-ERA5.05 (Figs. S33c,d). In summer the configurations behaved very similar for TSNA but differed for IPM, where FLEX-ERA5.05 and FLEX-WRF showed a considerable increase in day 1 compared with the maximum reached in the control configuration (Figs. S33e,f). In autumn for TSNA the furthest configuration from the control was FLEX-WRF, with a marked decrease up to day 4, while for IPM the values were well represented by most configurations (Figs. S33g,h). Overall, for the annual time series (Figs. S33j,k), the behavior of all configurations follows the control. The configuration that departs least from the TSNA was FLEX-ERA5.05 (followed by FLEX-ERA5.1 and FLEX-WRF) and FLEX-ERA5.1 for IPM (but with similar results for FLEX-WRF and FLEX-ERA5.05, being slightly better for the first one).

c. *Representation of the moisture contribution for precipitation from the MED and the NATL sources*

In this section, the aim is to test the ability of the three configurations to represent the sinks over the continents for the moisture coming from the MED and NATL sources. The $(P - E)_{[1-10]} > 0$ patterns are plotted in Fig. 7 for MED and Fig. 8 for NATL, showing the moisture sinks associated with both sources. The MED unequivocally influences the moisture budget in its surrounding continental area and, through the dominant local flows for the transport of air masses (Peixoto et al. 1982; Ward 1998; Nieto et al. 2010). The sinks identified by the control configuration FLEX-ERA-I.1 (Figs. 7d,i,n,s,x) over southern Europe, the Italian Peninsula, east of the IP, and north of the African continent [as in Gimeno et al. (2010b) or Ciric et al. (2016)] are congruent with the convergence pattern of the integrated vertical moisture flux (Figs. 7e,j,o,t,y), with maximum values over most of the areas mentioned above.

In winter, the three configurations showed high correlations with the control (0.7–0.8), and the STD ranged between 0.5 and 1.3 mm day^{-1} (Fig. 8a). There is a decrease for all the configurations, with lower values for FLEX-ERA5.1 (~0.04 mm day^{-1}) followed by FLEX-WRF (~0.09 mm day^{-1}) and FLEX-ERA5.05 (0.25 mm day^{-1}). The MAE values were very similar to the other configurations, with a slightly lower error for FLEX-ERA5.1 (~0.39 mm day^{-1}, Fig. 6c) and the RMSE showing worse behavior. FLEX-WRF showed the lowest RMSE (~0.82 mm day^{-1}) followed by FLEX-ERA5.05 (~0.87 mm day^{-1}), as shown in Fig. 6d. The higher values of RSME for FLEX-ERA5.1 could be induced by the differences observed over the Balkan region (Fig. 7b).

In spring, the correlation decreased with respect to winter (0.6–0.7). The *B* (Fig. 8b) showed the smallest decrease for FLEX-WRF (~0.02 mm day^{-1}), followed by FLEX-ERA5.1 (~0.06 mm day^{-1}) and FLEX-ERA5.05 (~0.10 mm day^{-1}). STD showed a greater dispersion for FLEX-WRF and FLEX-ERA5.1 with values in the range of 1–1.5 mm day^{-1}. There was a slight increase in error behavior compared to

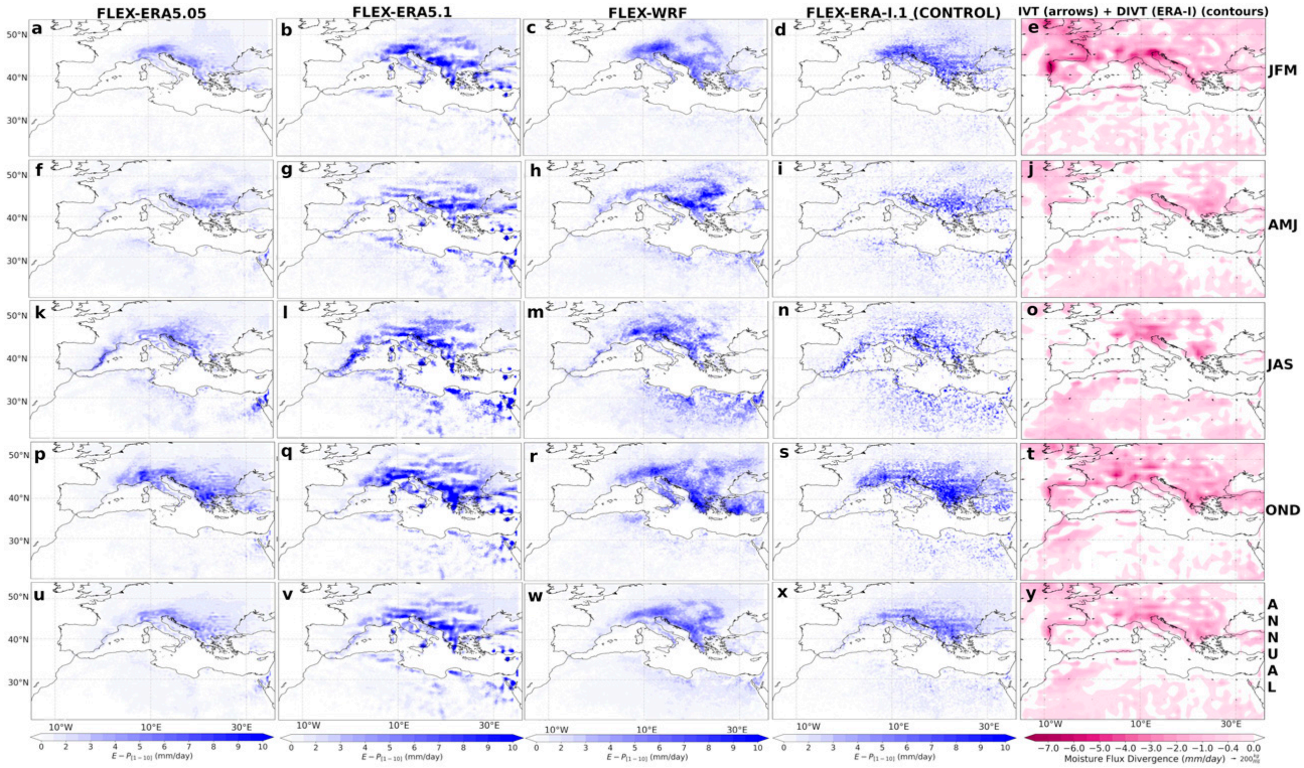

FIG. 7. Moisture sink patterns $(P - E)_{[1–10]} > 0$; mm day^{-1}) for the MED region from the Lagrangian outputs of FLEX-ERA5.05, FLEX-ERA5.1, FLEX-WRF, and FLEX-ERA-I.1. The right column represents the IVT field (arrows; kg m^{-1} s^{-1}) and its divergence (contours; mm day^{-1}) from ERA-I at 1°. The fields displayed correspond to (a)–(e) JFM, (f)–(j) AMJ, (k)–(o) JAS, (p)–(t) OND, and (u)–(y) annual.

winter. The maximum values for the MAE were founded for FLEX-WRF, followed by FLEX-ERA5.1 and FLEX-ERA5.05 (see Fig. 6c) but with values equal to or lower than 0.50 mm day^{-1}. Regarding the RMSE values, it was observed that all are similar, with the highest values for FLEX-ERA5.1 (~1.11 mm day^{-1}), followed by FLEX-WRF (~1.09 mm day^{-1}) and FLEX-ERA5.05 (~1.00 mm day^{-1}).

During summer, FLEX-ERA-I.1 showed a decrease in the moisture contribution associated with MED (Fig. 8n), and the configurations show the highest STDs values, in the range of 0.7–1.8 mm day^{-1}, and the lowest R values (~0.6) of all seasons. FLEX-WRF presents a slight increase of ~0.03 mm day^{-1} with respect to the control, in contrast to the decrease observed of FLEX-ERA5.1 and FLEX-ERA5.05 (Fig. 8c). The three configurations showed the highest MAE and RMSE compared with the other seasons, with values from 1.30 to 1.48 mm day^{-1} (Figs. 6c,d).

For autumn, the correlation ranged from approximately 0.7–0.8, superior to previous seasons, but higher STD values were also reached, with approximately 0.92–1.52 mm day^{-1}, only surpassed by the summer season. All configurations decreased the precipitation over continental areas, but the lower B was achieved for FLEX-WRF (~0.02 mm day^{-1}) with similar values for FLEX-ERA5.1 ~ 0.03 mm day^{-1}). The MAE decreased for FLEX-ERA5.1 and FLEX-ERA5.05 but had a similar behavior for FLEX-WRF compared to summer. The RMSE also decreased concerning the previous period, with the best results for FLEX-ERA5.05 (~1.1 mm day^{-1}) (Fig. 6d).

Finally, the correlations for the annual pattern showed values from 0.7 to 0.8, with a lower decrease for FLEX-WRF (Fig. 8e). The MAE was lower for FLEX-ERA5.05 and slightly higher with similar values for FLEX-ERA5.1 and FLEX-WRF; however, the highest RMSE was achieved by FLEX-ERA5.1

The patterns for individual days $(P - E)_{[d]} > 0$ (for $d = 1$, 3, 5, and 10) are plotted in Figs. S15–S18; the Taylor diagrams for these days are shown in Figs. S19–S22. In general, R values were higher at day 1 in a range of 0.6–0.7, reaching values in certain seasons up to approximately 0.85, and with a considerable decrease to day 10, with values between 0.2 and 0.5. Overall, there were decreases for all configurations, although there was a marked increase for FLEX-WRF on day 1. The highest dispersion for the sink field was observed for FLEX-ERA5.1, and the lower correlation occurred for FLEX-WRF. The MAE followed a similar behavior for the analyzed days, with day 3 standing out for its high values for FLEX-ERA5.05 and FLEX-WRF. The RSME remained very similar for the three configurations for all seasons (see Fig. S23).

Analogous to the MED analysis, the sink patterns for the NATL moisture source are shown in Fig. 9. In winter, the three configurations showed similar contributions for precipitation compared to the control configuration. However, some differences can be observed, such as the smoother pattern for

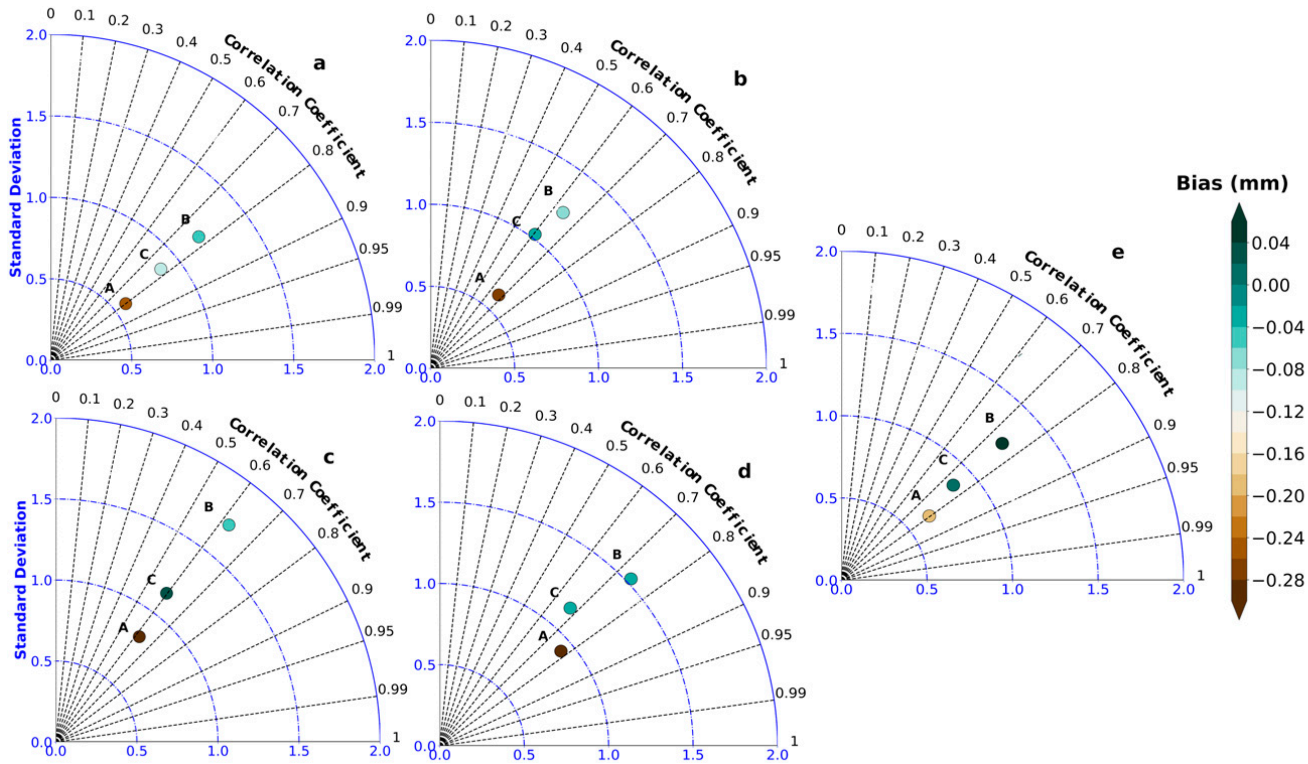

FIG. 8. Taylor diagrams to compare the $(P - E)_{[1–10]} > 0$ fields of FLEX-ERA5.05, FLEX-ERA5.1, and FLEX-WRF with respect to the control field FLEX-ERA-I for the moisture sinks for the MED in terms of B, correlation coefficient, and STD. (a) JFM, (b) AMJ, (c) JAS, (d) OND, and (e) annual. The letters A, B, and C correspond to the configurations FLEX-ERA5.05, FLEX-ERA5.1, and FLEX-WRF, respectively.

FLEX-ERA5.05 (Fig. 9a) or the more intense values for FLEX-ERA5.1 (Fig. 9b). Compared with the remaining seasons, winter achieved the maximum correlation values (~0.7–0.8) for the three configurations versus the control one, with FLEX-ERA5.05 at the top. The STD ranged around 2–4 mm day^{-1}, showing that FLEX-ERA5.1 had a greater dispersion and that FLEX-WRF had the lowest (with a $R \sim 0.7$). Although FLEX-WRF and FLEX-ERA5.05 tended to decrease the pattern (with 0.66 and 0.78 mm day^{-1}, respectively), FLEX-ERA5.1 increased it (0.04 mm day^{-1}), as shown in Fig. 10a. On the other hand (see Figs. 6e,f), this last configuration presented the lowest MAE (~1.36 mm day^{-1}), followed by FLEX-ERA5.05 and FLEX-WRF (with values of 1.48 and 1.60 mm day^{-1}, respectively). FLEX-ERA5.05 had the lowest the

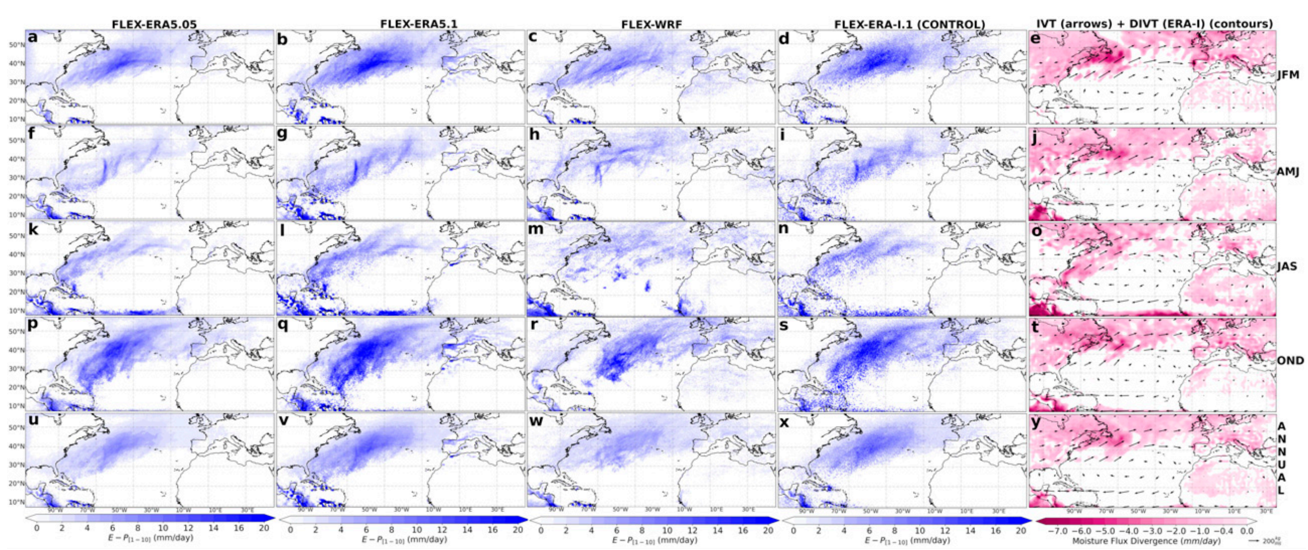

FIG. 9. As in Fig. 7, but for the moisture sinks from the NATL source.

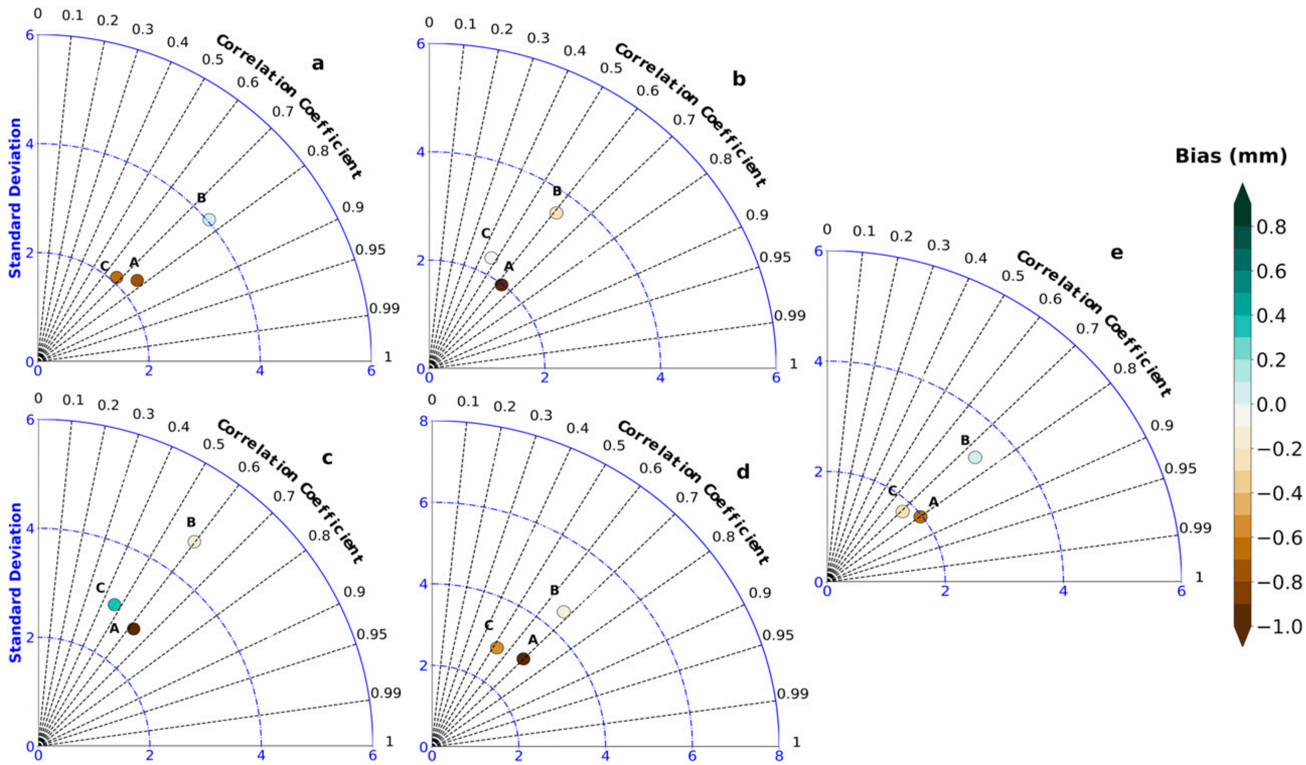

FIG. 10. Taylor diagrams as in Fig. 8, but for the moisture sinks from the NATL.

RMSE (~2.52 mm day^{-1}) followed by FLEX-ERA5.1 and FLEX-WRF (with values of 2.67 and 2.74 mm day^{-1}, respectively).

In spring, there was a decrease in the contribution pattern and in its intensity (Fig. 9i). The correlation values were lower than in winter reaching the maximum values for FLEX-ERA5.05 and FLEX-ERA5.1, with ~0.6 and ~0.5, respectively. The STD presents values in the range of 2–4 mm day^{-1}, showing a decrease of the pattern with the highest value of B (absolute value) for FLEX-ERA5.05 (~1 mm day^{-1}), followed by FLEX-WRF (~0.6 mm day^{-1}) and finally FLEX-ERA5.1 (~0.2 mm day^{-1}) (see Fig. 10b). The MAE showed the same values of ~1.5 mm day^{-1} for FLEX-ERA5.05 and FLEX-ERA5.1, and 1.68 mm day^{-1} for FLEX-WRF (see Fig. 6e). The RMSE showed that more marked differences were maintained in certain mesh points for FLEX-ERA5.1 represented by values of ~3 mm day^{-1}, followed by FLEX-WRF with ~2.88 mm day^{-1}, and FLEX-ERA5.05 ~ 2.78 mm day^{-1}.

For the summer, a very weak pattern of $(P - E)_{[1\text{–}10]} > 0$ continued with a very dispersed structure, as shown in Figs. 9k–n, with maximums located at low latitudes. The contribution pattern is located very close to the east coast of the United States and Canada, influencing the islands of the Caribbean and Central America at more than 20 mm day^{-1}. In relation to the statistics, the FLEX-WRF statistics presents an $R \sim 0.4$; for the rest of the configurations, it was ~0.6. The STD shows very similar values for FLEX-ERA5.05 and FLEX-WRF but higher values for FLEX-ERA5.1 at ~4.68 mm day^{-1}. On the other hand, B showed decreases for FLEX-ERA5.05 and FLEX-ERA5.1 with values ~ 1 and ~0.15 mm day^{-1}, respectively; these were different from FLEX-WRF, which increased the pattern by 0.32 mm day^{-1} (see Fig. 10c). Furthermore, FLEX-ERA5.1 shows the maximum RMSE for the entire time interval at ~3.56 mm day^{-1} (see Fig. 6f).

In autumn, the STD decreases with respect to the previous one, with only FLEX-ERA5.1 exceeding 4 mm day^{-1}. For all simulations, the decrease with the highest value corresponded to FLEX-ERA5.05 with ~1.14 mm day^{-1}. The highest value of MAE was obtained for FLEX-ERA5.05 (~2.3 mm day^{-1}), while the RMSE for FLEX-WRF and FLEX-ERA5.1 reached ~3.8 mm day^{-1} (see Fig. 10d).

For the annual period Fig. 10e shows that the correlation for all configurations was high with values in the 0.7–0.8 range, and with an STD < 2 mm day^{-1} for FLEX-WRF and FLEX-ERA5.05; this was relatively higher for FLEX-ERA5.1. The B showed that FLEX-ERA5.1 presented a slight increase; for the remaining ones there were a lower decrease, with values of ~0.2 mm day^{-1} for FLEX-WRF. The MAE showed a similar behavior close to 1 mm day^{-1} for FLEX-ERA5.05 and FLEX-ERA5.1 but slightly higher for FLEX-WRF (see Fig. 6e). The RMSE values were <2 mm day^{-1} for FLEX-WRF and FLEX-ERA5.05 but >2 mm day^{-1} for FLEX-ERA5.1, showing that it presents difficulties in representing the sink pattern for certain regions.

The representation of the seasonal and annual sink patterns for day 1, 3, 5, and 10 are shown in Figs. S24–S26. Overall, by seasons the B showed differences between the configurations with some tendency to increase in the first days for FLEX-WRF and FLEX-ERA5.1. Correlation values (R) were more stable for NATL than MED, ranging ~0.4–0.6, reaching slightly lower values for FLEX-WRF. The three configurations show similarities to the case of MED in terms of dispersion, increasing the STD from day 1 to day 10 (see Figs. S28–S31). Finally, all configurations show a tendency to increase MAE and RSME from day 1 to day 10 with maxima for FLEX-WRF and FLEX-ERA5.1, respectively. Annually, it was observed that FLEX-ERA5.05 and FLEX-WRF tend to have slightly higher MAE values than FLEX-ERA5.1, while the latter configuration predominantly has higher RMSE values than the other two configurations (Figs. S14, S23, and S32). The Taylor diagrams for the individual days (Fig. S34) show that the R decreases as the days increased backward. FLEX-WRF presents the lower R in most cases, while the highest dispersion is associated with FLEX-ERA5.1. For FLEX-ERA5.05, there is a tendency to decrease the positive or negative $E - P$ values in all cases.

4. Discussions and uncertainty analysis

The results obtained for the analysis of the moisture sources that contribute to the IP show that, in the four seasons and the annual period, the correlation for the moisture sources pattern with respect to the FLEX-ERA-I.1 (the control simulation) for the three configurations analyzed varied from 0.4 to 0.6, higher for FLEX-ERA5.05 and lower for FLEX-WRF. In addition, there were few marked differences between the configurations in terms of MAE and RMSE, and according to these statistics the lowest performance was observed for summer and the best for winter and autumn. These results were corroborated by R^2 values, being the maximum for FLEX-ERA5.05 in most of the studied periods, ranging from 0.25 (winter) to 0.55 (annual period). However, the reverse occurs for the VAR, reaching the minimum for winter and the maximum for the annual period. This is due to the lower mean moisture values for the annual period, which increases the value of the VAR (see Table S1). According to these statistics, FLEX-ERA5.1 and FLEX-WRF showed very similar behavior for R^2, although the VAR was slightly lower for FLEX-WRF (Table S1).

On the other hand, the FLEX-WRF configuration indicates some difficulty in representing the source above 40°N over the North Atlantic Ocean, areas with significant differences (at 99%) are observed with respect to the control experiment (Fig. S38). This fact could be due to the regional characteristics of the model. Therefore, a certain number of particles disappear across the boundaries (see Fig. 1a) in their movement, limiting their contribution to the moisture budget balance. This could also influence the statistics that characterize the comparative study between the different set of configurations for the analysis of the moisture source patterns. However, FLEX-WRF is the configuration that represents better the pattern for the moisture sources in regions with complex orography, especially during spring and summer, the periods when the precipitation is due to recycling processes (see Fig. S36). This shows that the use of the WRF-ARW allows a detailed representation of the most local processes of moisture transport (e.g., on the IP). This could be associated with the surface parameterization of WRF-ARW using the Noah LSM model that allows a better representation of the sensible and latent heat fluxes provided to the boundary layer scheme and of the longwave and shortwave radiation reflected, variables involved in moisture transport from the surface to different levels of the atmosphere.

For the analysis of moisture sinks for the MED region, the three configurations compared showed a low dispersion in their fields compared with the control. This is shown by the high values of $R \geq 0.6$. In addition, R^2 values ranged from 0.3 to 0.6, showing a good correlation, being higher in all periods for FLEX-ERA5.05, and the VAR was lower for FLEX-WRF (1.6–2.37) followed by FLEX-ERA5.05 (1.89–2.32) (Table S2). This behavior for FLEX-ERA5.05 may be associated with the fact that over the moisture sinks a larger number of areas with significant differences are observed (Fig. S39), mainly in the mountainous regions of northern Italy and the Balkan Peninsula. Also, for FLEX-WRF it is important to note that the most significant differences founded around 30°W (Fig. S39) could be related to the closeness of the boundary of the FLEXPART-WRF domain, increasing possible errors due to the possible crossing of some trajectories through it. In addition, a lower MAE was achieved although the order of magnitude of the moisture budget for the MED was higher. The RMSE was considerable, showing an increase in summer and then a decrease in autumn. On the other hand, similar to the results for the IP, FLEX-WRF showed the best behavior for the moisture sink pattern in mountainous regions such as the Alps, the Balkan Peninsula, and eastern Europe (Fig. S37).

Finally, in general, the contribution pattern of moisture sinks from the NATL tends to be larger in latitudinal and longitudinal dimension, causing the errors to be more noticeable at each season compared to those obtained for MED. The correlation between the three configurations and FLEX-ERA-I.1 ranged ~0.4–0.7; however, in this case, there is an increase in the magnitude of MAE and RMSE, ranging from 1 to 2.5 mm day^{-1} and from 2 to 4.5 mm day^{-1}, respectively. For this target region, the lowest values for the coefficient of variation were from 0.9 to 1.5, being better than for the other target regions analyzed. Regarding the R^2, FLEX-ERA5.05 showed values from 0.3 to 0.6, followed by FLEX-ERA5.1, and with lower values for FLEX-WRF (Table S3). In this case, it is observed that FLEX-ERA5.1 shows the least number of points with significant differences (at 99%) compared to FLEX-ERA-I.1, although the values of the sink pattern are higher for the entire North Atlantic region. On the other hand, FLEX-ERA5.05 shows a behavior with small differences for the spring, summer, and autumn, but for winter and annual scale some areas showed significant differences due to regions with lower values compared to the control experiment (Fig. S40). FLEX-WRF shows difficulty in representing the pattern, with very low values in the region of maximum values shown by FLEX-ERA-I.1. For this oceanic region FLEX-WRF could present some limitations and therefore the use of FLEX-ERA5.05 or FLEX-ERA5.1 would be more efficient.

The behavior of the errors obtained in the comparison of the configurations with respect to ERA-I shows that there are few differences for the patterns of moisture sources and sinks with the use of different versions of reanalysis, similar to that obtained by Durán-Quesada et al. (2010, 2017).

5. Summary and conclusions

Here, we compared the representation of moisture sources and sinks for three different simulations of the Lagrangian model FLEXPART, using the latest FLEXPART model version (v10.3) with the new ERA5 reanalysis as input data at two horizontal resolutions (1° and 0.5°), and the FLEXPART-WRF version fed with the dynamic downscaling WRF-ARW outputs (at a 0.18° horizontal resolution) previously forced with ERA5. The simulations were done over the extended area of the North Atlantic and European region, because it comprises two of the main oceanic global moisture sources, the so-called NATL (North Atlantic ocean) and MED (the whole Mediterranean Sea). So, the target regions analyzed were the moisture sinks for these two oceanic sources, and the moisture sources for the Iberian Peninsula (IP). The year selected for analysis was a year with neutral characteristics in terms of the climate variability patterns affecting the region, which is 2014. The outputs of the previous FLEXPARTv9.0 model version forced with ERA-I (at 1°) were used as control experiments.

An analysis of variables related to the water cycle (such as total precipitation, evaporation, total column water, integrated water vapor transport, specific humidity at 850 hPa) showed that there are few significant differences (at 95%) between the ERA5 and ERA-I reanalyses. Nogueira (2020) affirms that this is enough for an improved representation of moisture sink/source patterns. This improvement in ERA5 versus ERA-I is crucial for our study of moisture transport, because in addition some of the regions with significant improvements are located in our study region, acting as sources of moisture.

Annually, the FLEX-ERA5.05 configuration showed the most similar representation compared to the control experiment. Statistics show the maximum correlation and the lowest error values compared to the FLEX-ERA-I.1 simulations, albeit with a tendency to decrease the values of the moisture budget. The FLEX-WRF configuration was the second in representing sources and sinks, showing a slight increase for MED. Finally, FLEX-ERA5.1 had the lowest representation, with the maximum errors and maximum deviation for the three target regions.

For all configurations, winter is when the three simulations showed the greatest similarity with respect to the control one, indicating discrepancies higher in summer and autumn. In general, the best results for all configurations were obtained for the sinks associated with the MED moisture source, with maximum correlation values reached for all seasons and the lowest MAE compared to the control experiment.

On the other hand, it should be noted that FLEX-WRF is the configuration that represents better the pattern of moisture source or sink in regions with complex orography and for recycling processes over the IP or in the mountainous regions around the Mediterranean Sea. This shows that the use of WRF-ARW allows a detailed representation of the most local processes of moisture transport.

The analysis per day shows greater differences for each configuration compared to the integrated pattern along the 10 days of the trajectories; this may be associated with a smoothing of the pattern when adding all the values (positive and negative) from day 1 to 10.

The main differences of FLEX-ERA5.1 versus FLEX-ERA5.05 are related to the number of particles modeled. The global run experiment for these configurations use 9 and 30 million particles, respectively, generating readjustments in the moisture content distribution due to different vertical and horizontal resolutions compared to the 2 million particles used for FLEX-ERA-I.1, but with a higher standard deviation for FLEX-ERA5.1 and a smoother pattern for FLEX-ERA5.05.

In summary, climatological studies using FLEXPARTv10.3 forced with ERA5 reanalysis data at various horizontal resolutions (0.5° and 1°) represent well the position and extension of moisture sources and sink patterns when forced by ERA-Interim (1°), as well as the amounts of moisture modeled. In addition, the FLEXPART version fed with the dynamic downscaled WRF-ARW outputs at a higher resolution (~0.25°, about ~20 km), previously forced with ERA5, accurately represents these patterns but with more detail, in particular in orographic regions. This improvement even in climatological studies, such as this one, in which the fields are smoothed through the seasonal or annual averages carried out, indicates that for shorter periods, specific events or case studies (e.g., tropical or extratropical cyclones) the smaller scale supported by the WRF-ARW data would help to determine transport patterns or structures in more detail.

Acknowledgments. J.C.F.-A. and M.V. acknowledge the support from the Xunta de Galicia (Galician Regional Government) under Grants ED481A-2020/193 and ED481B 2018/062, respectively. A.P.-A. acknowledges a PhD grant from the University of Vigo. This work is supported by the SETESTRELO project (PID2021-122314OB-I00) funded by the Ministerio de Ciencia, Innovación y Universidades, Spain. Partial support was also obtained from the Xunta de Galicia under the project "Programa de Consolidación e Estructuración de Unidades de Investigación Competitivas (Grupos de Referencia Competitiva)" (ED431C 2021/44). In addition, this work has been possible thanks to the computing resources and technical support provided by CESGA (Centro de Supercomputación de Galicia) and Red Española de Supercomputación (RES) (AECT-2022-3-0009 and DATA-2021-1-0005).

Data availability statement. ERA5 reanalysis data can be obtained from https://cds.climate.copernicus.eu/cdsapp#!/dataset/reanalysis-era5-single-levels-monthly-means?tab=form and ERA-Interim data from https://apps.ecmwf.int/datasets/data/interim-full-daily/levtype=sfc/. The FLEXPART and FLEXPART-WRF outputs are available upon request to the corresponding author.

REFERENCES

Bechtold, P., M. Köhler, T. Jung, F. Doblas-Reyes, M. Leutbecher, M. J. Rodwell, F. Vitart, and G. Balsamo, 2008: Advances in simulating atmospheric variability with the ECMWF model: From synoptic to decadal time-scales. *Quart. J. Roy. Meteor. Soc.*, **134**, 1337–1351, https://doi.org/10.1002/qj.289.

Berkowicz, R., and L. P. Prahm, 1982: Sensible heat flux estimated from routine meteorological data by the resistance method. *J. Appl. Meteor.*, **21**, 1845–1864, https://doi.org/10.1175/1520-0450(1982)021%3C1845:SHFEFR%3E2.0.CO;2.

Brioude, J., and Coauthors, 2013: The Lagrangian particle dispersion model FLEXPART-WRF version 3.1. *Geosci. Model Dev.*, **6**, 1889–1904, https://doi.org/10.5194/gmd-6-1889-2013.

Brown, B., E. Ebert, T. Fowler, E. Gilleland, P. Kucera, and L. Wilson, 2013: Verification methods for tropical cyclone forecasts. WMO Tech. Doc. WWRP 2013-7, 89 pp.

Castillo, R., R. Nieto, A. Drumond, and L. Gimeno, 2014: Estimating the temporal domain when the discount of the net evaporation term affects the resulting net precipitation pattern in the moisture budget using a 3-D Lagrangian approach. *PLOS ONE*, **9**, e99046, https://doi.org/10.1371/journal.pone.0099046.

Ciric, D., M. Stojanovic, A. Drumond, R. Nieto, and L. Gimeno, 2016: Tracking the origin of moisture over the Danube River Basin using a Lagrangian approach. *Atmosphere*, **12**, 162, https://doi.org/10.3390/atmos7120162.

Cloux, S., D. Garaboa-Paz, D. Insua-Costa, G. Miguez-Macho, and V. Pérez-Muñuzuri, 2021: Extreme precipitation events in the Mediterranean area: Contrasting Lagrangian and Eulerian models for moisture sources identification. *Hydrol. Earth Syst. Sci.*, **25**, 6465–6477, https://doi.org/10.5194/hess-25-6465-2021.

Dee, D. P., and Coauthors, 2011: The ERA-Interim reanalysis: Configuration and performance of the data assimilation system. *Quart. J. Roy. Meteor. Soc.*, **137**, 553–597, https://doi.org/10.1002/qj.828.

Drumond, A., R. Nieto, L. Gimeno, and T. Ambrizzi, 2008: A Lagrangian identification of major sources of moisture over central Brazil and La Plata Basin. *J. Geophys. Res.*, **113**, D14128, https://doi.org/10.1029/2007JD009547.

——, ——, and ——, 2011a: On the contribution of the Tropical Western Hemisphere Warm Pool source of moisture to the Northern Hemisphere precipitation through a Lagrangian approach. *J. Geophys. Res.*, **116**, D00Q04, https://doi.org/10.1029/2010JD015397.

——, ——, E. Hernandez, and L. Gimeno, 2011b: A Lagrangian analysis of the variation in moisture sources related to drier and wetter conditions in regions around the Mediterranean Basin. *Nat. Hazards Earth Syst. Sci.*, **11**, 2307–2320, https://doi.org/10.5194/nhess-11-2307-2011.

Durán-Quesada, A. M., L. Gimeno, J. A. Amador, and R. Nieto, 2010: Moisture sources for Central America: Identification of moisture sources using a Lagrangian analysis technique. *J. Geophys. Res.*, **115**, D05103, https://doi.org/10.1029/2009JD012455.

——, ——, and J. Amador, 2017: Role of moisture transport for Central American precipitation. *Earth Syst. Dyn.*, **8**, 147–161, https://doi.org/10.5194/esd-8-147-2017.

Emanuel, K. A., and M. Živković-Rothman, 1999: Development and evaluation of a convection scheme for use in climate models. *J. Atmos. Sci.*, **56**, 1766–1782, https://doi.org/10.1175/1520-0469(1999)056%3C1766:DAEOAC%3E2.0.CO;2.

Gimeno, L., R. Nieto, R. Trigo, S. M. Vicente-Serrano, and J. I. López-Moreno, 2010a: Where does the Iberian Peninsula moisture come from? An answer based on a Lagrangian approach. *J. Hydrometeor.*, **11**, 421–436, https://doi.org/10.1175/2009JHM1182.1.

——, A. Drumond, R. Nieto, R. M. Trigo, and A. Stohl, 2010b: On the origin of continental precipitation. *Geophys. Res. Lett.*, **37**, L13804, https://doi.org/10.1029/2010GL043712.

——, and Coauthors, 2012: Oceanic and terrestrial sources of continental precipitation. *Rev. Geophys.*, **50**, RG4003, https://doi.org/10.1029/2012RG000389.

——, and Coauthors, 2020: Recent progress on the sources of continental precipitation as revealed by moisture transport analysis. *Earth-Sci. Rev.*, **201**, 103070, https://doi.org/10.1016/j.earscirev.2019.103070.

Gómez-Hernández, M., A. Drumond, L. Gimeno, and R. Garcia-Herrera, 2013: Variability of moisture sources in the Mediterranean region during the period 1980-2000. *Water Resour. Res.*, **49**, 6781–6794, https://doi.org/10.1002/wrcr.20538.

Grythe, H., N. I. Kristiansen, C. D. Groot-Zwaaftink, S. Eckhardt, P. Tunved, R. Krejci, J. Ström, and A. Stohl, 2017: A new aerosol wet removal scheme for the Lagrangian particle model FLEXPART v10. *Geosci. Model Dev.*, **10**, 1447–1466, https://doi.org/10.5194/gmd-10-1447-2017.

Hanna, S. R., 1982: Applications in air pollution modeling. *Atmospheric Turbulence and Air Pollution Modelling*, F. T. M. Nieuwstadt and H. Van Dop, Eds., D. Reidel Publishing Company, 275–310.

Hersbach, H., and D. Dee, 2016: ERA5 reanalysis is in production. *ECMWF Newsletter*, No. 147, ECMWF, Reading, United Kingdom, 7, http://www.ecmwf.int/sites/default/files/elibrary/2016/16299-newsletter-no147-spring-2016.pdf.

——, and Coauthors, 2020: The ERA5 global reanalysis. *Quart. J. Roy. Meteor. Soc.*, **146**, 1999–2049, https://doi.org/10.1002/qj.3803.

Hong, S. Y., and J. O. J. Lim, 2006: The WRF single-moment 6-class microphysics scheme (WSM6). *J. Korean Meteor. Soc.*, **42**, 129–151.

——, Y. Noh, and J. Dudhia, 2006: A new vertical diffusion package with an explicit treatment of entrainment processes. *Mon. Wea. Rev.*, **134**, 2318–2341, https://doi.org/10.1175/MWR3199.1.

Iacono, M. J., J. S. Delamere, E. J. Mlawer, M. W. Shephard, S. A. Clough, and W. D. Collins, 2008: Radiative forcing by long–lived greenhouse gases: Calculations with the AER radiative transfer models. *J. Geophys. Res.*, **113**, D13103, https://doi.org/10.1029/2008JD009944.

Insua-Costa, D., and G. Miguez-Macho, 2018: A new moisture tagging capability in the Weather Research and Forecasting model: Formulation, validation and application to the 2014 Great Lake-effect snowstorm. *Earth Syst. Dyn.*, **9**, 167–185, https://doi.org/10.5194/esd-9-167-2018.

——, ——, and M. C. Llasat, 2019: Local and remote moisture sources for extreme precipitation: A study of the two catastrophic 1982 western Mediterranean episodes. *Nat. Hazards Earth Syst. Sci.*, **23**, 3885–3900, https://doi.org/10.5194/hess-23-3885-2019.

Jimenez, P. A., J. Dudhia, J. F. Gonzalez-Rouco, J. Navarro, J. P. Montavez, and E. Garcia–Bustamante, 2012: A revised scheme for the WRF surface layer formulation. *Mon. Wea. Rev.*, **140**, 898–918, https://doi.org/10.1175/MWR-D-11-00056.1.

Kain, J. S., 2004: The Kain–Fritsch convective parameterization: An update. *J. Appl. Meteor.*, **43**, 170–181, https://doi.org/10.1175/1520-0450(2004)043<0170:TKCPAU>2.0.CO;2.

Kalnay, E., and Coauthors, 1996: The NMC/NCAR 40-Year Reanalysis Project. *Bull. Amer. Meteor. Soc.*, **77**, 437–471, https://doi.org/10.1175/1520-0477(1996)077<0437:TNYRP>2.0.CO;2.

Lavers, D. A., and G. Villarini, 2013: The nexus between atmospheric rivers and extreme precipitation across Europe. *Geophys. Res. Lett.*, **40**, 3259–3264, https://doi.org/10.1002/grl.50636.

——, ——, R. P. Allan, E. F. Wood, and A. J. Wade, 2012: The detection of atmospheric rivers in atmospheric reanalyses and their links to British winter floods and the large-scale climatic circulation. *J. Geophys. Res.*, **117**, D20106, https://doi.org/10.1029/2012JD018027.

Lehner, B., K. Verdin, and A. Jarvis, 2008: New global hydrography derived from spaceborne elevation data. *Eos, Trans. Amer. Geophys. Union*, **89**, 93–94, https://doi.org/10.1029/2008EO100001.

Lionello, P., and Coauthors, 2006: The Mediterranean climate: An overview of the main characteristics and issues. *Dev. Earth Environ. Sci.*, **4**, 1–26, https://doi.org/10.1016/S1571-9197(06)80003-0.

Miguez-Macho, G., G. L. Stenchikov, and A. Robock, 2004: Spectral nudging to eliminate the effects of domain position and geometry in regional climate model simulations. *J. Geophys. Res.*, **109**, D13104, https://doi.org/10.1029/2003JD004495.

Nieto, R., L. Gimeno, and R. M. Trigo, 2006: A Lagrangian identification of major sources of Sahel moisture. *Geophys. Res. Lett.*, **33**, L18707, https://doi.org/10.1029/2006GL027232.

——, ——, A. Drumond, and E. Hernandez, 2010: A Lagrangian identification of the main moisture sources and sinks affecting the Mediterranean area. *WSEAS Trans. Environ. Dev.*, **6**, 365–374.

Nogueira, M., 2020: Inter-comparison of ERA-5, ERA-Interim and GPCP rainfall over the last 40 years: Process-based analysis of systematic and random differences. *J. Hydrol.*, **583**, 124632, https://doi.org/10.1016/j.jhydrol.2020.124632.

Numaguti, A., 1999: Origin and recycling processes of precipitating water over the Eurasian continent: Experiments using an atmospheric general circulation model. *J. Geophys. Res.*, **104**, 1957–1972, https://doi.org/10.1029/1998JD200026.

Peixoto, J. P., M. De Almeida, R. D. Rosen, and D. A. Salstein, 1982: Atmospheric moisture transport and the water balance of the Mediterranean Sea. *Water Resour. Res.*, **18**, 83–90, https://doi.org/10.1029/WR018i001p00083.

Pisso, I., and Coauthors, 2019: The Lagrangian particle dispersion model FLEXPART version 10.4. *Geosci. Model Dev.*, **12**, 4955–4997, https://doi.org/10.5194/gmd-12-4955-2019.

Quante, M. V., and V. Mathias, 2006: Water in the Earth's atmosphere. *J. Phys. IV France*, **139**, 37–61, https://doi.org/10.1051/jp4:2006139005.

Rahimi, S., W. Krantz, Y.-H. Lin, B. Bass, N. Goldenson, A. Hall, Z. J. Lebo, and J. Norris, 2022: Evaluation of a reanalysis-driven configuration of WRF4 over the western United States from 1980 to 2020. *J. Geophys. Res. Atmos.*, **127**, e2021JD035699, https://doi.org/10.1029/2021JD035699.

Ramos, A. M., M. J. Martins, R. Tomé, and R. M. Trigo, 2018: Extreme precipitation events in summer in the Iberian Peninsula and its relationship with atmospheric rivers. *Front. Earth Sci.*, **6**, 110, https://doi.org/10.3389/feart.2018.00110.

Randhir, T. O., 2012: Water for life and ecosystem sustainability. *Earth Sci. Climatic Change*, **3**, e107, https://doi.org/10.4172/2157-7617.1000e107.

Rios-Entenza, A., and G. Miguez-Macho, 2014: Moisture recycling and the maximum of precipitation in spring in the Iberian Peninsula. *Climate Dyn.*, **42**, 3207–3231, https://doi.org/10.1007/s00382-013-1971-x.

——, P. M. M. Soares, R. M. Trigo, R. M. Cardoso, and G. Miguez-Macho, 2014: Moisture recycling in the Iberian Peninsula from a regional climate simulation: Spatiotemporal analysis and impact on the precipitation regime. *J. Geophys. Res. Atmos.*, **119**, 5895–5912, https://doi.org/10.1002/2013JD021274.

Schicker, I., S. Radanovics, and P. Seibert, 2010: Origin and transport of Mediterranean moisture and air. *Atmos. Chem. Phys.*, **10**, 5089–5105, https://doi.org/10.5194/acp-10-5089-2010.

Skamarock, W. C., and Coauthors, 2008: A description of the Advanced Research WRF version 3. NCAR Tech. Note NCAR/TN-475+STR, 113 pp., http://dx.doi.org/10.5065/D68S4MVH.

Sodemann, H., and A. Stohl, 2013: Moisture origin and meridional transport in atmospheric rivers and their association with multiple cyclones. *Mon. Wea. Rev.*, **141**, 2850–2868, https://doi.org/10.1175/MWR-D-12-00256.1.

Stohl, A., 1998: Computation, accuracy and applications of trajectories—A review and bibliography. *Atmos. Environ.*, **32**, 947–966, https://doi.org/10.1016/S1352-2310(97)00457-3.

——, and D. J. Thomson, 1999: A density correction for Lagrangian particle dispersion models. *Bound.-Layer Meteor.*, **90**, 155–167, https://doi.org/10.1023/A:1001741110696.

——, and P. A. James, 2004: Lagrangian analysis of the atmospheric branch of the global water cycle. Part I: Method description, validation, and demonstration for the August 2002 flooding in Central Europe. *J. Hydrometeor.*, **5**, 656–678, https://doi.org/10.1175/1525-7541(2004)005<0656:ALAOTA>2.0.CO;2.

——, and ——, 2005: A Lagrangian analysis of the atmospheric branch of the global water cycle: Part II: Moisture transports between Earth's ocean basins and river catchments. *J. Hydrometeor.*, **6**, 961–984, https://doi.org/10.1175/JHM470.1.

——, C. Forster, A. Frank, P. Seibert, and G. Wotawa, 2005: Technical note: The Lagrangian particle dispersion model FLEXPART version 6.2. *Atmos. Chem. Phys.*, **5**, 2461–2474, https://doi.org/10.5194/acp-5-2461-2005.

Tewari, M., and Coauthors, 2004: Implementation and verification of the Unified NOAH land surface model in the WRF Model. *20th Conf. on Weather Analysis and Forecasting/16th Conf. on Numerical Weather Prediction*, Seattle, WA, Amer. Meteor. Soc., 14.2a, https://ams.confex.com/ams/84Annual/techprogram/paper_69061.htm.

Thomson, D. J., 1987: Criteria for the selection of stochastic models of particle trajectories in turbulent flows. *J. Fluid Mech.*, **180**, 529–556, https://doi.org/10.1017/S0022112087001940.

Trigo, I. F., T. D. Davies, and G. R. Bigg, 1999: Objective climatology of cyclones in the Mediterranean region. *J. Climate*, **12**, 1685–1696, https://doi.org/10.1175/1520-0442(1999)012<1685:OCOCIT>2.0.CO;2.

——, ——, and ——, 2000: Decline in Mediterranean rainfall caused by weakening of Mediterranean cyclones. *Geophys. Res. Lett.*, **27**, 2913–2916, https://doi.org/10.1029/2000GL011526.

van der Ent, R. J., and O. A. Tuinenburg, 2017: The residence time of water in the atmosphere revisited. *Hydrol. Earth Syst. Sci.*, **21**, 779–790, https://doi.org/10.5194/hess-21-779-2017.

Vázquez, M., R. Nieto, M. L. R. Liberato, and L. Gimeno, 2020: Atmospheric moisture sources associated with extreme precipitation during the peak precipitation month. *Wea. Climate Extremes*, **30**, 100289, https://doi.org/10.1016/j.wace.2020.100289.

Ward, M. N., 1998: Diagnosis and short-lead predictions of summer rainfall in tropical North Africa at interannual and multidecadal timescales. *J. Climate*, **11**, 3167–3191, https://doi.org/10.1175/1520-0442(1998)011<3167:DASLTP>2.0.CO;2.

Warner, T. T., R. A. Peterson, and R. E. Peterson, 1997: A tutorial on lateral boundary conditions as a basic and potentially serious limitation to regional weather prediction. *Bull. Amer. Meteor. Soc.*, **78**, 2599–2617, https://doi.org/10.1175/1520-0477(1997)078<2599:ATOLBC>2.0.CO;2.

Zhang, Z., F. M. Ralph, and M. Zheng, 2019: The relationship between extratropical cyclone strength and atmospheric river intensity and position. *Geophys. Res. Lett.*, **46**, 1814–1823, https://doi.org/10.1029/2018GL079071.

Zhao, N., A. Manda, X. Guo, K. Kikuchi, T. Nasuno, M. Nakano, Y. Zhang, and B. Wang, 2021: A Lagrangian view of moisture transport related to the heavy rainfall of July 2020 in Japan: Importance of the moistening over the subtropical regions. *Geophys. Res. Lett.*, **48**, e2020GL091441, https://doi.org/10.1029/2020GL091441.

4.4 Projected changes in atmospheric moisture transport contributions associated with climate warming in the North Atlantic

Fernández-Alvarez, J. C.; Pérez-Alarcón, A., Eiras-Barca, J. Rahimi, S., Nieto, R. & Gimeno, L. Projected changes in atmospheric moisture transport contributions associated with climate warming in the North Atlantic. *Nat. Commun.* 14, 6476 (2023)

Table 4.4: Detailed description of the journal where the third article was published. The data is updated from 2022 according to the Web of Science (JCR). **IF**: impact factor.

Journal	Description	Journal metrics
Nature Communications	**Publisher**: Nature Publishing Group, **Scope**: Nature Communications publishes in all areas of life, health, social, physical, chemical, and Earth sciences. This journal presents important advances of significance to specialists within each field.	**IF:** 16.6, 5-year **IF**: 17.0, **Ranking**: 7 out of 133 in Multidisciplinary Sciences (**Q1**)

nature communications

Article https://doi.org/10.1038/s41467-023-41915-1

Projected changes in atmospheric moisture transport contributions associated with climate warming in the North Atlantic

Received: 3 May 2022

Accepted: 21 September 2023

Published online: 14 October 2023

Check for updates

José C. Fernández-Alvarez [1,2], Albenis Pérez-Alarcón [1,2], Jorge Eiras-Barca[1,3], Stefan Rahimi[4,5], Raquel Nieto [1] & Luis Gimeno [1]

Global warming and associated changes in atmospheric circulation patterns are expected to alter the hydrological cycle, including the intensity and position of moisture sources. This study presents predicted changes for the middle and end of the 21st century under the SSP5-8.5 scenario for two important extratropical moisture sources: the North Atlantic Ocean (NATL) and Mediterranean Sea (MED). Changes over the Iberian Peninsula—considered as a strategic moisture sink for its location—are also studied in detail. By the end of the century, moisture from the NATL will increase precipitation over eastern North America in winter and autumn and on the British Isles in winter. Moisture from the MED will increase precipitation over the southern and western portions of the Mediterranean continental area. Precipitation associated with the MED moisture source will decrease mainly over eastern Europe, while that associated with the NATL will decrease over western Europe and Africa. Precipitation recycling on the Iberian Peninsula will increase in all seasons except summer for mid-century. Climate change, as simulated by CESM2 thus modifies atmospheric moisture transport, affecting regional hydrological cycles.

It is predicted that thermal warming of the atmosphere will exceed the 1.5 °C or 2 °C targets in the 21st century unless steep reductions in CO_2 and other greenhouse gas emissions are made in the coming decades[1]. The thermodynamic response to a warmed atmosphere per degree of warming is a 6–7% increase in low-level atmospheric water vapour[2], according to the Clausius–Clapeyron relationship[3–5], and this will have a strengthening impact on moisture transport worldwide[5]. In addition to warming, an increase in global mean annual evaporation is expected[5], affecting the evaporation rates of most oceans[6]. Moisture transport will also increase[2,7,8] and so will the vertically integrated water vapour transport (IVT)[9]. It has been shown that this effect dominates over circulation changes in the mid-latitudes[10]. Moreover, changes in the atmospheric circulation patterns will also occur as the planet retains more heat, which will affect the atmospheric water balance at global and regional levels[11].

The net effect of dynamic (circulation) and thermodynamic processes is therefore extremely relevant when analysing future changes in moisture sources for precipitation over a region[12]. It is estimated that continental moisture recycling will decrease by 2–3% per °C globally[13], being systematically higher in the past and lower in the future[14]. However, there will be exceptions: an increase of ~2–8% is expected in West Africa and the Iberian Peninsula[14] by the end of the 21st century. Thus, the projected decrease in global recycling, coupled with the inherent moisture limitations of the land's surface, implies

[1]Centro de Investigación Mariña, Universidade de Vigo, Environmental Physics Laboratory (EPhysLab), Campus As Lagoas s/n, Ourense 32004, Spain. [2]Departamento de Meteorología, Instituto Superior de Tecnologías y Ciencias Aplicadas, Universidad de La Habana, La Habana, Cuba. [3]Defense University Center at the Spanish Naval Academy, Group of Applied Mathematics for Defense, Plaza de España s/n, 36920 Marín, Spain. [4]Department of Atmospheric Science, University of Wyoming, Laramie, WY 82071, USA. [5]Center for Climate Science, University of California Los Angeles, Los Angeles, CA 90095, USA. e-mail: l.gimeno@uvigo.es

that the importance of oceans as land moisture sources will increase with warming[15].

It is thus essential to investigate the links between moisture sources and sinks, the role of climate change in modifying atmospheric moisture transport, and how this influences continental precipitation[16]. To our knowledge, previous studies based on Lagrangian approaches have not considered how climate change will alter the location and importance of moisture source regions and the future transport of moisture from such regions to continental areas.

Specifically, we analysed future changes in the moisture source–sink relationship around the Iberian Peninsula (IP), which is one of the hotspot mid-latitude areas affected by more than one moisture source[6]. This region is optimal for conducting a detailed study since its climate is highly dependent on the moisture intrusion from two of the major global oceanic sources[17,18] (Supplementary Fig. 1), the North Atlantic Ocean (NATL), main source of moisture for neighbouring continents in winter months[19,20] and the Mediterranean Sea (MED), known to be particularly sensitive to climate change and its implications[21,22]. The IP is also affected by strong recycling processes[20] (see Supplementary Section 1.3 for more information) and—along with the British Isles—it is the most active region in the North Atlantic for atmospheric river activity[23].

The scope of this study—although giving greater relevance to the Iberian Peninsula—reaches all the regions that have NATL and MED as a relevant source of moisture; North Africa, Western and Eastern Europe and Eastern North America. The analysis is performed using the Lagrangian dispersion model FLEXPART-WRF initialized with WRF-ARW (WRF with the dynamic core Advanced Research WRF—ARW—) dynamically downscaled outputs. Three representative climatic periods have been used for the comparison. Firstly, a historical period (HIST: 1985–2014), followed by a mid-century representative period (MC: 2036–2065), and finally, a late (end)-century representative period (EC: 2071–2100). The latter two have been selected under the SSP5-8.5 scenario of CMIP6[24,25] (see Data Description in Supplementary Section 1.1 and 'Methods'). The methodology used is a powerful tool for studying regional climate processes, by providing high-resolution historical and future climate data. It will allow us to gain better insights of future changes in the moisture source-sink relationship in the study area[26].

The results presented herein, relying on projected climate conditions under a warming atmosphere throughout the 21st century, reveal a general increase in oceanic moisture transport in the North Atlantic latitudes over its surrounding continental areas, an increase in the recycling processes for the Iberian Peninsula, and a projected decrease in the precipitation contribution from the MED mainly over Eastern Europe and from the NATL for Western Europe.

Results

Future projections in precipitation and geopotential height as per the CESM2 model

The study of changes in the moisture source regions must be contextualized within the framework of the general changes in the precipitation regime of the regions analysed. Thus, Supplementary Fig. 2 shows the seasonal and annual changes in the cumulative amount of precipitation (in mm/day) for both MC (2036–2065) and EC (2071–2100) with respect to the historical period (1985–2014) for the area of interest.

In annual terms, a decrease in precipitation close to 1 mm day^{-1} is observed for EC over the entire Iberian Peninsula and the Mediterranean Sea. Decreases over 2 mm day^{-1} are observed in the southwestern sector of the domain. On the other hand, increases close to 1 mm day^{-1} are expected in almost the entire east coast of the USA and Canada, as well as in the Bermudas region. Specifically, the most notable increases in precipitation are observed in mid and high latitudes—as well as along the entire North American East Coast—for the winter months. Significant increases are also observed in the Gulf of Mexico region and particularly in Bermudas for the autumn months. On the other hand, decreases in precipitation are characteristic of (sub)tropical latitudes for almost the entire year. In general terms, the patterns of precipitation changes are coincident between MC and EC; more accentuated in the latter.

Previous studies[27–29] already proposed a reduction in average precipitation for southern Europe. Specifically—and based on these previous studies—the expected precipitation reduction for the IP ranges from 10% to 15% for all seasons except winter. These changes would be in terms of a reduction in the number of wet days and an extension of drought periods by the end of the century[30].

It should be taken into account that a determining factor in the changes of the precipitation regime—and the associated sources of moisture—may be the variations in the atmospheric dynamics of the future climate, with regard to the present one. In order to infer these, a study analogous to the one shown for accumulated precipitation in Supplementary Fig. 2 is presented for the geopotential height at 500 hPa (Z500) in Supplementary Fig. 3.

In this regard, what is observed is a complex pattern, which can be summarized as a generalized increase of Z500 in the study region. The areas most affected by this increase are the subtropical regions, as well as the Atlantic coast of Canada and the northeastern USA. The areas least affected in annual terms—and particularly in the winter months—are the regions of usual influence of the Icelandic low. These results are in correspondence to those shown by Christidis et al.[31], where using seven climate models demonstrated that a significant global increase in the annual and seasonal mean Z500 is projected. Finally, it is noteworthy that this generalized—albeit moderate—increase in mid-level pressures for this particular region has been identified in the literature as a potential trigger for the easing of the westerly flow over the North Atlantic, which could affect the position of the jet stream located over this region[31].

Future projections for integrated water vapour transport (IVT) in the North Atlantic Ocean

To better frame our assessment of the moisture transport processes, we also analysed changes in mean IVT fields within the extended area of the North Atlantic Ocean for MC and EC with respect to the historical pattern (Supplementary Fig. 4). The general trend (particularly for EC) is for an increase in IVT fields in the mid-latitudes of the North Atlantic, as well as in the Caribbean Sea and on the American east coast. In contrast, a decrease of roughly 40 kg m^{-1} s^{-1} is observed in the (sub) tropical latitudes of the North Atlantic. Intermediate seasons show transitional patterns: in spring, minimal changes are expected (with the exception of the East Caribbean Sea and Central Atlantic, where negative values are projected), and positive values are expected in autumn, mainly in the subtropical regions above 30°N.

Both MC and EC show similar patterns of change, being more accentuated in EC for almost all the regions. The only exception in this regard is observed on the European west coast in the summer months; where the increase is only observed for EC.

In addition, a northward shift of the maximum IVT fields is observed. This shift is coincident with the changes in precipitation already analysed in the previous section, and shown in Supplementary Fig. 2. These results are consistent with previous studies that have projected a poleward shift of subtropical high-pressure areas and of the frequent locations of atmospheric rivers[7]. A summary of the mean percentage differences with respect to the historical period is presented in Supplementary Table 2. In general, the maximum percentage values follow the Clausius–Clapeyron[3–5] relationship, showing an increase of ~7% K^{-1}.

Changes in moisture sources for the Iberian Peninsula

The backward Lagrangian approach was used to evaluate future changes in the moisture sources for the IP, our featured target region

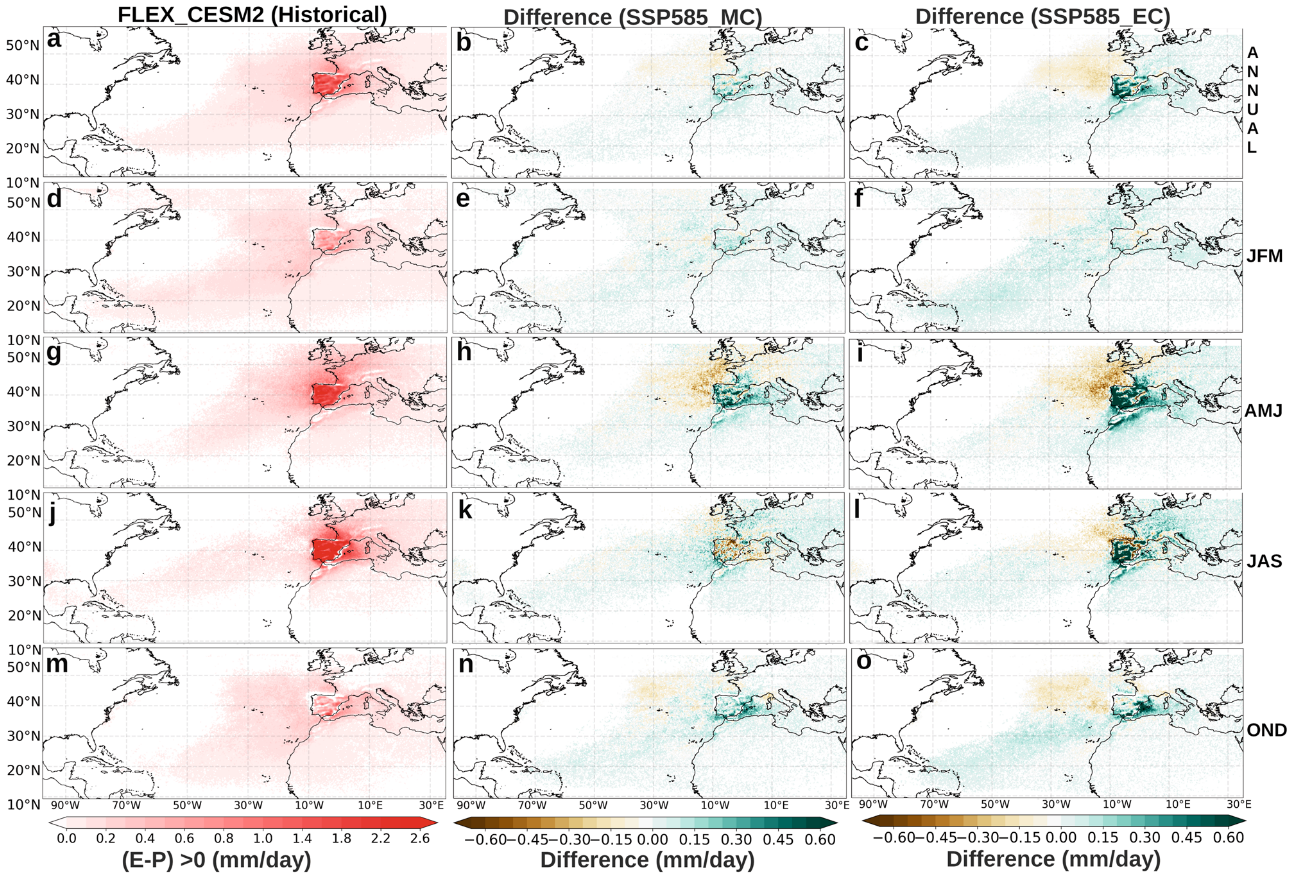

Fig. 1 | Future changes in the absolute contribution (in mm day^{-1}) of the moisture sources to the Iberian Peninsula (IP). Moisture sources fields (E-P > 0) for the IP in the historical reference period (1985–2014, (**a**, **d**, **g**, **j**, **m**)) and differences under the SSP5-8.5 scenario for the mid- and end 21st century (2036–2065, MC (**b**, **e**, **h**, **k**, **n**), and 2071–2100, EC (**c**, **f**, **i**, **l**, **o**), respectively) expressed in mm day^{-1}. The fields displayed from top to bottom correspond to annual, winter, spring, summer and autumn periods (ANNUAL, JFM, AMJ, JAS and OND).

(see ‘Methods’). Figure 1 (left column) shows the moisture sources (E-P > 0) of the Iberian Peninsula during the historical period for CESM2.

In annual terms, it is observed that the precipitation recycling processes (PRPs)—processes that trigger the portion of precipitation whose origin lies in evaporation over the region[32]—have a practically homogeneous contribution in the whole Iberian Peninsula close to 1.4 mm/day.

In addition, this figure reveals known seasonal variations[20], with a greater contribution in winter from the North Atlantic reaching as far as the Caribbean Sea (~0.4–1.4 mm/day), and predominant influences from the Iberian Peninsula and the Mediterranean Sea in summer and spring (>1.8 mm/day). In autumn, the influence of oceanic sources and PRPs predominates in the east of the IP, with values that do not reach 1 mm/day.

A general and progressive intensification in the moisture sources is found in all seasons for the MC and EC periods under the SSP5-8.5 scenario. As for MC (Fig. 1, middle column) in annual terms it is observed is a slight increase in contributions from southern North Atlantic, western Mediterrenean Sea and Iberian Peninsula; the latter showing the largest increment. In addition, a pronounced intensification of PRPs are found in spring, while a decrease in these is observed in the summer months. The same signal is observed for the contribution from the western Mediterranean region. In autumn, the greatest increase is seen for the western Mediterranean region, varying in the range from 0.3-0.45 mm/day.

In regard to EC (Fig. 1, right column), an amplified version of the changes already described for MC is observed. In this respect there is only the exception for the contribution of the PRPs in the summer months, which in MC was negative, while for EC it turns out to be positive. It is also worth noting that for EC there is a clear decrease in the contribution of the North Atlantic region located above latitude 40°N and nearby the European coast. This decrease is observed in annual terms, and is particularly intense in spring.

For a better interpretation of the results described in the previous paragraphs, Fig. 2 shows the spatially integrated changes for each source region, in terms of percentage change. This figure shows that, although the most relevant changes in absolute terms (mm day^{-1}) are observed for the PRPs, in percentage terms the expected changes are similar for the three source regions, and even slightly higher in MED and NATL. Quantitatively, the percentage changes obtained are relatively large, exceeding annual increases of 30% for both MED and NATL. In any case—as discussed below—it should be noted that when working with the SSP5-8.5 scenario, these results should be interpreted as the upper bound of what should actually be expected.

Having very long time series has also allowed us to analyse changes in the variability of the results presented. In particular, Supplementary Fig. 5 shows the changes relative to the historical period in the standard deviation of the time series of the contribution of the different sources to precipitation in the Iberian Peninsula. The cited figure shows the percentage changes in the standard deviation of the future periods with respect to the standard deviation of the historical period. Thus, positive values will indicate an increase in variability; while negative values will show a decrease in variability. In general terms, the variability is also expected to increase, particularly for EC, in values close to 15%. There are some exceptions, such as the case of PRP

 https://doi.org/10.1038/s41467-023-41915-1

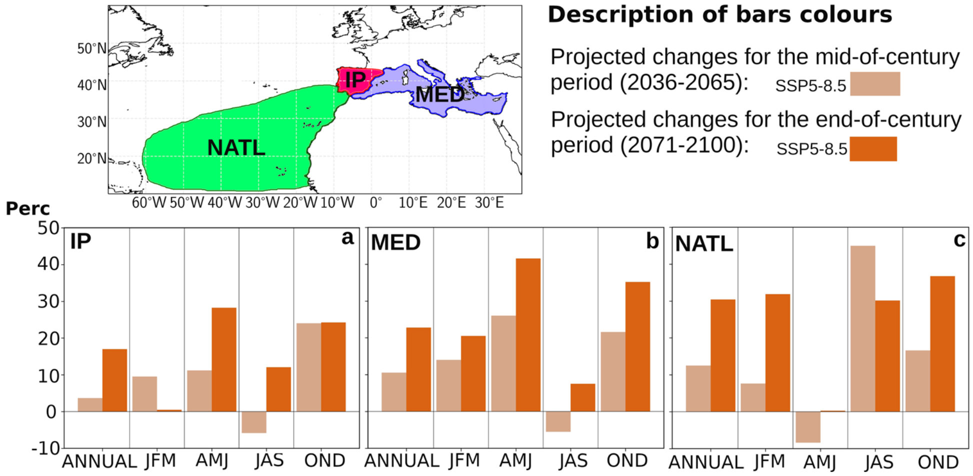

Fig. 2 | Future changes in the relative contribution (in %) of the moisture sources to the Iberian Peninsula. Relative changes are shown for (**a**) the precipitation recycling processes (PRPs) in the Iberian Peninsula (IP), (**b**) Mediterranean Sea (MED) and (**c**) North Atlantic Ocean (NATL) over the four seasons as well as in annual terms both for the mid- and end 21st century (2036–2065, MC, and 2071–2100, EC, respectively).

variability, which is expected to decrease slightly in the winter months for both EC and MC.

Changes in precipitation contribution from the Mediterranean and North Atlantic moisture sources

Beyond the analysis carried out for the Iberian Peninsula, the forward trajectories from the oceanic moisture sources (NATL and MED) were used to evaluate future changes in their precipitation contributions (PCs, total mean amount of precipitation (in mm/day) provided by the sources to the study region[33]) over the surrounding continental areas (see 'Methods' section). Figure 3 (left column) provides regions with P-E > 0 having quantified the moisture balance for the air parcels originating from MED for the historical period. Overall, a remarkable PC is observed in northern and eastern Europe, as well as in regions of North Africa, with contributions of between 3 and 7 mm/day (Fig. 3a). In addition, these PC patterns show that MED provides a similar contribution over the continent adjacent to both the north and east of the MED basin in winter and autumn (Fig. 3d, m). In the warm season, the most intense PCs move westward and have a greater effect during spring on Europe and during summer on Africa (Fig. 3g, j). These results agree with those of previous studies[17,18].

The projections of the PCs for MC (Fig. 3, middle column) show results that depend on the season considered. In annual terms, seasonal signals tend to counterbalance each other, with a decrease near the Italian Peninsula and a slight increase between the Iberian Peninsula and the British Isles (Fig. 3b). Also, a reduction of the PCs is observed for the regions bordering MED to the north and this is particularly strong in the winter months (Fig. 3e). There is also an important signal of a reduction of the contribution in central Europe in spring (Fig. 3h) and a certain increase of the contribution over central Europe in autumn (Fig. 3n).

Regarding the projections of PCs for EC (Fig. 3, right column); overall, an amplified version of what is observed for MC is found, with the exception of the summer months, where a clear decrease in the contribution is shown for Central Europe (Fig. 3l). Relevant decreases are also observed throughout the year in the south-eastern European region (Fig. 3c) with a significant increase in North Africa. On the other hand, relevant increases in contribution are observed in Central Europe in the winter and autumn months (Fig. 3f, o), with particularly relevant increases in the summer months (Fig. 3l). In autumn, there is a longitudinal increase in the contribution, especially in North Africa, Fig. 3o).

Figure 4 shows the changes already described for MC and EC in Fig. 3, but in relative percentage terms and spatially integrated over the four most relevant sink regions for MED; the Iberian Peninsula (IP), Western Europe (EUwest), Eastern Europe (EUeast) and North Africa (NAfrica). This figure allows to observe how the most remarkable relative changes are expected over EUwest, where in the winter months the contribution will grow by 40% for EC[34], while in the summer months the contribution will decrease by 40% in the same period. Also notable are the expected changes in NAfrica, which grow in all seasons with an average annual contribution close to 30%. On the other hand, the changes in EUeast—even though they may present significant seasonal values—tend to be temporarily compensated in annual terms. In relation to IP, it is observed how MED will continue to be a main source of moisture for this region in the summer months increasing its influence in values close to +20% for EC, relative to the current values[35]. In the autumn and winter seasons, the role that MED will presumably play in IP is more complex, observing opposite behaviours between MC and EC, which do not allow obtaining clear conclusions in this regard[36].

It is observed a no a priori result concerning the local contribution (particularly associated to the MED, Fig. 4) for regions such as EUwest in AMJ and EUeast in JFM and JAS in which accentuated behaviours are observed for MC with respect to EC or even opposites are observed between both periods. This behaviour would have an explanation of dynamic character, and the explanation can be intuited by considering together the IVT fields (shown in Supplementary Fig. 8) together with the changes in Z500 (Supplementary Fig. 3). Particularly, in the latter, a latitudinal shift of the geopotential height fields is expected to determine different stability conditions for EC and MC over central Europe[37]. The aforementioned changes in stability conditions would decrease the convergence of moisture flux, and thus precipitation; this could be an explanation for the existence of more pronounced local changes in EC and MC at these seasons.

Supplementary Fig. 6 shows a variability analysis analogous to that presented in Supplementary Fig. 5 but for the contribution of precipitation from the MED source to its sinks (IP, EUwest, EUeast and NAfrica). In general, an increase in variability with region-dependent values is again observed. For example, the highest values—close to 25% in annual terms for EC—of variability increase are expected for NAfrica, while for IP they remain close to 15%. The case of EUwest is particularly noteworthy, as it shows an increase of 40 percent for JFM, while a decrease in the summer months is expected for the end of the century.

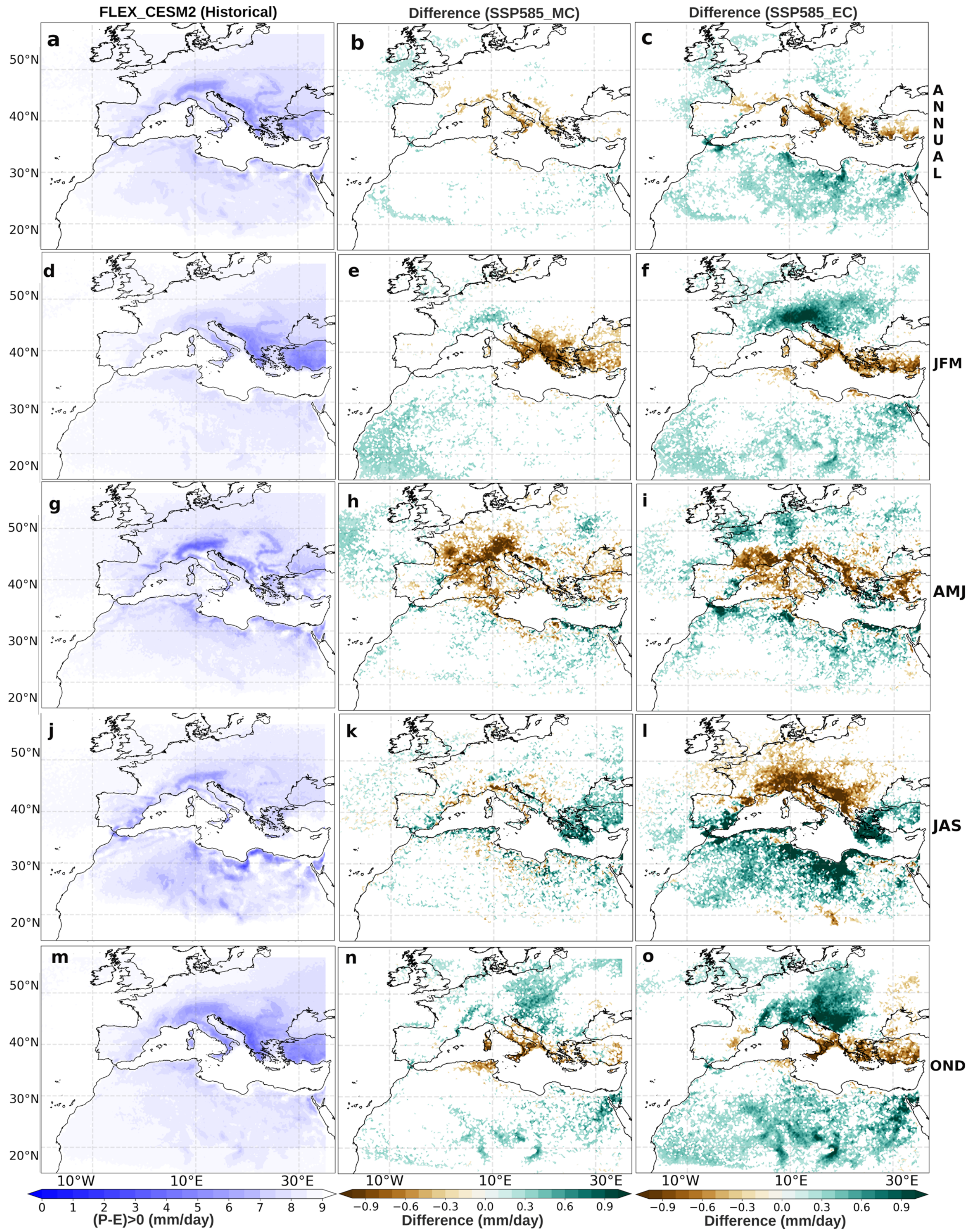

Fig. 3 | Future changes in the absolute contribution of precipitation (in mm day^{-1}) to moisture sinks from the Mediterranean source. Moisture sinks fields (P-E > 0) for the Mediterranean Sea source (MED) for the historical reference period (1985–2014, (**a**, **d**, **g**, **j**, **m**)) and differences under the SSP5-8.5 scenario for the mid- and end 21st century (2036–2065, MC (**b**, **e**, **h**, **k**, **n**), and 2071–2100, EC (**c**, **f**, **i**, **l**, **o**), respectively). The fields displayed from top to bottom correspond to annual, winter, spring, summer and autumn periods (ANNUAL, JFM, AMJ, JAS and OND).

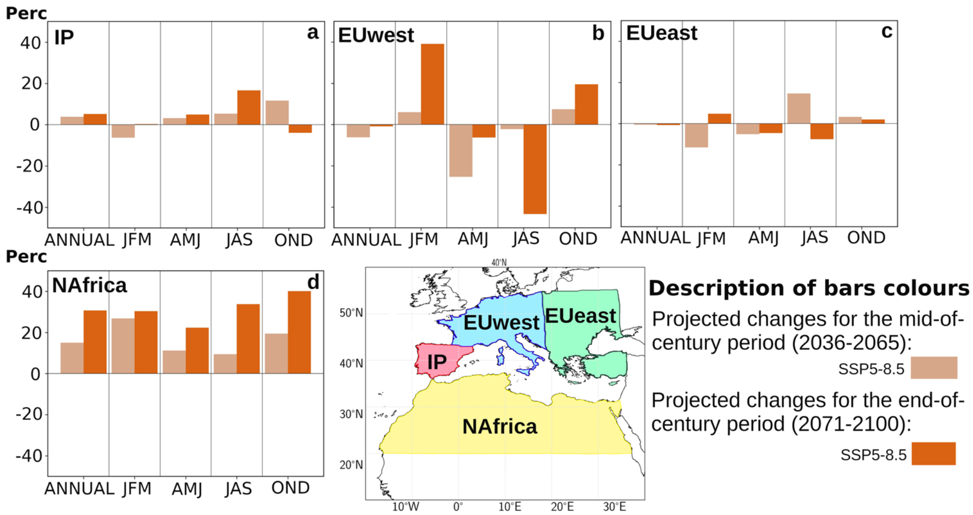

Fig. 4 | Future changes in the relative contribution of precipitation (in %) to moisture sinks from the Mediterranean source. Percentage of projected future changes in precipitation contribution over: (**a**) Iberian Peninsula (IP), (**b**) Western Europe (EUwest), (**c**) Eastern Europe (EUeast) and (**d**) North Africa (Nafrica) associated with the Mediterranean Sea (MED) source.

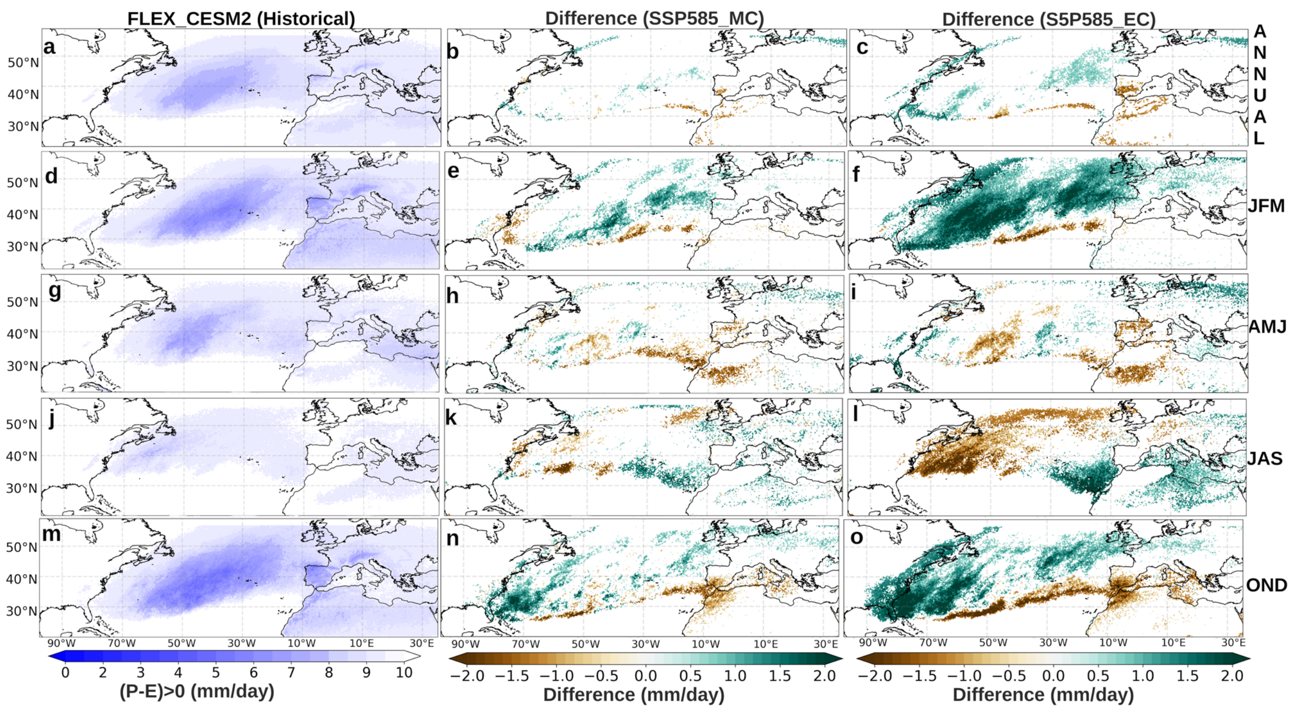

Fig. 5 | Future changes in the absolute contribution of precipitation (in mm day⁻¹) to moisture sinks from the North Atlantic source. Moisture sink fields (P-E > 0) for the North Atlantic Ocean (NATL) source for the historical reference period (1985–2014, (**a**, **d**, **g**, **j**, **m**)) and differences under the SSP5-8.5 scenario for the mid- and end 21st century (2036–2065, MC (**b**, **e**, **h**, **k**, **n**) and 2071–2100, EC (**c**, **f**, **i**, **l**, **o**), respectively). The fields displayed from top to bottom correspond to annual, winter, spring, summer and autumn periods (ANNUAL, JFM, AMJ, JAS and OND).

Figure 5 shows results analogous to those presented for Fig. 3, but now for the NATL moisture source. The first column shows how this source of moisture is relevant not only for itself but also for much of Europe[20] and North Africa, particularly in the winter, spring and autumn months and annually (Fig. 5a, d, g, m), as well as for the Mediterranean[18] itself and—although to a lesser extent—for the U.S. East Coast. In the summer months (Fig. 5j), this influence, although persisting, is much more limited, due to the reduction of the baroclinic dynamical systems responsible for most of the oceanic advection.

In relation to the expected changes for MC (Fig. 5, middle column), there is a significant seasonality in these results, which in annual terms tend to cancel each other. For example, a strong increase in the contribution is observed near the North American east coast, together with an intense decrease in the southern IP and Maghreb area for the autumn months[38] (Fig. 5n). This signal is observed—although to a lesser extent—for the winter months (Fig. 5e) and fits with the already predicted northward shift of the PCs[39,40].

Likewise, in the winter months, the contribution along the North Atlantic corridor seems to strengthen with values ranging from 1 to 2 mm/day (Fig. 5e).

Again, for EC (Fig. 5, right column) what is observed is an amplified version of the pattern for MC. In addition to the results already

 https://doi.org/10.1038/s41467-023-41915-1

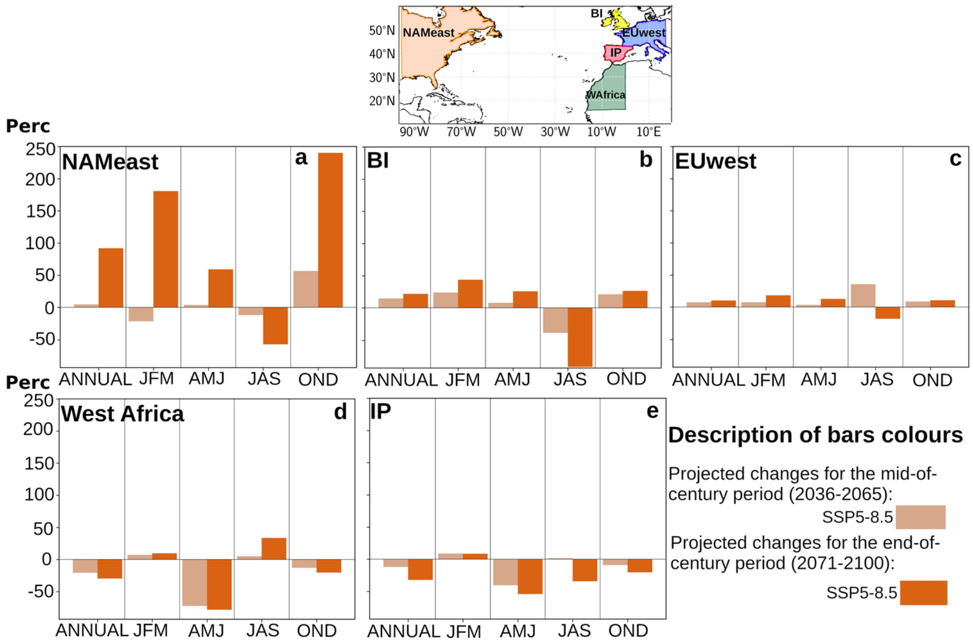

Fig. 6 | Future changes in the relative contribution of precipitation (in %) to moisture sinks from the North Atlantic source. Percentage future changes in the precipitation contribution over: (**a**) North American East Coast (NAMeast), (**b**) British Isles (BI), (**c**) European West Coast (EUwest), (**d**) West Africa (WAfrica) and (**e**) Iberian Peninsula (IP) associated with the North Atlantic Ocean (NATL) source.

discussed, it is observed an intense decrease of the contribution in the summer months (>2.0 mm/day) in the northern part of the North American west coast (Fig. 5l). All these results fit with others previously obtained with alternative methodologies, such as those predicting an increase in Atlantic PCs in winter and autumn for south-eastern North America[41] and the generalized decrease in contribution for the African coast[42] or the southern Iberian Peninsula[2,43]. It is also noted that the shift between positive and negative contributions in the North Atlantic —particularly in the winter months—is most likely related to the gradual northward shift of the North Atlantic baroclinic corridor.

Figure 6 shows the observed changes in the contribution of NATL to its main sinks—North American East Coast (NAMeast), British Isles (BI), European West Coast (EUwest), West Africa (WAfrica), and the Iberian Peninsula (IP)—in relative terms. This figure is especially enlightening as it shows, for example, how for EC the contribution on NAMeast increases in annual terms by almost 100%, being the autumn and winter months the largest contributor to this increase. Likewise, the gradual loss of relevance of NATL for WAfrica and IP, as well as for BI in the summer months, is striking. All these results denote a gradual northward shift of the North Atlantic baroclinic corridor, which extends its zones of influence northward, particularly in the extended winter months[1,33,44].

Finally, Supplementary Fig. 7 shows analogous results presented for MED in Supplementary Fig. 6, but for the increased variability in the relative contribution of NATL precipitation over its sources (BI, EUwest, IP, West Africa and NAMeast). Again, with some exceptions at the seasonal level, an increase in variability is expected for all sources except West Africa, particularly for EC. NAMeast stands out at the top, with an increase of 30% in annual terms. In the case of West Africa, a decrease in variability is observed, quantified at −10% in annual terms.

Synthesis

The hydrological cycle is projected to increase in intensity under climate change[45]. We found a general increase in moisture reaching continental areas in the extratropical North Atlantic and Mediterranean belts. We also observed a significant increase—although to a lesser extent—of the precipitation recycling processes (PRPs) over the Iberian Peninsula (IP) in the winter months. In annual terms, we observed an increase in these PRPs of between 2 and 8%, within the range previously established by Findell et al.[14] although these are doubled for EC. In any case, the projections presented in this article coincide with those that had already identified an increase in the contribution of moisture from oceanic sources—and, to a lesser extent, from the recycling processes—with global warming[15].

The results obtained in relation to the increases in NATL and MED moisture contributions to the IP are consistent with expectations. In particular, they show for the end of the century an increase in the water storage capacity of the atmosphere compatible with Clausius-Clapeyron amplification[46]. This would imply an increased evaporation in the source regions such as the MED and NATL, with an accentuated moisture supply that, at least in part, would end up affecting the IP. Specifically, Supplementary Fig. 9 shows a comparison for North Atlantic Ocean and the Mediterranean Sea of the evaporation field obtained from WRF-ARW outputs between the historical period and MC and EC for the SSP5-8.5 scenario. This figure shows a remarkable increase in evaporation over the entire Mediterranean Sea, particularly for EC. On the other hand, the North Atlantic region shows a clear differentiated pattern between the Northern and Southern sectors, with evaporation decreasing in the former and increasing in the latter; also particularly noticeable for EC. Moreover, they show a slight latitudinal shift from this source region to the EC. Finally, the results show a clear decrease in the contribution of the NATL source in the areas located to the northeast of the North Atlantic near the European shores. These changes may be related to a considerable decrease in evaporation for MC and EC in the aforementioned areas (Supplementary Fig. 9). In addition, the increase of the Z500 field could influence the general anticyclonic circulation, as well as an increase of atmospheric stability situations (Supplementary Fig. 3). This Supplementary Fig. 3 is similar to Supplementary Fig. 9 but considering the Z500 field and the outputs of the CESM2 model. It is highlighted that with this increase of Z500, a greater increase of blocking situations in future periods can be expected mainly in regions such as Europe and the Mediterranean Sea, where the increase is more noticeable. This is referenced from the results found by Davini and d'Andrea[47] with different CMIP6 climate models. However, there are numerous discrepancies in the results provided by the different models in the work of these authors; as well as considerable biases in the representation of the present climate[47] regarding blocking situations. Thus, it is hasty to take these conclusions into account when determining the climate change signal. Instead, a future evaluation of the behaviour of this model in the Z500 representation becomes necessary.

Higher contributions of the MED moisture source to precipitation are observed in the regions located south of the Mediterranean Sea, both for MC and EC. This contribution will also increase—although to a lesser extent—over the Iberian Peninsula, mainly in the summer season, being more noticeable for EC. There is also observed a decrease in the contribution in Eastern Europe and Western Europe (in summer and spring)[48–50]. This result may be associated with the projected latitudinal shift of storm trajectories in the future climate[40]. In addition, much of this behaviour could be attributed to changes in atmospheric dynamics for both MC and EC. Specifically, Supplementary Fig. 8 shows the changes in the IVT fields for MC and EC with respect to the historical period for the Mediterranean area under the SSP5-8.5 scenario. This figure shows that for both periods changes in the moisture flux patterns are to be expected. Over the Mediterranean region, changes are more noticeable in the eastern region where a weakening of moisture transport towards Eastern Europe is observed. On the other hand, Z500 fields are expected to strengthen in general, with notable values on a regional scale (e.g. Western European and Mediterranean Sea regions). This behaviour could favour a stronger anticyclonic atmospheric circulation in the future, as well as greater stability. For regions with a local strengthening, it could also lead to an eventual increase in the frequency of blocking flows from their moisture sources. This evidence indicates that these changes in atmospheric dynamics may be as or more relevant than the thermodynamic changes that lead to greater availability of moisture in the atmosphere. Further, these results show correspondence with those obtained by Batibeniz et al.[51] over Eastern Europe, showing negative trends for seasonal precipitation trends per year using four reanalyses in summer.

The contribution from the NATL source will increase on the east coast of North America (mainly in winter and autumn), followed by the British Isles (mostly in winter), and gradually decrease in latitude from the northern areas of Western Europe, IP and west coast of Africa. It is notable that a decrease is projected in summer for all the regions analysed. Moreover, these results are consistent with the decrease in moisture transport from the North Atlantic source over parts of the western European regions in winter and summer[51]. These results show that although the NATL source will intensify in the future and provide more moisture to the IP (Fig. 2c), it will not positively contribute to the final amount of precipitation over the IP. Moisture from the NATL source may not necessarily precipitate if the appropriate conditions are absent, such as favourable moisture convergence, forcing for vertical ascent, and instability[52]. This will be a consequence of the poleward shift of the storm tracks and the upward expansion of the midlatitude baroclinic regions[53]. This result can be corroborated with the projections of the total precipitation field according to the CESM2 model for IP, where a general decrease is expected, being more notable at the end of the century[27–29] (Supplementary Fig. 2, analogous to Supplementary Fig. 3 but for the precipitation field). This behaviour in the precipitation contribution from the NATL source to its sink areas agrees with the projections of the poleward movement[1] of the general circulation[33,40]. This displacement will be clearly related to the shift in the trajectories of extratropical cyclones, since these are the main mechanism of this poleward transport of moisture[54]. This potential shift, which has already been observed in recent decades, is also expected to intensify under less optimistic climate change scenarios[55]. Therefore, these regions, mainly Europe, will receive a reduced contribution from NATL source, which will have an impact on the precipitation regime and a reduction in rainfall, as previously reported for the Mediterranean area[53], especially in IP during winter or autumn and mainly at the EC[7]. This behaviour may be due to the possible extension of stable and dry summer conditions and a decoupling between moisture availability and dynamic forcing[7], but it could also be the product of a circulation that relates to the mean shift of the humidity corridors and the associated atmospheric rivers toward the poles[7,56].

This study makes a significant contribution to the hydrological cycle research because no previous studies based on Lagrangian approaches have considered how climate change will alter the location and importance of moisture source regions or the future moisture transport in the north Atlantic area. These results show that climate change has a large influence on moisture transport around the Atlantic Ocean, which will result in changes in availability of water resources in various regions. These changes could result in water stress, particularly in southern Europe, accentuating long periods of drought and heat waves (very noticeable in summer), generating serious stress on ecosystems and society[57]. As consequences of this warming and the increase in food demand, they can lead to the northward expansion of world agriculture, weakening those of these regions[58]. On the other hand, in winter the events of extreme precipitation in higher latitudes would increase, generating floods for these regions[59] associated with a greater number of atmospheric rivers that reach these latitudes and in turn accentuating winter droughts in southern Europe.

Methods

Data employed

The available outputs of the climate model Community Earth System Model Version 2 (CESM2)[60], from Phase 6 of the Coupled Model Intercomparison Project (CMIP6), were dynamically downscaled. The CESM2 data were downloaded from the Earth System Grid Federation (ESGF2) and obtained for the native "gn" grid with a resolution of 0.9 × 1.25 (~1°) presented as an output mesh with 288 × 192 longitude/latitude, 32 vertical levels (top level at 2.25 mb). Specifically, Weather Research and Forecasting model (WRF-ARW) in its version 3.8.1[61] was used to downscaled CESM2 data (see Supplementary Section 1.2). The highest shared socioeconomic pathway (SSP) scenario from the CMIP6 climate projections (SSP5-8.5) has been also used to analyse the different ranges of future forcing pathways to 2100 (see Supplementary Section 1.1). A set of 30-year periods were compared spanning the historical period 1985–2014 and the intervals 2036–2065 (for the mid-century: MC) and 2071–2100 (for the end-century: EC). ERA5[62] reanalysis data were also used to evaluate the results for the historical period. ERA5 is chosen as a reference since this model provides the advantages of high resolution (31 km horizontally and 137 levels vertically) and a large number of assimilated historical observations. In addition, ERA5 significantly improves upon its predecessor, ERA-Interim reanalysis, particularly with respect to precipitation fields both over extratropical regions and tropical oceanic areas. A more detailed description is presented in the Supplementary Information.

WRF-ARW and FLEXPART-WRF setups

The parameterisations employed in the WRF-ARW configuration were as follows: the WSM6 microphysics scheme[63], Yonsei University planetary boundary layer (PBL) scheme[64], revised MM5 surface layer scheme[65], United Noah Land Surface Model[66], shortwave and longwave RRTMG schemes[67] and the Kain-Fritsch Ensemble cluster scheme[68]. The WRF-ARW outputs had 40 vertical layers from the surface to 50 hPa with a horizontal spacing of 20 km and they covered an area of 115.39–42.02°W and 19.41°S–59.51°N (see Supplementary Fig. 1). For the FLEXPART-WRF[69] configuration, we used Hanna's[70] scheme for turbulence parameterisation with the convection scheme activated. This scheme is based on the boundary layer parameters PBL height,

https://doi.org/10.1038/s41467-023-41915-1

Monin–Obukhov length, convective velocity scale, roughness length and friction velocity[69]. We assumed skewed rather than Gaussian turbulence in the convective PBL. The FLEXPART-WRF has forty levels and 400 × 777 points, where in the output mesh where the particles are released. The outputs had spatial and temporal resolutions of 20 km and 6 h, respectively.

Identification of moisture sources and sinks

To estimate the moisture sources and sinks, a Lagrangian methodology was applied to follow the changes in the specific moisture content (q) over time (t, every 6 h) along the tracks described by each atmospheric particle that the atmosphere was divided into. Therefore, these changes[71] can be calculated by

$$(e-p)=m\left(\frac{dq}{dt}\right) \tag{1}$$

where m is the mass of the particle, and the difference between e and p considers the increase or decrease in the water vapour ratio along the trajectory. Once the individual trajectories of all particles have been calculated, the total surface freshwater flux in each grid cell can be calculated by summing the contributions of all particles traversing a grid area (A) at a given time. The total budget was calculated as follows,

$$(E-P)=\frac{\sum_{k=1}^{N}(e-p)_k}{A} \tag{2}$$

where E represents evaporation, P is precipitation, and N is the total number of particles over the grid area. For this analysis, the particle trajectories were followed for 10 days, the considered average residence time of water vapour particles in the atmosphere[72–74], and the final computed E-P fields were considered as integrated values during this period.

Moisture particles can be tracked backward (forward) in time from a given region to track their direction and determine their sources (sinks)[71,75]. In a backward experiment, the moisture source of a region is defined as an area in which evaporation dominates over precipitation (i.e. absolute positive values of (E-P), E-P > 0), and in a forward mode projection, air masses with a net loss of moisture are detected to determine areas that are moisture sinks (i.e. areas where precipitation dominates over evaporation, E-P < 0 or P-E > 0).

The moisture field patterns were evaluated using a different dataset, periods and statigraphs (see Supplementary Section 1.4). The post-processing of the results for E-P was carried out with the TRansport Of water Vapor (TROVA) software[76].

Assessment of projected changes

Future changes were assessed as the difference between the (E-P) fields obtained in 30-year intervals for the MC and EC periods (2036–2065 and 2071–2100, respectively), and the historical reference period 1985–2014.

As the Lagrangian model uses dynamically downscaled CESM2 data (WRF-CESM2), we first conducted simulations using ERA5 data in the historical period (see Supplementary Figs. 10–14). Simulations were then conducted using the FLEXPART-WRFv3.3.2 dispersion model[69] to study moisture changes, and the experiments were forced with WRF-CESM2 outputs every 6 h (herein FLEX-CESM2). According to the distribution of the atmospheric mass, the simulation domain (covering 100°W to 40°E and from 15°S to 57°N, see Supplementary Fig. 1) was homogeneously divided into 2 million air parcels (or particles), which were subsequently advected forward in time for the entire study period. Finally, to obtain the (E-P) fields for comparison, the moisture sources and sinks for the target regions selected in this study (NATL, MED and IP) were identified and computed (Supplementary Section 1).

Limitations

The results presented in this research show acceptable limitations, mainly related to the nature of the climate models used for WRF-ARW forcing. The considered scenario—SSP5-8.5—assumes a social development based almost exclusively on fossil fuels with a radiative forcing of 8.5 W m^{-2}. It is therefore the most pessimistic of those considered in CMIP6, and has a low probability of occurrence. Therefore, the results presented in this research should be understood with caution, assuming that the signals presented in them are likely to be amplified signals of the reality. This is a very common way of proceeding, and is used to detect signals that in other more optimistic scenarios would probably go unnoticed.

It should be noted that the CESM2 model can be considered a warm model, since it projects a warming close to 4 °C by the end of the century[77]. In order to determine the impact that this could have on the results presented in this manuscript, we have proceeded to replicate the simulations presented here using an Ensemble that includes 18 climate models for five years of simulation, and to compare their results with those obtained for CESM2 alone for the same period. The results of this comparison are presented in Supplementary Figs. 15–17. In essence, it has been verified that some differences exist for some seasons of the year. However, these differences are limited. In any case, it should be noted that the results presented in this article may be slightly overestimating the expected changes.

Likewise, the WRF-ARW is also subject to uncertainties derived from certain subjectivity in its configuration. Although the parameterizations used in these simulations—aimed at resolving physical processes occurring at sub-grid scales—have been carefully selected based on the literature, the selection of another set of parameterizations could have slightly modified the achieved results.

Throughout the development of this research, a non-negligible overestimation of the IVT fields carried out by the WRF-ARW model when initialized with ERA5 has been detected. This overestimation affects regions such as the North Atlantic corridor, the Caribbean Sea and, to a lesser extent, the Amazon basin and the west coast of Africa. We have verified that this overestimation of IVT is due to an overestimation in the near-surface wind fields. Likewise, we have also detected a certain tendency of WRF-ERA5 to overestimate E-P values over the Caribbean Sea, the central Atlantic and the Mediterranean Sea. The results could be slightly affected by this circumstance.

Finally, the methodology used by FLEXPART in the Lagrangian dispersion of particles is also not free of uncertainty. Previous studies in the literature have detected an overestimation of evaporation and precipitation values. These fluctuations are mainly due to non-physical processes relevant to the phenomenology[75]. Lagrangian models are also victims of necessary simplifications in their formulation, which can lead to biases. In particular, FLEXPART is known to progressively increase the uncertainty of the air cell trajectories with time[78].

Data availability

ERA5 reanalysis data can be obtained from https://cds.climate.copernicus.eu/cdsapp#!/dataset/reanalysis-era5-single-levels-monthly-means?tab=form and CESM2 model data from https://esgf-data.dkrz.de/search/cmip6-dkrz/. The WRF-ARW outputs are available upon request to the corresponding author. The request for the data is due to the large volume it occupies, which makes it impossible for it to be stored in an online repository.

Code availability

Code that supports the findings of this study is available upon request from the corresponding author.

References

1. IPCC. Climate change. In *The Physical Science Basis. Contribution of Working Group I to the Sixth Assessment Report of the*

Intergovernmental Panel on Climate Change (Cambridge University Press, 2021).
2. O'Gorman, P. A. & Muller, C. J. How closely do changes in surface and column water vapor follow Clausius-Clapeyron scaling in climate change simulations? *Environ. Res. Lett.* **5**, 025207 (2010).
3. Wentz, F. & Schabel, M. Precise climate monitoring using complementary satellite data sets. *Nature* **403**, 414–416 (2000).
4. Trenberth, K. E., Dai, A., Rasmussen, R. M. & Parsons, D. B. The changing character of precipitation. *Bull. Am. Meteor. Soc.* **84**, 1205–1217 (2003).
5. Held, I. M. & Soden, B. J. Robust responses of the hydrological cycle to global warming. *J. Clim.* **19**, 5686–5699 (2006).
6. Gimeno, L. et al. Oceanic and terrestrial sources of continental precipitation. *Rev. Geophys.* **50**, RG4003 (2012).
7. Sousa, P. M. et al. North Atlantic integrated water vapor transport—from 850 to 2100 CE: impacts on Western European rainfall. *J. Clim.* **33**, 263–279 (2020).
8. Lavers, D. A. & Villarini, G. The contribution of atmospheric rivers to precipitation in Europe and the United States. *J. Hydrol.* **522**, 382–390 (2015).
9. Espinoza, V., Waliser, D. E., Guan, B., Lavers, D. A. & Ralph, F. M. Global analysis of climate change projection effects on atmospheric rivers. *Geophys. Res. Lett.* **45**, 4299–4308 (2018).
10. Huang, X., Swain, D. L. & Hall, A. D. Future precipitation increase from very high resolution ensemble downscaling of extreme atmospheric river storms in California. *Sci. Adv.* **6**, eaba1323 (2020).
11. Allan, R. P. et al. Advances in understanding large-scale responses of the water cycle to climate change. *Ann. N. Y. Acad. Sci.* **1472**, 49–75 (2020).
12. Benedict, I., Van Heerwaarden, C. C., Van Der Ent, R. J., Weerts, A. H. & Hazaleger, W. Decline in terrestrial moisture sources of the Mississippi river basin in a future climate. *J. Hydrometeorol.* **21**, 299–316 (2020).
13. Keys, P., Wang-Erlandsson, L., Gordon, L., Galaz, V. & Ebbesson, J. Approaching moisture recycling governance. *Glob. Environ. Change* **45**, 15–23 (2017).
14. Findell, K. L. et al. Rising temperatures increase importance of oceanic evaporation as a source for continental precipitation. *J. Clim.* **32**, 7713–7726 (2019).
15. Langenbrunner, B. Shifting moisture source. *Nat. Clim. Chang.* **9**, 728 (2019).
16. Gimeno, L. et al. Recent progress on the sources of continental precipitation as revealed by moisture transport analysis. *Earth. Sci. Rev.* **201**, 103070 (2020).
17. Gimeno, L., Drumond, A., Nieto, R., Trigo, R. M. & Stohl, A. On the origin of continental precipitation. *Geophys. Res. Lett.* **37**, L13804 (2010).
18. Nieto, R., Gimeno, L., Drumond, A. & Hernandez, E. A Lagrangian identification of the main moisture sources and sinks affecting the Mediterranean area. *WSEAS Trans. Environ. Dev.* **6**, 365–374 (2010).
19. Eckhardt, S. et al. A 15 year climatology of warm conveyor belts. *J. Clim.* **17**, 218–237 (2004).
20. Gimeno, L., Nieto, R., Trigo, R., Vicente-Serrano, S. M. & López-Moreno, J. I. Where does the Iberian Peninsula moisture come from? An answer based on a Lagrangian approach. *J. Hydrometeorol.* **11**, 421–336 (2010).
21. Lionello, P. & Scarascia, L. The relation between climate change in the Mediterranean region and global warming. *Reg. Environ. Change* **18**, 1481–1493 (2018).
22. Cramer, W. et al. Climate change and interconnected risks to sustainable development in the Mediterranean. *Nat. Clim. Change* **8**, 972–980 (2018).
23. Algarra, I. et al. Significant increase of global anomalous moisture uptake feeding landfalling atmospheric rivers. *Nat. Commun.* **11**, 1–7 (2020).
24. O'Neill, B. C. et al. The scenario model intercomparison project (ScenarioMIP) for CMIP6. *Geosci. Model Dev.* **9**, 3461–3482 (2016).
25. Riahi, K. et al. The shared socioeconomic pathways and their energy, land use, and greenhouse gas emissions implications: an overview. *Glob. Environ. Change* **42**, 153–168 (2017).
26. Rahimi, S. et al. Evaluation of a reanalysis-driven configuration of WRF4 over the Western United States From 1980 to 2020. *J. Geophys. Res. Atmos.* **127**, e2021JD035699 (2022).
27. Pereira, S. C., Carvalho, D. & Rocha, A. Temperature and precipitation extremes over the Iberian peninsula under climate change scenarios: a review. *Climate* **9**, 139 (2021).
28. Vautard, R. et al. The European climate under a 2 C global warming. *Environ. Res. Lett.* **9**, 034006 (2014).
29. Maule, C. F., Mendlik, T. & Christensen, O. B. The effect of the pathway to a two degrees warmer world on the regional temperature change of Europe. *Clim. Serv.* **7**, 3–11 (2017).
30. IPCC. Summary for Policymakers, World Meteorological Organization, Geneva, Switzerland. https://www.ipcc.ch/sr15/chapter/spm/ (2018).
31. Christidis, N. & Stott, P. A. Changes in the geopotential height at 500 hPa under the influence of external climatic forcings. *Geophys. Res. Lett.* **42**, 10–798 (2015).
32. Van der Ent, R. J., Savenije, H. H., Schaefli, B. & Steele-Dunne, S. C. Origin and fate of atmospheric moisture over continents. *Water Res.* **46**, 1–12 (2010).
33. Nieto, R., Ciric, D., Vázquez, M., Liberato, M. L. & Gimeno, L. Contribution of the main moisture sources to precipitation during extreme peak precipitation months. *Adv. Water Resour.* **131**, 103385 (2019).
34. Swain, D. L., Langenbrunner, B., Neelin, J. D. & Hall, A. Increasing precipitation volatility in twenty-first-century California. *Nat. Clim. Chang.* **8**, 427–433 (2018).
35. Ciric, D., Nieto, R., Losada, L., Drumond, A. & Gimeno, L. The Mediterranean moisture contribution to climatological and extreme monthly continental precipitation. *Water* **10**, 519 (2018).
36. Totz, S., Tziperman, E., Coumou, D., Pfeiffer, K. & Cohen, J. Winter precipitation forecast in the European and Mediterranean regions using cluster analysis. *Geophys. Res. Lett.* **44**, 12–418 (2018).
37. Ozturk, T., Matte, D. & Christensen, J. H. Robustness of future atmospheric circulation changes over the EURO-CORDEX domain. *Clim. Dyn.* **59**, 1799–1814 (2022).
38. Gimeno, L., Nieto, R., Drumond, A., Castillo, R. & Trigo, R. Influence of the intensification of the major oceanic moisture sources on continental precipitation. *Geophys. Res. Lett.* **40**, 1443–1450 (2013).
39. Sinclair, V. A., Rantanen, M., Haapanala, P., Räisänen, J. & Järvinen, H. The characteristics and structure of extra-tropical cyclones in a warmer climate. *Weather Clim. Dyn.* **1**, 1–25 (2020).
40. Woollings, T., Gregory, J. M., Pinto, J. G., Reyers, M. & Brayshaw, D. J. Response of the North Atlantic storm track to climate change shaped by ocean–atmosphere coupling. *Nat. Geosci.* **5**, 313–317 (2012).
41. Almazroui, M. et al. Projected changes in temperature and precipitation over the United States, Central America, and the Caribbean in CMIP6 GCMs. *Earth. Syst. Environ.* **5**, 1–24 (2021).
42. Dosio, A. et al. What can we know about future precipitation in Africa? Robustness, significance and added value of projections from a large ensemble of regional climate models. *Clim. Dyn.* **53**, 5833–5858 (2019).

43. Santos, J. A., Belo-Pereira, M., Fraga, H. & Pinto, J. G. Understanding climate change projections for precipitation over western Europe with a weather typing approach. *J. Geophys. Res. Atmos.* **121**, 1170–1189 (2016).
44. Harvey, B. J., Shaffrey, L. C., Woollings, T. J., Zappa, G. & Hodges, K. I. How large are projected 21st century storm track changes? *Geophys. Res. Lett.* **39**, L18707 (2012).
45. Sun, Y., Solomon, S., Dai, A. & Portmann, R. W. How often will it rain? *J. Clim.* **20**, 4801–4818 (2007).
46. Shukla, P. R. et al. *IPCC: Climate Change and Land: An IPCC Special Report on Climate Change, Desertification, Land Degradation, Sustainable Land Management, Food Security, and Greenhouse Gas Fluxes in Terrestrial Ecosystems* (2019).
47. Davini, P. & d'Andrea, F. From CMIP3 to CMIP6: Northern Hemisphere atmospheric blocking simulation in present and future climate. *J. Clim.* **33**, 10021–10038 (2020).
48. Vautard, R. et al. The European climate under a 2 °C global warming. *Environ. Res. Lett.* **9**, 034006 (2014).
49. Forzieri, G. et al. Ensemble projections of future streamflow droughts in Europe. *Hydrol. Earth Syst. Sci.* **18**, 85–108 (2014).
50. Schleussner, C. F. et al. Differential climate impacts for policy-relevant limits to global warming: the case of 1.5 C and 2 C. *Earth Syst. Dyn.* **7**, 327–351 (2016).
51. Batibeniz, F. et al. Identification of major moisture sources across the Mediterranean Basin. *Clim. Dyn.* **54**, 4109–4127 (2020).
52. Hernandez-Duenas, G., Smith, L. M. & Stechmann, S. N. Stability and instability criteria for idealized precipitating hydrodynamics. *J. Atmos. Sci.* **72**, 2379–2393 (2015).
53. Jacob, D. et al. Climate Impacts in Europe Under +1.5 °C Global Warming. *Earth's Future* **6**, 264–285 (2018).
54. Villamil-Otero, G. A., Zhang, J., He, J. & Zhang, X. Role of extratropical cyclones in the recently observed increase in poleward moisture transport into the Arctic Ocean. *Adv. Atmos. Sci.* **35**, 85–94 (2018).
55. Bender, F. A. M., Ramananthan, V. & Tselioudis, G. Changes in extratropical storm track cloudiness 1983–2008: observational support for a poleward shift. *Clim. Dyn.* **38**, 2037–2053 (2012).
56. Yin, J. H. A consistent poleward shift of the storm tracks in simulations of 21st century climate. *Geophys. Res. Lett.* **32**, L18701 (2018).
57. Chiang, F., Mazdiyasni, O. & AghaKouchak, A. Amplified warming of droughts in southern United States in observations and model simulations. *Sci. Adv.* **4**, eaat2380 (2018).
58. King, M. et al. Northward shift of the agricultural climate zone under 21st-century global climate change. *Sci. Rep.* **8**, 1–10 (2018).
59. Lehtonen, I., Ruosteenoja, K. & Jylhä, K. Projected changes in European extreme precipitation indices on the basis of global and regional climate model ensembles. *Int. J. Climatol.* **34**, 1208–1222 (2014).
60. Danabasoglu, G. et al. The community earth system model version 2 (CESM2). *J. Adv. Model. Earth Syst.* **12**, e2019MS001916 (2020).
61. Skamarock, W. et al. Description of the Advanced Research WRF Version 3, Technical Report, https://doi.org/10.5065/D6DZ069T (2008).
62. Hersbach, H. et al. The ERA5 global reanalysis. *Q. J. R. Meteorol. Soc.* **146**, 1999–2049 (2020).
63. Hong, S. Y. & Lim, J. O. J. The WRF single-moment 6-class microphysics scheme (WSM6). *J. Korean Meteorol. Soc.* **42**, 129–151 (2006).
64. Hong, S. Y., Noh, Y. & Dudhia, J. A new vertical diffusion package with an explicit treatment of entrainment processes. *Mon. Weather Rev.* **134**, 2318–2341 (2006).
65. Jimenez, P. A. et al. A revised scheme for the WRF surface layer formulation. *Mon. Weather Rev.* **140**, 898–918 (2012).
66. Tewari, M. et al. Implementation and verification of the unified Noah land surface model in the WRF model. in *20th Conference on Weather Analysis and Forecasting/16th Conference on Numerical Weather Prediction, Seattle, WA* (2004).
67. Iacono, M. J. et al. Radiative forcing by long-lived greenhouse gases: calculations with the AER radiative transfer models. *J. Geophys. Res.* **113**, D13103 (2008).
68. Kain, J. S. The Kain–Fritsch convective parameterization: an update. *J. Appl. Meteorol.* **43**, 170–181 (2004).
69. Brioude, J. et al. The Lagrangian particle dispersion model FLEXPART-WRF version 3.1. *Geosci. Model Dev.* **6**, 1889–1904 (2013).
70. Hanna, S. R. in *Atmospheric Turbulence and Air Pollution Modelling* 275–310 (Reidel Publishing Company, 1982).
71. Stohl, A. & James, P. A. A Lagrangian analysis of the atmospheric branch of the global water cycle: Part II: Earth's river catchments ocean basins, and moisture transports between them. *J. Hydrometeorol.* **6**, 961–984 (2005).
72. Numaguti, A. Origin and recycling processes of precipitating water over the Eurasian continent: experiments using an atmospheric general circulation model. *J. Geophys. Res.* **104**, 1957–1972 (1999).
73. van der Ent, R. J. & Tuinenburg, O. A. The residence time of water in the atmosphere revisited. *Hydrol. Earth Syst. Sci.* **21**, 779–790 (2017).
74. Gimeno, L. et al. The residence time of water vapour in the atmosphere. *Nat. Rev. Earth Environ.* **2**, 558–569 (2021).
75. Stohl, A. & James, P. A Lagrangian analysis of the atmospheric branch of the global water cycle. Part I: Method description, validation, and demonstration for the August 2002 flooding in central Europe. *J. Hydrometeorol.* **5**, 656–678 (2004).
76. Fernández-Alvarez, J. C., Pérez-Alarcón, A., Nieto, R. & Gimeno, L. TROVA: TRansport Of water VApor. *SoftwareX* **20**, 101228 (2022).
77. Seneviratne, S. I. & Hauser, M. Regional climate sensitivity of climate extremes in CMIP6 versus CMIP5 multimodel ensembles. *Earth's Future* **8**, e2019EF001474 (2020).
78. Stohl, A. Computation, accuracy and applications of trajectories—a review and bibliography. *Atmos. Environ.* **32**, 947–966 (1998).

Acknowledgements

This work is supported by the SETESTRELO (PID2021-122314OB-I00) project funded by the Ministerio de Ciencia, Innovación y Universidades, Spain. Partial support was also obtained from the Xunta de Galicia under the Project ED431C 2021/44 (Programa de Consolidación e Estructuración de Unidades de Investigación Competitivas (Grupos de Referencia Competitiva) and Consellería de Cultura, Educación e Universidade). José C. Fernández-Alvarez acknowledges the support from the Xunta de Galicia under the grant no. ED481A-2020/193. Albenis Pérez-Alarcón acknowledges a PhD grant from the University of Vigo. J. Eiras-Barca thanks the Defense University Center at the Spanish Naval Academy (CUD-ENM) for the support provided for this research. In addition, this work has been possible thanks to the computing resources and technical support provided by CESGA (Centro de Supercomputación de Galicia) and Red Española de Supercomputación (RES) (AECT-2022-3-0009 and DATA-2021-1-0005).

Author contributions

L.G. and R.N. designed the study; J.C.F-A. and A.P-A. performed the research; J.C.F.-A., A.P.-A. and S.R.-E. analysed the data; J.C.F.-A., J.E.B. and R.N. wrote the paper; L.G., R.N., J.E.B., J.C.F.-A., S.R.-E. and A.P.-A. review the paper.

Competing interests

The authors declare no competing interests.

https://doi.org/10.1038/s41467-023-41915-1

Additional information

Supplementary information The online version contains supplementary material available at https://doi.org/10.1038/s41467-023-41915-1.

Correspondence and requests for materials should be addressed to Luis Gimeno.

Peer review information *Nature Communications* thanks the anonymous reviewers for their contribution to the peer review of this work. A peer review file is available.

4.5 Changes in Moisture Sources of Atmospheric Rivers Landfalling the Iberian Peninsula With WRF-FLEXPART

Fernández-Alvarez, J. C., Pérez-Alarcón, A., Eiras-Barca, J., Ramos, A. M., Rahimi-Esfarjani, S., Nieto, R., & Gimeno, L. (2023). Changes in moisture sources of atmospheric rivers landfalling the Iberian Peninsula with WRF-Flexpart. *Journal of Geophysical Research: Atmospheres*, e2022JD037612.

Table 4.5: Detailed description of the journal where the fourth article was published. The data is updated from 2022 according to the Web of Science (JCR). **IF**: impact factor.

Journal	Description	Journal metrics
Journal Geophysical Research (JGR): Atmospheres	**Publisher**: American Geophysical Union, **Scope**: This journal's scope is original studies for a better understanding of the properties and processes of the atmosphere, its interaction with other components, and how climate change impacts atmospheric variables.	**IF:** 4.4, 5-year **IF**: 5.302, **Ranking**: Ranking: 28 of 109 in Meteorology & Atmospheric Sciences (**Q2**)

ADVANCING EARTH AND SPACE SCIENCE

JGR Atmospheres

RESEARCH ARTICLE

10.1029/2022JD037612

Changes in Moisture Sources of Atmospheric Rivers Landfalling the Iberian Peninsula With WRF-FLEXPART

J. C. Fernández-Alvarez[1,2], A. Pérez-Alarcón[1,2], J. Eiras-Barca[1,3], A. M. Ramos[4,5], S. Rahimi-Esfarjani[6], R. Nieto[1], and L. Gimeno[1]

[1]Environmental Physics Laboratory (EPhysLab), Centro de Investigación Mariña, Universidade de Vigo, Ourense, Spain, [2]Departamento de Meteorología, Instituto Superior de Tecnologías y Ciencias Aplicadas, Universidad de La Habana, La Habana, Cuba, [3]Defense University Center, The Spanish Naval Academy, Marín, Spain, [4]Institute of Meteorology and Climate Research, Karlsruhe Institute of Technology, Karlsruhe, Germany, [5]Facultade de Ciências, Instituto Dom Luiz (IDL), Universidade de Lisboa, Lisbon, Portugal, [6]Department of Atmospheric and Oceanic Sciences, University of California, Los Angeles, La Jolla, CA, USA

Key Points:

- FLEXPART-WRF forced with CESM2 model has been able to reproduce the historical conditions of Atmospheric River over the Iberian Peninsula
- A northward shift of the main source regions is projected, notable in summer and fall and particularly by the end of the century
- Gradual strengthening in the intensity of Atmospheric Rivers is expected, observable from an increase in the amount of moisture transported

Supporting Information:

Supporting Information may be found in the online version of this article.

Correspondence to:

J. C. Fernández-Alvarez,
jose.carlos.fernandez.alvarez@uvigo.es

Citation:

Fernández-Alvarez, J. C., Pérez-Alarcón, A., Eiras-Barca, J., Ramos, A. M., Rahimi-Esfarjani, S., Nieto, R., & Gimeno, L. (2023). Changes in moisture sources of atmospheric rivers landfalling the Iberian Peninsula with WRF-FLEXPART. *Journal of Geophysical Research: Atmospheres*, *128*, e2022JD037612. https://doi.org/10.1029/2022JD037612

Received 5 AUG 2022
Accepted 11 APR 2023

Abstract This paper makes use of a combination of FLEXPART-WRF simulations forced with ERA5 and the CESM2 model—incorporated in the CMIP6 project—to infer a series of changes over the present century in the behavior of the landfalling atmospheric rivers (ARs) arriving to the Iberian Peninsula. In addition, future changes in the intensity and position of their main moisture sources are studied. In overall terms, there is a noticeable increase in the amount of moisture transported by ARs in the study region, particularly accentuated by the end of the century. However, no significant changes in the number of events are observed. A northward shift of both the mean position of the ARs as well as their main sources of moisture is also detected, particularly for the end of the century, and in the summer and fall months. In relation to the latter, an increase in the contribution of moisture contribution is also observed, quantitatively compatible with Clausius-Clapeyron amplification.

Plain Language Summary This paper makes use of a combination of simulations forced with reanalysis data and a climate model to infer a series of changes over the present century in the behavior of the landfalling atmospheric river—ARs, regions of intense moisture transport located in the lower layers of the atmosphere—arriving at the Iberian Peninsula. In addition, future changes in the intensity and position of their main moisture sources are studied. In overall terms, there is a noticeable increase in the amount of moisture transported by ARs in the study region, particularly accentuated by the end of the century. However, no significant changes in the number of events are observed. A northward shift of both the mean position of the ARs as well as their main sources of moisture is also detected, particularly for the end of the century, and in the summer and fall months. In relation to the latter, an increase in the contribution of moisture contribution is also observed, in a ratio similar to that expected.

1. Introduction

Atmospheric rivers (ARs) are usually defined as narrow corridors—longer than 2,000 km—of anomalous moisture content in the lower levels of the troposphere. They are well known for contributing to the meridional advection of water vapor and latent heat with about 90% of the net transport (Zhu & Newell, 1998). Even though ARs can exist under different meteorological patterns (Gimeno, Algarra, et al., 2021), archetypical ARs are associated with the prefrontal sectors of the storm tracks in the extratropical regions (Gimeno et al., 2014), carrying water intaked by local convergence (Dacre et al., 2015) and particularly by tropical moisture exports mechanism (TME) (e.g., Eiras-Barca et al., 2017; Hu & Dominguez, 2019; Ramos et al., 2016, and others).

ARs account for 20–30% of the total precipitation in southern Europe, particularly in fall and winter months (Eiras-Barca et al., 2021). Even though most ARs may be considered as "beneficial" (Ralph et al., 2019), these phenomena are also the trigger mechanisms of most of the extreme precipitation and flood events over the region in these months (e.g., Eiras-Barca et al., 2016; Ionita et al., 2020; Lavers et al., 2011; Lavers & Villarini, 2013). Thus, ARs are sometimes undeniably responsible for extensive property damage and loss of lives (Dominguez et al., 2018; Gimeno et al., 2016; Ramos et al., 2015).

10.1029/2022JD037612

According to Shukla et al. (2019), a notable increase in the global surface temperature is projected throughout the 21st century. The Clausius-Clapeyron amplification of 7% K^{-1} predicted for the increase in the water holding capacity of the atmosphere has also been projected for the increase in moisture that ARs will be able to carry (Algarra et al., 2020). In addition, it is becoming increasingly clear that the frequency and intensity of extreme precipitation events associated with ARs will be increasing at similar rates (e.g., Espinoza et al., 2018; Lavers & Villarini, 2015, and others). Therefore, there is sufficient evidence in the literature to suggest that as the amount of moisture in the atmosphere increases, its flux will also increase. With a high probability, ARs will tend to increase in intensity in the context of a warmer climate; with a subsequent increase in extreme precipitation events (Lavers et al., 2011). All this in a context of enhanced dynamics in terms of wind modulus (Sousa et al., 2020; Zhang et al., 2019) that will have an impact on human activity and ecosystems.

However, there has not yet been sufficient discussion of future changes in the position of moisture sources, which, by their nature, have the potential to completely modify the spatial distribution of the most active regions of ARs. Thus, albeit indirectly, a potential change in the patterns of moisture sources will lead to a change in the global conditions of meridional transport of energy in the form of latent heat; which will also need to be adequately captured in models that predict the dynamics and thermodynamics of future climate. In this regard, only Algarra et al. (2020) has carried out a global study showing that there has been an increase in anomalous moisture uptake over the period 1980–2017 in regions that are currently considered as moisture sources for ARs. On a regional scale and using water vapor tracing methods, the literature includes some studies such as the one developed by Sodemann and Stohl (2013). These studies show the variability of the sources in the face of different events and as the climate evolves. Additionally, at Nusbaumer and Noone (2018) the CAM5 model is used in combination with water vapor tracers and isotopes to analyze the variability of moisture sources associated with ARs impacting the West Coast of the USA. In general, these studies agree that in future years moisture is expected to be advected from more distant regions for both ARs and similar moisture transport phenomena.

In this regard, not only is the insufficient number of results obtained to date remarkable, but also the low spatial resolution of the findings. Increasing the resolution would provide a better perspective of the physicodynamic processes involved, which could be resolved on a regional scale. Thus, this paper analyzes the expected changes in both the position and relative importance of the different moisture sources feeding the landfalling ARs (LARs) arriving in the Iberian Peninsula under the Coupled Model Intercomparison Project Phase 6 (CMIP6) Socioeconomic Scenario Pathway 5-8.5 (ssp585). For this purpose, a dynamic downscaling methodology that combines the potential of the high-resolution Eulerian mesoscale model Weather Research and Forecast (WRF) with the Lagrangian particle dispersion model FLEXPART has been used. Three sets of simulations of 30 years each were run with WRF initialized with ERA5 or CESM2 as appropriate. Subsequently, these outputs were used to initialize the Lagrangian dispersion FLEXPART-WRF for the same period and to identify the moisture sources in the region of interest.

The area of interest for this study is the Iberian Peninsula, an area that is particularly active in the detection of LARs where they play a relevant role in the hydrological cycle (Eiras-Barca et al., 2021). Likewise, in this region, it has been demonstrated that the socioeconomic impacts of LARs are relevant (Pereira et al., 2016; Trigo et al., 2016; Zêzere et al., 2014).

Beyond presenting a single result of interest for the Iberian Peninsula, this study presents a new methodology that can be replicated in the future under other conditions and in other regions of interest. This methodology—although relatively expensive in computational terms—is reproducible and can provide relevant information to determine the nature of changes in the source regions of moisture associated with ARs and LARs at several locations around the world. This identification is essential for understanding and predicting the actual changes that will occur in these phenomena as well as in the precipitation associated with them.

2. Methods

The main idea of the methodology adopted in this work is as follows: the outputs of the CESM2 model (described below) integrated into the CMIP6 project have been used to initialize high-resolution simulations with the Eulerian mesoscale WRF model for both a historical and two future periods. Later, a detection of ARs located over the North Atlantic with a time-frequency of 6h has been carried out. For this purpose, an innovative methodology based on image analysis (IPART, as detailed in Section 2.3) has been applied. Subsequently, the results of

10.1029/2022JD037612

Table 1
Socioeconomic Scenario Pathways (SSP) and Periods Used in the Analysis

Abbrev.	Scenario	Period
HIST	Historical	1985–2014
MC	ssp585	2036–2065
EC	ssp585	2071–2100

Note. HIST: historical; MC: midcentury; EC: end-century.

these simulations have been used to identify all the LARs events reaching the Iberian Peninsula, and then to operate FLEXPART-WRF (Lagrangian dispersion model) to identify the moisture source regions associated with each of these events; both for the historical period and for the future. This methodology allows us to identify changes in the position and nature of these source regions when the historical and future periods are compared. Details of this methodology and the models used will be described below.

2.1. CESM2 Climate Model (Community Earth System Model Version 2)

Outputs from the Community Earth System Model V2 (CESM2, Danabasoglu et al., 2020) included in the sixth phase of the Coupled Model Intercomparison Project (CMIP6, O'Neill et al., 2016) were used to initialize the simulations. The data were downloaded from the Earth System Grid Federation (ESGF2) at a ≈1° horizontal resolution, and includes 32 vertical levels. Historical data for the period 1985–2014 and future data for midcentury (MC) and end-century (EC) under the ssp585 scenario were used as detailed in Table 1. As discussed in O'Neill et al. (2016), the ssp585 is considered as the "worst-case scenario," with sufficiently high emissions to produce a radiative forcing of 8.5 W m^{-2} which will amplify all signals detected in this analysis.

2.2. Mesoscale Simulations and Lagrangian Dispersions

The Weather Research and Forecast model v3.8.1 (WRF, Skamarock et al., 2019) was used not only to increase the spatial resolution of the simulations but also to lay the necessary basis for carrying out the subsequent Lagrangian particle dispersion. The first simulation was carried out for the HIST period initializing WRF with the fifth generation of the European Reanalysis (ERA5, Hersbach et al., 2020). The WRF simulations initialized with ERA5 (hereinafter referred to as WRF_ERA5) can be considered reliable and will be useful to evaluate the ability of CESM2 to correctly reproduce the atmospheric conditions over the historical period.

Three other sets of simulations were carried out initializing WRF with CESM2. Namely as WRF_CESM2 (HIST) for the historical period, WRF_CESM2 (MC) for midcentury and WRF_CESM2 (EC) for end-century as stated in Table 1. All the aforementioned simulations have been carried out under the same configuration conditions. They consider 40 vertical levels and a horizontal resolution of 20 km in both the simulations forced with ERA5 and CESM2. As for the domain of simulation, the whole North Atlantic Region was considered (115.39°W–42.02°E and 19.41°S–59.51°N, Figure S1 in Supporting Information S1). All simulations preserve time continuity over 30 years and a 1-month spin-up was used. The selected parametrizations were as follows: the WSM6 microphysics scheme (Hong et al., 2006), the Yonsei University PBL scheme (Hong & Lim, 2006), the revised MM5 surface layer scheme (Jiménez et al., 2012), the United Noah Land Surface Model (Tewari et al., 2004), the short and longwave RRTMG schemes (Iacono et al., 2008), and the Kain-Fritsch Ensemble cluster scheme (Kain, 2004). Additionally, a spectral nudging methodology has been applied on waves longer than 1,000 km to avoid the distortion of the large-scale circulation within the regional model domain. These distortions may appear due to the interaction between the model solutions and the boundary conditions (Miguez-Macho et al., 2004). The combination of these parametrizations with spectral nudging has been widely used and tested with very positive results (e.g., Insua-Costa et al., 2019; Insua-Costa & Miguez-Macho, 2018).

The FLEXPART-WRF v3.3.2 model (Brioude et al., 2013) uses the WRF outputs to trigger a Lagrangian dispersion of active moisture tracers—i.e., computational tracers with the ability to solve the mass balance at each iteration. In this case, the FLEXPART-WRF has been forced with WRF_CESM2 with a time step of 6h (FLEX_CESM2). The Hanna Scheme is used to solve the turbulence with convection scheme activated (Hanna, 1984). This parameterization addresses different boundary layer parameters, such as the PBL height, Monin-Obukhov length, convective velocity scale, roughness length and friction velocity (Brioude et al., 2013). FLEXPART-WRF simulations forced with CESM2 are fed with 2 million particles homogeneously distributed over the entire domain (40°E−100°W and 15°S–57°N, see Figure S1 in Supporting Information S1). Additionally, FLEXPART-WRF provides 40 vertical levels and 400 × 777 points available for particle release. The spatial and temporal resolutions

Journal of Geophysical Research: Atmospheres 10.1029/2022JD037612

of the outputs are 20 km and 6 hr, respectively. The particles move forward temporally throughout the period of interest, and a biased—rather than Gaussian—turbulence is assumed for them in the convective PBL.

Together with FLEX_CESM2, we conducted analogous simulations forcing FLEXPART-WRF with ERA5 instead of CESM2. This output (herein FLEX_ERA5) may be considered as "control" experiment. As proposed by Stohl and James (2004), at least one particle is guaranteed per point and vertical level. Additionally, the release of particles is also homogeneous in time, starting and ending with the simulation. To evaluate WRF_CESM2 and FLEX_CESM2 configurations; absolute errors (MAE), root mean square errors (RMSE), Pearson's correlations (R), and bias (B) statistics were obtained.

2.3. Detection of Atmospheric Rivers and Tracking of Moisture Sources

For the detection of atmospheric river events, the innovative Image-Processing-based Atmospheric River Tracking (IPART) method is used (Xu et al., 2020). This methodology applies thresholds to the natural spatiotemporal scale of ARs to achieve detection. Thus, the methodology is magnitude-independent and applicable to a Vertical Integrated Moisture Flux (IVT)-based detection. This method has been inspired by the image-processing by reconstruction (THR) technique (Vincent, 1993) and shows a low sensitivity to the choice of parameters that makes it less vulnerable to divergences between present and future climate. The IPART is fed with the IVT outputs in kg m^{-1} s^{-1} obtained from the zonal and meridional components of the water vapor flux, vertically integrated between the 300 and 1,000 hPa levels for both WRF-CESM2 and WRF-ERA5. Levels above 300 hPa have a negligible contribution to the IVT count (Ratna et al., 2016). Subsequently, the IVT fields are decomposed into background and anomaly components and ARs are detected for each time step. An analogous analysis has been carried out with CESM2 data for MC and EC. IPART must be configured with the selection of various detection parameters. The configuration used in this analysis is presented in Table S1 in Supporting Information S1.

With the detection of ARs carried out, LARs affecting the Iberian Peninsula are selected; and the moisture sources identification methodology starts for each period. Months from January to March (JFM), April to June (AMJ), July to September (JAS), and October to December (OND) were independently analyzed. Annual results (ANNUAL) are also provided. For this analysis, the "total AR cross-sectional moisture flux" variable provided by IPART is interpolated to the points considered in the target region at 00, 06, 12, and 18 UTC. If at least one of the considered points provides a nonzero value, the event is used in the subsequent methodology in order to identify its moisture source.

Active tracers dispersion methodology provided by FLEXPART-WRF is applied to each particle that is located over the target region during the detection of an event. The methodology used to identify moisture sources work as follows: changes in specific humidity q along the path described by each particle are estimated as detailed in Equation 1, where m is the mass of the particle and $e - p$ accounts for changes in q—either by evaporation or precipitation processes. Changes are analyzed every 6h.

$$e - p = m\left(\frac{dq}{dt}\right) \tag{1}$$

Once the described operation has been calculated for each individual trajectory of the particles, the total surface freshwater flux on each grid cell can be calculated by assuming the contribution of all trajectories which have traversed the grid area A at a given time (Stohl & James, 2005). The total budget "evaporation minus precipitation" is obtained as detailed in Equation 2, where N is the total number of particles k located over the grid area.

$$E - P = \frac{1}{A}\sum_{k=1}^{N}(e - p)_k \tag{2}$$

The residence time considered in this analysis for following the particles along their trajectory is 10 days (Gimeno, Eiras-Barca et al., 2021; Van Der Ent & Tuinenburg, 2017). Thus, $E - P$—which accounts for the average gains and losses of moisture of particles from day 1 to day 10—are calculated. $E > P$ regions are considered as moisture sources when analyzing particle backward trajectories. This methodology has been used in numerous studies, some of them recent (Cloux et al., 2021; Zhao, 2020). In any case, it should be noted that this methodology is not without limitations; in particular, an overestimation of evaporation and precipitation values associated mainly with nonphysical processes relevant to the phenomenology has been reported (Stohl & James, 2004).

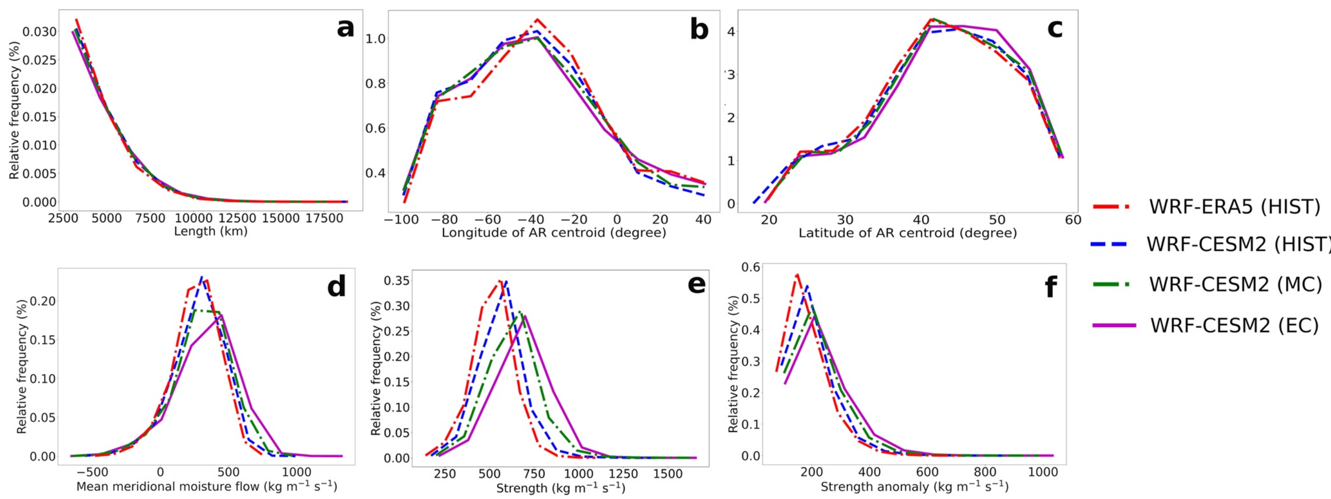

Figure 1. Probability density functions (PDFs) of Weather Research and Forecast (WRF) simulations considered in the analysis for different parameters of interest: (a) atmospheric river (AR) mean length, (b) longitude of AR centroid, (c) latitude of AR centroid, (d) mean meridional moisture flow, (e) AR strength, (f) AR strength anomaly. WRF-ERA5 (HIST) is shown in red dotted lines, WRF-CESM2 (HIST) is shown in blue dotted lines, WRF-CESM2 (MC) is shown in green dotted lines, and WRF-CESM2 (EC) shown in solid purple lines.

It is also noted that the FLEXPART progressively increases the uncertainty of particle trajectories with time (Stohl, 1998). That is, this methodology, although validated and widely used, should continue to be considered as approximation-based.

By choosing only particles (or air cells) implicated in Iberian LAR events, we are able to identify their sources for the desired combination of period, scenario, and simulation. The positive anomaly of the moisture sources is calculated and named anomalous moisture uptake (AMU) following the formalism proposed by Algarra et al. (2020). The AMU is calculated as the difference of the value of the integrated moisture sources $E - P > 0$ for the days with LARs at each grid point and the climatological value of $E - P > 0$ corresponding to that grid point. The climatology for each grid point was calculated as the average for the 30 years of either the seasonal or annual $E - P > 0$ values, regardless of whether a LAR is detected. Finally, the TRansport Of water VApor software (TROVA, Fernández-Alvarez et al., 2022) is used to process the results.

3. Results and Discussion

3.1. North Atlantic ARs Characteristics and Variability

The representation of the characteristics of the ARs and the variability was evaluated considering parameters of structure, intensity, and position of the ARs with probability density functions. Figure 1 and Figure S2 in Supporting Information S1 show the probability density functions (PDFs) of different parameters of interest for ARs landfalling the Iberian Peninsula under all combinations of WRF scenario plus forcings considered in the analysis. WRF-ERA5 (HIST) in red dotted lines and WRF-CESM (HIST) in blue dotted lines are both evaluated under the historical period, forcing WRF with ERA5 in the former and with CESM in the latter. Thus, they are expected to yield similar results if CESM was able to properly reproduce historical conditions. This is actually, in general terms, the result except for the strength (Figure 1e)—where WRF-CESM2 tends to overestimate the integrated water transport in kg m^{-1} s^{-1} when compared to WRF-ERA5—and strength anomaly (Figure 1f) where same conclusions can be obtained.

WRF-CESM2 (MC) in dotted green lines and WRF-CESM2 (EC) in solid purple lines account for the PDFs of WRF simulations forced with CESM in midcentury and end-century years, respectively. These distributions may be compared with WRF-CESM (HIST) to infer changes in the future with respect to the present years. On the whole, a northward displacement of the position of the AR centroids may be expected by the end of the century (Figure 1c). Additionally, a progressive strengthening (Figures 1e and 1f) of the LARs is expected throughout the century according to these results, showing the peak of the distribution of IVT at 750 kg m^{-1} s^{-1} for EC while for the historical period it is close to 500 kg m^{-1} s^{-1}. This progressive reinforcement strengthens the conclusions

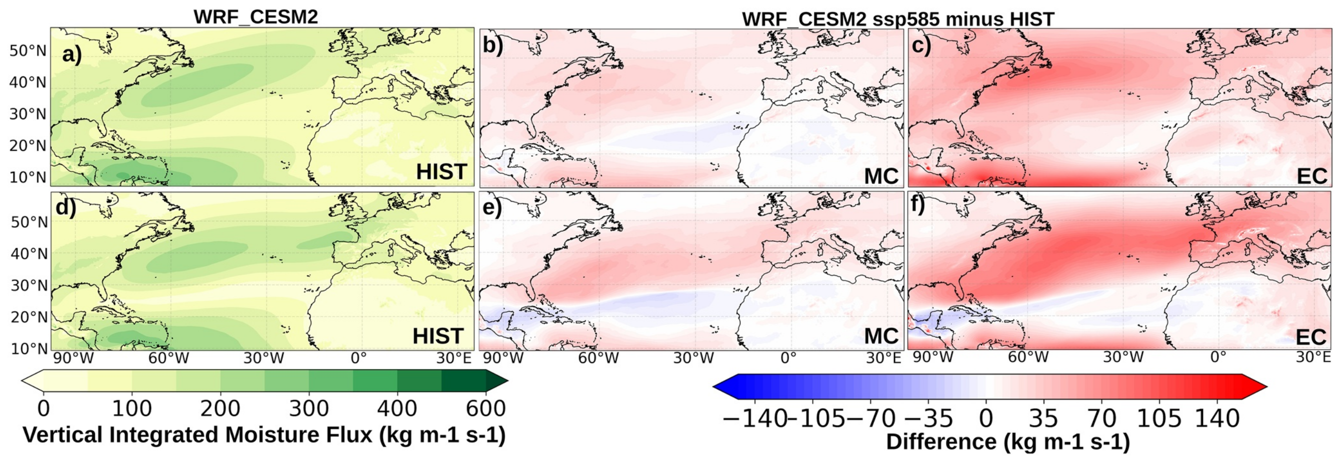

Figure 2. (a) Mean Integrated Moisture Flux (IVT) fields for the historical period. (b) Mean differences in the IVT fields between midcentury (MC) and historical (HIST) periods. (c) Mean differences in the IVT fields EC-Historical. Second row: same as the first row but considering days with landfalling AR (LAR) detection (d–f).

obtained by other studies in recent years. There seems to be a clear consensus that future ARs are expected to be more intense than current ARs in terms of moisture flux (e.g., Zhao, 2020). In addition, it is projected that the mean meridional moisture flux (Figure 1d) for EC will increase with values ranging between 500 and 1,000 kg m^{-1} s^{-1}. However, ARs are projected to be slightly smaller in length for MC and EC (Figure 1a). For the remaining parameters, the changes observed are less significant.

The results presented in Figure 1 project an overall increase in the strength of the ARs for the future. To provide a visual interpretation of this result, Figure 2 shows the mean IVT fields for the historical period and the differences between this and the MC and EC periods for both the climatology as a whole (Figures 2a–2c) and only for the days in which a LAR has been detected over the Iberian Peninsula (Figures 2d–2f). The figure clearly shows an increase in advective dynamics for the future; particularly noticeable in EC and particularly noticeable on LAR days. The strengthening of the ARs presented in Figure 1 is therefore fully compatible with the strengthening of the moisture transport fields observed in Figure 2, where it is also clearly observed that this is particularly intense in the corridors linking the Iberian Peninsula with its moisture sources on LAR days.

Figure 3 shows frequencies of occurrence of AR events—i.e., the relative amount of time steps where the algorithm detected an AR event for each grip point with regard to the total number of time steps considered for the whole period in annual terms—as well as some relevant differences in these frequencies for certain simulations. Particularly, Figure 3a shows the frequency of occurrence in WRF_CESM for the HIST simulation and Figure 3b shows the differences in these frequencies between the former and WRF forced with ERA5. If the degree of coincidence between ERA5 and CESM2 were absolute, no difference should be observed, since both simulations cover the same period. This is not the case, since CESM2 is not expected to reproduce the historical period as accurately as ERA5, but the differences are small and less than 4.5% in all regions, with an overestimation by CESM2 on the eastern U.S. and an underestimation by CESM2 on the North Atlantic corridor. Figures S3a and S3d in Supporting Information S1 provide statistical significance to the differences presented between WRF-CESM2 and WRF-ERA5 for the historical period, highlighting regions that are different in a significant manner with a *t* test significance of 95% and 99%, respectively. It is observed that, in any case, none of the relevant regions for the Iberian Peninsula present statistically significant differences between both sources. Considering, therefore, that this bias between WRF-CESM2 and WRF-ERA5 does not significantly affect the results presented in this manuscript, we do note that it should be taken into account in similar studies that focus on regions such as the east coast of the USA and, to a lesser extent, on the Mediterranean Sea.

Figure 3c shows the frequencies of occurrence of AR events in WRF_CESM2 simulation throughout the MC period, and Figure 3d the differences of the former with the historical period under the same conditions of the simulation. Analogously, Figures 3e and 3f show the same information for the EC period. Two main conclusions can be drawn from these results: on the one hand, it is observed that the pattern of differences is very similar for both periods in structure, but the increases are more marked for EC. On the other hand, there is a clear northward

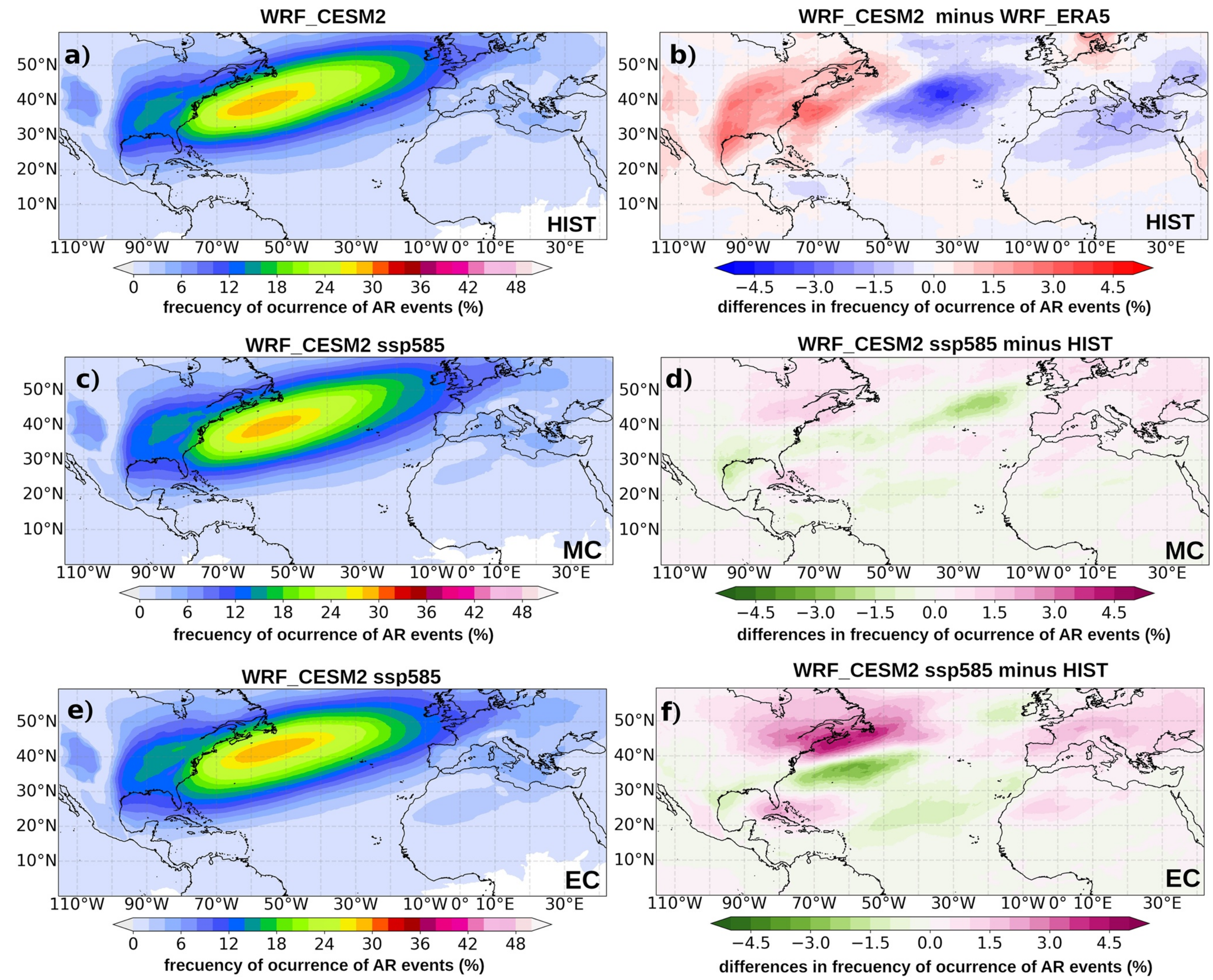

Figure 3. (a) Frequency of occurrence of atmospheric river (AR) events (in % of time steps where an AR has been detected by the Image-Processing-based Atmospheric River Tracking (IPART) out of the total) calculated considering the annual period for WRF_CESM2 (HIST). (b) Differences in frequency of AR events between WRF_CESM2 (HIST) and WRF_ERA5. (c) Same as (a) but for WRF_CESM2 (MC). (d) Differences in frequency of occurrence between WRF_CESM2 (MC) and WRF_CESM2 (HIST). (e) Same as (a) but for WRF_CESM2 (EC). (f) Differences in frequency of occurrence between WRF_CESM2 (EC) and WRF_CESM2 (HIST).

shift in the region of AR activity for the Atlantic coasts of the USA. This shift is particularly marked in EC and may be associated with the poleward shift of the annual mean position of the projected storm track in a warmer climate that has been detected in several generations of coupled climate simulations (Kidston & Gerber, 2010; Miller et al., 2006; Yin, 2005). On the European shores, a certain displacement is also observed, much less marked and in the opposite direction to that observed on the American shores.

In order to add statistical value to the results presented so far, Figure S3 in Supporting Information S1 shows in its second and third columns the points that present statistically significant differences between the time series of the historical period and MC and between the time series of the historical period and EC, respectively. The statistical test used is a *t* test with 95% and 99% significance in the first and second row, respectively. In general, it is observed that for MC the statistically significant differences are restricted to certain tropical regions and to Eastern Europe; as well as to the northwest of the Iberian Peninsula and Northern Italy. In the case of EC, the areas with statistically significant differences increase notably, highlighting a large extension in North America and most of Europe, as well as all of the north of the Iberian Peninsula.

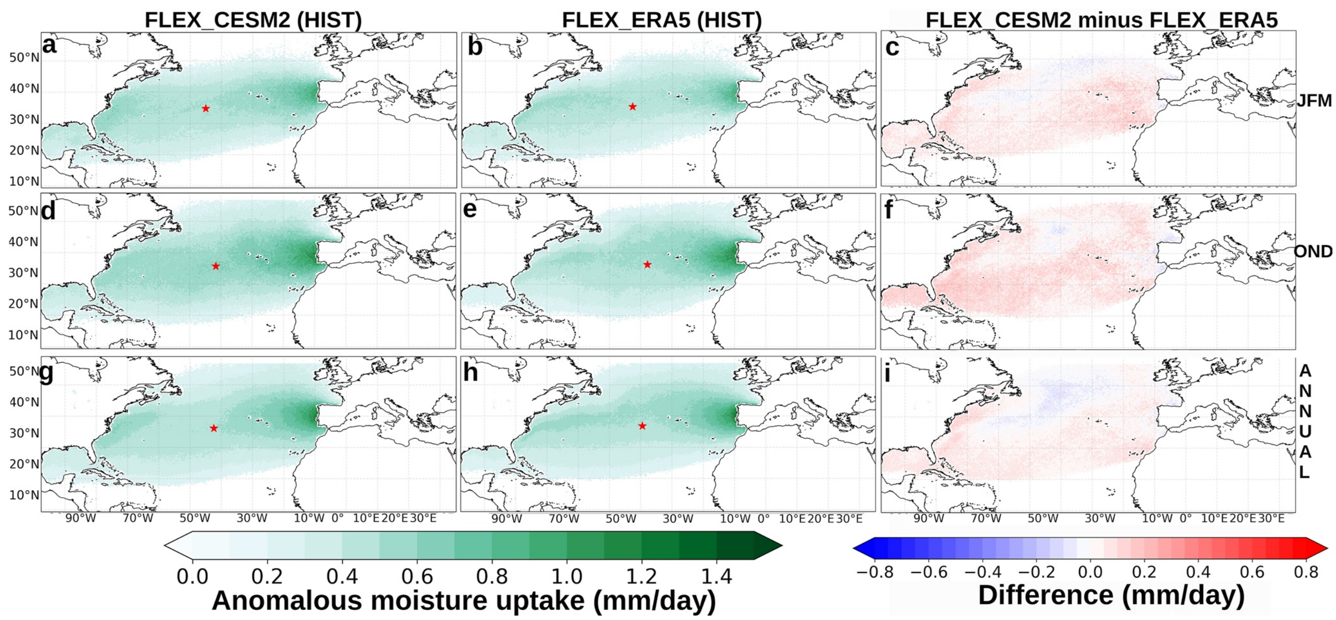

Figure 4. Anomalous moisture uptake (AMU) for FLEX_CESM2 (HIST), FLEX_ERA5 (HIST), and their differences in the first, second, and third columns, respectively. Results are shown for January to March (JFM, a–c), October to December (OND, d–f), and Annual results (ANNUAL, g–i) seasons. Weighted centroids of the AMU patterns are labeled with a red star.

Table S2 in Supporting Information S1 presents statistics of detections of both ARs over the whole domain and LARs over the Iberian Peninsula. It also shows the mean position of the centroid of ARs activity. In this table, it can also be seen how is expected an increase neither in the detections of ARs nor in the detections of LARs—which do not vary significantly between EC and HIST periods—but a displacement of approximately one degree northward in the position of the centroid of activity. This shift is especially marked in JAS, exceeding two degrees of latitude, and practically imperceptible in JFM. That is, most of the observable signal in Figure 3f is attributable to the summer monPerfeths.

3.2. Moisture Sources of Iberian LARs

3.2.1. Moisture Sources Over the Historical Period

Figures S4 and S5 in Supporting Information S1 show the climatology for the moisture sources for the ARs events as described in Section 2.3. These plots have been calculated taking into account all Iberian LAR events for the different periods considered in this analysis using FLEX_CESM2 and FLEX_ERA5 simulations. Specifically, the AMU fields—as detailed in Section 2.3—are shown in Figure 4 and Figure S6 in Supporting Information S1 for the historical simulations on JFM, AMJ, JAS, OND, and ANNUAL separately. These results provide us with a new indicator of the degree of adequacy between the simulations performed with FLEX_CESM2 (HIST) and FLEX_ERA5 (HIST).

The most relevant statistical variables are summarized in Table S3 in Supporting Information S1. In particular, it was found that the value of the value of the Pearson's correlation coefficient R varies in the range of 0.90–0.97, denoting a high temporal correlation between both simulations; mean absolute errors (MAE) ranges from 0.04 to 0.08 mm day^{-1} depending on the season, this in relative terms is a value close to 5% compared to the maximum $E - P > 0$ values, which can be considered relatively low. The same is true for the root mean square error (RMSE), which yields values within the range of 0.05–0.12 mm day^{-1}. The BIAS of the AMU patterns shows discrepancies of about 0.01–0.03 mm day^{-1} when they are compared.

On the other hand, Figure 4 and Figure S6 in Supporting Information S1 show the spatial differences between FLEX_CESM2 and FLEX_ERA5 for the historical period. There is a tendency for FLEX_CESM2 to overestimate the AMU in the central Atlantic and Caribbean Sea regions, although with values below 0.4 mm/day in annual terms throughout the region (Figure 4i).

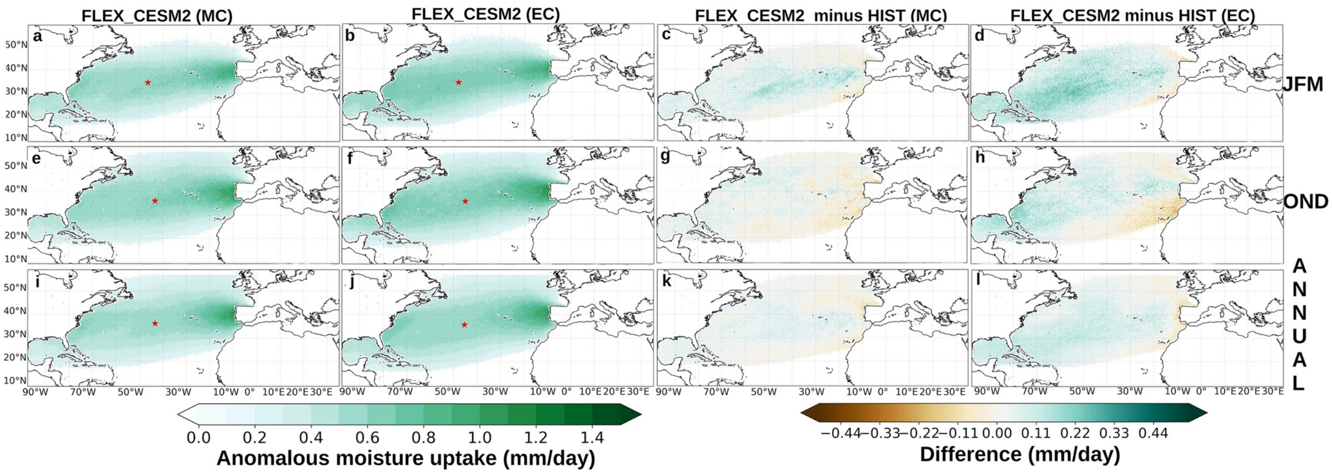

Figure 5. Anomalous moisture uptake for FLEX_CESM2 (midcentury and end-century) and their differences with regard to the historical simulation in the first, second, third, and fourth columns, respectively. Results are shown for January to March (JFM, a–d), October to December (OND, e–h), and Annual results (ANNUAL, i–l) seasons, located in the different rows. Weighted centroids of the anomalous moisture uptake (AMU) patterns are labeled with a red star.

Thus, the results presented in the previous paragraphs show that the representation by FLEX_CESM2 (HIST) for both the moisture sources ($E - P > 0$) and the AMU pattern is realistic when compared to FLEX_ERA5 (HIST). Finally, a relevant feature to compare are the weighted centroids of the AMU patterns. The representation of these centroids allows to analyze the mean positions of the pattern both in present and future climate. These are represented with a red star in Figures 4a, 4b, 4d, 4e, 4g, 4h and Figures S6a, S6b, S6d, S6e, S6g, S6h in Supporting Information S1. Overall, it is observed that the positions are very similar between FLEX_CESM2 (HIST) and FLEX_ERA5 (HIST) for each of the seasons, which is a further indication of the degree of similarity between the two simulations.

3.2.2. Projected Changes in the Moisture Sources

The first two columns in Figure 5 and Figure S7 in Supporting Information S1 show the same results shown in Figure 4 and Figure S6 in Supporting Information S1, but with FLEX_CESM2 for the ssp585 scenario in MC and EC, respectively. The last two columns of these figures show the differences between these simulations and the historical period. It is precisely these last two columns that provide the projections in the foreseeable changes in intensity and position of the source regions where the LARs that affect the Iberian Peninsula would take up moisture anomalously in the medium and long term. In general terms, a gradual increase in the AMU is observed, as well as a northward shift of the regions that act as main sources associated with Iberian LARs. Specifically, Figure 5 shows the expected changes for JFM, OND, and ANNUAL seasons. Figures 5c, 5g, and 5k correspond to MC where an increase is expected above 20°N and located mainly in the central North Atlantic. The opposite is mainly true below 20°N where a slight decrease is expected. For EC, the change pattern signal intensifies with higher values in winter, where the highest anomalous moisture uptakes would be located over the Central and Western Atlantic, the Caribbean Sea, and the Gulf of Mexico. However, for the autumn, the sources are expected to be farther apart because the maximum changes are expected close to the Atlantic coast of the United States. In the annual means, the pattern is very similar but smoother with respect to these seasons. Essentially, a region of lower latitude decrease and upper latitude increase is always observed, which is a robust signal of climate change. For spring, a generally more noticeable decrease is projected for the region between 10°W and 30°W, being of greater intensity for EC (see Figures S7c and S7d in Supporting Information S1). In summer, the increase is mainly projected above 40°N, for source regions located close to the IP (see Figures S7g and S7h in Supporting Information S1). On the other hand, a pattern of moisture sources associated with ARs (Figures S4 and S5 in Supporting Information S1) that is longer in length and organized latitudinally is projected for future periods.

Therefore, in general terms, what is observed is, on the one hand, a reinforcement of the AMU, and on the other hand, a displacement of the AMU toward more southern latitudes. Both signals are particularly clear in the winter months (with an increase of 9% and 24% by MC and EC, respectively) compared to spring months (with an increase of barely 2% for MC and 9% by EC). Particularly noteworthy is the case of summer, showing an increase

Table 2
Projected Seasonal Changes (%) in AMU for MC and EC With Respect to the Historical Patterns

	JFM	AMJ	JAS	OND	ANNUAL
MC	9 (4.5)	2 (1)	17 (8)	3 (1.5)	6 (3)
EC	24 (6)	9 (2.3)	22 (5.5)	9 (2.3)	12 (3)

Note. In parentheses, the percentage change for each degree of temperature that increases for MC and EC under the ssp585 scenario (% K^{-1}).

in the range of 17–22% for MC and EC in the regions with anomalous moisture uptake (see Table 2). These results strengthen the conclusions obtained by the previous studies which state that the contribution of moisture from the sources will increase progressively following a ratio similar to that predicted by the Clausius-Clapeyron amplification of 7% K^{-1} for the maximum amount of moisture that an air cell can contain (Algarra et al., 2020; Bao et al., 2017; Prein et al., 2017). As stated in Table 2, this is particularly observable in winter and summer and is not so clearly evident in the transition months. It is important to note that this increase in the amount of moisture contained in the cells may lead to an increase in precipitation in extreme events, particularly when the orographic and thermodynamic conditions are propitious for it (Algarra et al., 2020; Eiras-Barca et al., 2016, and references therein).

The aforementioned northward shift of the main sources of moisture causes relevant changes in this respect in different regions of the North Atlantic that are worth mentioning. The most significant variations in the position patterns of AMU associated with the Iberian LAR occur in the Central and Western regions of the North Atlantic and in summer in the Cantabrian Sea. Based on these results, the archetypal contribution of moisture from the Gulf of Mexico is expected to be less important throughout the century, as it is gained by the northernmost regions where AMU maxima are located. This behavior is observed in Figure S8 in Supporting Information S1 with the latitudinal displacement of the weighted centroids for the AMU, particularly notable in summer and fall. In the case of winter and annually, a shift of the moisture sources to the west seems to predominate. These displacement results may be associated with the fact that for the future is expected a global increase in water vapor residence time of 3%–6% K^{-1}, lengthening the distance traveled between evaporation and precipitation (Gimeno, Eiras-Barca et al., 2021). Finally, Figure S9 in Supporting Information S1 plots the position of AMU centroids, showing that the greatest displacement to be expected throughout the century is westward in winter months and northward in summer months.

Finally, Figures S10 and S11 in Supporting Information S1 show a statistical significance analysis analogous to those shown so far, but for the AMU both in the form of seasonal and annual means. In summary, it is observed that in winter, autumn and in annual terms, the Gulf of Mexico, western and central Atlantic regions stand out—both for 95% significance and 99% significance—. These statistically significant differences with respect to the historical series are observed for both MC and EC, although they continue to be more accentuated for the latter.

3.3. Limitations and Uncertainties

The limitations and uncertainties associated with this study are mainly related to being restricted to the ssp585 scenario for model forcing. This scenario assumes a development absolutely based on fossil energies that trigger a forcing level of 8.5 W m^{-2}. This scenario is the most pessimistic of all those considered in the CMIP6 and is therefore not the most likely. However, it amplifies the signals and allows us to clearly detect behaviors that in other scenarios, although occurring, would go unnoticed. In any case, it is important to bear in mind that the actual changes will depend on the scenario that finally occurs, and that the real behavior of the projected changes will probably occur with less strength than described in the preceding paragraphs.

Additionally, the detection of ARs (IPART) is dependent on a subjective selection of parameters. These have been selected on the basis of all the literature written on ARs and the researchers' own experience. However, an alternative selection of these parameters would also lead to slightly different results. In addition, the IPART method is sensitive in the interplay between candidate region detection and the subsequent geometric filtering (Xu et al., 2020).

4. Conclusions

Throughout this study, we have made use of a set of simulations that have allowed us to obtain a series of conclusions related to the expected changes in the intensity and position of the main sources of moisture associated with landfalling atmospheric river events over the Iberian Peninsula. First, we conclude that FLEXPART-WRF forced with the CESM2 model included in CMIP6 has been able to reproduce the historical conditions of atmospheric river detection over the Atlantic margin of the Iberian Peninsula. This conclusion has been obtained by comparing its results with those provided by FLEXPART-WRF forced with ERA5, and finding a high degree of similarity between both. However, there is a westward bias in the frequency of ARs for WRF-CESM2 that—while not significantly affecting the results of this study—could influence the results when analyzing activity involving the east coast of the USA.

Then—and once it was assumed that the FLEXPART-WRF plus CESM2 combination is reliable in relation to the detection of moisture sources—a comparison was made between 30 years of the historical period, 30 years of a midcentury period and 30 years of an end-of-century period assuming the ssp585 scenario. This procedure has allowed inferring the projection of the expected changes in both the strength and distribution of the aforementioned sources.

The most relevant conclusions that this study has obtained in regard to the foreseeable changes that the sources of moisture associated with atmospheric river events over the peninsula will undergo are the following: first, a progressive strengthening of the intensity of the atmospheric rivers reaching the Iberian Peninsula is to be expected, mainly in terms of moisture content, as has been described in the literature previously. Second, a northward shift of the mean position of the AR centroids is also observed, an outcome that has also been predicted by the literature. Third, and in relation to the sources of moisture associated with these events, a progressive increase in the contribution of moisture from the main sources is observed, as well as a northward displacement of these sources—which will result in a relative loss of importance in critical regions for moisture supply, such as the Gulf of México—mainly in the summer and fall months. In addition, a statistical significance of 99% is observed in these changes in moisture sources with respect to the historical period. Finally, it is observed that the increase in moisture input coincides with the values predicted by Clausius-Clapeyron amplification.

Data Availability Statement

The data sets used in this study are freely available on the internet. ERA5 reanalysis data (Hersbach et al., 2020) and CESM2 model outputs (Danabasoglu et al., 2020) are used for the initial and boundary conditions of the WRF-ARW model. In addition, a description of the WRF-ARW model can be consulted in Skamarock et al. (2019) and for FLEXPART-WRF in Brioude et al. (2013). Finally, Image-Processing-based Atmospheric River Tracking (IPART) method (Xu et al., 2020) and TROVA software (Fernández-Alvarez et al., 2022) are used.

Acknowledgments

J. C. Fernández-Alvarez acknowledges the support from the Xunta de Galicia under Grant ED481A-2020/193. A. Pérez-Alarcón acknowledges the PhD Grant from the University of Vigo. J. Eiras-Barca thanks the Defense University Center at the Spanish Naval Academy (CUD-ENM) for the support provided for this research. A.M.R was supported by the Helmholtz "Changing Earth" program. This work is supported by the SETESTRELO project (Grant PID2021-122314OB-I00) funded by the Ministerio de Ciencia, Innovación y Universidades, Spain. Partial support was also obtained from the Xunta de Galicia under Project ED431 C 2021/44 (Programa de Consolidación e Estructuración de Unidades de Investigació Competitivas (Grupos de Referencia Competitiva) and Consellería de Cultura, Educación e Universidade). In addition, this work has been possible thanks to the computing resources and technical support provided by CESGA (Centro de Supercomputación de Galicia) and Red Española de Supercomputación (RES) (AECT-2022-3-0009 and DATA-2021-1-0005). Funding for open access charge: Universidade de Vigo/CISUG.

References

Algarra, I., Nieto, R., Ramos, A. M., Eiras-Barca, J., Trigo, R. M., & Gimeno, L. (2020). Significant increase of global anomalous moisture uptake feeding landfalling atmospheric rivers. *Nature Communications*, *11*(1), 1–7. https://doi.org/10.1038/s41467-020-18876-w

Bao, J., Sherwood, S. C., Alexander, L. V., & Evans, J. P. (2017). Future increases in extreme precipitation exceed observed scaling rates. *Nature Climate Change*, *7*(2), 128–132. https://doi.org/10.1038/nclimate3201

Brioude, J., Arnold, D., Stohl, A., Cassiani, M., Morton, D., Seibert, P., et al. (2013). The Lagrangian particle dispersion model FLEXPART-WRF version 3.1 [software]. Geoscientific Model Development, *6*(6), 1889–1904. https://doi.org/10.5194/gmd-6-1889-2013

Cloux, S., Garaboa-Paz, D., Insua-Costa, D., Miguez-Macho, G., & Pérez-Muñuzuri, V. (2021). Extreme precipitation events in the mediterranean area: Contrasting two different models for moisture source identification. *Hydrology and Earth System Sciences*, *25*(12), 6465–6477. https://doi.org/10.5194/hess-25-6465-2021

Dacre, H. F., Clark, P. A., Martinez-Alvarado, O., Stringer, M. A., & Lavers, D. A. (2015). How do atmospheric rivers form? *Bulletin of the American Meteorological Society*, *96*(8), 1243–1255. https://doi.org/10.1175/BAMS-D-14-00031.1

Danabasoglu, G., Lamarque, J.-F., Bacmeister, J., Bailey, D., DuVivier, A., Edwards, J., et al. (2020). The community Earth system model version 2 (cesm2) [Dataset]. Journal of Advances in Modeling Earth Systems, *12*, e2019MS001916. https://doi.org/10.1029/2019MS001916

Dominguez, F., Dall'Erba, S., Huang, S., Avelino, A., Mehran, A., Hu, H., et al. (2018). Tracking an atmospheric river in a warmer climate: From water vapor to economic impacts. *Earth System Dynamics*, *9*(1), 249–266. https://doi.org/10.5194/esd-9-249-2018

Eiras-Barca, J., Brands, S., & Miguez-Macho, G. (2016). Seasonal variations in north Atlantic atmospheric river activity and associations with anomalous precipitation over the iberian atlantic margin. *Journal of Geophysical Research: Atmospheres*, *121*, 931–948. https://doi.org/10.1002/2015JD023379

Eiras-Barca, J., Dominguez, F., Hu, H., Garaboa-Paz, D., & Miguez-Macho, G. (2017). Evaluation of the moisture sources in two extreme landfalling atmospheric river events using an Eulerian WRF tracers tool. *Earth System Dynamics*, *8*(4), 1247–1261. https://doi.org/10.5194/esd-8-1247-2017

Eiras-Barca, J., Ramos, A. M., Algarra, I., Vázquez, M., Dominguez, F., Miguez-Macho, G., et al. (2021). European West Coast atmospheric rivers: A scale to characterize strength and impacts. *Weather and Climate Extremes*, *31*, 100305. https://doi.org/10.1016/j.wace.2021.100305

Espinoza, V., Waliser, D. E., Guan, B., Lavers, D. A., & Ralph, F. M. (2018). Global analysis of climate change projection effects on atmospheric rivers. *Geophysical Research Letters*, *45*, 4299–4308. https://doi.org/10.1029/2017GL076968

Pérez-Alarcón, A., Nieto, R., & Gimeno, L. (2022). Trova: Transport of water vapor [software]. SoftwareX, *20*, 101228. https://doi.org/10.1016/j.softx.2022.101228

Gimeno, L., Algarra, I., Eiras-Barca, J., Ramos, A. M., & Nieto, R. (2021a). Atmospheric river, a term encompassing different meteorological patterns. *Wiley Interdisciplinary Reviews: Water*, *8*(6), e1558. https://doi.org/10.1002/wat2.1558

Gimeno, L., Dominguez, F., Nieto, R., Trigo, R., Drumond, A., Reason, C. J., et al. (2016). Major mechanisms of atmospheric moisture transport and their role in extreme precipitation events. *Annual Review of Environment and Resources*, *41*(1), 117–141. https://doi.org/10.1146/annurev-environ-110615-085558

Gimeno, L., Eiras-Barca, J., Durán-Quesada, A. M., Dominguez, F., van der Ent, R., Sodemann, H., et al. (2021b). The residence time of water vapour in the atmosphere. *Nature Reviews Earth & Environment*, *2*(8), 558–569. https://doi.org/10.1038/s43017-021-00181-9

Gimeno, L., Nieto, R., Vázquez, M., & Lavers, D. A. (2014). Atmospheric rivers: A mini-review. *Frontiers of Earth Science*, *2*. https://doi.org/10.3389/feart.2014.00002

Hanna, S. (1984). Applications in air pollution modeling. In *Atmospheric turbulence and air pollution modelling* (pp. 275–310). Springer.

Hersbach, H., Bell, B., Berrisford, P., Hirahara, S., Horányi, A., Muñoz-Sabater, J., et al. (2020). The era5 global reanalysis [Dataset]. Quarterly Journal of the Royal Meteorological Society, *146*(730), 1999–2049. https://doi.org/10.1002/qj.3803

Hong, S.-Y., & Lim, J.-O. J. (2006). The WRF single-moment 6-class microphysics scheme (wsm6). *Asia-Pacific Journal of Atmospheric Sciences*, *42*(2), 129–151.

Hong, S.-Y., Noh, Y., & Dudhia, J. (2006). A new vertical diffusion package with an explicit treatment of entrainment processes. *Monthly Weather Review*, *134*(9), 2318–2341. https://doi.org/10.1175/mwr3199.1

Hu, H., & Dominguez, F. (2019). Understanding the role of tropical moisture in atmospheric rivers. *Journal of Geophysical Research: Atmospheres*, *124*, 13826–13842. https://doi.org/10.1029/2019JD030867

Iacono, M. J., Delamere, J. S., Mlawer, E. J., Shephard, M. W., Clough, S. A., & Collins, W. D. (2008). Radiative forcing by long-lived greenhouse gases: Calculations with the AER radiative transfer models. *Journal of Geophysical Research*, *113*, D13103. https://doi.org/10.1029/2008JD009944

Insua-Costa, D., & Miguez-Macho, G. (2018). A new moisture tagging capability in the weather research and forecasting model: Formulation, validation and application to the 2014 great lake-effect snowstorm. *Earth System Dynamics*, *9*(1), 167–185. https://doi.org/10.5194/esd-9-167-2018

Insua-Costa, D., Miguez-Macho, G., & Llasat, M. C. (2019). Local and remote moisture sources for extreme precipitation: A study of the two catastrophic 1982 Western Mediterranean episodes. *Hydrology and Earth System Sciences*, *23*(9), 3885–3900. https://doi.org/10.5194/hess-23-3885-2019

Ionita, M., Nagavciuc, V., & Guan, B. (2020). Rivers in the sky, flooding on the ground: The role of atmospheric rivers in inland flooding in central Europe. *Hydrology and Earth System Sciences*, *24*(11), 5125–5147. https://doi.org/10.5194/hess-24-5125-2020

Jiménez, P. A., Dudhia, J., González-Rouco, J. F., Navarro, J., Montávez, J. P., & García-Bustamante, E. (2012). A revised scheme for the WRF surface layer formulation. *Monthly Weather Review*, *140*(3), 898–918. https://doi.org/10.1175/mwr-d-11-00056.1

Kain, J. S. (2004). The Kain-Fritsch convective parameterization: An update. *Journal of Applied Meteorology*, *43*(1), 170–181. https://doi.org/10.1175/1520-0450(2004)043<0170:TKCPAU>2.0.CO;2

Kidston, J., & Gerber, E. (2010). Intermodel variability of the poleward shift of the austral jet stream in the CMIP3 integrations linked to biases in 20th century climatology. *Geophysical Research Letters*, *37*, L09708. https://doi.org/10.1029/2010GL042873

Lavers, D. A., Allan, R. P., Wood, E. F., Villarini, G., Brayshaw, D. J., & Wade, A. J. (2011). Winter floods in Britain are connected to atmospheric rivers. *Geophysical Research Letters*, *38*, L23803. https://doi.org/10.1029/2011GL049783

Lavers, D. A., & Villarini, G. (2013). The nexus between atmospheric rivers and extreme precipitation across Europe. *Geophysical Research Letters*, *40*, 3259–3264. https://doi.org/10.1002/grl.50636

Lavers, D. A., & Villarini, G. (2015). The contribution of atmospheric rivers to precipitation in Europe and the United States. *Journal of Hydrology*, *522*, 382–390. https://doi.org/10.1016/j.jhydrol.2014.12.010

Miguez-Macho, G., Stenchikov, G. L., & Robock, A. (2004). Spectral nudging to eliminate the effects of domain position and geometry in regional climate model simulations. *Journal of Geophysical Research*, *109*(D13), 1097. https://doi.org/10.1029/2003JD004495

Miller, R., Schmidt, G., & Shindell, D. (2006). Forced annular variations in the 20th century intergovernmental panel on climate change fourth assessment report models. *Journal of Geophysical Research*, *111*, D18101. https://doi.org/10.1029/2005JD006323

Nusbaumer, J., & Noone, D. (2018). Numerical evaluation of the modern and future origins of atmospheric river moisture over the west coast of the United States. *Journal of Geophysical Research: Atmospheres*, *123*, 6423–6442. https://doi.org/10.1029/2017JD028081

O'Neill, B. C., Tebaldi, C., Van Vuuren, D. P., Eyring, V., Friedlingstein, P., Hurtt, G., et al. (2016). The scenario model intercomparison project (ScenarioMip) for cmip6. *Geoscientific Model Development*, *9*(9), 3461–3482. https://doi.org/10.5194/gmd-9-3461-2016

Pereira, S., Ramos, A. M., Zêzere, J. L., Trigo, R. M., & Vaquero, J. (2016). Spatial impact and triggering conditions of the exceptional hydro-geomorphological event of December 1909 in Iberia. *Natural Hazards and Earth System Sciences*, *16*(2), 371–390. https://doi.org/10.5194/nhess-16-371-2016

Prein, A. F., Liu, C., Ikeda, K., Trier, S. B., Rasmussen, R. M., Holland, G. J., & Clark, M. P. (2017). Increased rainfall volume from future convective storms in the us. *Nature Climate Change*, *7*(12), 880–884. https://doi.org/10.1038/s41558-017-0007-7

Ralph, F. M., Rutz, J. J., Cordeira, J. M., Dettinger, M., Anderson, M., Reynolds, D., et al. (2019). A scale to characterize the strength and impacts of atmospheric rivers. *Bulletin of the American Meteorological Society*, *100*(2), 269–289. https://doi.org/10.1175/BAMS-D-18-0023.1

Ramos, A. M., Nieto, R., Tomé, R., Gimeno, L., Trigo, R. M., Liberato, M. L., & Lavers, D. A. (2016). Atmospheric rivers moisture sources from a Lagrangian perspective. *Earth System Dynamics*, *7*(2), 371–384. https://doi.org/10.5194/esd-7-371-2016

Ramos, A. M., Trigo, R. M., Liberato, M. L., & Tomé, R. (2015). Daily precipitation extreme events in the iberian peninsula and its association with atmospheric rivers. *Journal of Hydrometeorology*, *16*(2), 579–597. https://doi.org/10.1175/JHM-D-14-0103.1

Ratna, S. B., Cherchi, A., Joseph, P., Behera, S., Abish, B., & Masina, S. (2016). Moisture variability over the indo-pacific region and its influence on the indian summer monsoon rainfall. *Climate Dynamics*, *46*(3–4), 949–965. https://doi.org/10.1007/s00382-015-2624-z

Shukla, P. R., Skeg, J., Buendia, E. C., Masson-Delmotte, V., Pörtner, H.-O., Roberts, D., et al. (2019). *Climate change and land: An IPCC special report on climate change, desertification, land degradation, sustainable land management, food security, and greenhouse gas fluxes in terrestrial ecosystems*.Intergovernmental Panel on Climate Change.

Skamarock, W. C., Klemp, J. B., Dudhia, J., Gill, D. O., Liu, Z., Berner, J., et al. (2019). A description of the advanced research WRF model version 4 [Software]. National Center for Atmospheric Research, *145*. https://doi.org/10.5065/1dfh-6p97

Sodemann, H., & Stohl, A. (2013). Moisture origin and meridional transport in atmospheric rivers and their association with multiple cyclones. *Monthly Weather Review*, *141*(8), 2850–2868. https://doi.org/10.1175/MWR-D-12-00256.1

Sousa, P. M., Ramos, A. M., Raible, C. C., Messmer, M., Tomé, R., Pinto, J. G., & Trigo, R. M. (2020). North Atlantic integrated water vapor transport—From 850 to 2100 ce: Impacts on Western European rainfall. *Journal of Climate*, *33*(1), 263–279. https://doi.org/10.1175/JCLI-D-19-0348.1

Stohl, A. (1998). Computation, accuracy and applications of trajectories—A review and bibliography. *Atmospheric Environment*, *32*(6), 947–966.

10.1029/2022JD037612

Stohl, A., & James, P. (2004). A Lagrangian analysis of the atmospheric branch of the global water cycle. part i: Method description, validation, and demonstration for the august 2002 flooding in central Europe. *Journal of Hydrometeorology*, *5*(4), 656–678. https://doi.org/10.1175/1525-7541(2004)005<0656:ALAOTA>2.0.CO;2

Stohl, A., & James, P. (2005). A Lagrangian analysis of the atmospheric branch of the global water cycle. part ii: Moisture transports between Earth's ocean basins and river catchments. *Journal of Hydrometeorology*, *6*(6), 961–984. https://doi.org/10.1175/JHM470.1

Tewari, M., Chen, F., Wang, W., Dudhia, J., LeMone, M., Mitchell, K., et al. (2004). Implementation and verification of the unified Noah land surface model in the WRF model. In *20th conference on weather analysis and forecasting/16th conference on numerical weather prediction* (Vol. 1115, pp. 2165–2170). American Meteorological Society.

Trigo, R. M., Ramos, C., Pereira, S. S., Ramos, A. M., Zêzere, J. L., & Liberato, M. L. (2016). The deadliest storm of the 20th century striking Portugal: Flood impacts and atmospheric circulation. *Journal of Hydrology*, *541*, 597–610. https://doi.org/10.1016/j.jhydrol.2015.10.036

Van Der Ent, R. J., & Tuinenburg, O. A. (2017). The residence time of water in the atmosphere revisited. *Hydrology and Earth System Sciences*, *21*(2), 779–790. https://doi.org/10.5194/hess-21-779-2017

Vincent, L. (1993). Morphological grayscale reconstruction in image analysis: Applications and efficient algorithms. *IEEE Transactions on Image Processing*, *2*(2), 176–201. https://doi.org/10.1109/83.217222

Xu, G., Ma, X., Chang, P., & Wang, L. (2020). Image-processing-based atmospheric river tracking method version 1 (ipart-1) [software]. Geoscientific Model Development, *13*(10), 4639–4662. https://doi.org/10.5194/GMD-13-4639-2020

Yin, J. H. (2005). A consistent poleward shift of the storm tracks in simulations of 21st century climate. *Geophysical Research Letters*, *32*, L18701. https://doi.org/10.1029/2005GL023684

Zêzere, J. L., Pereira, S., Tavares, A., Bateira, C., Trigo, R., Quaresma, I., et al. (2014). Disaster: A GIS database on hydro-geomorphologic disasters in Portugal. *Natural Hazards*, *72*(2), 503–532. https://doi.org/10.1007/s11069-013-1018-y

Zhang, Z., Ralph, F. M., & Zheng, M. (2019). The relationship between extratropical cyclone strength and atmospheric river intensity and position. *Geophysical Research Letters*, *46*, 1814–1823. https://doi.org/10.1029/2018GL079071

Zhao, M. (2020). Simulations of atmospheric rivers, their variability, and response to global warming using GFDL's new high-resolution general circulation model. *Journal of Climate*, *33*(23), 10287–10303. https://doi.org/10.1175/JCLI-D-20-0241.1

Zhu, Y., & Newell, R. E. (1998). A proposed algorithm for moisture fluxes from atmospheric rivers. *Monthly Weather Review*, *126*(3), 725–735. https://doi.org/10.1175/1520-0493(1998)126<0725:APAFMF>2.0.CO;2

4.6 Dynamic downscaling of wind speed over the North Atlantic Ocean using CMIP6 projections: Implications for offshore wind energy density

Fernández-Alvarez, J. C., Costoya, X., Pérez-Alarcón, A., Rahimi, S., Nieto, R., & Gimeno, L. (2023). Dynamic downscaling of wind speed over the North Atlantic Ocean using CMIP6 projections: Implications for offshore wind power density. *Energy Reports*, 9, 873-885.

Table 4.6: Detailed description of the journal where the fifth article was published. The data is updated from 2022 according to the Web of Science (JCR). **IF**: impact factor.

Journal	Description	Journal metrics
Energy Reports	**Publisher**: Elsevier, **Scope**: This journal's scope is scientific research with an energy focus on engineering, social research, and numerical modelling.	**IF:** 5.2, 5-year **IF**: 5.6, **Ranking**: 67 out of 151 in Energy & Fuels (**Q2**)

Energy Reports 9 (2023) 873–885

Contents lists available at ScienceDirect

Energy Reports

journal homepage: www.elsevier.com/locate/egyr

Research paper

Dynamic downscaling of wind speed over the North Atlantic Ocean using CMIP6 projections: Implications for offshore wind power density

José C. Fernández-Alvarez [a,b,*], Xurxo Costoya [a], Albenis Pérez-Alarcón [a,b], Stefan Rahimi [c], Raquel Nieto [a], Luis Gimeno [a]

[a] Centro de Investigación Mariña, Universidade de Vigo, Environmental Physics Laboratory (EPhysLab), Campus As Lagoas s/n, Ourense, 32004, Spain
[b] Departamento de Meteorología, Instituto Superior de Tecnologías y Ciencias Aplicadas, Universidad de La Habana, La Habana, Cuba
[c] Department of Atmospheric and Oceanic Sciences, University of California, Los Angeles, United States

ARTICLE INFO

Article history:
Received 22 July 2022
Received in revised form 7 November 2022
Accepted 11 December 2022
Available online xxxx

Dataset link: https://cds.climate.copernicus.eu/cdsapp#!/dataset/reanalysis-era5-single-levels-monthly-means?tab=form, https://esgf-data.dkrz.de/search/cmip6-dkrz/

Keywords:
Wind power density (WPD)
Dynamic downscaling
WRF-ARW model
CMIP6
Climate change

ABSTRACT

Offshore wind energy is an important agent to fight climate change. However, it is simultaneously very sensitive to climate change. This study analyzes the future changes in wind speed of 10 m above sea surface (V10) in the North Atlantic Ocean and how these variations may affect offshore wind energy resources for three potential subregions (the United States (US) East Coast, western Iberian Peninsula, and the Caribbean Sea). Dynamic downscaling of three different future scenarios of the CESM2 global climate model (CMIP6 project) was performed using the WRF-ARW atmospheric model. V10 is expected to decrease in the winter and spring seasons but increase in summer and autumn, mainly in tropical regions up to 30 °N. Annually, it shows the maximum increase in the tropical region. For the Iberian Peninsula subregion, significant increases in summer are expected for wind power density (WPD) along the 21st century, but there is uncertainty for the other seasons. A WPD decrease in winter and increases in summer and autumn are expected along the 21st century for the US subregion. No significant changes were observed at annual scale. Finally, for the Caribbean Sea, a decrease is projected in the Yucatan Basin and considerable increases are foreseen for the Colombia and Venezuela basins.

1. Introduction

Climate change presents a real challenge to society. According to the sixth report of the Intergovernmental Panel on Climate Change (IPCC), an increase in global surface temperature of 1.5 °C and 2 °C will be exceeded during the 21st century unless significant reductions in CO_2 and other greenhouse gas emissions are achieved in the coming decades (IPCC, 2021). Although temperature has received the most attention in relation to climate change, it is important to analyse other atmospheric variables that are instrumental for the climate system. One of these variables is wind speed of 10 m above sea surface (V10). V10 is a key variable in climate studies because its variations have substantial impacts on human society and the natural environment (Pryor et al., 2006). For example, V10 intensification can exacerbate soil erosion, leading to more severe dust storms (Alizadeh-Choobari et al., 2014; Wang et al., 2017) and result in heat and humidity fluxes at the air–sea interface (Renault et al., 2017).

Renewable energy sources are important alternatives to alleviate the dependence on fossil fuels and reduce greenhouse gas emissions. Offshore wind energy is a mature marine renewable energy source that still has high growth potential owing to technological advances, such as floating structures that allow the installation of offshore wind farms at greater depths. Although an increase in the offshore wind installation capacity is expected worldwide (GWEC, 2021), it is important to consider that V10 changes due to climate change may have a significant impact on offshore wind energy production because the wind power generated depends on the wind speed cubed. Therefore, while offshore wind energy is an agent to fight climate change, it is simultaneously very sensitive to climate change.

Numerous studies have focused on analysing possible future changes in V10 using global climate models (GCMs) and how they may influence wind energy production worldwide or in specific regions. These models can be employed to obtain climate simulations and projections, modelling changes in the physical processes of the atmosphere, ocean, land surface, and cryosphere by considering different scenarios of increasing greenhouse gases

* Corresponding author at: Centro de Investigación Mariña, Universidade de Vigo, Environmental Physics Laboratory (EPhysLab), Campus As Lagoas s/n, Ourense, 32004, Spain.
E-mail address: jose.carlos.fernandez.alvarez@uvigo.es (J.C. Fernández-Alvarez).

https://doi.org/10.1016/j.egyr.2022.12.036
2352-4847/

(Stocker et al., 2013). Recently, an extensive selection of GCMs and Earth system models (ESMs) was made available through the 6th phase of the Coupled Model Intercomparison Project (CMIP6) (Eyring et al., 2016). The Scenario Model Intercomparison Project (ScenarioMIP), in particular (O'Neill et al., 2016), occupies a prominent position among the activities covered in this phase, and provides climate projections based on new alternative scenarios of future greenhouse gas emissions and land use (O'Neil et al. 2017) for CMIP6. These updated scenarios are produced with integrated assessment models and driven by the updated pathways of societal development, namely the shared socioeconomic pathways (SSPs) (Riahi et al., 2017). The CMIP6 project and new SSPs were the basis for establishing future climate projections in the most recent IPCC report (IPCC, 2021). Therefore, the GCMs involved in CMIP6 represent the most recent tools for analysing future projections in the context of current climate change.

However, the coarse resolution of GCMs is generally insufficient to provide useful climate change information and impacts for a specific area, particularly where climate and weather are inhomogeneous. This includes areas with complex terrains and tropical regions, where precipitation is strongly driven by convection at finer scales than can be adequately resolved by GCMs. Accurate numerical systems for climate simulation and projection at sufficiently high resolutions are required for effective climate change mitigation and adaptation. The only tool to obtain these high spatial resolution climate projections is regional climate models (RCMs), which can be used to force state-of-the-art CMIP6 GCMs. This process is called dynamic downscaling, and allows for improved understanding of the possible modifications of V10 and the subsequent changes in wind energy resources.

The objective of this work is to project and analyse future changes in V10 and its geographical distribution over the North Atlantic Ocean by means of dynamic downscaling of the CMIP6 project data using the WRF-ARW model. To the best of our knowledge, the present study is the first attempt to analyse the impact of climate change on offshore wind energy and V10 patterns by means of dynamic downscaling in the North Atlantic Ocean (NATL) using CMIP6 data, which contains the most recent future climate projections.

Area under scope

This study focused on analysing V10 changes in the NATL region (Fig. 1a). This region has significant offshore wind energy potential. The North Sea, located in the Atlantic Ocean, has the highest density of offshore wind energy farms worldwide; as a result, North Sea wind energy resources have been studied extensively. Countries such as the United Kingdom, Germany, and China, are global leaders in installed offshore wind energy capacity (GWEC, 2021). The number of offshore wind farms installed in other areas of the North Atlantic is expected to increase over the next few decades due to the development of floating platforms that are suitable for the narrow continental shelf in this area. The first floating offshore wind farm was recently installed along the western Atlantic coast of the Iberian Peninsula (Ramírez et al., 2021). For this reason, the Atlantic coast of the Iberian Peninsula was selected for a more in-depth analysis of the impact future variability in offshore wind energy resources (Fig. 1b). The development of offshore renewable energy is also expected to increase over the next few years along the Atlantic coast of the United States (US) (Fig. 1c) (deCastro et al., 2019; Costoya et al., 2020b) as there is currently little development of this offshore technology (Musial et al., 2016). Finally, future changes in offshore wind energy will also be analysed in the Caribbean Sea (CS) because this area involves many islands with isolated electrical systems, where the development of offshore wind energy is of great interest. In addition, it must be noted that some islands in the Caribbean Sea have already implemented onshore wind farms including Cuba, Curaçao, Jamaica, Martinique, and Guadeloupe (Wright, 2001). Below, various investigations of the changes in V10 and WPD in the future climate for each of these three subregions are detailed.

Regarding the Atlantic coast of the Iberian Peninsula (IP), Soares et al. (2017) used the WRF-ARW model, which was forced by the climatic simulations of the Coordinated Regional Climate Downscaling Experiment (CORDEX) project (scenarios RCP4.5 and RCP8.5), to project future changes in offshore wind power. These authors demonstrated that the majority of climate models project reductions in wind speed and power for all seasons, except for the summer. Moreover, Santos et al. (2018) analysed the variations in the WPD using various RCMs from the CORDEX project, and found a slight increase for the period 2019–2045 under the RCP8.5 scenario. Finally, Costoya et al. (2020a) applied a combination of two bias correction methods to reduce WPD error in climate models and used CORDEX simulations to determine the future WPD reduction across most of the western IP. In addition, they found that a WPD increase was projected for summer months and a decrease in WPD was projected during autumn and spring.

Different authors have investigated future changes in WPD along the Atlantic coast of the US. For example, Liu et al. (2014) used dynamic downscaling to obtain future climate projections from a GCM of the CMIP3 project with the WRF model. They determined that the mean annual wind speed increased from 0.1 to 0.2 m/s in the northern Great Lakes region until the middle of the century. However, until 2090 an even greater increase in the wind speed of 0.1 to 0.4 m/s is projected for this region. In addition, Johnson and Erhardt (2016) determined that the offshore wind resource projections have a slight tendency to decrease along the east coast and increase along the west coast of the US, considering that these changes are less than 2%. These authors used the output from four RCMs from North American Regional Climate Change Assessment Program (NARCCAP), assuming the SRES A2 emission scenario. Recently, Costoya et al. (2020b) used 12 CORDEX simulations of approximately 0.22° spatial resolution to analyse future WPD variations on both the east and west coasts of the US. Overall, the authors found a decline in offshore wind power resource throughout the 21st century in the US, particularly on the east coast.

For the CS subregion, very few studies have focused on the future changes in V10 and WPD. Angeles et al. (2010) found that an increase in easterly winds is expected for this region between 2070 and 2098, especially along the coast. Furthermore, Yao et al. (2016) analysed the differences in wind speed using statistical downscaling of a single GCM (GFDL CM2.1). Finally, Costoya et al. (2019) showed that a maximum annual wind increase of approximately 0.4 m/s is projected for most of the Caribbean at the end of the 21st century, except in the Yucatan Basin. This increase occurred mainly during the rainy season, $\sim$0.5 ms^{-1}. Furthermore, these authors found that a moderate increase in wind, approximately 0.2 m/s is expected during the dry season restricted to the southeast coast. This study was conducted using the CORDEX project at a resolution of approximately 0.44°.

2. Data and methodology

2.1. Data

The outputs of the CESM2 climate model (Community Earth System Model Version 2) (Danabasoglu et al., 2020) from the CMIP6 project were used to run the WRF regional dynamic model with ARW (Advanced Research WRF) dynamic core. These variables were downloaded from the Earth System Grid Federation (ESGF2). These were obtained for the native grid "gn" and with a spatial resolution of 0.9 × 1.25 ($\sim$1°). In addition, these variables corresponded to a mesh with 288 × 192 longitude/latitude

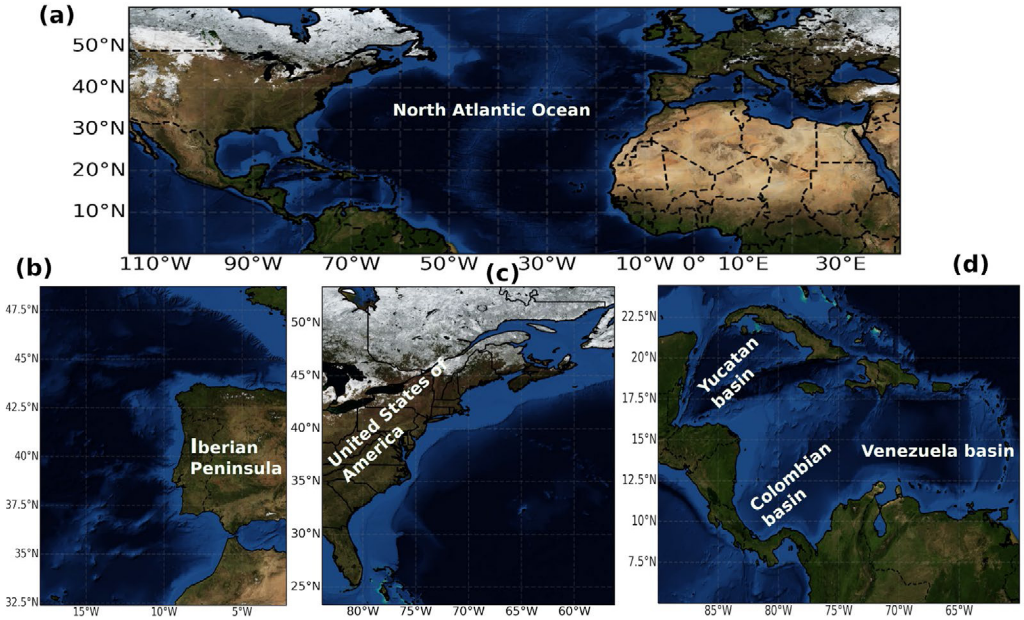

Fig. 1. The area selected for the study of the wind speed of 10 m above sea surface (V10) using the WRF-ARW for the NATL is shown in (a). The subregions for the study on wind power density (WPD) are shown as follows: (b) US East Coast, and (c) Iberian Peninsula, and (d) Caribbean Sea.

and 32 levels. Historical data from 2010–2014 and the scenarios for the three climate projections (MIP Scenario 21C: SSP2-4.5, SSP3-7.0, and SSP5-8.5) were used. These projections cover the intervals 2049–2053 (mid-century (MC)) and 2096–2100 (end-century (EC)). The selection criteria of 5 years are based on achieving stability between the simulation time and the available and necessary computational resources for the runs when using a forced regional model with outputs of a climate model. It is important to mention that several previous analyses have considered time periods in the 5–11 year interval to analyse the impact of climate change on renewable resources, but always considering one scenario or two at most, unlike this research which considers three of the new SSPs (e.g. Alsarraf and Van Den Broeke, 2015; Fant et al., 2016; González et al., 2017; Cai and Breon, 2021; Martinez and Iglesias, 2021).

The CESM2 model selection was based on two main reasons. Firstly, CESM2 has been evaluated for the representation of jet streams and storm tracks, stationary waves, global divergent circulation, annular modes, North Atlantic oscillation, and blocking. Moreover, it ranks within the top 10% of CMIP class models in many of these features (Simpson et al., 2020). In addition, Shen et al. (2022) demonstrated that the CESM2 has the best ability in reproducing the observed near-surface wind speed trends simulated by CMIP6 models. Secondly, CESM2 provides all the necessary variables (see NCAR Technical Notes NCAR/TN 515+STR, Bruyère et al., 2015) to force the WRF-ARW with better resolution compared to the rest of the models that have a resolution of ~250 km. For its use, it was necessary to process these variables of the different periods to generate the CESM2 intermediate files (26 vertical levels) that were used as the initial and boundary conditions for forcing the WRF-ARW. For it, software was developed in NCL and Fortran based on the methodology proposed by Bruyère et al. (2015) for we can execute el WRF.

The SSPs used in the research present differences; for example, SSP2-4.5 is a scenario that represents the medium part of the range of future forcing pathways and updates the RCP4.5 pathway with a radiative forcing of 4.5 W/m^2 for 2100 (O'Neill et al., 2016). Additionally, SSP2-4.5 features land use and aerosol pathways that are not extreme relative to the other SSPs. In this regard, it is considered that while environmental systems experience degradation, there are some improvements, and overall, the intensity of resource and energy use declines (Riahi et al., 2017). In contrast, the SSP3-7.0 scenario represents the medium to high end of the range of future forcing pathways with radiative forcing of 7.0 W/m^2 in 2100. In particular, SSP3-7.0 is a scenario with both substantial land use changes (particularly decreased global forest cover) and high Near-Term Climate Forcers (NTCF) emissions (particularly SO_2) (O'Neill et al., 2016). Finally, the SSP5-8.5 scenario represents the high end of the range of future pathways. It is the only SSP scenario with sufficiently high emissions to produce a radiative forcing of 8.5 W/m^2 in 2100, according to O'Neill et al. (2016).

The V10 simulated using WRF-ARW was evaluated with respect to the ERA5 reanalysis (Hersbach et al., 2020). ERA5 is the most recent (5th generation) global atmospheric reanalysis of the European Centre for Medium-Range Weather Forecasts (ECMWF) and stands out for its high resolution (31 km horizontally and 137 vertical levels) as well as for a large amount of assimilated historical observations. This represents a significant improvement over its predecessor, ERA-I reanalysis. The characteristics of the surface and low-level winds in ERA5 over the ocean, in relation to observations and other reanalyses, have been evaluated by numerous investigations (e.g., Olauson, 2018; Belmonte and Stoffelen, 2019; Kalverla et al., 2019) and ERA5 has been found to work well for the representation of these fields.

2.2. Model setup and methodology

As mentioned in the Introduction, the objective of this work is mainly to analyse the future changes for V10 in future climate (mid- and end- of the century) and their implications in the offshore WPD for selected regions of interest (IP, US and CS). The flowchart of the research is explained below: (1) simulations with dynamic downscalling are performed using WRF-ARW forced by historical CESM2 data, (2) an evaluation of the configuration is then carried out with respect to ERA5 reanalysis data. Once the configuration has been evaluated, (3) the future conditions are simulated to study future changes of the V10 field in the Atlantic Ocean and (4) the WPD variable is then regionalized for IP, US and CS and the future projections are analysed. A more detailed explanation is presented below.

Dynamic downscaling was performed with WRFv3.8.1 (Skamarock et al., 2008) using the ARW dynamic core. This was forced using the CESM2 model outputs every 6 h. The simulations have 40 vertical layers from the surface to 50 hPa and 480 × 800 grids with a horizontal spacing of 20 km centred on the North Atlantic Ocean. The parameterizations employed in the WRF-ARW setup are as follows: the WSM6 microphysics scheme (Hong and Lim, 2006), Yonsei University PBL scheme (Hong et al., 2006), revised MM5 surface layer scheme (Jimenez et al., 2012), United Noah Land Surface Model (Tewari et al., 2004), shortwave and longwave RRTMG schemes (Iacono et al., 2008), and Kain–Fritsch ensemble cluster scheme (Kain, 2004). These have been used in several investigations in the region within the computational domain of WRF-ARW by Insua-Castro and Miguez-Macho (2018) and Insua-Castro et al. (2019). On the other hand, spectral nudging of waves longer than 1000 km is employed to avoid distortion of the large-scale circulation within the regional model domain owing to the interaction between the model solution and lateral boundary conditions (Miguez-Macho et al., 2004). For the WRF-ARW simulations, a 6-month spin-up was performed before the period to be simulated, and the restart mode was used when the WRF-ARW was stopped.

The WPD was calculated by considering the V10 field of the WRF-ARW outputs. WPD (W/m^2) represents the energy available at a specific site that can be converted by a wind turbine. This value was calculated using the following equation:

$$WPD = \frac{1}{2}\rho v^3 \tag{1}$$

where ρ represents the density of air with a value of approximately 1225 kg/m^3 at sea level and at 15 °C (Salvador et al., 2018; Ulazia et al., 2019), and v is the wind speed (m/s). To determine the WPD, the wind speed data were extrapolated up to 120 m, which is the typical height of marine wind turbines (Swart et al., 2009) considering an atmosphere with neutral stability. The wind speed values were extrapolated following the expression of the logarithmic wind profile:

$$u_z = u_{zm} * ln\left(\frac{h}{z_0}\right) / ln\left(\frac{h_m}{z_0}\right) \tag{2}$$

where u_{zm} is the wind speed near the surface (m/s), h_m is the height (m) at which the wind is measured near the surface (10 m in this study), u_z is the mean wind speed (m/s) at the extrapolated height (h) of 120 m, and z_0 is the local roughness length (a value of 1.52×10^{-4} m above the ocean surface is considered). This method has been used by Yamada and Mellor (1975) and Salvador et al. (2018) in previous research. The WPD was calculated for the WRF-ARW domain, but was analysed mainly in the IP, US, and CS subregions. This methodology is considered and not a mathematical interpolation to obtain the wind at 120 m to be able to compare the results as homogeneous as possible with previous investigations where this physical relationship has been considered.

Subsequently, to use this configuration of WRF-ARW to simulate future projections with different SSPs, it was evaluated in comparison with ERA5. This analysis was performed on the area shown in Fig. 1a. The statistical graphs presented in Table 1 were used, where x_i and y_i are the simulated and observed values, respectively, and n is the number of data points. In addition, $\overline{x_i}$ and $\overline{y_i}$ are the mean values of the simulations and observations, respectively. Furthermore, the evaluation and analysis of the different SSPs were conducted annually and seasonally. In this case, boreal winter (JFM), spring (AMJ), summer (JAS), and autumn (OND) are considered for the analysis of the IP and US subregions. However, for the CS the dry season (DS) from December to April and wet season (WS) from May to November are considered because the Caribbean climate is characterized by two seasons (Enfield and Alfaro, 1999). From here on, the simulations with the historical CESM2 for 2010–2014 will be referred to as WRF-CESM2_HIST, and for the climatic scenarios, it will be WRF_CESM2_x_MC or WRF_CESM2_x_EC, where x represents the SSPs and MC or EC the time periods. Fig. 1b–d shows the areas considered in the WPD study.

Table 1
Statigraphs used in the evaluation of the configuration of the WRF-ARW.
Source: Modified from Brown et al. (2013).

Statigraphs	Equation
Absolute error (MAE)	$\frac{\sum_{i=1}^{n} \lvert x_i - y_i \rvert}{n}$
Root mean square error (RMSE)	$\sqrt{\frac{\sum_{i=1}^{n} (x_i - y_i)^2}{n}}$
Pearson's correlation (R)	$\frac{\sum_{i=1}^{n} (x_i - \overline{x_i})(y_i - \overline{y_i})}{\sqrt{\sum_{i=1}^{n} (x_i - \overline{x_i})^2 (y_i - \overline{y_i})^2}}$
Bias (B)	$\frac{\sum_{i=1}^{n} (x_i - y_i)}{n}$

3. Results and discussion

3.1. Evaluation of the downscaling methodology

Fig. 2 shows the V10 field for WRF-ARW_HIST and ERA5 for the period 2010–2014. In addition, the spatial differences calculated from WRF-ARW_HIST and ERA5 were presented. Overall, spatial differences were less than 1 m/s in the North Atlantic region. In winter, WRF-CESM2_HIST shows a greater wind speed than ERA5 in the region between 40–50°N that extends mainly towards the coast of Europe. However, the opposite was observed in the tropical and subtropical latitudes, where speeds lower than ERA5 were detected. For spring and summer, similar behaviour was observed with two zones where wind speed was overestimated, one near the coast of the US and another from the central Atlantic to the coast of Western Europe. For autumn, the WRF-CESM2_HIST projections showed a tendency to underestimate the wind speed (<1 m/s) in most of the North Atlantic. Annually, simulated data show very similar behaviour with spatial differences of ∼0.8 m/s or less across the entire study region. It should be highlighted that WRF-ARW_HIST shows an adequate representation compared to ERA5 in areas where future changes in the WPD will be studied.

A summary of the previously proposed statistics is shown in Fig. 3. The Pearson correlation coefficients present values higher than 0.8 in all the time periods studied and are lower during summer. The MAE varies from 0.5 to 1 m/s, being higher in summer and lower in autumn, with an annual value of ∼0.5 m/s. On the other hand, B increases from winter to summer and decreases considerably for autumn, presenting a mean value for the entire period of ∼0.1 m/s; which is an overestimation. Finally, the RMSE presents values that oscillate between 0.8 and 1.2 m/s and are ∼0.6 m/s annually. In general, the use of the forced WRF-ARW model with the CESM2 provides an adequate representation of V10.

3.2. Future changes for V10 North Atlantic Ocean determined using WRF-ARW and SSPs

Future changes will be determined as the difference between the simulations using the WRF-ARW forced with different SSPs minus the WRF-ARW forced with historical data from the CMIP6.

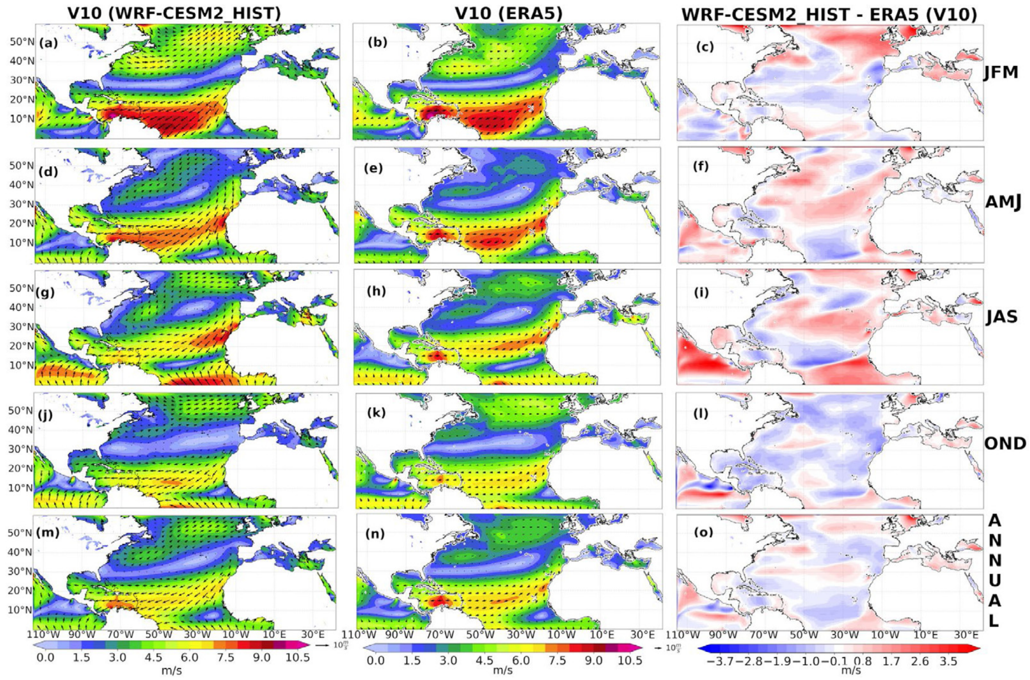

Fig. 2. The V10 fields for WRF-CESM2_HIST (first column) and ERA5 (second column) and the spatial difference (third column). The fields displayed from top to bottom correspond to boreal winter (JFM), spring (AMJ), summer (JAS), autumn (OND), and annually (ANNUAL) values. The modular value of V10 is represented by contours and the direction of V10 by arrows. Historical period: 2010–2014.

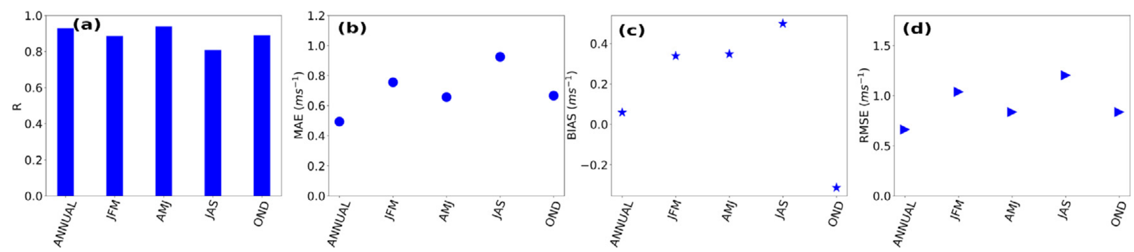

Fig. 3. Statigraphs calculated with the WRF-CESM2_HIST simulations and the ERA5 reanalysis of the V10 field for the study area (Fig. 1a). (a) R, (b) MAE, (C) B and (d) RMSE. Historical period: 2010–2014.

Therefore, positive values indicate future increases and negative values indicate decreases. Future changes were determined for the mid-21st century (2049–2053) and the end of the 21st century (2096–2100). Fig. 4 shows the comparison of V10 from WRF-ARW_HIST and the differences in the simulations of WRF-ARW for each SSP with respect to the MC. Considering SSP2-4.5, a decrease was expected above latitudes of 30°N during winter for the MC period (Fig. 4b). However, positive values prevailed south of 30°N, with the exception of the eastern Caribbean Sea. In spring, a decrease was maintained across most of the North Atlantic Ocean, except in the Caribbean Sea. Positive values prevailed for summer and autumn, with the exception of the southern region of the US coast (Fig. 4j, n). An increase was projected in most tropical regions, with little annual change in the rest of the study area (Fig. 4r).

On the other hand, using SSP3-7.0 for winter, the tendency for V10 to decrease continues to be represented, with two exceptions: the Iberian Peninsula and the West African zone (see Fig. 4c). In spring, negative values increased throughout the area, and were greater than those observed using SSP2-4.5. Moreover, mainly positive values for summer and autumn are expected over the CS, the US coast, and IP, but the values were relatively lower than those shown for SSP2-4.5 (Fig. 4j, n). Regarding the annual average, there is a tendency to show little change, with the exception of the tropical zone near the coast of Africa and northwest of the Iberian Peninsula (Fig. 4s). Considering SSP5-8.5, the most significant changes occur in winter, with a considerable decrease (∼3.5 m/s) in the Caribbean Sea, along the African coast, and latitudes above 50°N (Fig. 4d). A few changes in the general form can be seen for EC compared to MC considering SSP2-4.5 and SSP3-7.0. However, under SSP5-8.5, positive values were expected throughout the North Atlantic Ocean region for summer and autumn, showing an increasing trend with more extreme conditions at the end of the 21st century (Figure S1).

In general, these results differ from previous research (e.g., Collins et al., 2013; Gallagher et al., 2016) which found that the average wind changes due to climate change over the North Atlantic Ocean at the end of the 21st century were small and negative. These authors used data corresponding to CMIP5 models to obtain the results. However, this research showed a notable increase for summer and autumn, mainly in the tropical zone and areas near the coast of Western Europe. This result is similar to that reported by Ruosteenoja et al. (2019), wherein the frequency of strong westerly geostrophic winds was found to increase by 50% in northern Europe and the northern North Atlantic Ocean in autumn. In addition, the projected increase in the tropical region is in correspondence with the projected increase for WPD over most mid- to low-latitudes ocean areas (30°S–30°N) according to Zheng et al. (2019). Finally, these projections are in correspondence with that found for the surface wind speed for the period

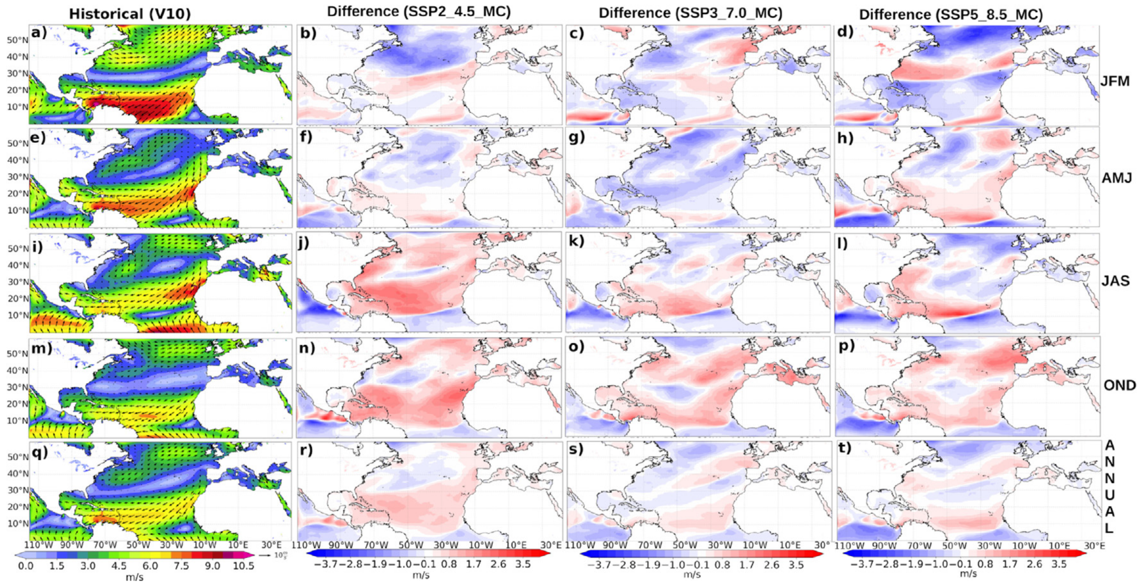

Fig. 4. The V10 for the historical period and the differences in the simulations of WRF-ARW for each SSP. The fields displayed from top to bottom correspond to boreal winter (JFM), spring (AMJ), summer (JAS), autumn (OND), and annually (ANNUAL), respectively. The modular value of V10 is represented by the contours and direction of V10 by the arrows. Period: 2049–2053 (MC).

1988–2011 by Zheng et al. (2016). These authors show positive trends (5–11 (cm/s)/yr) in the North Atlantic region mainly on the east coast of the United States, northwest Africa, and the Atlantic coast of the IP extending to the Cantabrian Sea using Cross-Calibrated, Multi-Platform (CCMP) wind data.

3.3. Future changes for WPD in the Iberian Peninsula subregion

Fig. 5 shows a comparison of the historical WPD and differences in the WRF-ARW simulation results for each SSP with respect to the WPD for the Iberian Peninsula. Under SSP2-4.5, the WPD is projected to decrease in winter, with maximum values occurring in the north of the IP. In spring, positive values for WPD were projected for most of the west coast of the IP, but considerable increases were noted in the northwestern corner of the IP (Fig. 5f). Positive values were observed very close to the coast of the Iberian Peninsula in summer (>100 W/m^2), but the coast of Galicia to the north of Portugal stood out. Furthermore, few changes were expected in autumn and annually (Fig. 5n, r). Considering SSP3-7.0, an increase is projected for winter, with a maximum in the north of Galicia; however, a notable decrease in the entire coast of the IP is expected for spring (Fig. 5c, g). This behaviour is contrary to the previous scenario analysed for both seasons. On the other hand, increases are projected northwest of the IP for summer and autumn, but there is very little change in the annual analysis (Fig. 5k, o). Considering SSP5-8.5, the most notable difference is the increase projected for the north of the IP for the autumn.

Regarding the EC period and considering all SSPs (see Fig. 6), positive changes were projected to the north of the IP in winter, extending up to 40°N. The intensity of the changes was greatest for SSP5-8.5. A similar pattern was noted in summer, where positive differences with greater magnitudes are expected for the WPD considering the projected scenario in which emissions are high enough to create a radiative forcing of 8.5 W/m^2 in 2100 (see Fig. 6). This result could be related to the increase in V10 at the end of the 21st century in this region, as described in the previous section.

In summary, according to the SSPs, a considerable increase is expected for autumn and summer for both study periods, although slight annual WPD variations were detected, especially in summer. Previous studies (e.g.,; Soares et al., 2017; Moemken et al., 2018; Costoya et al., 2020a; Carvalho et al., 2021) have shown a projected increase for this subregion but always with a slight discrepancy in percentage values. Therefore, summer is maintained as the season with the greatest increase, which will allow a higher stability of the offshore energy resource throughout the year, as this is the season with the lowest WPD on average. Stable wind power generation benefits the gathering and conversion of wind energy, whereas unstable WPD negatively affects the productivity of wind energy conversion (Zheng and Pan, 2014; Zheng, 2018). Moreover, for MC, different behaviours are expected for winter, where SSP2-4.5 and SSP5-8.5 project a decrease, and SSP3-7.0 does not. This may be attributed to the fact that SSP3-7.0 is a scenario involving substantial land use change (particularly decreased global forest cover) and high NTCF emissions (particularly SO_2). However, for EC, a notable increase is expected for all the SSPs north of the Iberian Peninsula. These results coincide with those of Costoya et al. (2020a), which projected an increase for this period but used the RCP8.5 scenario. Also, Zheng et al. (2019) project for the period 2080–2099 an increase of 100–150 W/m^2 for the west coast of the IP with a maximum in the north-northwest. Finally, using ERA-Interim data (1979–2014), Zheng et al. (2022) show a significant (at 95% level) positive annual trend for WPD (1–2 (W/m^2)/yr) in the Atlantic coast of the IP. This shows that there is correspondence between the results of this research and what was found for past climate.

3.4. Future changes for WPD in the US subregion

According to SSP2-4.5, the WPD in winter is projected to decrease at latitudes above 35°N with maximum values along the Maine, Massachusetts, New Hampshire, and New Jersey coasts, for the period 2049–2053 (Fig. 7b). During summer positive WPD values were projected mainly along the North Carolina, South Carolina, and Virginia coasts (Fig. 7j). Negligible changes were observed during the other periods. Additionally, when considering SSP3-7.0, the WPD was projected to decrease in winter (Fig. 7c). However, a different behaviour in autumn is expected along with an increase in the northernmost states of the US (Fig. 7o). The remaining periods exhibited a few distinct and significant changes.

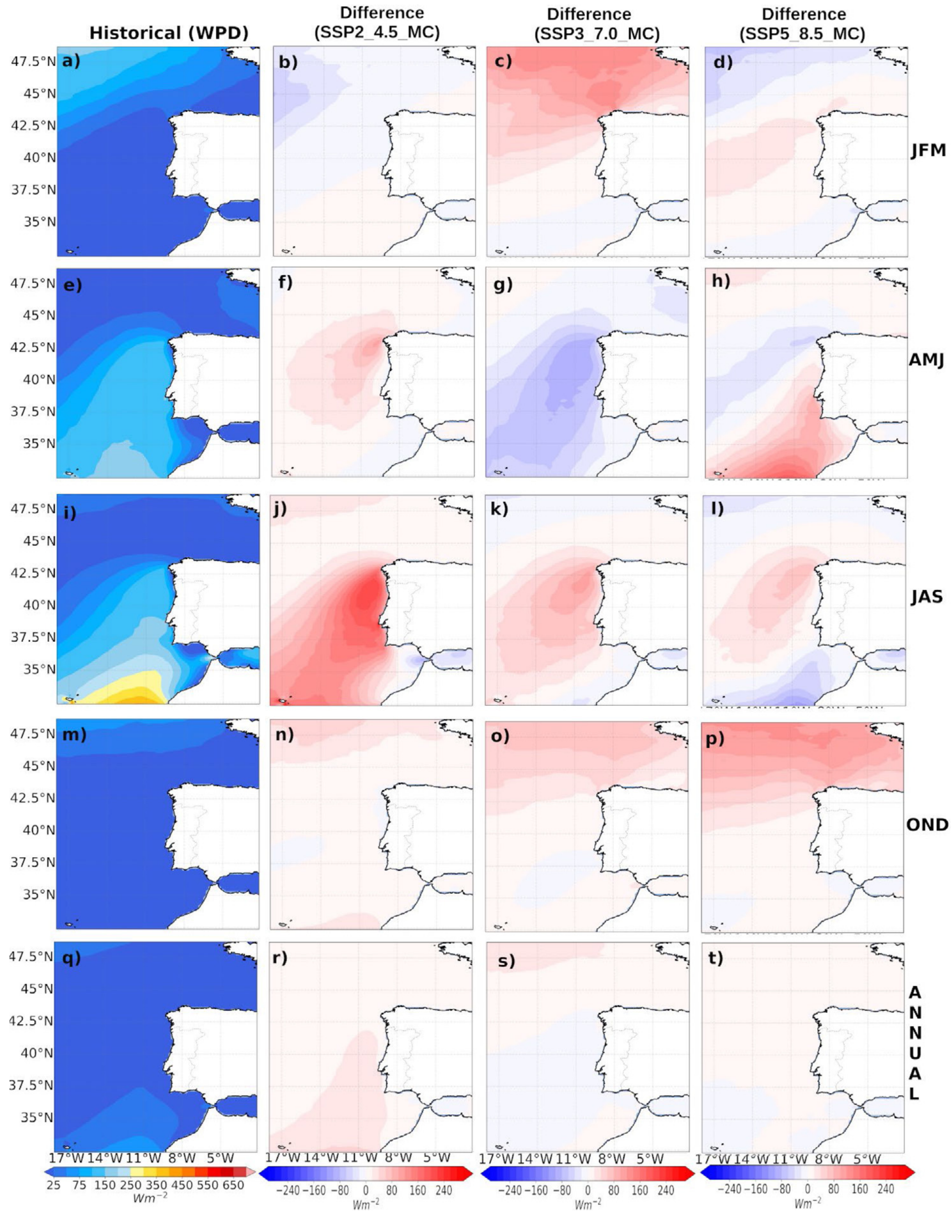

Fig. 5. The WPD for the historical period and the differences between the simulations of WRF-ARW for each of the SSPs in the IP subregion. The boreal winter (JFM), spring (AMJ), summer (JAS), autumn (OND), and annually (ANNUAL) fields are displayed from top to bottom. Period: 2049–2053 (MC).

Fig. 7d shows the behaviour using SSP5-8.5, where there is a different pattern, with positive values below 40°N and negative values above 40°N. In general, the rest of the periods show little change, except in summer, where there is some correspondence with SSP2-4.5 and the positive values are projected for states near 35°N. During 2096–2100, the most significant changes are the maximum decreases in WPD values according to SSP3-7.0 and the increase in summer as per SSP5-8.5 (Fig. 8).

In general, there is a decrease in WPD in winter considering all SSPs, an increase in summer, and little change over the remaining periods, except in autumn, as it is expected that towards the end of the 21st century, a slight increase in WPD will occur in the northern region of the Atlantic coast. These results correspond with those of Costoya et al. (2020b) but differ from those of Kulkarni and Huang (2014), who determined a decrease in WPD during summer and an increase during winter. This study corroborated the findings of Costoya et al. (2020b), which showed that the central zone of the east coast of the US (e.g., Virginia, North Carolina, and South Carolina) constitutes an important target area for the present as well as the future, as it presents good conditions for wind resource development. It was also observed that the northern section, mainly the coastline of the states of Maine, Massachusetts, and New Hampshire, also has a projected increase in WPD. Besides, Zheng et al. (2022) show that the US Atlantic coast has a significant positive annual trend at 95% level for WPD (2–4 (W/m^2)/yr) but based on the ERA-Interim wind product.

3.5. Future changes for WPD in the Caribbean Sea subregion

In the analysis of the Caribbean Sea subregion, it must be considered that only two seasons are considered (dry (DS) and wet (WS)); hence, analyses will be carried out for these seasons and for the annual variation. Considering SSP2-4.5 for 2049–2053 in the DS, a strengthening of the WPD pattern is projected compared to the historical pattern for the Venezuelan Basin that extends to the Caribbean Sea. However, there was a slight decrease in WPD values close to the coast of Colombia (Fig. 9b). Regarding the WS, a more notable increase is projected with respect to the

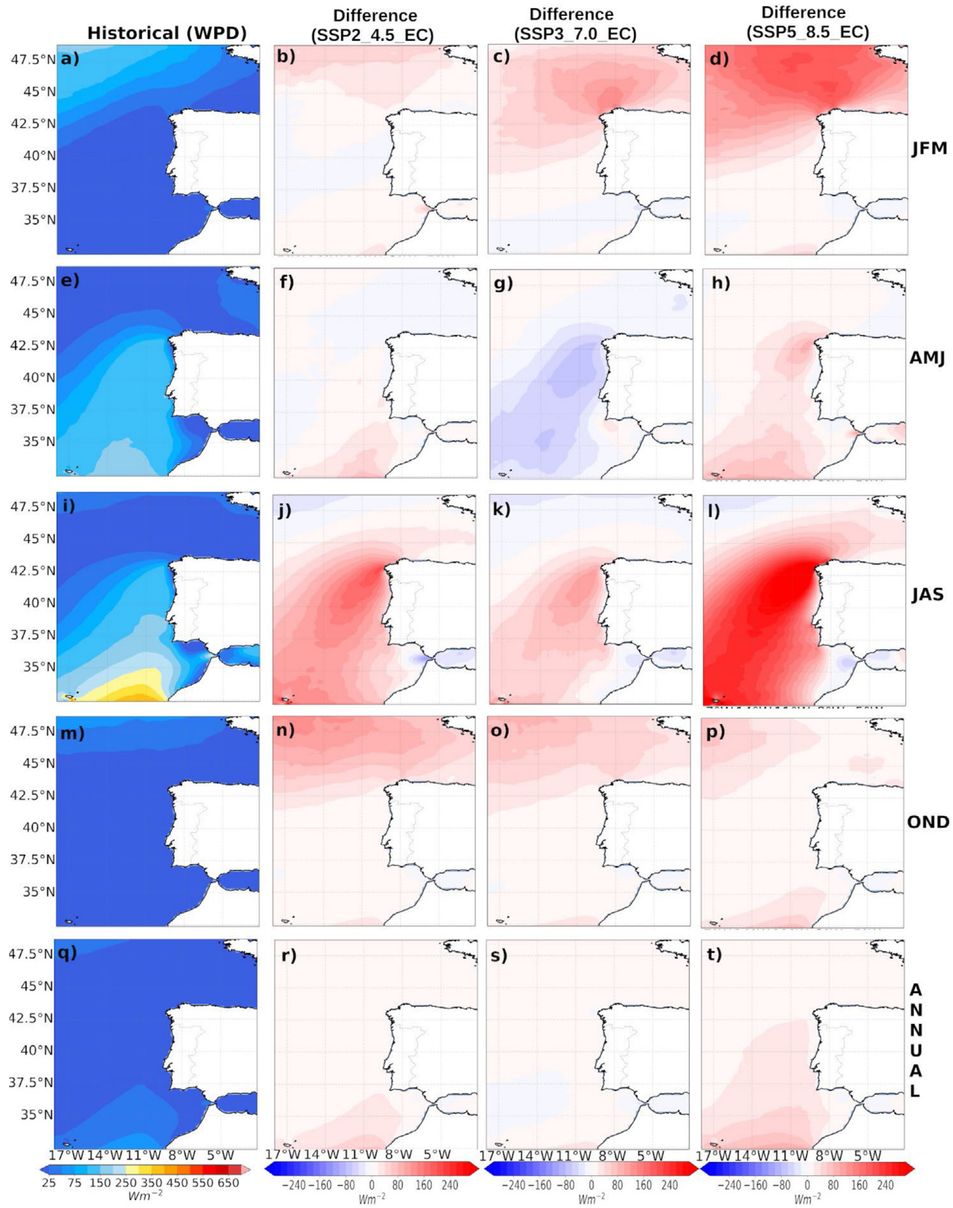

Fig. 6. The WPD for the historical period and the differences between the simulations of WRF-ARW for each of the SSPs in the IP subregion. The boreal winter (JFM), spring (AMJ), summer (JAS), autumn (OND), and annually (ANNUAL) fields are displayed from top to bottom. Period: 2096–2100 (EC).

historical WPD (see Fig. 9f), with maximum values located in the Colombian Basin, Venezuela Basin, near the south and north coast of Española, and in the eastern region of Cuba. However, little change is expected in the Yucatan Basin. As an annual average, an increase is projected mainly over the Venezuelan Basin with values of 80–160 W/m^2 (Fig. 9j).

Considering SSP3-7.0, it is projected that there will be a decrease over the entire CS area during the DS, with maximum values occurring in the Colombian Basin. However, the behaviour will be different in the WS, where an increase is expected near the coast of Colombia and Venezuela, but limited significant changes projected for the rest of the study area (see Fig. 9c, g). The annual average changes will be insignificant, except for along the coast of Colombia (mainly along the Barranquilla and San Marta coastal states). The expected changes for MC considering SSP5-8.5 are similar to the patterns obtained using SSP3-7.0, but differ from those observed considering SSP2-4.5, which projects a majority increase throughout the entire region.

For the period 2096–2100, a decrease in the WPD values in the Yucatan and Colombia basins was projected for all SSPs in the DS, but a slight increase was observed in the Venezuela Basin (Fig. 10b, c, d). For the rest of the periods analysed, a notable increase in WPD values (>240 W/m^2) was projected throughout the CS, with the exception of the Yucatan Basin, which showed little change (Fig. 10). The results are similar to those obtained by Costoya et al. (2019) using the RCP8.5 and CORDEX scenario data. Costoya et al. (2019) found a decrease in wind energy for most of the Caribbean region during the dry season at the end of the 21st century, with the Colombian Basin standing out and a moderate increase in wind energy in the Venezuela Basin. In contrast, during the WS, they detected an increase in wind energy in the Colombian and Venezuelan basins with a decrease in the wind energy for the Yucatan Basin with maximum values projected at the middle of the 21st century, but little change towards the end of the 21st century. In general, the most notable projected increase in the WPD is expected in the wet season over the Colombian basin, being higher under the SSP585 scenario at

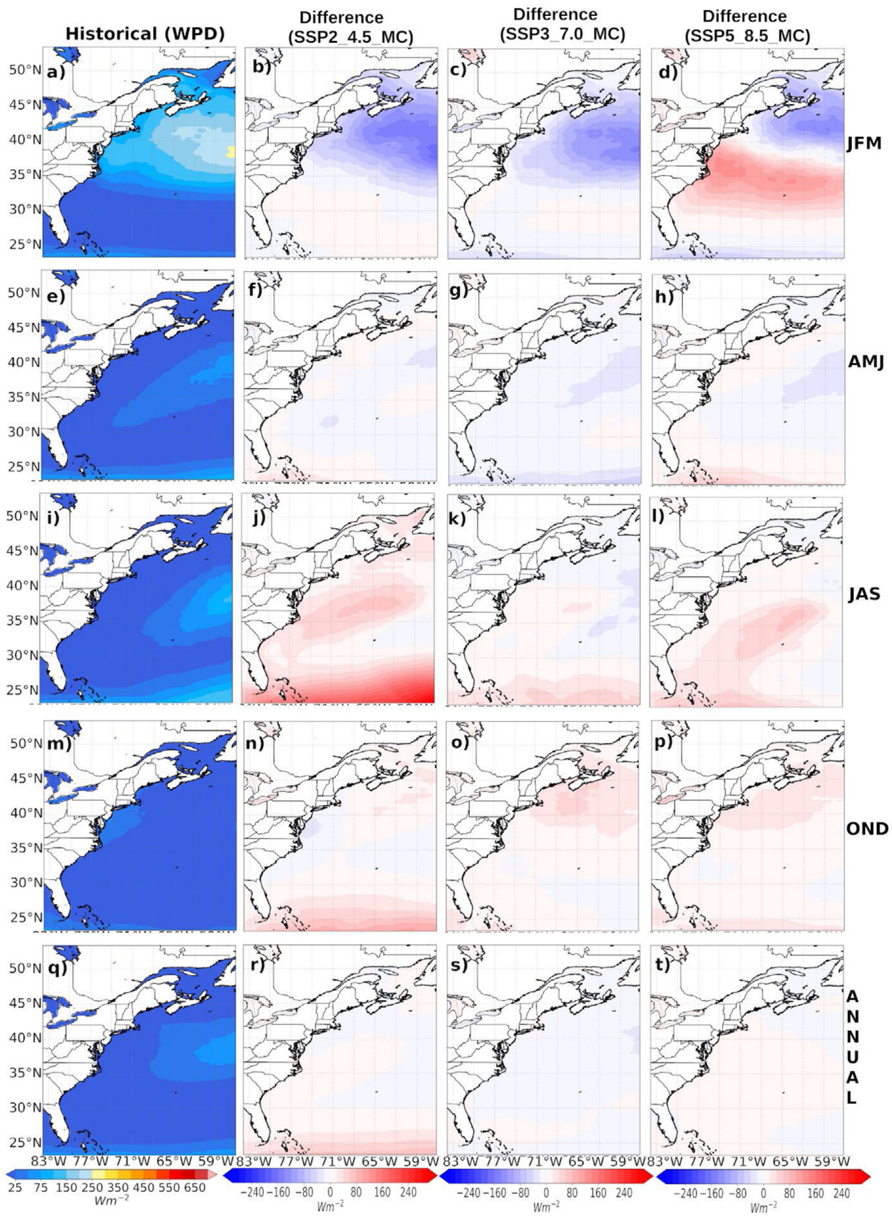

Fig. 7. The WPD for the historical period and the differences between the simulations of WRF-ARW for each of the SSPs in the US subregion. The boreal winter (JFM), spring (AMJ), summer (JAS), autumn (OND), and annually (ANNUAL) fields are displayed from top to bottom. Period: 2049–2053 (MC).

the end of the century. This may be associated with the increase in wind speed in this area (Fig. 4, S1). This variable, in turn, could be related to the expected increase in sea surface temperature throughout the basin and to the decrease in sea level atmospheric pressure towards the southern Caribbean Sea, reported by Bustos-Usta and Torres-Parra (2021). The former would affect wind shear and thus increase wind speed (Vecchi and Soden, 2007; Nolan and Rappin, 2008), while the latter would increase spatial gradients of atmospheric pressure. An increase in wind speed was found by Bustos-Usta and Torres-Parra (2022) especially towards the south of the Colombian basin. Finally, Zheng et al. (2019) observed an increase (>150 W/m^2) of WPD in the period 2080–2099 with respect to the historical period mainly in the Colombian basin.

4. Conclusion and remarks

In this study, we investigated large-scale future changes in the V10 patterns for the North Atlantic Ocean and in terms of WPD for the three subregions of interest in the context of climate change. Dynamic downscaling was performed using the WRF-ARW and CESM2 climate scenarios which belong to CMIP6 project. The results of this research provide more information on future changes for the variable V10 and its influence on WPD, but with the advantage of considering high spatial resolution data and several scenarios with different characteristics and having a representation of different radiative forcing of low–medium–high scale in the spectrum according to the IPCC. To the best of our knowledge, this is the first study to carry out dynamical downscaling of CMIP6 data with the aim of analysing offshore wind energy resources in the North Atlantic Ocean.

Overall, the projected future changes in V10 show a decrease for the winter and spring seasons, with some exceptions where positive values are projected such as the west coast of the Iberian Peninsula and Africa. For summer and autumn, the increase was notable for most of the North Atlantic Ocean, but with maximum values seen in the tropical region on an annual scale. In addition, the changes intensify towards the end of the 21st century, and these are greater considering SSP5-8.5. Moreover, for the Iberian

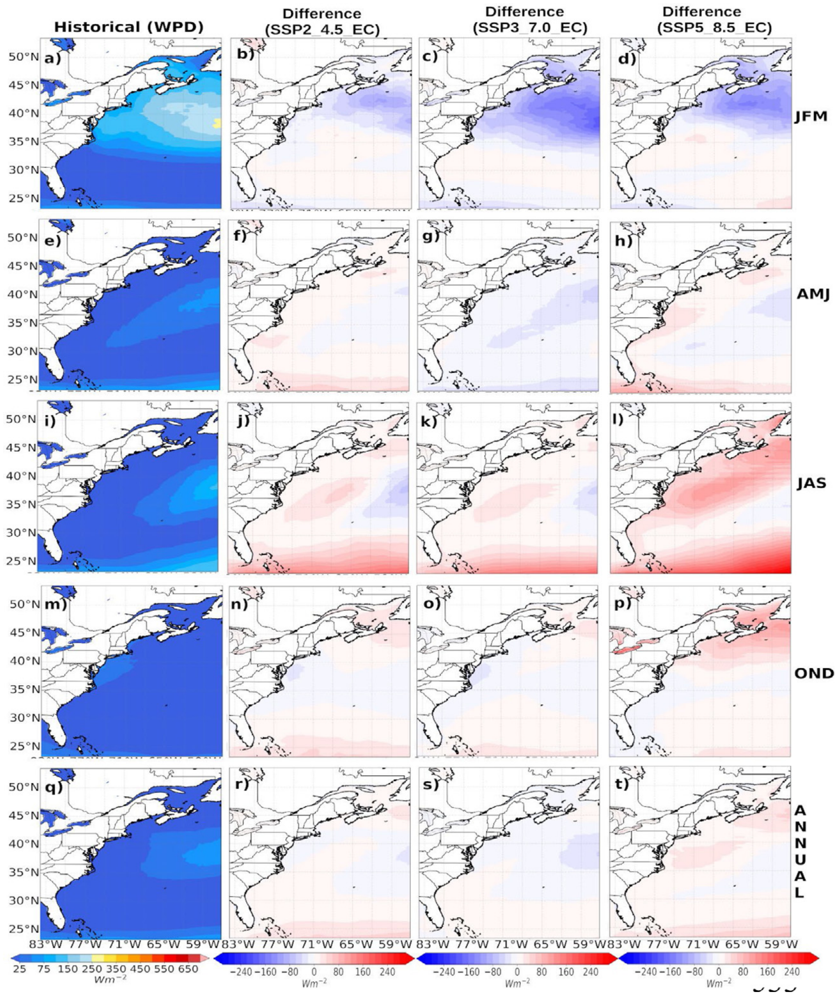

Fig. 8. The WPD for the historical period and the differences between the simulations of WRF-ARW for each of the SSPs in the US subregion. The boreal winter (JFM), spring (AMJ), summer (JAS), autumn (OND), and annually (ANNUAL) fields are displayed from top to bottom. Period: 2096–2100 (EC).

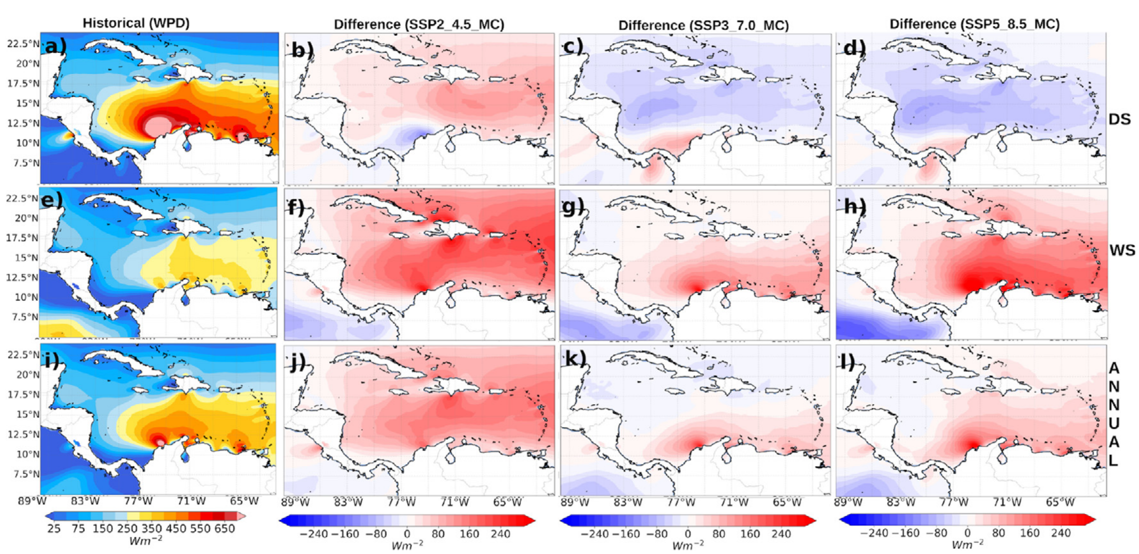

Fig. 9. The WPD for the historical period and the differences between the simulations of WRF-ARW for each of the SSPs in the Caribbean Sea subregion. The dry season (DS), wet season (WS), and annually (ANNUAL) fields are displayed from top to bottom. Period: 2049–2053 (MC).

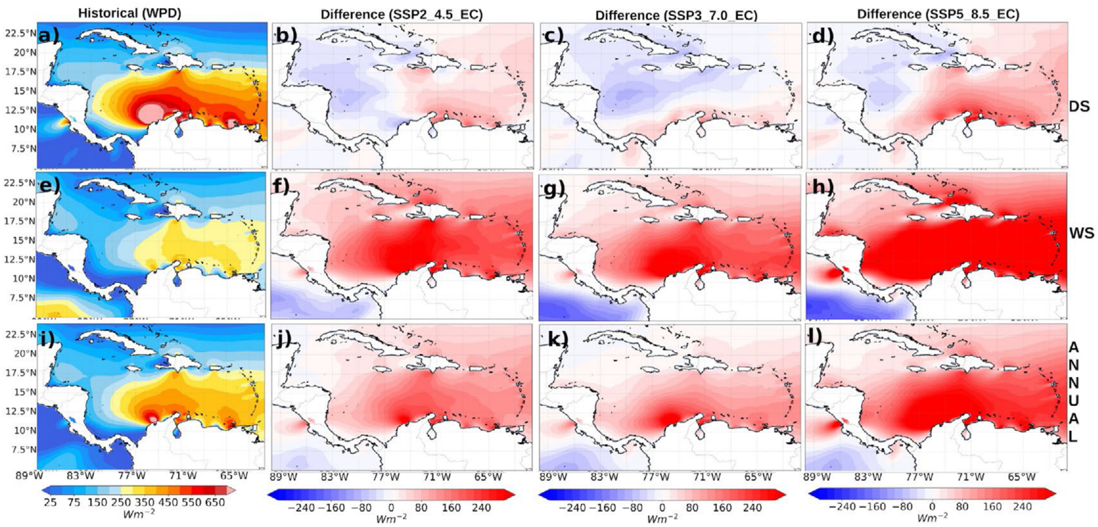

Fig. 10. The WPD for the historical period and the differences between the simulations of WRF-ARW for each of the SSPs in the Caribbean Sea subregion. The dry season (DS), wet season (WS), and annually (ANNUAL) fields are displayed from top to bottom. Period: 2096–2100 (EC).

Peninsula subregion, using the SSPs, will project a considerable increase in autumn and summer for the middle and end of the 21st century. Towards the middle of the 21st century, WRF-ARW using SSP2-4.5 and SSP5-8.5 project a decrease in V10 in winter, except for SSP3-7.0. However, by the end of the 21st century, a notable increase was projected for all the SSPs north of the Iberian Peninsula.

Regarding the US subregion and considering all SSPs, a decrease in WPD is projected in winter and an increase in summer, with limited changes foreseen for the remaining periods. Autumn, for example, is expected to show a slight increase in the northern region of the Atlantic coast at the end of the 21st century. Therefore, the Virginia, North Carolina, and South Carolina coastlines constitute potential wind resource development areas in the future. For the Caribbean Sea subregion, according to the SSPs, a decrease is projected in the dry season in the Yucatan and Colombia basins, which became more pronounced at the end of the 21st century. However, a considerable annual increase in offshore wind power is expected for the Colombia and Venezuela basins and the region north of Española and Cuba. Minimal change was projected for the rest of the area.

The present analysis represents the first attempt to provide WPD projections at high spatial resolution for the whole North Atlantic Ocean. In addition, three areas where a future development of the offshore wind energy industry is expected were analysed more in detail because this information can help policymakers to adapt or modify strategies to improve the efficiency of future offshore wind farms. The approach used in the present analysis can be extended in future research with the aim of downscaling more GCMs to increase the robustness of the results. In addition, the time period and the SSPs can be increased to provide a greater representation of the WPD changes towards the middle and end of the 21st century.

CRediT authorship contribution statement

José C. Fernández-Alvarez: Conceptualization, Methodology, Software, Writing – original draft, Writing – review & editing, Data curation, Formal analysis. **Xurxo Costoya:** Conceptualization, Methodology, Writing – review & editing, Formal analysis. **Albenis Pérez-Alarcón:** Data curation, Software, Methodology, Formal analysis. **Stefan Rahimi:** Software, Data curation. **Raquel Nieto:** Conceptualization, Writing – review & editing, Investigation, Supervision. **Luis Gimeno:** Conceptualization, Writing – review & editing, Investigation, Supervision.

Declaration of competing interest

The authors declare that they have no known competing financial interests or personal relationships that could have appeared to influence the work reported in this paper.

Data availability

ERA5 reanalysis data can be obtained from https://cds.climate.copernicus.eu/cdsapp#!/dataset/reanalysis-era5-single-levels-monthly-means?tab=form and CESM2 model data from https://esgf-data.dkrz.de/search/cmip6-dkrz/. The WRF-ARW outputs are available upon request to the corresponding author.

Acknowledgements

José C. Fernández-Alvarez acknowledge the support from the Xunta de Galicia under the grant no. ED481A-2020/193. Albenis Pérez-Alarcón acknowledges a PhD grant from the University of Vigo. José C. Fernández-Alvarez and Albenis Pérez-Alarcón thank the EU-IACOBUS scholarship. Xurxo Costoya is supported by the Spanish Government through a Juan de la Cierva Postdoctoral Fellowship (JC2020-043745-I). This work is supported by the SETESTRELO project (PID2021-122314OB-I00) funded by the Ministerio de Ciencia, Innovación *y* Universidades, Spain. Partial support was also obtained from the Xunta de Galicia under the project "Programa de Consolidación e Estructuración de Unidades de Investigación Competitivas (Grupos de Referencia Competitiva)" (ED431C 2021/44). In addition, this work has been possible thanks to the computing resources and technical support provided by CESGA (Centro de Supercomputación de Galicia).

Appendix A. Supplementary data

Supplementary material related to this article can be found online at https://doi.org/10.1016/j.egyr.2022.12.036.

References

Alizadeh-Choobari, O., Zawar-Reza, P., Sturman, A., 2014. The wind of 120 days and dust storm activity over the Sistan Basin. Atmos. Res. 143, 328–341. http://dx.doi.org/10.1016/j.atmosres.2014.02.001.

Alsarraf, H., Van Den Broeke, M., 2015. Using the WRF regional climate model to simulate future summertime wind speed changes over the Arabian Peninsula. J. Climatol. Weather Forecast. 1–8. http://dx.doi.org/10.4172/2332-2594.1000144.

Angeles, M.E., González, J.E., Erickson, III.D.J., Hernández, J.L., 2010. The impacts of climate changes on the renewable energy resources in the Caribbean region. J. Sol. Energy Eng. 132, 031009-1-031009-13. http://dx.doi.org/10.1115/1.4001475.

Belmonte, Rivas M., Stoffelen, A., 2019. Characterizing ERA-Interim and ERA5 surface wind biases using ASCAT. Ocean Sci. 15, 831–852. http://dx.doi.org/10.5194/os-15-831-2019.

Brown, B., Ebert, E., Fowler, T., Gilleland, E., Kucera, P., Wilson, L., 2013. Verification Methods for Tropical Cyclone Forecasts. WMO Technical Document WWRP 2013-7, p. 7.

Bruyère, C.L., Monaghan, A.J., Steinhoff, D.F., Yates, D., 2015. Bias-corrected CMIP5 CESM data in WRF/MPAS intermediate file.

Bustos-Usta, D.F., Torres-Parra, R.R., 2021. Ocean and atmosphere changes in the Caribbean Sea during the twenty-first century using CMIP5 models. Ocean Dyn. http://dx.doi.org/10.1007/s10236-021-01462-z.

Bustos-Usta, D.F., Torres-Parra, R.R., 2022. Projected wind changes in the Caribbean Sea based on CMIP6 models. Clim. Dyn. 1–15. http://dx.doi.org/10.1007/s00382-022-06535-3.

Cai, Y., Breon, F.M., 2021. Wind power potential and intermittency issues in the context of climate change. Energy Convers. Manage. 240, 114276. http://dx.doi.org/10.1016/j.enconman.2021.114276.

Carvalho, D., Rocha, A., Costoya, X., deCastro, M., Gómez-Gesteira, M., 2021. Wind energy resource over Europe under CMIP6 future climate projections: What changes from CMIP5 to CMIP6. Renew. Sust. Energ. Rev. 151, 111594. http://dx.doi.org/10.1016/j.rser.2021.111594.

Collins, M., et al., 2013. Long-term climate change: projections, commitments and irreversibility. In: Climate Change 2013-the Physical Science Basis: Contribution of Working Group I To the Fifth Assessment Report of the Intergovernmental Panel on Climate Change (1029–1136). Cambridge University Press.

Costoya, X., DeCastro, M., Carvalho, D., Gómez-Gesteira, M., 2020b. On the suitability of offshore wind energy resource in the United States of America for the 21st century. Appl. Energy 262, 114537. http://dx.doi.org/10.1016/j.apenergy.2020.114537.

Costoya, X., DeCastro, M., Santos, F., Sousa, M.C., Gómez-Gesteira, M., 2019. Projections of wind energy resources in the Caribbean for the 21st century. Energy 178, 356–367. http://dx.doi.org/10.1016/j.energy.2019.04.121.

Costoya, X., Rocha, A., Carvalho, D., 2020a. Using bias-correction to improve future projections of offshore wind energy resource: A case study on the Iberian Peninsula. Appl. Energy 262, 114562. http://dx.doi.org/10.1016/j.apenergy.2020.114562.

Danabasoglu, G., Lamarque, J.F., Bacmeister, J., Bailey, D.A., DuVivier, A.K., Edwards, J., et al., 2020. The community earth system model version 2 (CESM2). J. Adv. Model. Earth Syst. 12, e2019MS001916. http://dx.doi.org/10.1029/2019MS001916.

deCastro, M., Salvador, S., Gómez-Gesteira, M., Costoya, X., Carvalho, D., Sanz-Larruga, F.J., Gimeno, L., 2019. Europe, China and the United States: Three different approaches to the development of offshore wind energy. Renew. Sust. Energ. Rev. 109, 55–70. http://dx.doi.org/10.1016/j.rser.2019.04.025.

Enfield, D.B., Alfaro, E.J., 1999. The dependence of Caribbean rainfall on the interaction of the tropical Atlantic and Pacific Oceans. J. Clim. 12, 2093–2103. http://dx.doi.org/10.1175/1520-04421999.012<2093:TDOCRO>2.0.CO;2.

Eyring, V., Bony, S., Meehl, G.A., Senior, C.A., Stevens, B., Stouffer, R.J., Taylor, K.E., 2016. Overview of the Coupled Model Intercomparison Project Phase 6 (CMIP6) experimental design and organization. Geosci. Model Dev. 9, 1937–1958. http://dx.doi.org/10.5194/gmd-9-1937-2016.

Fant, C., Schlosser, C.A., Strzepek, K., 2016. The impact of climate change on wind and solar resources in southern africa. Appl. Energy 161, 556–564. http://dx.doi.org/10.1016/j.apenergy.2015.03.042.

Gallagher, S., Gleeson, E., Tiron, R., McGrath, R., Dias, F., 2016. Twenty-first century wave climate projections for Ireland and surface winds in the North Atlantic Ocean. Adv. Sci. Res. 13, 75–80. http://dx.doi.org/10.5194/asr-13-75-2016.

González, A., Pérez, J.C., Díaz, J.P., Expósito, F.J., 2017. Future projections of wind resource in a mountainous archipelago, Canary Islands. Renew. Energy 104, 120–128. http://dx.doi.org/10.1016/j.renene.2016.12.021.

GWEC, 2021. Global offshore wind report 2020. Global wind energy council. https://gwec.net/global-offshore-wind-report-2021/ Accessed 12 2021.

Hersbach, H., Bell, B., Berrisford, P., Hirahara, S., Horányi, A., J., Muñoz-Sabater, et al., 2020. The ERA5 global reanalysis. Q. J. R. Meteorol. Soc. 146, 1999–2049. http://dx.doi.org/10.1002/qj.3803.

Hong, S.Y., Lim, JOJ., 2006. The WRF single-moment 6-class microphysics scheme (WSM6). J. Meteorol. Soc. Japan 42, 129–151. http://dx.doi.org/10.1155/2010/707253.

Hong, S.Y., Noh, Y., Dudhia, J., 2006. A new vertical diffusion package with an explicit treatment of entrainment processes. Mon. Weather Rev. 134, 2318–2341. http://dx.doi.org/10.1175/MWR3199.1.

Iacono, M.J., Delamere, J.S., Mlawer, E.J., Shephard, M.W., Clough, S.A., Collins, W.D., 2008. Radiative forcing by long–lived greenhouse gases: Calculations with the AER radiative transfer models. J. Geophys. Res. 113, D13103. http://dx.doi.org/10.1029/2008JD009944.

Insua-Castro, D., Miguez-Macho, G., 2018. A new moisture tagging capability in the Weather Research and Forecasting model: formulation, validation and application to the 2014 Great lake-effect snowstorm. Earth Syst. Dyn. 9, 167–185. http://dx.doi.org/10.5194/esd-9-167-2018.

Insua-Castro, D., Miguez-Macho, G., Llasat, M.C., 2019. Local and remote moisture sources for extreme precipitation: a study of the two catastrophic 1982 western Mediterranean episodes. Hydrol. Earth Syst. Sci. 23, 3885–3900. http://dx.doi.org/10.5194/hess-23-3885-2019.

IPCC, 2021. Climate change 2021: The physical science basis. In: Contribution of Working Group I To the Sixth Assessment Report of the Intergovernmental Panel on Climate Change. Cambridge University Press, In Press.

Jimenez, P.A., Dudhia, J., Gonzalez-Rouco, J.F., Navarro, J., Montavez, J.P., Garcia-Bustamante, E., 2012. A revised scheme for the WRF surface layer formulation. Mon. Weather Rev. 140, 898–918. http://dx.doi.org/10.1175/MWR-D-11-00056.1.

Johnson, D.L., Erhardt, R.J., 2016. Projected impacts of climate change on wind energy density in the United States. Renew. Energy 85, 66–73. http://dx.doi.org/10.1016/j.renene.2015.06.005.

Kain, J.S., 2004. The Kain–Fritsch convective parameterization: An update. J. Appl. Meteorol. 43, 170–181. http://dx.doi.org/10.1175/1520-04502004.043<0170:TKCPAU>2.0.CO;2.

Kalverla, P.C., Duncan, Jr., J.B., Steeneveld, G.J., Holtslag, A.A.M., 2019. Low-level jets over the North Sea based on ERA5 and observations: together they do better. Wind Energy Sci. 4, 193–209. http://dx.doi.org/10.5194/wes-4-193-2019.

Kulkarni, S., Huang, H.P., 2014. Changes in surface wind speed over North America from CMIP5 model projections and implications for wind energy. Adv. Meteorol. 2014.

Liu, B., Costa, K.B., Xie, L., Semazzi, F.H., 2014. Dynamical downscaling of climate change impacts on wind energy resources in the contiguous United States by using a limited-area model with scale-selective data assimilation. Adv. Meteorol. 2014, http://dx.doi.org/10.1155/2014/897246.

Martinez, A., Iglesias, G., 2021. Wind resource evolution in Europe under different scenarios of climate change characterised by the novel Shared Socioeconomic Pathways. Energy Convers. Manage. 234, 113961. http://dx.doi.org/10.1016/j.enconman.2021.113961.

Miguez-Macho, G., Stenchikov, G.L., Robock, A., 2004. Spectral nudging to eliminate the effects of domain position and geometry in regional climate model simulations. J. Geophys. Res.: Atmos. 109, 1–15. http://dx.doi.org/10.1029/2003JD004495.

Moemken, J., Reyers, M., Feldmann, H., Pinto, J.G., 2018. Future changes of wind speed and wind energy potentials in EURO-CORDEX ensemble simulations. J. Geophys. Res. Atmos. 123, 6373–6389. http://dx.doi.org/10.1029/2018JD028473.

Musial, W., Heimiller, D., Beiter, P., Scott, G., Draxl, C., 2016. Offshore Wind Energy Resource Assessment for the United States. Technical Report, NREL/TP-5000-66599, National Renewable Energy Laboratory.

Nolan, D.S., Rappin, E.D., 2008. Increased sensitivity of tropical cyclogenesis to wind shear in higher SST environments. Geophys. Res. Lett. 35, 148–165. http://dx.doi.org/10.1029/2008GL034147.

Olauson, J., 2018. ERA5: The new champion of wind power modelling? Renew. Energy 126, 322–331. http://dx.doi.org/10.1016/j.renene.2018.03.056.

O'Neill, B.C., et al., 2016. The scenario model intercomparison project (scenariomip) for CMIP6. Geosci. Model Dev. 9, 3461–3482. http://dx.doi.org/10.5194/gmd-9-3461-2016.

Pryor, S.C., Schoof, J.T., Barthelmie, R.J., 2006. Winds of change? Projections of near-surface winds under climate change scenarios. Geophys. Res. Lett. 33, L11702. http://dx.doi.org/10.1029/2006GL026000.

Ramírez, L., Brindley, G., Fraile, D., 2021. Offshore wind in Europe: Key trends and statistics 2020. https://windeurope.org/intelligence-platform/product/offshore-wind-in-europe-key-trends-and-statistics-2020/. Accessed 21 2021.

Renault, L., McWilliams, J.C., Masson, S., 2017. Satellite observations of imprint of oceanic current on wind stress by air-sea coupling. Sci. Rep. 7, 17747. http://dx.doi.org/10.1038/s41598-017-17939-1.

Riahi, K., Van Vuuren, D.P., Kriegler, E., Edmonds, J., O'neill, B.C., Fujimori, S., Bauer, N., Calvin, K., Dellink, R., Fricko, O., 2017. The shared socioeconomic pathways and their energy, land use, and greenhouse gas emissions implications: an overview. Glob. Environ. Change 42, 153–168. http://dx.doi.org/10.1016/j.gloenvcha.2016.05.009.

Ruosteenoja, K., Vihma, T., Venäläinen, A., 2019. Projected changes in European and North Atlantic seasonal wind climate derived from CMIP5 simulations. J. Clim 32, 6467–6490. http://dx.doi.org/10.1175/JCLI-D-19-0023.s1.

Salvador, S., Costoya, X., Sanz-Larruga, F.J., Gimeno, L., 2018. Development of offshore wind power: Contrasting optimal wind sites with legal restrictions in Galicia, Spain. Energies 11, 731. http://dx.doi.org/10.3390/en11040731.

Santos, F., Gómez-Gesteira, M., Añel, J.A., Carvalho, D., Costoya, X., Dias, J.M., 2018. On the accuracy of CORDEX RCMs to project future winds over the Iberian Peninsula and surrounding ocean. Appl. Energy 228, 289–300. http://dx.doi.org/10.1016/j.apenergy.2018.06.08608.

Shen, C., Zha, J., Li, Z., Molina, C.Azorin., Deng, K., Minola, L., Chen, D., 2022. Evaluation of global terrestrial near-surface wind speed simulated by CMIP6 models and their future projections. Ann. New York Acad. Sci. http://dx.doi.org/10.1111/nyas.14910.

Simpson, I.R., et al., 2020. An evaluation of the large-scale atmospheric circulation and its variability in CESM2 and other CMIP models. Geophys. Res. Atmos. 125, e2020JD032835. http://dx.doi.org/10.1029/2020JD032835.

Skamarock, W., Klemp, J., Dudhi, J., Gill, D., Barker, D., Duda, M., Huang, X., Wang, W., Powers, J., 2008. A Description of the Advanced Research WRF Version 3. Technical Report, 113, http://dx.doi.org/10.5065/D6DZ069T.

Soares, P.M., Lima, D.C., Cardoso, R.M., Nascimento, M.L., Semedo, A., 2017. Western Iberian offshore wind resources: More or less in a global warming climate? Appl. Energy 203, 72–90. http://dx.doi.org/10.1016/j.apenergy.2017.06.004.

Stocker, T.F., Dahe, Q., Plattner, G.-K., 2013. Climate change 2013: the physical science basis. Work. Group Contrib. Fifth Assess. Rep. Intergov. Panel Clim. Change Summ. Policymakers IPCC 2013.

Swart, R., Coppens, C., Gordijn, H., Piek, M., Ruyssenaars, P., Schrander, J., Smet, P.D., Hoogwijk, M., Papalexandrou, M., deVisser, E., et al., 2009. Europe's Onshore and Offshore Wind Energy Potential: An Assessment of Environmental and Economic Constraints. (No. 6/2009). European Environment Agency.

Tewari, M., Chen, F., Wang, W., Dudhia, J., LeMone, M., Mitchell, K., et al., 2004. Implementation and verification of the unified noah land surface model in the WRF model. In: 20th Conference on Weather Analysis and Forecasting/16th Conference on Numerical Weather Prediction. Seattle, WA.

Ulazia, A., Nafarrate, A., Ibarra-Berastegi, G., Sáenz, J., Carreno-Madinabeitia, S., 2019. The consequences of air density variations over northeastern scotland for offshore wind energy potential. Energies 12, 2635. http://dx.doi.org/10.3390/en12132635.

Vecchi, G.A., Soden, B.J., 2007. Increased tropical atlantic wind shear in model projections of global warming. Geophys. Res. Lett. 34, 87–102. http://dx.doi.org/10.1029/2006GL028905.

Wang, R., Liu, B., Li, H., et al., 2017. Variation of strong dust storms events in northern China during 1978–2007. Atmos. Res. 183, 166–172. http://dx.doi.org/10.1016/j.atmosres.2016.09.002.

Wright, R.M., 2001. Wind energy development in the Caribbean. Renew. Energy 24, 439–444. http://dx.doi.org/10.1016/j.renene.2018.05.090.

Yamada, T., Mellor, G., 1975. A simulation of the Wangara atmospheric boundary layer data. J. Atmos. Sci. 32, 2309–2329. http://dx.doi.org/10.1175/1520-04691975.032<2309:ASOTWA>2.0.CO;2.

Yao, Z., Xue, Z., He, R., Bao, X., Song, J., 2016. Statistical downscaling of IPCC sea surface wind and wind energy predictions for US east coastal ocean, Gulf of Mexico and Caribbean Sea. J. Ocean Univ. China 15, 577e82. http://dx.doi.org/10.1007/s11802-016-2869-0.

Zheng, C.W., 2018. Wind energy evaluation of the 21st Century MaritimeSilk Road. J. Harbin Eng. Univ. 39 (1), 16–22.

Zheng, C.W., Li, X.Y., Luo, X., Chen, X., Qian, Y.H., Zhang, Z.H., Chen …, Y.G., 2019. Projection of future global offshore wind energy resources using CMIP data. Atmos. - Ocean 57 (2), 134–148. http://dx.doi.org/10.1080/07055900.2019.1624497.

Zheng, C.W., Pan, J., 2014. Assessment of the global ocean wind energyresource. Renew. Sustain. Energy Rev. 33, 382–391.

Zheng, C.W., Pan, J., Li, C.Y., 2016. Global oceanic wind speed trends. Ocean Coast. Manag. 129, 15–24. http://dx.doi.org/10.1016/j.ocecoaman.2016.05.001.

Zheng, C.W., et al., 2022. A positive climatic trend in the global offshore wind power. Front. Energy Res. 10, 867642. http://dx.doi.org/10.3389/fenrg.2022.867642.

5

Summary, conclusions, limitations, and future works

The study of the moisture source-sink relationship is important for understanding the hydrological cycle, even more so under climate change, with a greater capacity of the atmosphere to retain a greater amount of water vapour according to the Clausius–Clapeyron equation. Consequently, a higher evaporation rate over the ocean and increased IVT have been projected. However, modifications to the V10 pattern and offshore wind energy density are expected, which may influence energy planning for future climates in regions such as the North Atlantic. Therefore, the general objective of this thesis was to determine the future changes in atmospheric moisture and wind field using numerical simulation and its implications for moisture transport and wind energy.

To fulfil the objectives, this study used a dynamic downscaling methodology that considered the WRF-ARW atmospheric model and FLEXPART-WRF dispersion model. The ability to represent moisture sources and sinks in the present climate was evaluated and compared to that of a control experiment. The data used for the present climate were ERA-I and ERA5 reanalyses and those for the future climate were the CESM2 model outputs. To study the wind field, the following periods were used: historical 2010–2014 (HIST_5Y), mid-century 2049–2053 (MC_5Y), and end of the century 2096–2100 (EC_5Y). In addition, the climate scenarios SSP2-4.5, SSP3-7.0, and SSP5-8.5 were considered. Regarding the analysis of moisture transport, only SSP5-8.5 was used but over 30 years (HIST: 1985–2014, MC: 2036–2065, and EC: 2071–2100). Finally, future changes in the intensity and position of the moisture sources associated with the LARs arriving at the Iberian Peninsula were analysed for future climate considering the SSP5-8.5 scenario and the long (30 years) HIST, MC, and EC periods. An original free online software (TROVA) was developed to process the outputs of these models and obtain the necessary fields for the different studies. The results presented below are ordered according to the objectives set in the development of this doctoral thesis.

5.1 Main results

5.1.1 TROVA software

The results of the first article are mainly associated with the advantages of the TROVA software. These are as follows:

- TROVA facilitates the application of different methodologies for quantifying the moisture source-sink relationship using the outputs from the Lagrangian FLEXPART and FLEXPART-WRF models.
- This allows any resolution of the input and output data to be used in moisture source and sink studies, similar to the masks used.
- The software can be used for the outputs of the dispersion models forced by both ERA-I and ERA5.
- As TROVA allows the use of FLEXPART-WRF model outputs, it can be used to analyse high-resolution WRF regional model outputs. It is a regional model through which it is possible to obtain data from CMIP6 models adapted to run with FLEXPART-WRF. Thus, it is possible to analyse modifications in the strength and location of moisture sources and sinks using this software.
- TROVA has good computational efficiency because it was developed using parallel programming, allowing its use in supercomputers.
- It is free software (open source) implemented in Fortran and Python and is available to the scientific community.

5.1.2 Moisture sources and sinks representation using the ERA5 reanalysis

The results in this study correspond to the evaluation of ERA5 data to reproduce the pattern of moisture sources or sinks (at 1° and 0.5° resolutions) using the FLEXPART model and a dynamic downscaling methodology using WRF-ARW and FLEXPART-WRF. They were compared to the climatological field used in numerous investigations with FLEXPART but using ERA-I at 1° ("control experiment"). The evaluated moisture sources were the Mediterranean Sea (MED) and North Atlantic (NATL) and the moisture sink was the Iberian Peninsula (IP).

Moisture sources

- The seasonal and annual results for the moisture source patterns that contribute to the Iberian Peninsula considered as a sink are as follows:
  - The correlation of the moisture source pattern using ERA5 with the control values for the three configurations ranged from 0.4–0.6. The configuration with the highest correlation was FLEXPART using ERA5 at 0.5°; while FLEX-WRF exhibited the lowest correlation.
  - The configurations did not differ much in absolute error and root mean square error but the maximum errors were observed in summer, with different behaviours in winter and spring.
  - In spring and summer, the FLEX-WRF model showed the best representation of the source pattern in mountainous regions, in addition to the periods where precipitation recycling processes predominated.
  - The ability of the WRF-ARW and FLEXPART-WRF models to adequately represent the local moisture transport processes outstanding compared to the other configurations used.

Sink sources

- For the moisture sink study from the Mediterranean Sea source, the three configurations evaluated with the control experiment showed a low dispersion and maximum values of R $\geq$ 0.6. Additionally, the following observations were made:
  - The coefficient of determination varied from 0.3 to 0.6, showing high correlation values. FLEX-ERA5.05 showed the best behaviour reliability for these statisticians in the periods considered. However, the coefficient of variation was lower for the FLEX-WRF model.
  - A lower mean absolute error was obtained compared to the values showed for the moisture sources associated with the Iberian Peninsula, which is notable considering that the magnitude of the humidity budget for the Mediterranean source was greater.
  - The root mean square error was greater in summer but decreased in autumn.
  - Similar to the Iberian Peninsula results, FLEX-WRF was the most appropriate configuration to represent the moisture sink pattern in regions with complex orography (e.g., the Alps, Balkan Peninsula, and Eastern Europe).

- The sinks determined by the North Atlantic source had greater longitudinal and latitudinal extensions, implying greater difficulty in the configurations in representing the pattern of associated sinks. Specifically, in this case, the following was obtained.
  - The correlation between the three configurations and control experiment ranged from 0.4–0.7.
  - The mean absolute errors and the root mean square error show values up to 2.5 mm/day and 4.5 mm/day respectively. This increase was notable compared to when masks of the Iberian Peninsula and Mediterranean Sea were used.
  - FLEX-WRF showed a lower ability to show the pattern compared with the control experiment, showing an underestimation of the values in areas with maxima.
  - Over the North Atlantic Basin, FLEX-WRF presented certain deficiencies; therefore, for the present climate, FLEXPART forced with ERA5 at 0.5° and 1° should be used.

5.1.3 Future changes in atmospheric moisture transport for the North Atlantic region

The results below show the future changes in moisture sources and sinks under SSP5-8.5 scenario and the following future periods: MC: 2036–2065 and EC: 2071–2100. Other fields related to moisture transport and atmospheric configurations (e.g., geopotential height at 500 hPa (Z500), precipitation, and vertical integral of water vapour transport (IVT)) were previously validated and analysed for future climates to complete the study of the extended North Atlantic region.

Changes in the precipitation field, geopotential height at 500 hPa and IVT

- **Precipitation**
  - Annually, by the end of the century (2071–2100), a decrease in precipitation was projected over the Iberian Peninsula, the Mediterranean Sea, and its surroundings.
  - Increases were projected over the Atlantic coast of the United States and Canada and in the Bermuda region and greater in the southwestern region of the North Atlantic.
  - Future changes in the precipitation field showed a spatial similarity between the MC and EC but the signal was amplified in the latter period.
- **Geopotential height at 500 hPa**
  - A generalised increase in Z500 was projected over the North Atlantic during both periods. The largest increase during these periods is expected over subtropical regions (e.g., the northeastern United States and Canada's Atlantic coast).
  - Conversely, little annual change was projected over regions influenced by the Icelandic Low, shows, mainly in winter.

- <u>**Vertical integral of water vapor transport**</u>
  - An increase in IVT was projected over mid-latitude regions of the North Atlantic, Caribbean Sea, and United States Atlantic coast; however, a decrease in summer was projected over tropical and subtropical regions located in the North Atlantic.
  - The maximum IVT fields project a latitudinal shift and the maximum percentage values of the IVT versus the HIST follow a Clausius–Clapeyron relationship.
  - These changes were notable in both periods but more pronounced at end of the century.

Future changes associated with the moisture that contributes to the Iberian Peninsula

- The Iberian Peninsula will receive a greater moisture contribution from the extratropical regions, North Atlantic, and Mediterranean Sea in both future periods.
- In MC, a smaller annual increase was projected over the southern North Atlantic Ocean basin and western Mediterranean Sea. Regarding the EC, a more accentuated version of the changes with respect to MC was projected.
- A significant increase in precipitation recycling processes was projected over the Iberian Peninsula in winter, with annual increases between 2 and 8 %.

Future changes in the precipitation contribution from moisture sources: Mediterranean Sea and North Atlantic

- The increases in the North Atlantic and Mediterranean Sea moisture contributions over the Iberian Peninsula were compatible with the Clausius-Clapeyron amplification. For both MC and EC, a noticeable increase in evaporation was projected over the North Atlantic and a smaller increase for the Mediterranean Sea.
- The results showed a slight latitudinal shift for moisture coming from the North Atlantic source region at EC and a decrease in its contribution in regions close to Europe and above 40 °N.
- The Mediterranean Sea moisture source was projected to notably increase for northern Africa (southern region) in both periods and on the east coast of the Iberian Peninsula, mainly in summer (more accentuated at the end of the century). However, a general decrease was projected for the eastern part of Europe, and for the western part in spring and summer.

- The contribution of the North Atlantic source to the Atlantic coast of the United States in the winter and autumn and to a lesser extent to the British Isles in winter was projected to increase. However, a decrease is expected in its contribution to the western coast of Europe to the coast of Africa.

5.1.4 Future changes in moisture sources associated with Atmospheric Rivers arriving at the Iberian Peninsula

The study of the ARs in the North Atlantic Basin, particularly those that make landfall (LARs) to the Iberian Peninsula, shows important changes in both position and intensity, mainly at the end of the century, but are most notable in the anomalous moisture uptake, as will be shown below. For this analysis, the WRF-ARW model fed with CESM2 and FLEXPART-WRF model fed with the outputs of this regional climate model were used. Furthermore, to ensure a correct representation of the analysed climatological variables, simulations were carried out using FLEXPART-WRF and evaluated. For this purpose, ERA5 was used as a forcer. Specifically, the same procedure was followed as used for CESM2 but with these simulations and reanalysis as a control experiment. The results demonstrated a high degree of similarity between the forced model and climate data. After the ability to detect ARs and their moisture sources was confirmed, future changes in the intensity and position of ARs for the IVT in the North Atlantic region, the distribution of moisture sources, and AMU were determined. The future periods considered were MC (2036–2065) and EC (2071–2100) under SSP5-8.5.

Changes in intensity and position of the North Atlantic Atmospheric Rivers

- A position northward shift for centroids AR was projected at EC and a progressive strengthening of ARs was simulated throughout the century, with maximum values of approximately 750 kg m^{-1} s^{-1} for IVT at EC. The mean meridional moisture flux will increase at EC.

- The northward shift was related to the displacement of the North Atlantic Storm Track simulated under different scenarios.

- The ARs at MC and EC are expected to be slightly smaller in length than those at HIST.

- Advective dynamics were projected to increase in the future of ARs, particularly notable in LARs and at EC. This is particularly greater in regions where moisture transport predominates, allowing the intrusion of moisture from its sources to the Iberian Peninsula for days with LAR.

Projected Changes in the Moisture Sources associated with ARs arriving the Iberian Peninsula

- In general, a reinforcement of the anomalous moisture uptake (AMU) and a displacement of this pattern with respect to the historical period towards high latitudes was observed.
- The reinforcement of AMU was observed in winter, with percentage changes of 9 % and 24 % at MC and EC, respectively. Seasonal differences were observed; the change was lower in spring, at 2 % (MC) and 9 % (EC), but was greater in summer, at 17 % (MC) and 22 % (EC).
- It is expected that during MC in winter, autumn, and annually, the AMU will increase in the region over the central North Atlantic and at latitudes greater than 20 °N; however, below 20 °N, it will decrease slightly.
- In winter, at EC, the maximum changes in the AMU variable were projected to be in regions in the Western-Central Atlantic and Gulf of Mexico.
- In autumn, moisture sources were simulated to be more remote because the maximum changes in AMU are observed around the east coast of the United States.
- The moisture source from the Gulf of Mexico was projected to provide less moisture contribution to the LARs at EC because the maximum values of AMU were located in more northern regions of the North Atlantic.

5.1.5 Future changes for wind speed and wind power density (WPD) over the North Atlantic Ocean

The results below correspond to variations in wind speed at 10 m (V10) in the North Atlantic Ocean and wind power density (WPD) for three subregions with wind potential (the Atlantic coast of the Iberian Peninsula, the east coast of the United States, and the Caribbean Sea region) in the context of climate change. Dynamic downscaling of data from the CESM2 climate model was performed using the WRF-ARW regional model. Three SSPs were considered: SSP2-4.5, SSP3-7.0, and SSP5-8.5. The V10 field was compared to the ERA5 reanalysis for the historical period (HIST). For the analysis, 5-year periods were used: HIST, 2010–2014 (HIST_5Y); mid-century 2049–2053 (MC_5Y); and end of the century 2096–2100 (EC_5Y).

Future changes for V10 in the North Atlantic Ocean for the SSPs

In the following subparagraphs, the changes for V10 in the North Atlantic Ocean in the MC_5Y period under the three different SSPs are presented. It is highlighted that few changes are observed in the general shape for EC_5Y compared to MC_5Y under SSP2-4.5 and SSP3-7.0; however, under SSP5-8.5 for EC_5Y these changes are amplified with the increase in radiative forcing.

- Under SSP2-4.5, V10 decreased above latitudes of 30 °N during winter for MC_5Y but increased below 30 °N, excluding the eastern Caribbean Sea. A decline was projected in spring for most of the North Atlantic Ocean, except for the Caribbean Sea. In addition, increases were projected for summer and autumn, excluding the southern United States coastal regions.
- Under SSP3-7.0, V10 decreased except over the Iberian Peninsula and the West African zone. Furthermore, in the summer and autumn seasons, an increase was projected over the Caribbean Sea, United States coast, and Atlantic coast of the Iberian Peninsula, but the values were relatively lower than those shown under SSP2-4.5. Regarding the annual average, few future changes were projected, except in areas along the coast of Africa and northwest of the Iberian Peninsula.
- Under SSP5-8.5, significant variations were observed V10 in winter, with marked decreases observed over the Caribbean Sea and African coast and at latitudes over 50 °N. In addition, a general increase in the North Atlantic Ocean region was observed during summer and autumn.

Future changes for the wind power density (WPD)

As previously mentioned, the regions analysed for the WPD study were located on each side of the North Atlantic Basin. The results for each region are presented below.

- **Atlantic coast of the Iberian Peninsula**

  The changes for WPD for the Atlantic coast of the Iberian Peninsula in the MC_5Y period considering the different SSPs are detailed below. Regarding EC_5Y under the three SSPs, increases were projected over the north of the Iberian Peninsula for the winter season, extending the pattern to 40 °N. An increase in the signal was observed under SSP5-8.5.

- Under SSP2-4.5, WPD decreased in winter, with maximum changes on the north of the Iberian Peninsula. However, in spring, an almost general increase was projected for the western coast of the Iberian Peninsula, with a maximum in the northwestern Iberian Peninsula. In summer, the expected changes on the coast of the Iberian Peninsula (> 100 W/m^2) stood out but were more marked from the Galician coast to the north of Portugal.
- Under SSP3-7.0, the WPD pattern increased in winter, with maximum values over the northern region of the Iberian Peninsula but a general decrease was observed over the entire coast of the Iberian Peninsula. In summer and autumn, notable changes were simulated on the northwest of the Iberian Peninsula, with little change on an annual scale.
- Under SSP5-8.5, in autumn, WPD increased over the Iberian Peninsula in the north.

- **United States east coast subregion**

  The WPD changes in the United States east coast subregion in the MC_5Y period under the SSPs are detailed below. For EC_5Y, using the three scenarios, a decrease in the WPD pattern in winter but an increase in summer was projected. Furthermore, there was little variation in the remaining seasons, except autumn. In addition, the northernmost states on the Atlantic coast were projected to increase slightly. Finally, a considerable decrease under SSP3-7.0 was projected for this region and increase for the summer under SSP5-8.5.

  - Under SSP2-4.5, WPD decreased north of 35 °N, with notable increases on the coast of Maine, Massachusetts, New Hampshire, and New Jersey, United States. However, in summer, notable increases were projected for North Carolina, South Carolina, and Virginia.
  - For the WPD pattern, a decrease in winter but increase were projected in autumn for the northern states under SSP3-7.0. Different changes were projected during the remaining periods.
  - Under SSP5-8.5, an opposite pattern was observed, with increases below and decreases above 40 °N for the winter season. No significant changes were observed during the remaining periods.

- **Caribbean Sea subregion**

  Similar to the previous subregions, the changes are presented for MC_5Y. In this case, for EC_5Y, a marked increase was observed, with WPD values > 240 W/m^2 in the study region except for the Yucatan Basin in the wet season (May-November) under the three SSPs. In the other seasons, the decrease in the Yucatan and Colombia basins was prominent, although a discrete increase was observed on the coast of Venezuela.

- In the dry season under SSP2-4.5 for MC_5Y, the WPD increased from the Venezuela Basin to the western Caribbean Sea but decreased near the coast of Colombia. During the wet season, an increase was projected over the Colombian and Venezuelan Basins and near La Española and Cuba. Annually, the Venezuelan basin showed an increase in WPD from 80–160 W/m^2.
- A general decrease was observed over the Caribbean Sea during the dry season under SSP3-7.0. During the wet season, increases were projected around the coasts of Colombia and Venezuela. Except for the coast of Colombia, little annual change was expected.
- Similar changes in WPD were observed under SSP5-8.5 and SSP3-7.0 but those predicted under SSP2-4.5 differed, with the latter projecting a general increase in the Caribbean Sea subregion.

5.2 General conclusions

Based on the previous results for each proposed objective, the following general conclusions were drawn.

1. The TROVA software benefits users who investigate moisture transport in the atmosphere and the variables related to this component of the hydrological cycle in studies of the present climate and future changes in moisture source-sink relationships and their relationship with precipitation.

2. The FLEXPARTv10.3 dispersion model fed with ERA5 data at different spatial resolutions reproduced the moisture source and sink regions, as represented by ERA-Interim. The configuration evaluation versus the ERA-I reanalysis showed little difference between the reanalyses in terms of moisture sources and sinks.

3. The dynamic downscaling methodology using WRF forced with ERA5 and FLEXPART-WRF (forced with the WRF outputs) can show moisture sources and sinks, which is an important tool in future research that requires an increase in spatial resolution, particularly for areas with complex orography because they correctly represent local moisture transport.

4. By the end of the century (2071–2100) under SSP5-8.5, moisture from the North Atlantic source will increase its contribution to precipitation in eastern North America in the winter and autumn seasons, but for the British Isles, it is only projected in winter. However, the contribution to precipitation from the Mediterranean Sea allows an increase in precipitation in the southern and western regions of this source.

5. The contribution to precipitation from North Atlantic sources will decrease in Europe and West Africa; however, the contribution associated with the Mediterranean Sea will decrease in Eastern Europe. Precipitation recycling processes will increase in the 21st century, except for summer, in the period 2036–2065 under SSP5-8.5.

6. Under SSP5-8.5, an increase in the strength and moisture transport in the ARs that reach the Iberian Peninsula is projected. A latitudinal shift of the ARs centroids is projected at the end of the century (2071–2100).

7. Moisture sources increase their progressive contribution to landfalling ARs arriving at the Iberian Peninsula, showing a latitudinal shift and a loss of importance in the moisture contribution for regions such as the Gulf of Mexico in summer and autumn.

8. V10 is projected to increase in tropical regions up to 30 °N in the summer and autumn seasons; however, it will decrease in winter and spring. Notable annual changes are projected in tropical belts.

9. Throughout the 21st century, a notable increase in wind energy density is projected in summer over the Atlantic coast of the Iberian Peninsula. A different behaviour is projected over the east coast of the United States, with decreases in winter but increases in summer and autumn. In the Caribbean Sea, marked increases are expected over the Columbia and Venezuela Basins but decreases in the Yucatan Basin.

These conclusions for moisture transport confirm the results obtained by several investigations demonstrating an increase in the moisture contribution from sources following the Clausius–Clapeyron relationship of 7 % K^{-1} (Algarra et al., 2020; Bao et al., 2017; Prein et al., 2017). In addition, the results obtained and the numerical simulations for periods of 30 years will allow the analysis of certain regions of both the present climate and the future occurrence of droughts or modifications in the important mechanisms of moisture transport on a regional scale. The results for wind and WPD will contribute to the improvement of the plan for the use of wind energy in regions of interest and the identification of potential regions for the installation of offshore wind farms, considering the current development and future plans for the exploitation of this resource in the short and long term. Therefore, the results for wind resources are adjusted in the strategic lines of the Xunta de Galicia RIS3 2021-2027 within Challenge 1, Priority 1.3, for the diversification of the Galician energy sector to achieve a significant improvement in the efficient use of Galician natural resources that prioritise offshore wind energy (https://ris3galicia.es/wp-content/uploads/ESTRATEXIA-_REXIONAL_RIS3_GALICIA-1.pdf).

5.3 Limitations and Uncertainties

The results obtained had some limitations. The main limitation was the use of a single climate model as forcer for WRF. Specifically, for the analysis of future changes in moisture transport and ARs in general over 30 years, only the SSP5-8.5 scenario was considered. SSP5-8.5 proposes a development that considers only fossil fuels reaching a radiative forcing of 8.5 W/m^2 at the end of the 21st century; therefore, it will have a low probability of occurrence, which indicates that the patterns could be amplified compared to reality. On the other hand, for the study of future changes associated with the wind field and WPD, three climate change scenarios were considered but the periods were 5 years. However, the ideal approach would have been to use a longer period.

Furthermore, the ERA-I and ERA5 reanalyses used as forcing in this study had certain limitations. First, ERA-I and ERA5 are dependent on the location, timescale, and variables analysed. Variables involved in the hydrological cycle must be considered cautiously. Furthermore, the combination or assimilation of both observed and simulated data can generate spurious variations and trends in reanalyses (AROCT, 2023).

Similarly, the WRF-ARW mesoscale model presents limitations associated with its configuration, which depends on its microphysics, cumulus, or boundary layer parameterisations, among others. However, they were selected those that showed the best results for the study region according to the updated literature. Furthermore, the Lagrangian methodology used can overestimate evaporation and precipitation values (Insua-Costa and Miguez-Macho, 2018) because it does not separate the evaporation and precipitation processes and does not consider ice and liquid water. According to Stohl and James (2004), the possible variations are associated with nonphysical processes determined by phenomenology. Specifically, FLEXPART increases the errors in parcel trajectories over time (Stohl, 1998). According to Insua-Costa and Miguez-Macho (2018), this error may be associated with the existence of vertical movements at the sub-region scale related to convection and turbulent transport, which are not considered in Lagrangian models. Finally, the IPART method is sensitive during the process of detecting regions of possible ARs and subsequent geometric filtering (Xu et al., 2020).

5.4 Future works

Any intensification or reduction in the transported moisture results in precipitation anomalies, including flooding and drought, when the moisture content is high or low, respectively (e.g., Gimeno et al., 2016; Liu et al., 2020; Gimeno et al., 2020). Some studies focusing on the North Atlantic region determined that there is a significant direct link between the occurrence of extreme drought events in Europe and the anomalies of moisture transported from North Atlantic sources (Sorí et al., 2020; García-Herrera et al., 2019) and Mediterranean Sea (Stojanovic et al., 2018). In addition, a reduction in the moisture contribution from the Gulf of Mexico-Caribbean Sea may be related to the occurrence of drought events in southern Mexico (Melgarejo et al., 2021). Recent studies conducted in continental regions in continental regions of the Northern Hemisphere (Herrera-Estrada and Diffenbaugh, 2020; Drumond et al., 2019) have also observed such relationships. Similar analyses have been conducted to identify the roles of North Atlantic and Mediterranean Sea sources in the occurrence of extreme precipitation in Europe (Insua-Costa et al., 2019; Tabari and Willems, 2018) and the Gulf of Mexico-Caribbean Sea as a source for extreme precipitation in Central America and the Caribbean (Vazquez et al., 2020; Huguenin et al., 2023). According to the IPCC (2021), floods and droughts are expected to become substantially more frequent under conditions of global warming. However, to date, no studies have revealed the future variability in moisture sources under the influence of global warming and different socioeconomic and environmental scenarios. Therefore, future research should analyse the following:

- **The influence of climate change on regional moisture transport in regions of interest.**
- **Future changes in atmospheric moisture sources associated with extreme precipitation at regional and global scales.**
- **The conditional probability of drought occurrence given a decrease in the contribution of moisture from a specific source under future climate.**

According to the IPCC (2021), one of the strongest signs of climate change is the increase in global average surface temperature, which leads to greater water retention capacity of the atmosphere. A more humid atmosphere leads to greater moisture transport. Given these projections, it is important to study the changes in the main meteorological structures of moisture transport at global and regional scales, including Atmospheric Rivers (ARs), Low-level jets (LLJs), monsoons, and tropical and extratropical cyclones (Gimeno et al., 2020). To date, changes in ARs in future climates have been determined (e.g., Ramos et al., 2016; Payne et al., 2020; O'Brien et al., 2022; Algarra et al., 2020), as well as future projections in the climatology of global LLJs (Torres-Alavez et al., 2021). In addition, detailed analyses of tropical and extratropical cyclones and monsoons have been conducted by Roberts et al. (2020), Priestley and Catto (2022), and Liang et al. (2023). However, further work is required to determine the relationships between moisture transport and changes associated with the mechanisms mentioned above using climate models corresponding to CMIP6. However, the importance of AR and LLJs has been highlighted in the North Atlantic region. It should be noted that Fernández-Alvarez et al. (2023c) investigated the changes in moisture sources of ARs but focused on landfalling the Iberian Peninsula with WRF plus FLEXPART. Therefore, in future research, the following should be studied:

- **Future changes in the occurrence and characteristics of LARs on the east coast of the United States and northern Europe.**
- **Future changes in the main LLJs in the North Atlantic (e.g., Caribbean low-level jet and Great Plains low-level jet).**

According to several investigations, moisture transport influences the extremes of precipitation more than its mean value. Furthermore, extreme precipitation depends on the available moisture content and other magnitudes that determine atmospheric instability but with greater moisture sensitivity (Emori and Brown, 2005; Nie et al., 2018). According to Gimeno et al. (2016), there must be a grid-scale dependence between IVT values and precipitation, which must be spatially and temporally heterogeneous. Gimeno-Sotelo and Gimeno (2022) found that the occurrence of AR explains the most extreme days of precipitation and simultaneous IVT with marked regional and seasonal differences. However, this study was limited by the resolution of the reanalysis used, which should be higher when analysing composite extremes of precipitation and IVT over a complex orography. Therefore, in future investigations, **the presence of concurrent extremes of precipitation and IVT for current and future climates will be studied with a higher resolution, considering the occurrence or not of ARs**.

Numerical simulations (CI, 2023) using GCMs were used to study the impact of climate change. A climate model is a numerical representation of atmospheric dynamics that considers different forcings in future climates. In addition, various models present physical differences; therefore, some have a better ability to represent a certain variable in a specific region. Therefore, each model has its own climatic variability. A common practice to avoid these limitations is to consider a climate model ensemble that makes it possible to address different sources of uncertainty (Hawkins and Sutton, 2009, 2012; Deser et al., 2012). Considering that the use of the CESM2 model is a limitation for future work, **the study of future changes in moisture sources and sinks will be carried out considering various climate models to eliminate uncertainties and the variability associated with a single model**.

For studies at the regional scale, it is necessary to considerably increase the spatial resolution to represent processes at very small scales. This allowed us to obtain more precise climate projections when considering the outputs of the climate models. Studies on variables such as climate extremes, agriculture, and air quality, among others, need these finer climate projections for future climate. Therefore, in future works, **we will carry out simulations with higher resolution but focused on a specific region (e.g., Iberian Peninsula) to analyse in detail local changes in moisture transport in future climate and determine what modifications are projected at a local scale in the hydrological cycle**.

The residence time of water vapour in the atmosphere (WVRT) allows for the compression of the hydrological cycle; therefore, this variable is an indicator of how climate change modifies the hydrological cycle (Trenberth, 1998). Changes in WVRT as a result of variations in atmospheric circulation are highly sensitive to surface evaporation and evapotranspiration, as well as to the development of synoptic-scale systems. Therefore, it is necessary to analyse the changes in the residence time of water vapour in the atmosphere for present and future climate conditions, as well as the relationships between these changes and the impact of warming on large-scale circulation, and the impacts of such changes on the moisture sources for precipitation and the modulation of moisture conveyors. Therefore, future work **will determine changes in the water vapour residence time influenced by changes in the large-scale circulation patterns and how these changes modulate moisture transport**.

A

Supplementary Material

In this section is presented the supplementary material linked to each article that makes up the main part of this thesis. All material related to published articles is available online from each journal.

Supplemental Material for

Comparison of moisture sources and sinks estimated with different versions of FLEXPART and FLEXPART-WRF models forced with ECMWF reanalysis data

José Carlos Fernández-Alvarez[1,2]*, Marta Vazquez[1], Albenis Pérez-Alarcón[1,2] ,Raquel Nieto[1], Luis Gimeno[1]

[1] Centro de Investigación Mariña, Universidade de Vigo, Environmental Physics Laboratory (EPhysLab), Campus As Lagoas s/n, Ourense, 32004, Spain

[2] Departamento de Meteorología, Instituto Superior de Tecnologías y Ciencias Aplicadas, Universidad de La Habana, La Habana, Cuba.

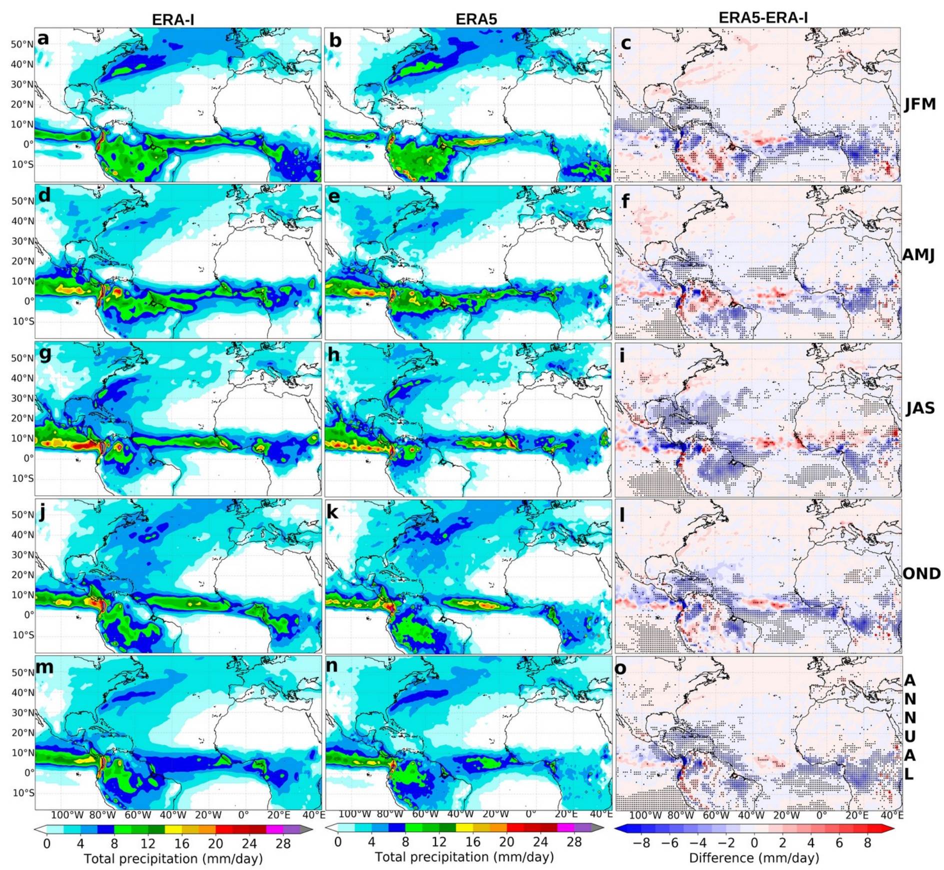

Figure S1. Comparison of the total precipitation (P) field corresponding to ERA-I, ERA5 and the difference ERA5-ERA-I. Black dots represent statistically significant differences at 95%. The fields displayed from top to bottom correspond to JFM, AMJ, JAS, OND, and ANNUAL.

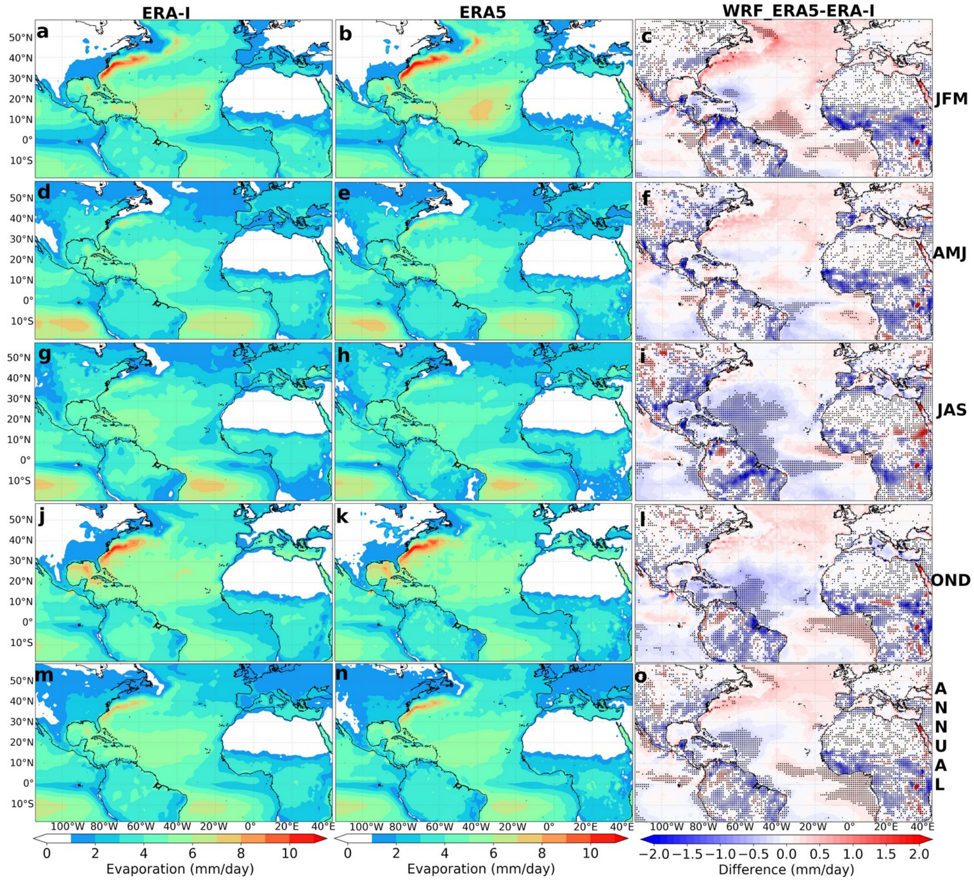

Figure S2. Same as Fig. S1 but for the evaporation field (E).

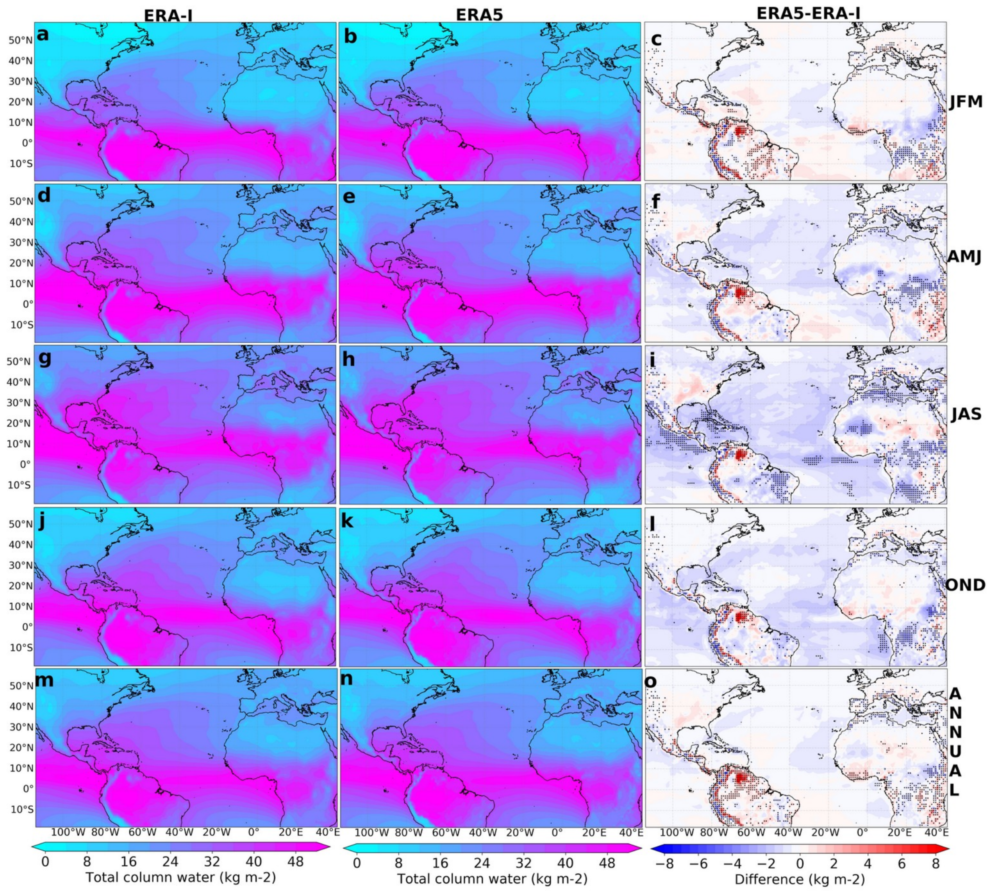

Figure S3. Same as Fig. S1 but for the total column water (TCW) field.

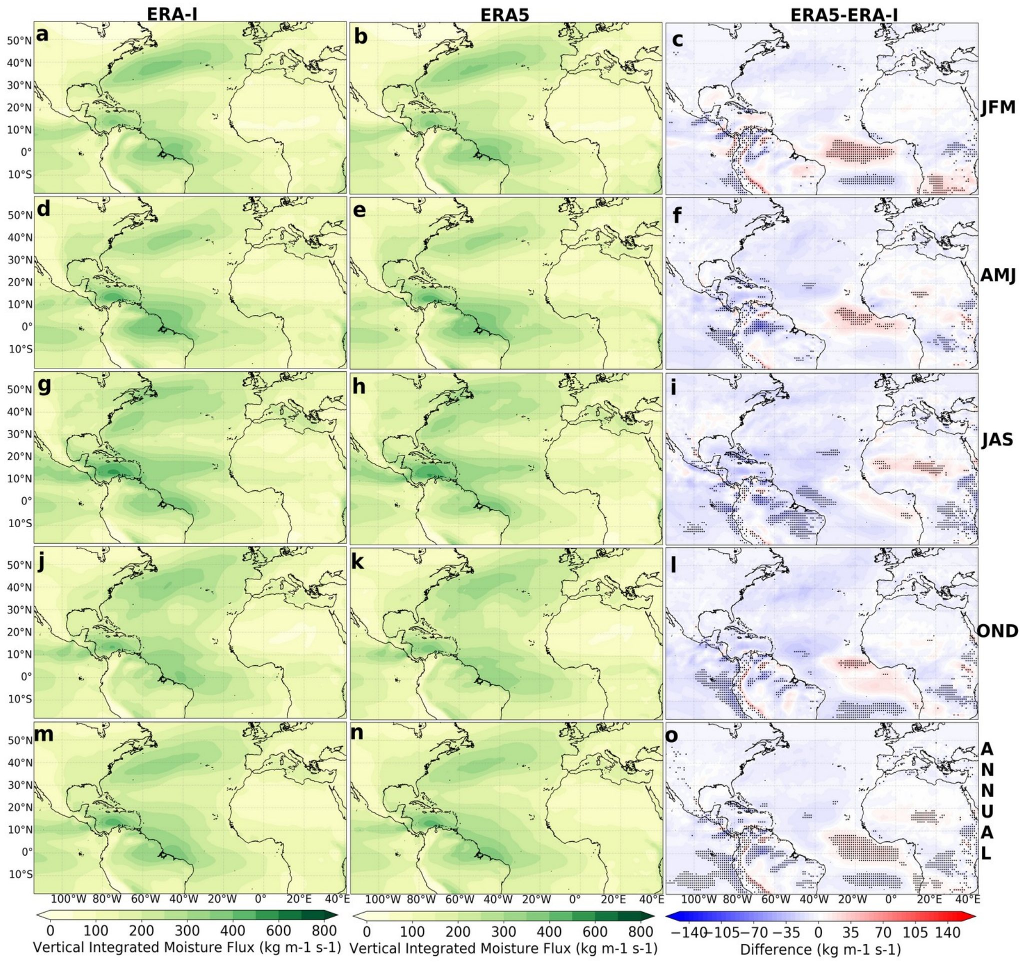

Figure S4. Same as Fig. S1 but for the IVT field.

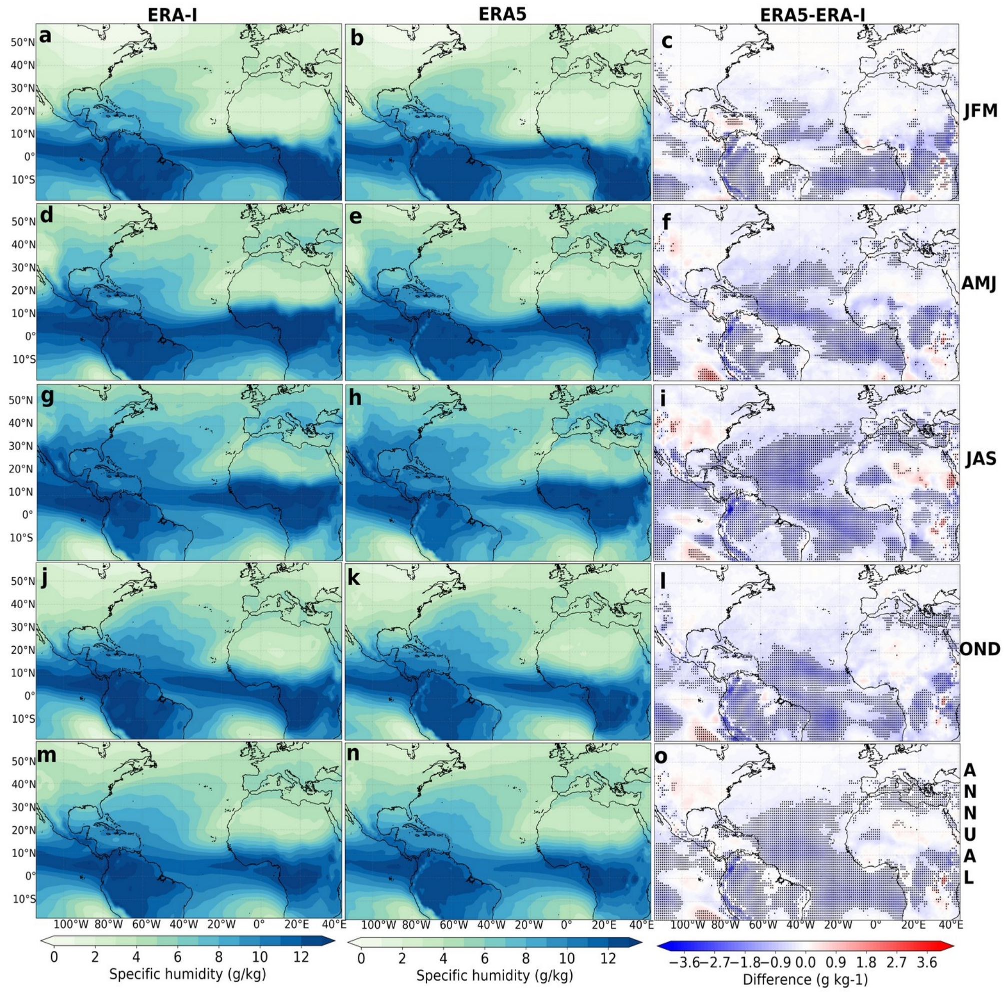

Figure S5. Same as Fig. S1 but for the specific humidity field at 850 hPa.

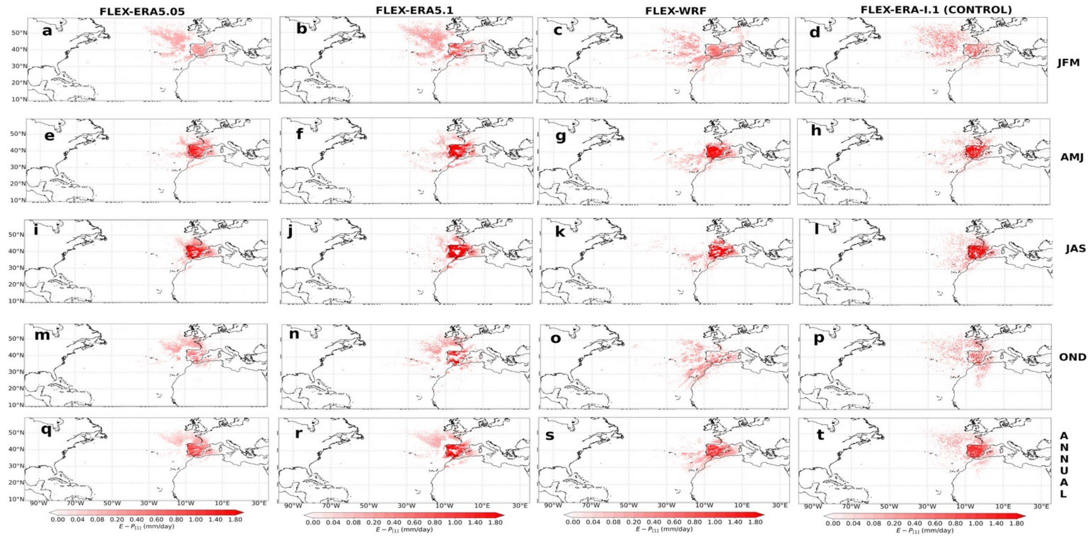

Figure S6. Average values of (E-P) $_{[1]}$ for all particles bound for the IP region determined from backward tracking for day 1. The fields displayed from top to bottom correspond to JFM, AMJ, JAS, OND, and ANNUAL. The columns from left to right are the following configurations FLEX-ERA5.05, FLEX-ERA5.1, FLEX-WRF and FLEX-ERA-I.1. Units for E-P values are mm day^{-1}.

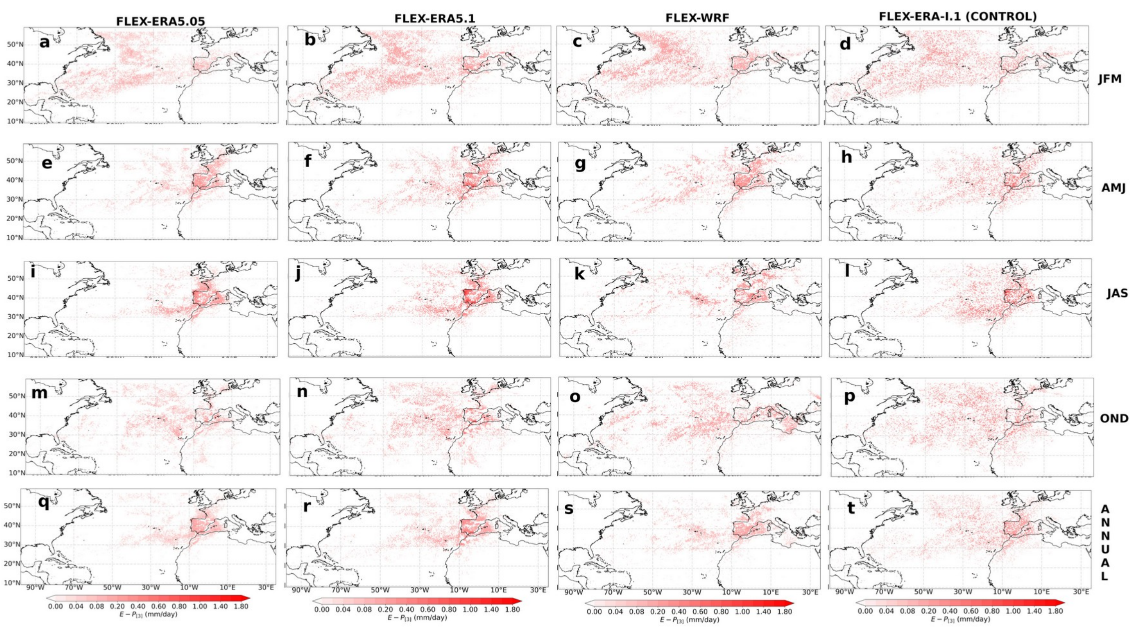

Figure S7. Average values of (E-P) $_{[3]}$ for all particles bound for the IP target region determined from backward tracking for day 3. The fields displayed from top to bottom correspond to JFM, AMJ, JAS, OND, and ANNUAL. The columns from left to right are the following configurations FLEX-ERA5.05, FLEX-ERA5.1, FLEX-WRF and FLEX-ERA-I.1. Units for E-P values are mm day^{-1}.

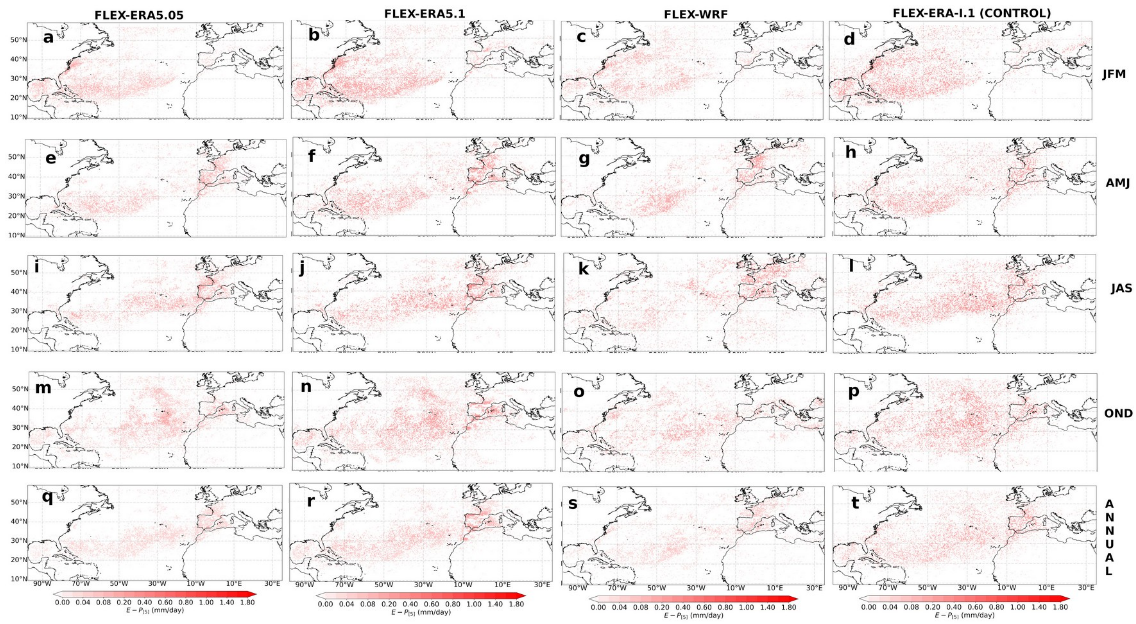

Figure S8. Average values of (E-P) $_{[5]}$ for all particles bound for the IP target region determined from backward tracking for day 5. The fields displayed from top to bottom correspond to JFM, AMJ, JAS, OND, and ANNUAL. The columns from left to right are the following configurations FLEX-ERA5.05, FLEX-ERA5.1, FLEX-WRF and FLEX-ERA-I.1. Units for E-P values are mm day^{-1}.

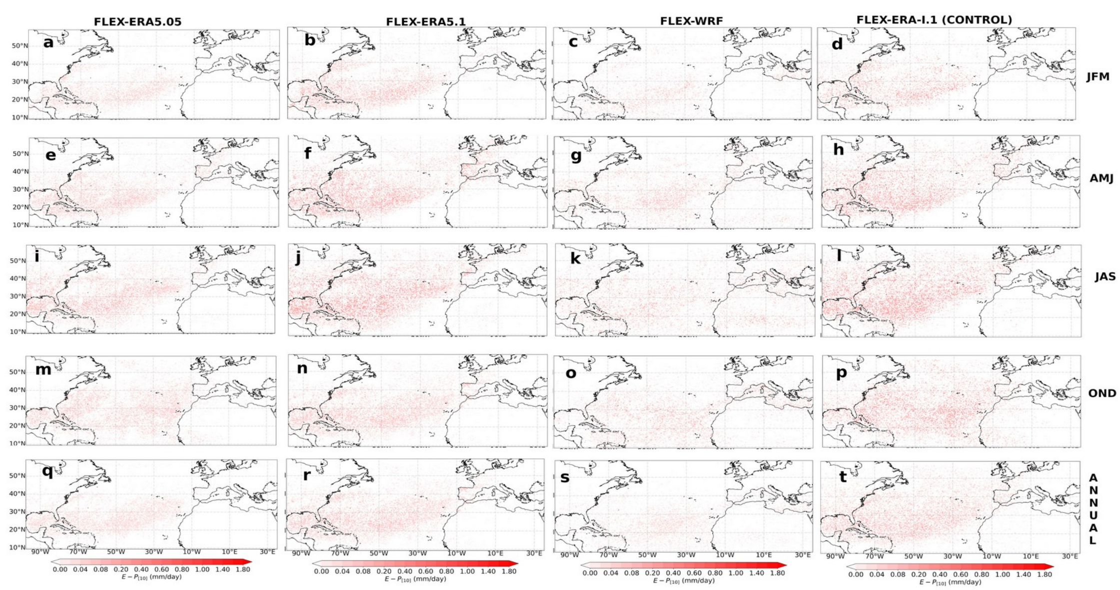

Figure S9. Average values of (E-P) $_{[10]}$ for all particles bound for the IP target region determined from backward tracking for day 10. The fields displayed from top to bottom correspond to JFM, AMJ, JAS, OND, and ANNUAL. The columns from left to right are the following configurations FLEX-ERA5.05, FLEX-ERA5.1, FLEX-WRF and FLEX-ERA-I.1. Units for E-P values are mm day^{-1}.

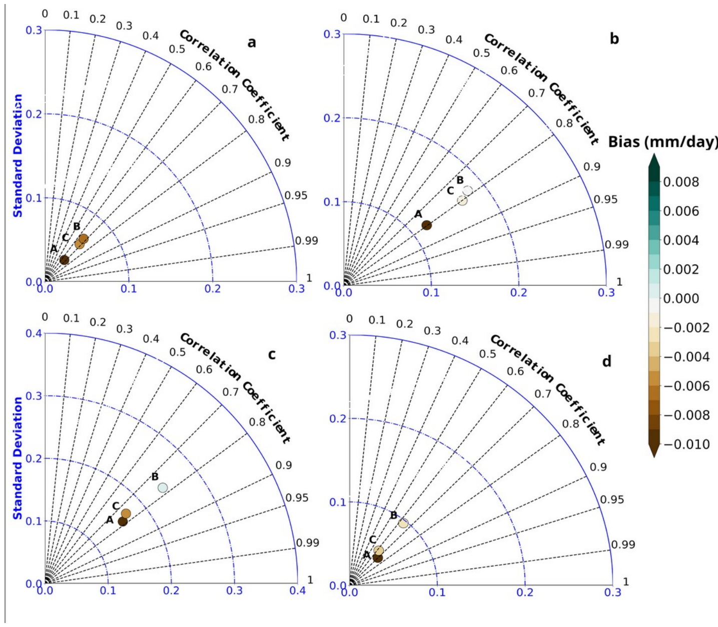

Figure S10. Taylor diagram for the values of (E-P) $_{[1]}$ corresponding to the IP target region. a) JFM b) AMJ c) JAS d) OND. The letters A, B, C correspond to the configurations FLEX-ERA5.05, FLEX-ERA5.1 and FLEX-WRF respectively.

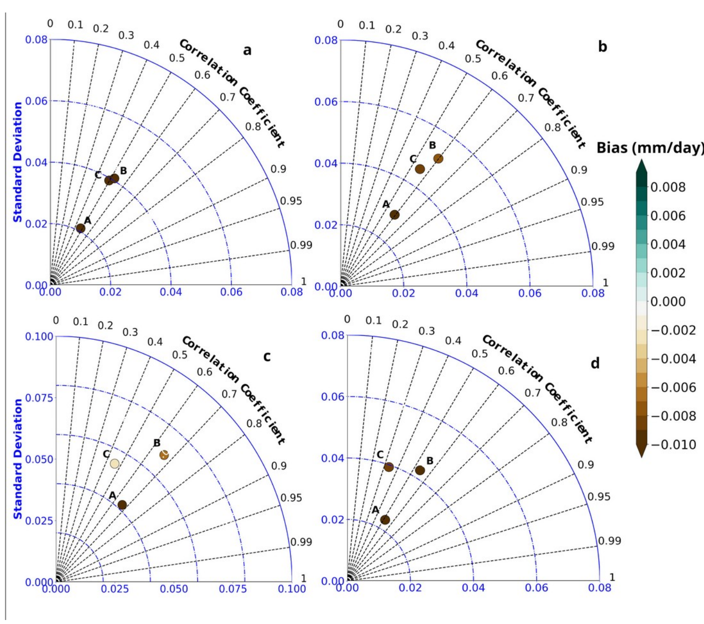

Figure S11. Taylor diagram for the values of (E-P) $_{[3]}$ corresponding to the IP target region. a) JFM b) AMJ c) JAS d) OND. The letters A, B, C correspond to the configurations FLEX-ERA5, FLEX-ERA5.1 and FLEX-WRF respectively.

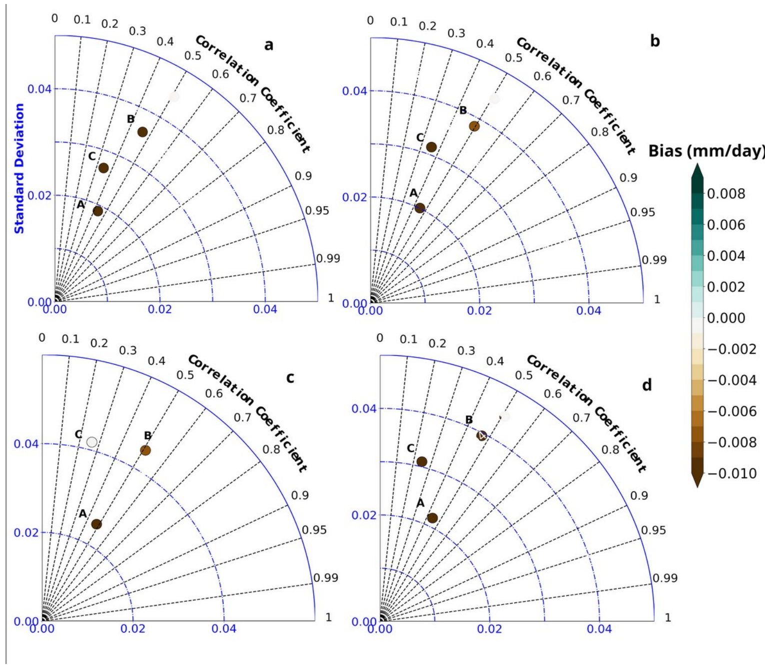

Figure S12. Taylor diagram for the values of (E-P) [5] corresponding to the IP target region. a) JFM b) AMJ c) JAS d) OND. The letters A, B, C correspond to the configurations FLEX-ERA5.05, FLEX-ERA5.1 and FLEX-WRF respectively.

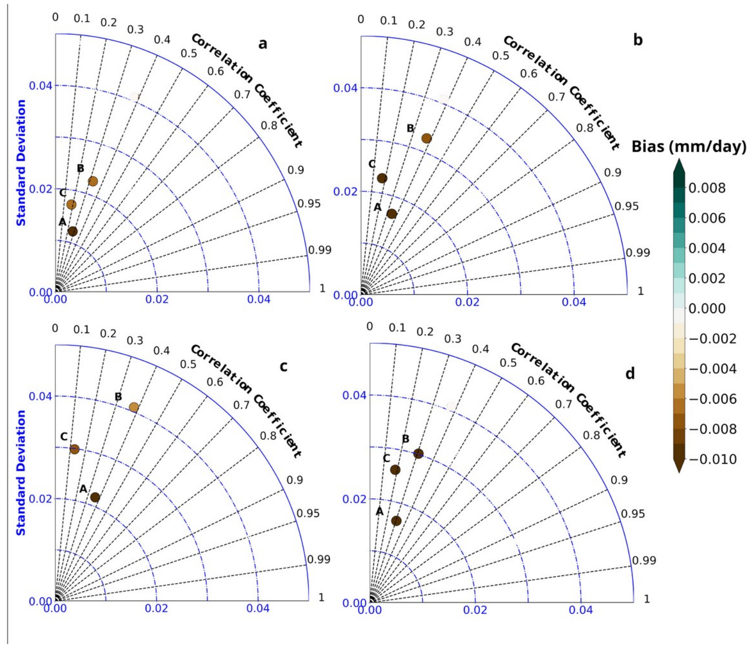

Figure S13. Taylor diagram for the values of (E-P) $_{[10]}$ corresponding to the IP target region. a) JFM b) AMJ c) JAS d) OND. The letters A, B, C correspond to the configurations FLEX-ERA5.05, FLEX-ERA5.1 and FLEX-WRF respectively.

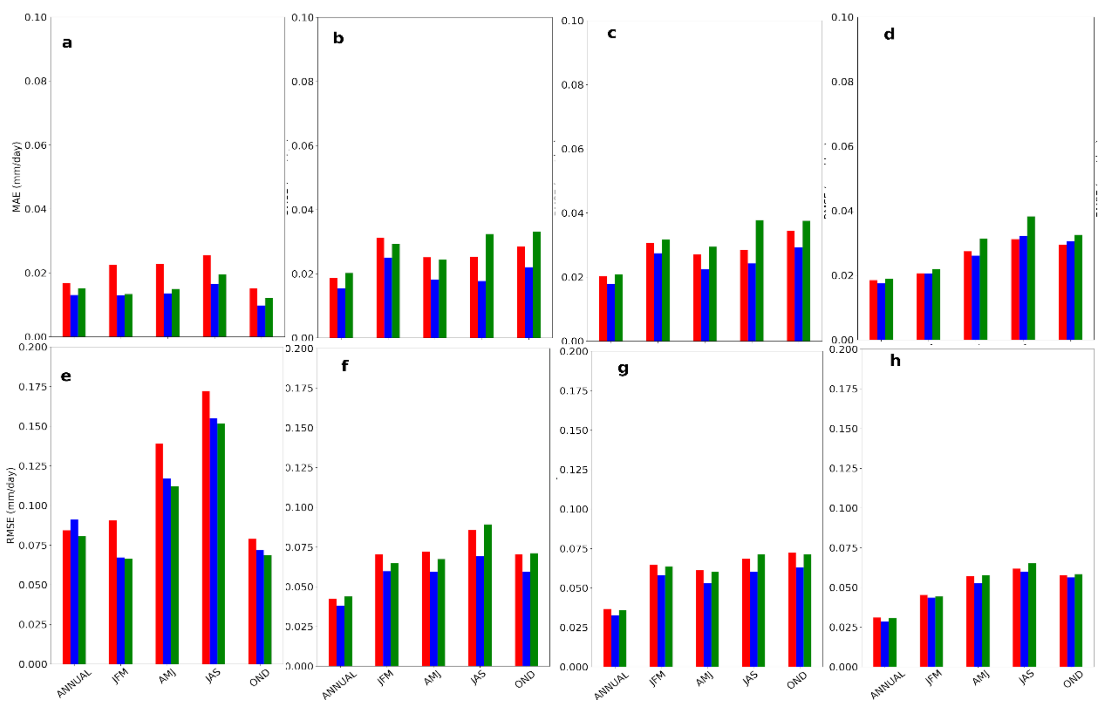

Figure S14. The MAE and RMSE calculated in each configuration for the IP target region at days 1 (a, e), 3 (b, f), 5 (c, g) and 10 (d, h) of backward tracking. The red, blue and green bars correspond to FLEX-ERA5.05, FLEX-ERA5.1 and FLEX-WRF respectively.

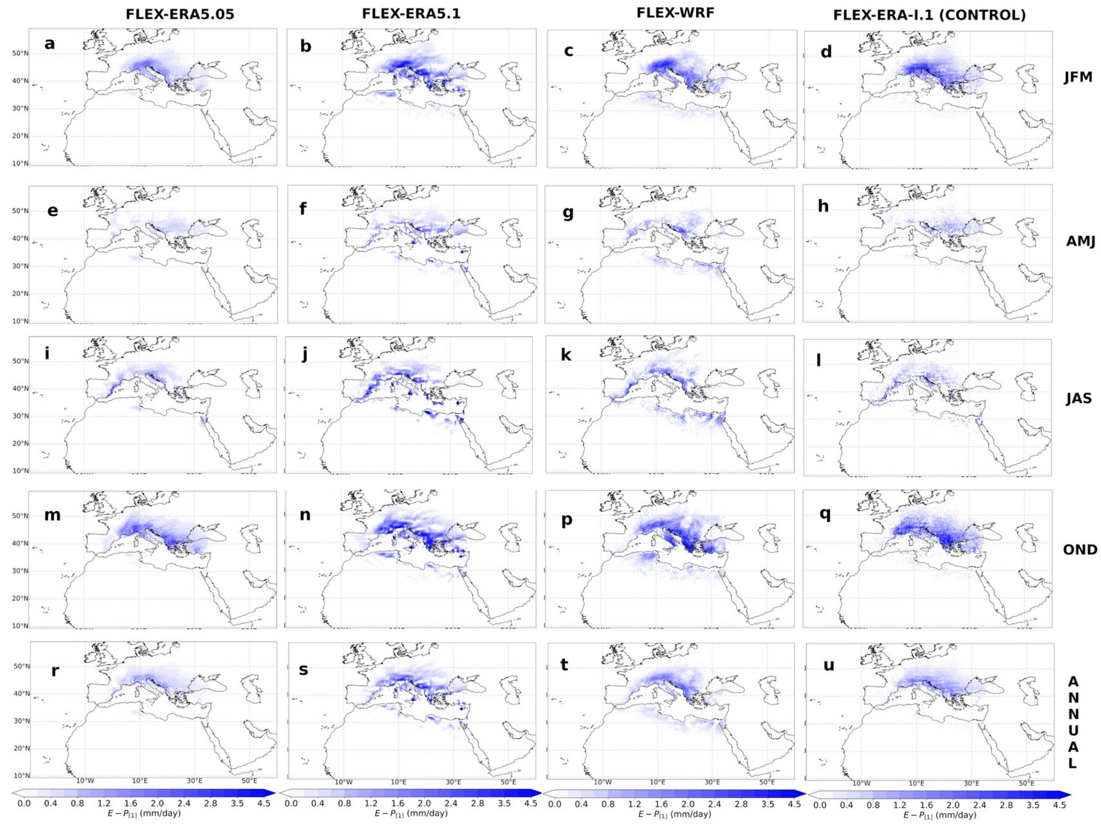

Figure S15. Average values of (P-E) [1] >0 for all particles bound for the MED target region determined from forward tracking. The fields displayed from top to bottom correspond to JFM, AMJ, JAS, OND, and ANNUAL. The columns from left to right are the following configurations FLEX-ERA5.05, FLEX-ERA5.1, FLEX-WRF and FLEX-ERA-I.1. Units for E-P values are mm day^{-1}.

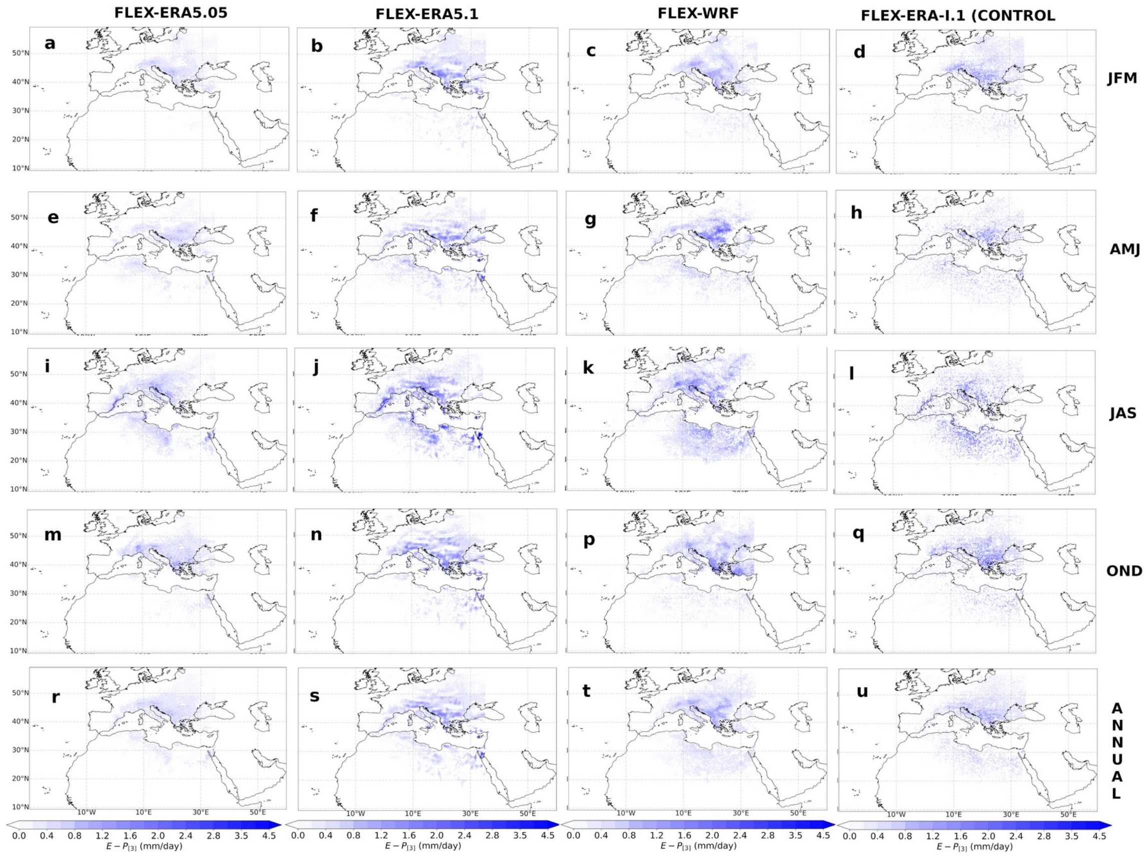

Figure S16. Average values of (P-E) $_{[3]}$ >0 for all particles bound for the MED target region determined from forward tracking. The fields displayed from top to bottom correspond to JFM, AMJ, JAS, OND, and ANNUAL. The columns from left to right are the following configurations FLEX-ERA5.05, FLEX-ERA5.1, FLEX-WRF and FLEX-ERA-I.1. Units for E-P values are mm day^{-1}.

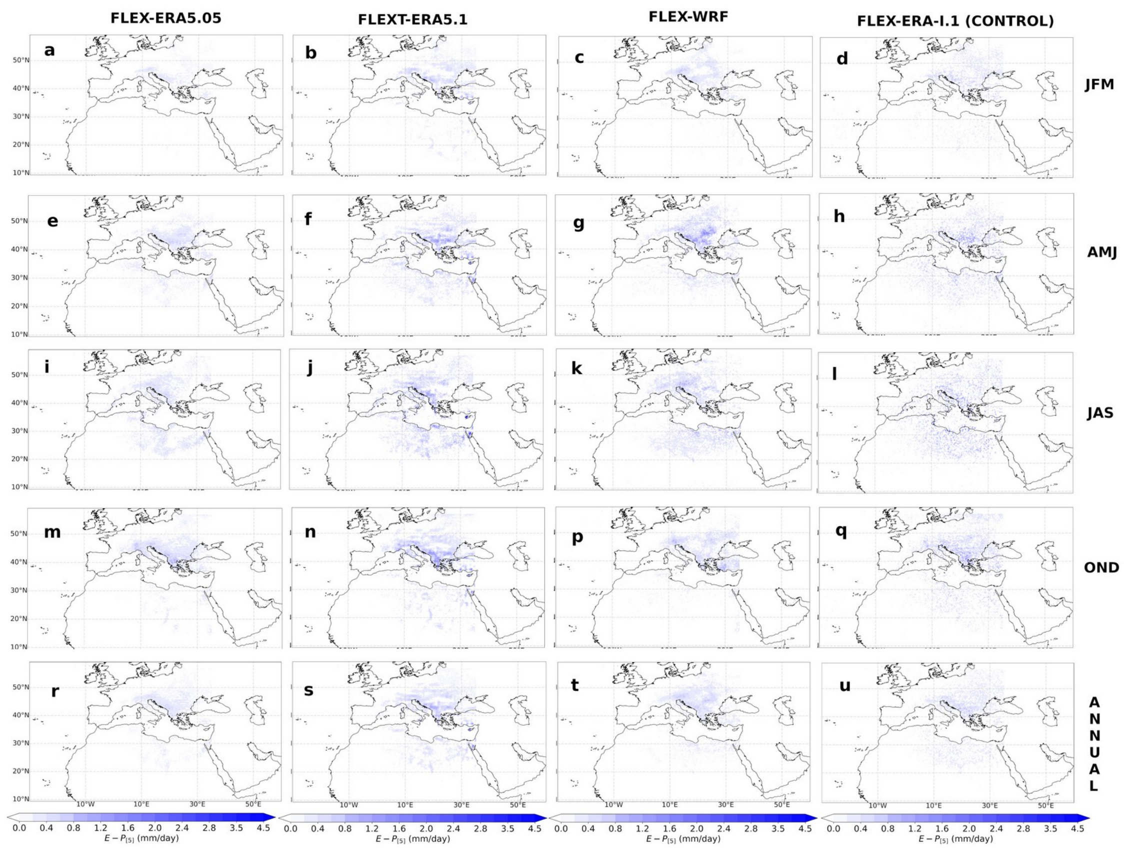

Figure S17. Average values of $(P\text{-}E)_{[5]}$ >0 for all particles bound for the MED target region determined from forward tracking. The fields displayed from top to bottom correspond to JFM, AMJ, JAS, OND, and ANNUAL. The columns from left to right are the following configurations FLEX-ERA5.05, FLEX-ERA5.1, FLEX-WRF and FLEX-ERA-I.1. Units for E-P values are mm day^{-1}.

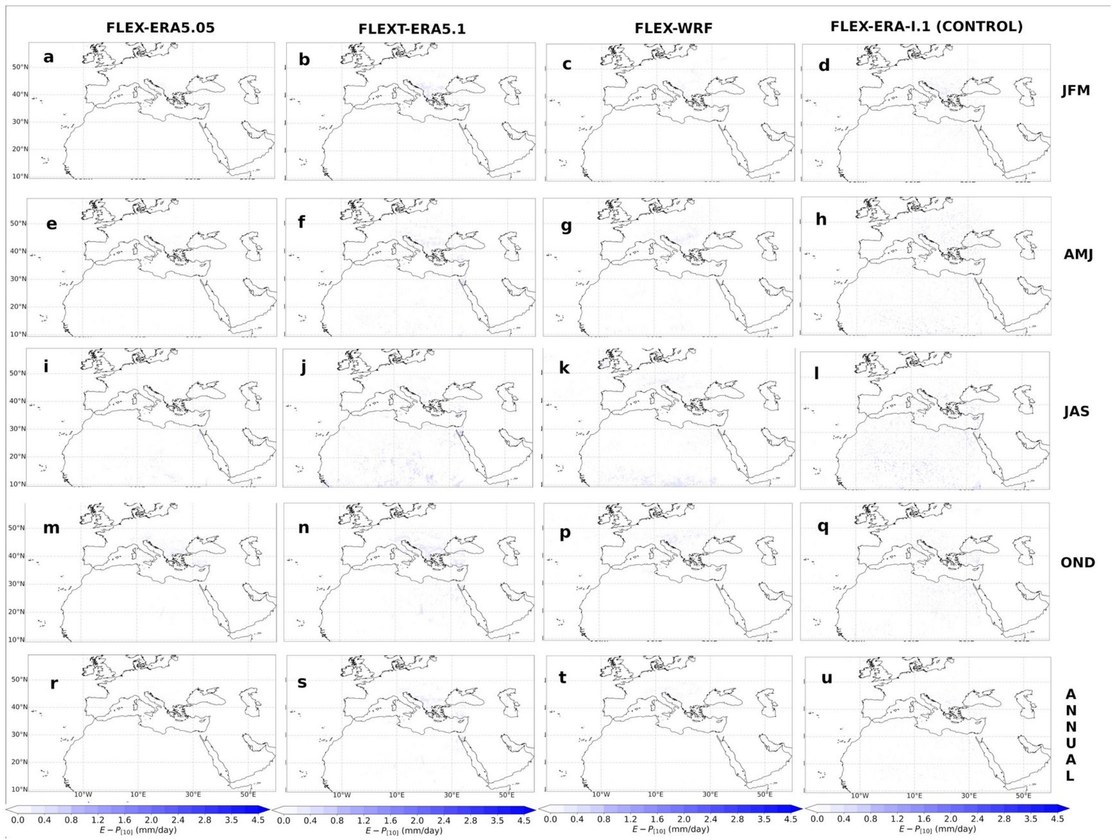

Figure S18. Average values of (P-E) $_{[10]}$ >0 for all particles bound for the MED target region determined from forward tracking. The fields displayed from top to bottom correspond to JFM, AMJ, JAS, OND, and ANNUAL. The columns from left to right are the following configurations FLEX-ERA5.05, FLEX-ERA5.1, FLEX-WRF and FLEX-ERA-I.1. Units for E-P values are mm day^{-1}.

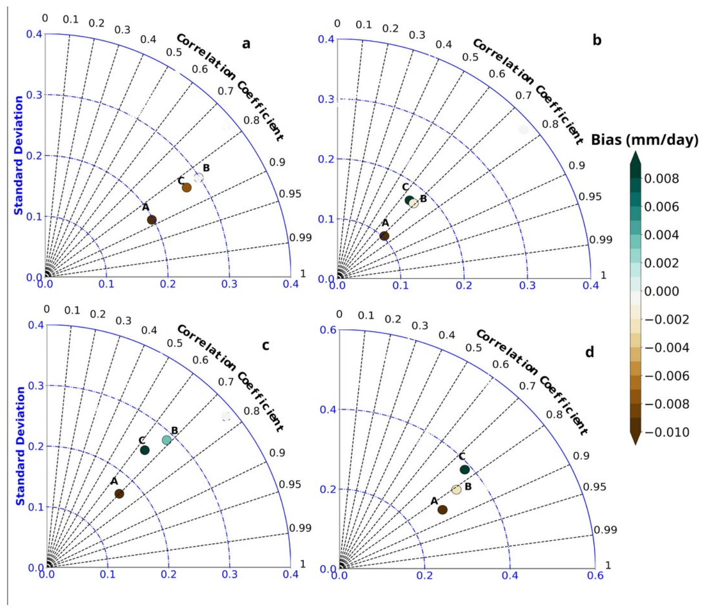

Figure S19. Taylor diagram for the values of (P-E)$_{[1]}$ >0 corresponding to the MED target region. a) JFM b) AMJ c) JAS d) OND. The letters A, B, C correspond to the configurations FLEX-ERA5.05, FLEX-ERA5.1 and FLEX-WRF respectively.

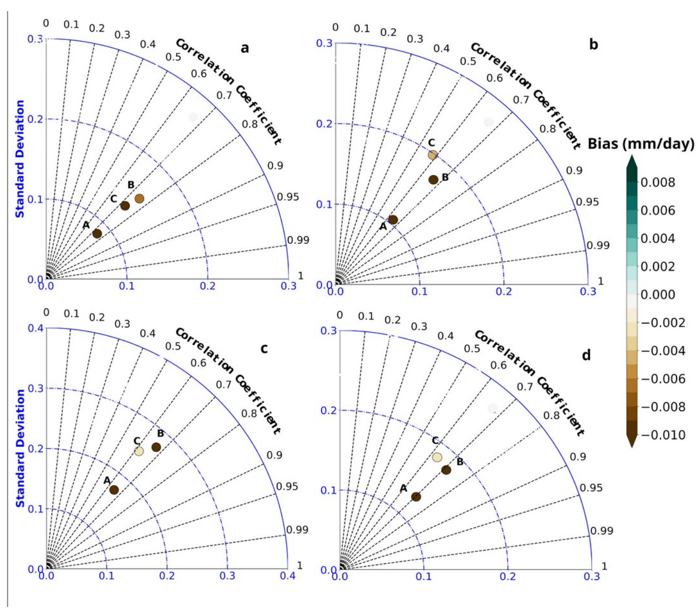

Figure S20. Taylor diagram for the values of (P-E)$_{[3]}$ >0 corresponding to the MED target region. a) JFM b) AMJ c) JAS d) OND. The letters A, B, C correspond to the configurations FLEX-ERA5.05, FLEX-ERA5.1 and FLEX-WRF respectively.

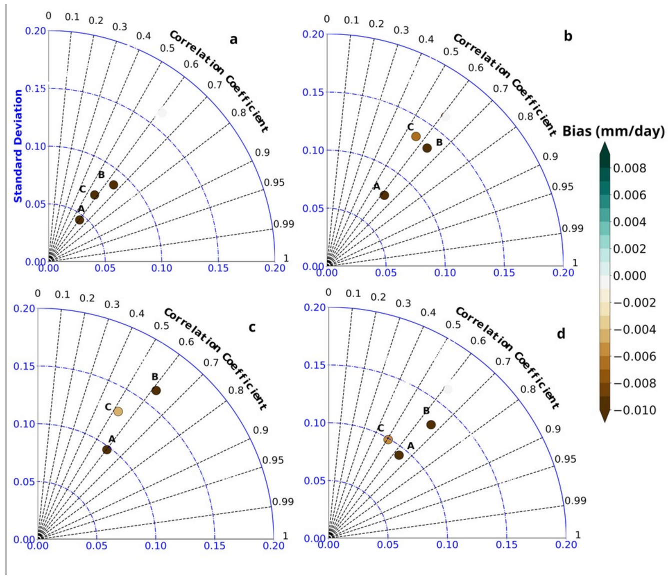

Figure S21. Taylor diagram for the values of $(P\text{-}E)_{[5]} > 0$ corresponding to the MED target region. a) JFM b) AMJ c) JAS d) OND. The letters A, B, C correspond to the configurations FLEX-ERA5.05, FLEX-ERA5.1 and FLEX-WRF respectively.

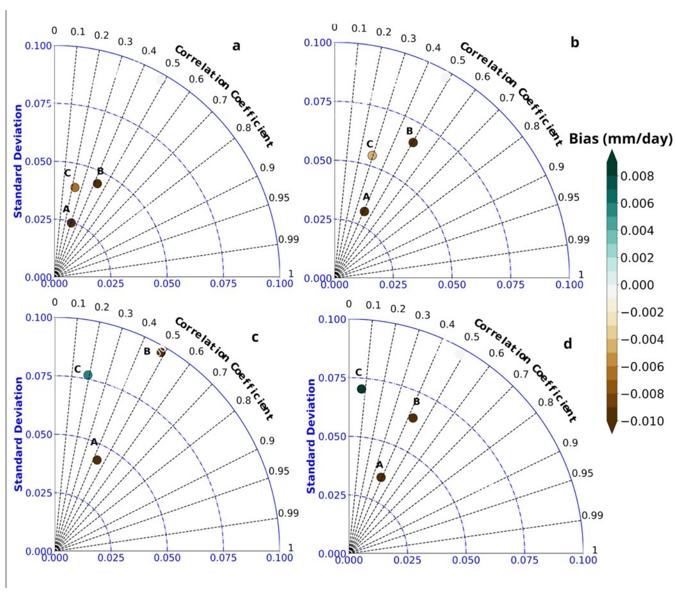

Figure S22. Taylor diagram for the values of $(P\text{-}E)_{[10]} > 0$ corresponding to the MED target region. a) JFM b) AMJ c) JAS d) OND. The letters A, B, C correspond to the configurations FLEX-ERA5.05, FLEX-ERA5.1 and FLEX-WRF respectively.

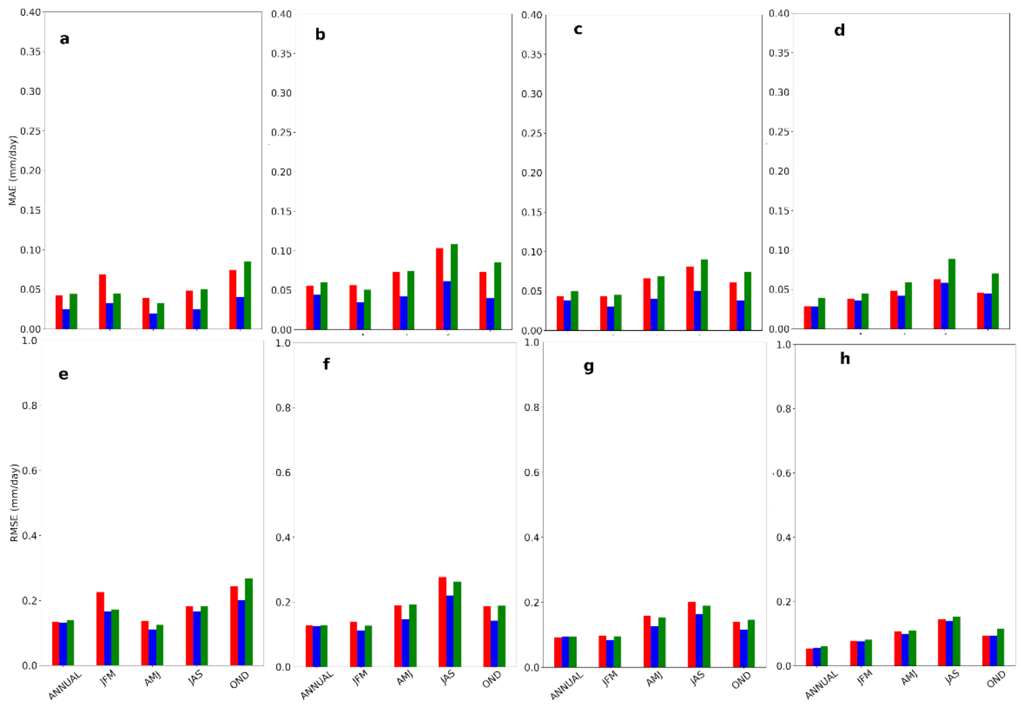

Figure S23. The MAE and RMSE calculated in each configuration for the MED target region at days 1 (a, e), 3 (b, f), 5 (c, g) and 10 (d, h) of forward tracking. The red, blue and green bars correspond to FLEX-ERA5.05, FLEX-ERA5.1 and FLEX-WRF respectively.

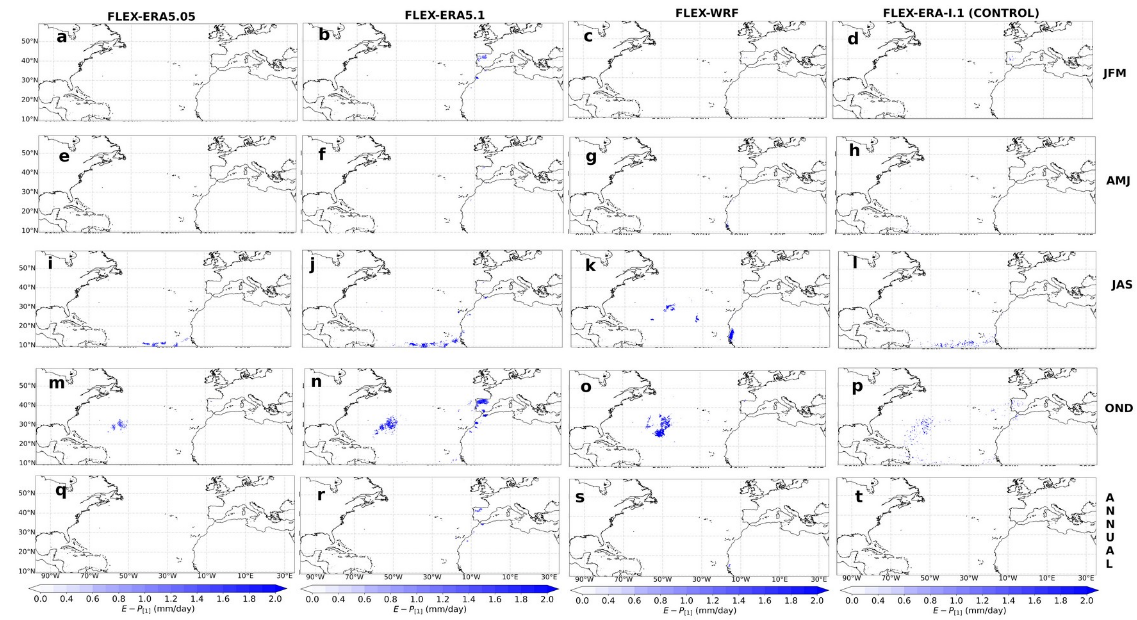

Figure S24. Average values of (P-E)$_{[1]}$ >0 for all particles bound for the NATL target region determined from forward tracking. The fields displayed from top to bottom correspond to JFM, AMJ, JAS, OND, and ANNUAL. The columns from left to right are the following configurations FLEX-ERA5.05, FLEXPART-ERA5.1, FLEX-WRF and FLEX-ERA-I.1. Units for E-P values are mm day^{-1}.

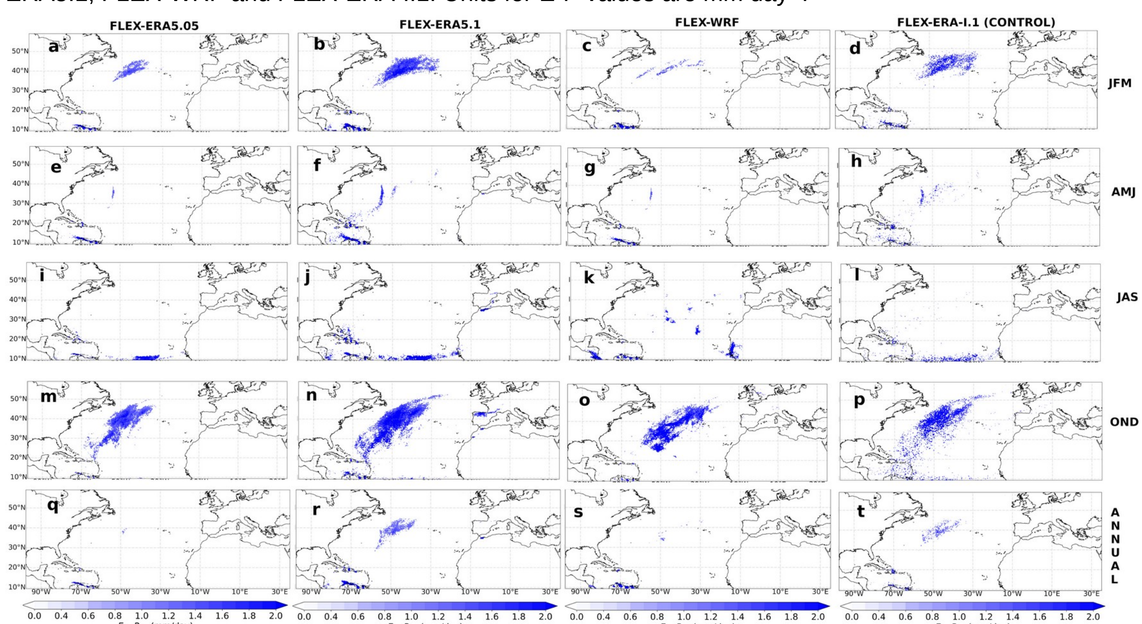

Figure S25. Average values of (P-E)$_{[3]}$> 0 for all particles bound for the NATL target region determined from forward tracking. The fields displayed from top to bottom correspond to JFM, AMJ, JAS, OND, and ANNUAL. The columns from left to right are the following configurations FLEX-ERA5.05, FLEX-ERA5.1, FLEX-WRF and FLEX-ERA-I.1. Units for E-P values are mm day^{-1}.

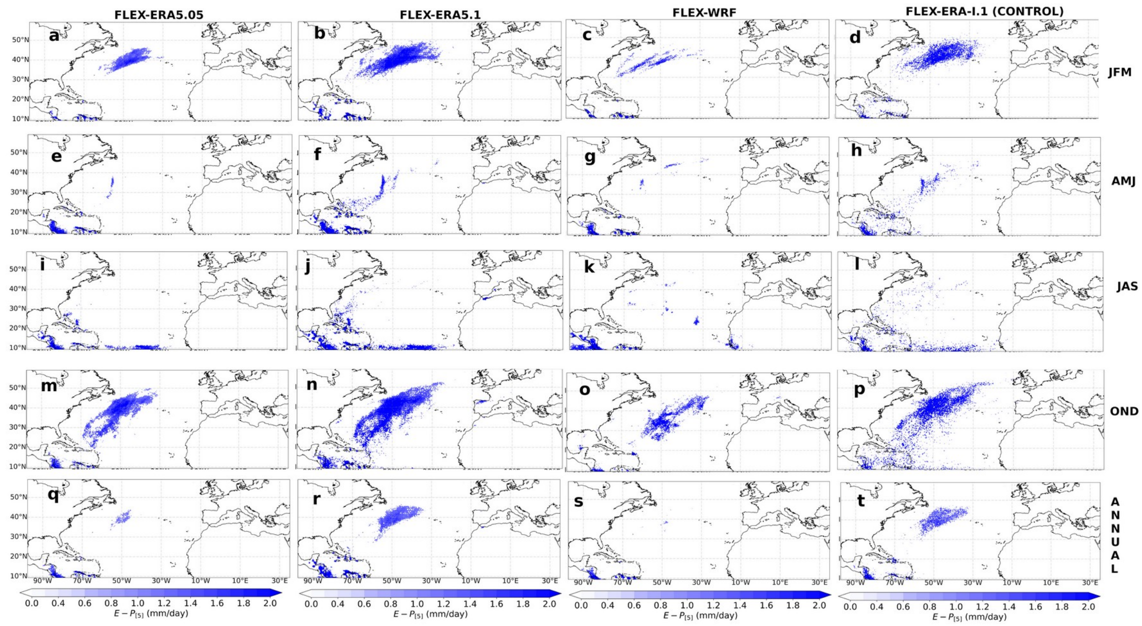

Figure S26. Average values of $(P\text{-}E)_{[5]} > 0$ for all particles bound for the NALT target region determined from backward tracking. The fields displayed from top to bottom correspond to JFM, AMJ, JAS, OND, and ANNUAL. The columns from left to right are the following configurations FLEX-ERA5.05, FLEX-ERA5.1, FLEX-WRF and FLEX-ERA-I.1. Units for E-P values are mm day^{-1}.

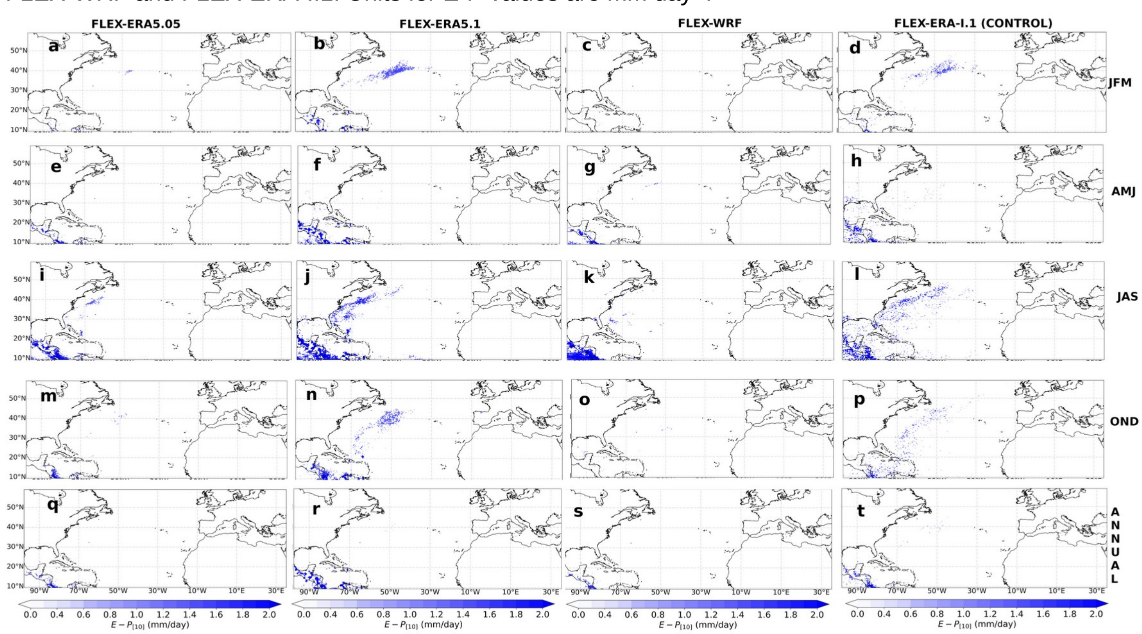

Figure S27. Average values of $(P\text{-}E)_{[10]} > 0$ for all particles bound for the NATL target region determined from backward tracking. The fields displayed from top to bottom correspond to JFM, AMJ, JAS, OND, and ANNUAL. The columns from left to right are the following configurations FLEX-ERA5.05, FLEX-ERA5.1, FLEX-WRF and FLEX-ERA-I.1. Units for E-P values are mm day^{-1}.

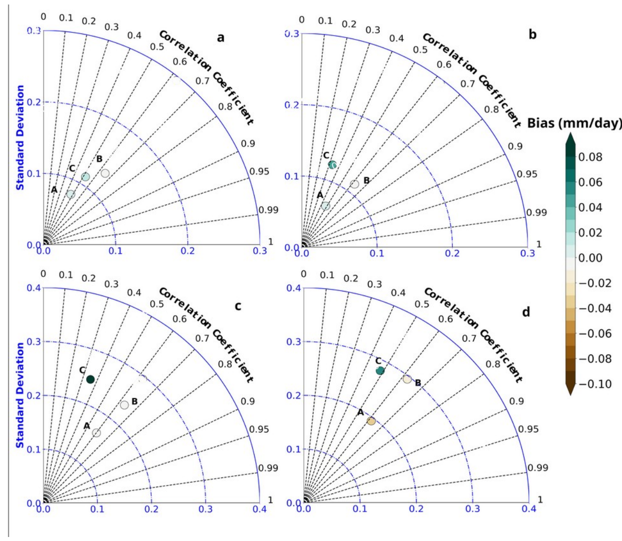

Figure S28. Taylor diagram for the values of $(P\text{-}E)_{[1]}$ >0 corresponding to the NATL target region. a) JFM b) AMJ c) JAS d) OND. The letters A, B, C correspond to the configurations FLEX-ERA5.05, FLEX-ERA5.1 and FLEX-WRF respectively.

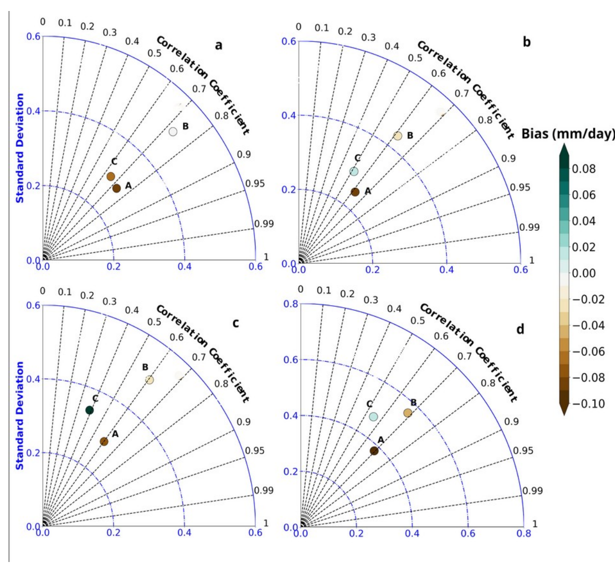

Figure S29. Taylor diagram for the values of $(P\text{-}E)_{[3]}$ >0 corresponding to the NATL target region. a) JFM b) AMJ c) JAS d) OND. The letters A, B, C correspond to the configurations FLEX-ERA5.05, FLEX-ERA5.1 and FLEX-WRF respectively.

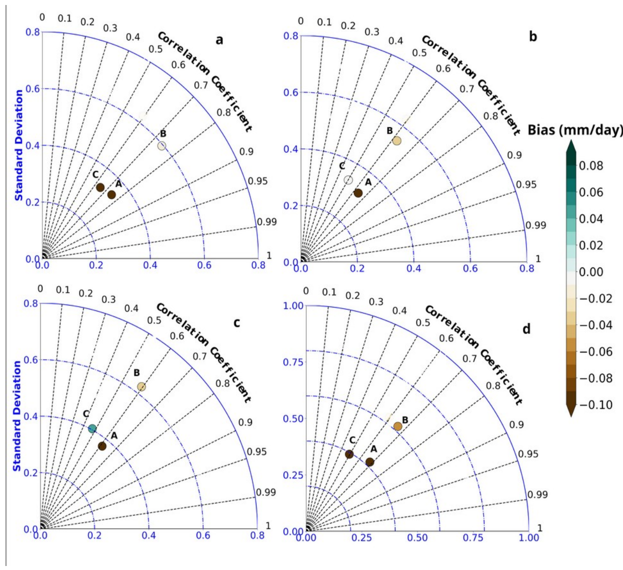

Figure S30. Taylor diagram for the values of $(P\text{-}E)_{[5]}$ >0 corresponding to the NATL target region. a) JFM b) AMJ c) JAS d) OND. The letters A, B, C correspond to the configurations FLEX-ERA5.05, FLEX-ERA5.1 and FLEX-WRF respectively.

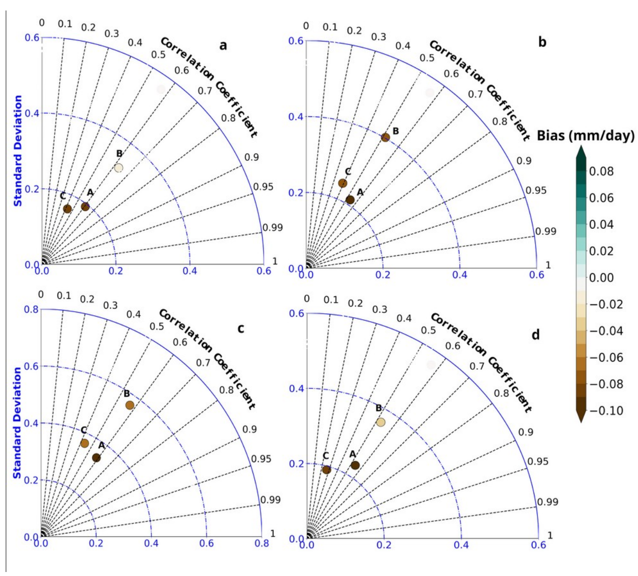

Figure S31. Taylor diagram for the values of $(P\text{-}E)_{[10]}$ >0 corresponding to the NATL target region. a) JFM b) AMJ c) JAS d) OND. The letters A, B, C correspond to the configurations FLEX-ERA5.05, FLEX-ERA5.1 and FLEX-WRF respectively.

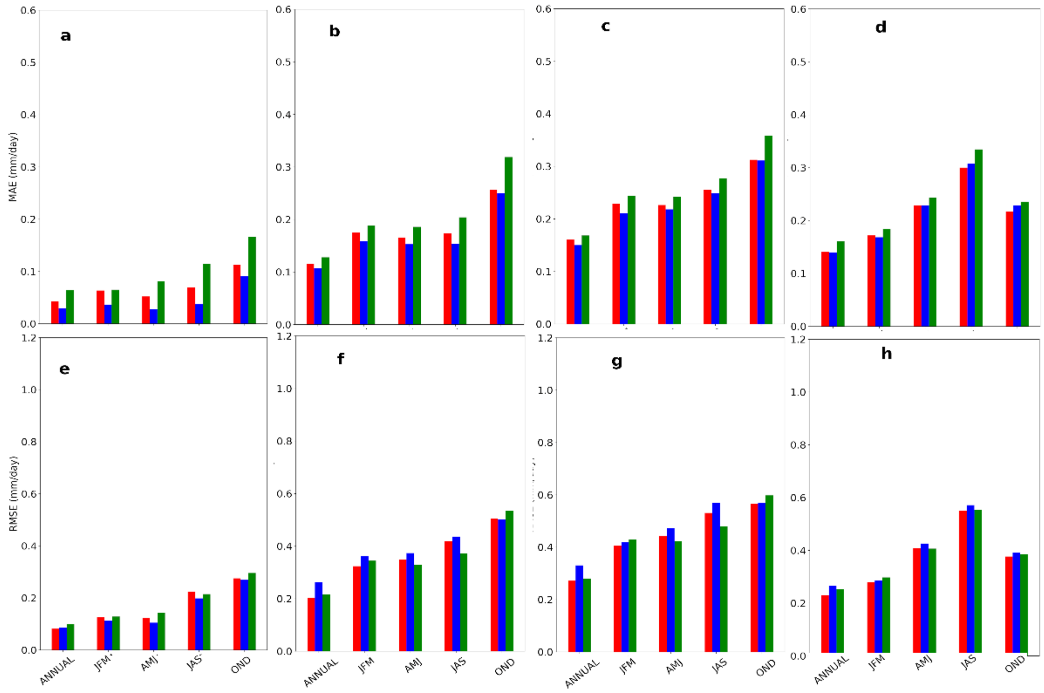

Figure S32. The MAE and RMSE calculated in each configuration for the NATL target region at days 1 (a, e), 3 (b, f), 5 (c, g) and 10 (d, h) of backward tracking. The red, blue and green bars correspond to FLEX-ERA5.05, FLEX-ERA5.1 and FLEX-WRF respectively.

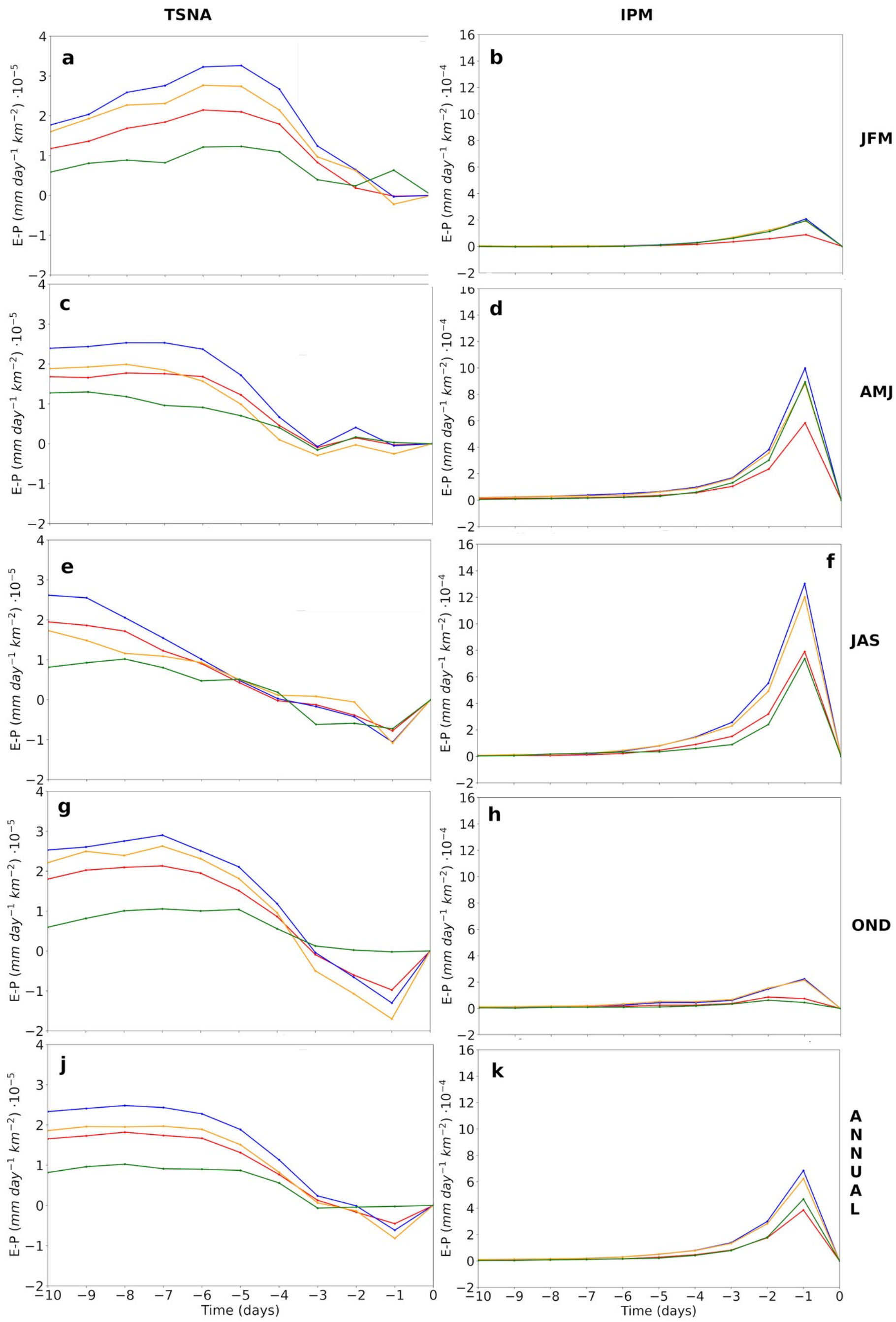

Figure S33. Time series of (E-P)[d] calculated backward for moisture over the IP integrated over the regions TSNA and IPM for configurations FLEX-ERA5.05 (red line), FLEX-ERA5.1 (blue line), FLEX-WRF (green line) and FLEX-ERA-I.1 (orange line). The series represents values of (E-P)[d] taking account the area of each region.

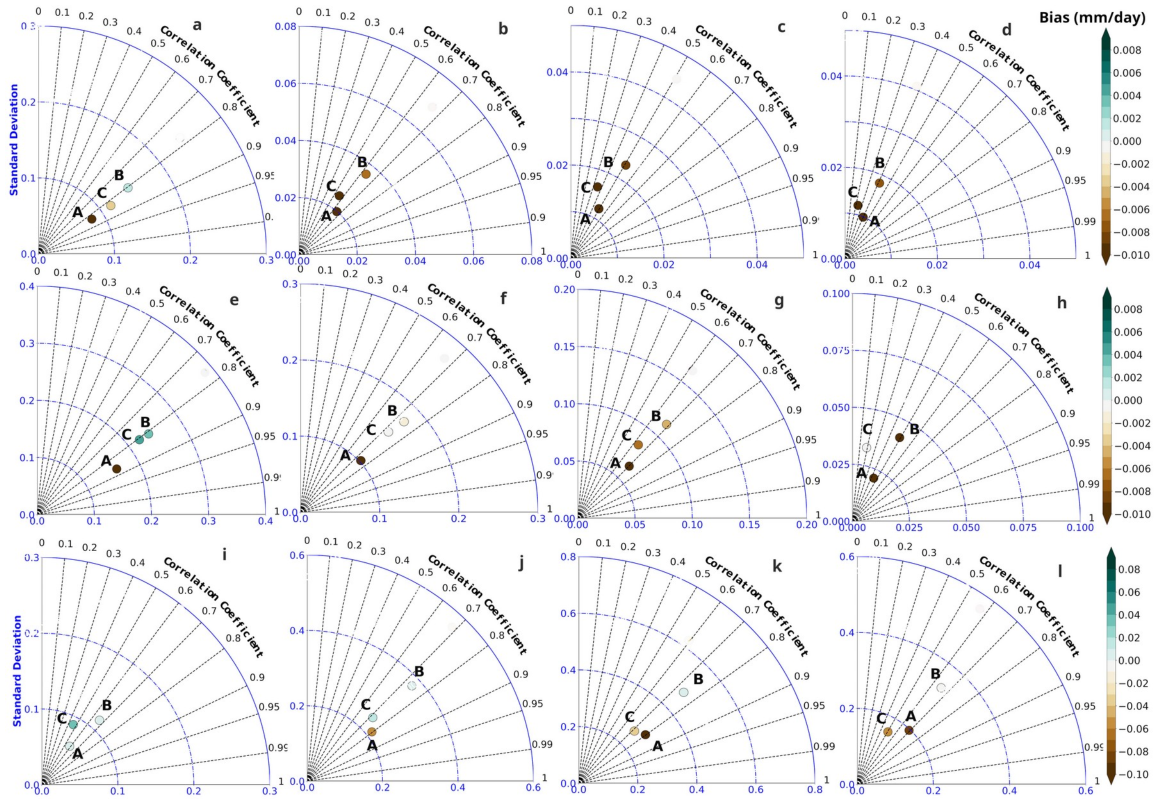

Figure S34. Annual Taylor diagram for days 1, 3, 5 and 10 corresponding to the target regions: IP (a-d), MED (e-h) and NATL (i-l). Letters A, B, C correspond to the configurations FLEX-ERA5.05, FLEX-ERA5.1 and FLEX-WRF respectively.

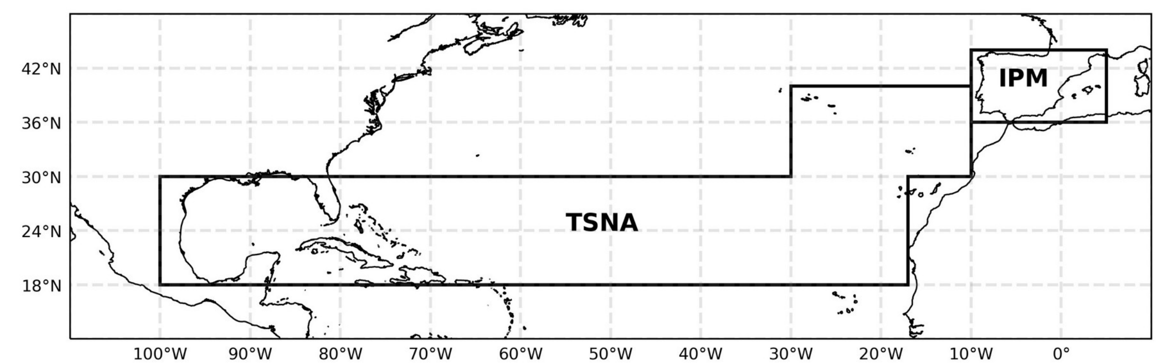

Figure S35. Main source regions for IP moisture: TSNA and IPM

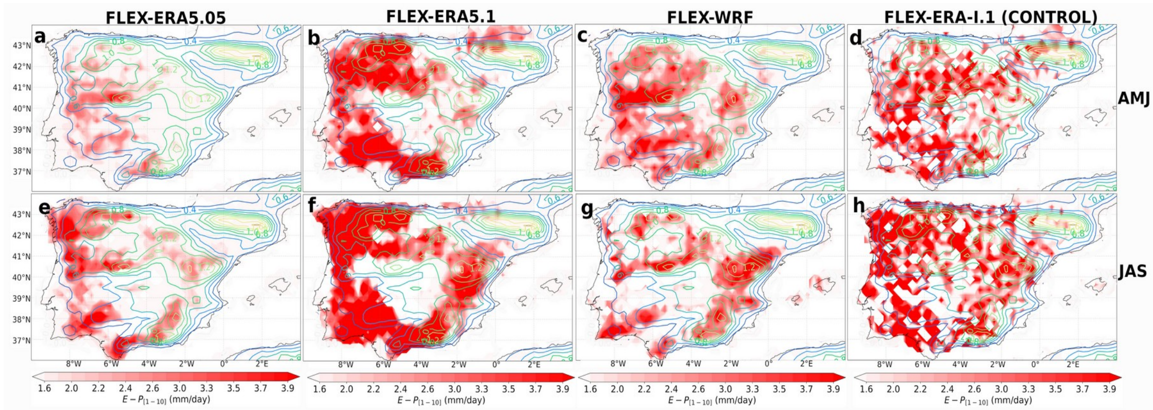

Figure S36. Moisture source patterns ($(E\text{-}P)_{[1\text{-}10]} > 0$ in mm day^{-1}) for the IP region from the Lagrangian outputs of FLEX-ERA5.05, FLEX-ERA5.1, FLEX-WRF, and FLEX-ERA-I.1. Orography at 0.25° spatial resolution is shown in contours (km). The fields displayed from top to bottom correspond to AMJ and JAS.

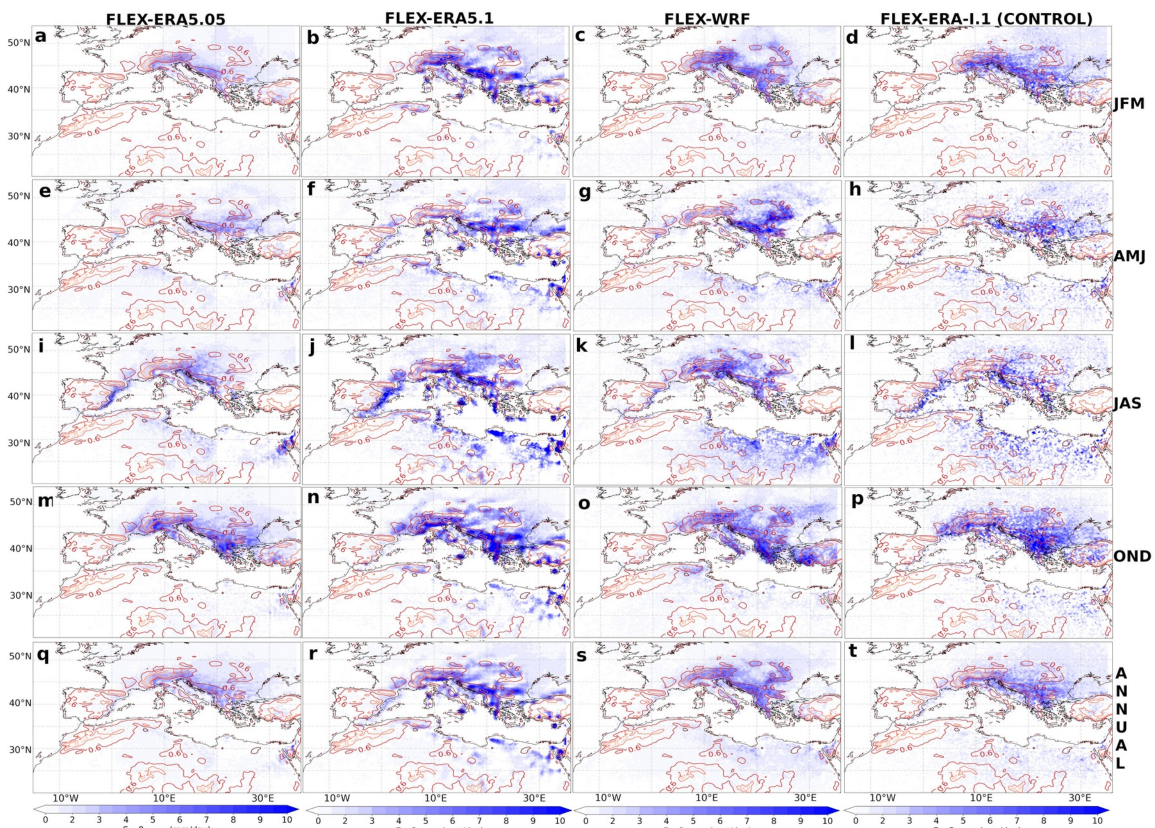

Figure S37. Moisture sink patterns ($(P\text{-}E)_{[1\text{-}10]} > 0$ in mm day^{-1}) for the MED region from the Lagrangian outputs of FLEX-ERA5.05, FLEX-ERA5.1, FLEX-WRF, and FLEX-ERA-I.1. Orography at 0.25° spatial resolution is shown in contours (km). The fields displayed from top to bottom correspond to JFM, AMJ, JAS, OND, and ANNUAL.

Table S1. Statistics added in the comparison for each configuration used for target region IP.

	Configurations	R^2	Mean [mm/day]	STD [mm/day]	VAR
JFM	FLEX-ERA5.05	0.256	0.075	0.086	1.141
	FLEX-ERA5.1	0.266	0.127	0.171	1.345
	FLEX-WRF	0.224	0.104	0.129	1.243
AMJ	FLEX-ERA5.05	0.503	0.101	0.225	2.220
	FLEX-ERA5.1	0.474	0.163	0.413	2.538
	FLEX-WRF	0.494	0.145	0.338	2.337
JAS	FLEX-ERA5.05	0.530	0.124	0.311	2.517
	FLEX-ERA5.1	0.509	0.196	0.558	2.855
	FLEX-WRF	0.424	0.174	0.353	2.034
OND	FLEX-ERA5.05	0.277	0.090	0.120	1.335
	FLEX-ERA5.1	0.241	0.149	0.256	1.713
	FLEX-WRF	0.180	0.119	0.143	1.203
ANNUAL	FLEX-ERA5.05	0.556	0.073	0.149	2.046
	FLEX-ERA5.1	0.510	0.120	0.294	2.450
	FLEX-WRF	0.528	0.092	0.194	2.107

Table S2. Statistics added in the comparison for each configuration used for target region MED.

	Configurations	R^2	Mean [mm/day]	STD [mm/day]	VAR
JFM	FLEX-ERA5.05	0.640	0.287	0.579	2.015
	FLEX-ERA5.1	0.593	0.479	1.187	2.481
	FLEX-WRF	0.596	0.421	0.881	2.090
AMJ	FLEX-ERA5.05	0.452	0.318	0.603	1.899
	FLEX-ERA5.1	0.408	0.531	1.234	2.324
	FLEX-WRF	0.367	0.509	1.026	2.015
JAS	FLEX-ERA5.05	0.386	0.409	0.829	2.027
	FLEX-ERA5.1	0.388	0.722	1.713	2.374
	FLEX-WRF	0.356	0.704	1.144	1.625
OND	FLEX-ERA5.05	0.602	0.410	0.925	2.257
	FLEX-ERA5.1	0.548	0.610	1.529	2.506
	FLEX-WRF	0.454	0.660	1.147	1.738
ANNUAL	FLEX-ERA5.05	0.634	0.326	0.645	1.978
	FLEX-ERA5.1	0.561	0.525	1.255	2.388
	FLEX-WRF	0.561	0.478	0.872	1.823

Table S3. Statistics added in the comparison for each configuration used for target region NATL.

	Configurations	R^2	Mean [mm/day]	STD [mm/day]	VAR
JFM	FLEX-ERA5.05	0.590	1.976	2.327	1.178
	FLEX-ERA5.1	0.584	2.866	4.036	1.408
	FLEX-WRF	0.457	1.941	2.097	1.080
AMJ	FLEX-ERA5.05	0.397	1.579	1.988	1.259
	FLEX-ERA5.1	0.370	2.327	3.617	1.554
	FLEX-WRF	0.218	2.093	2.308	1.103
JAS	FLEX-ERA5.05	0.387	1.895	2.750	1.451
	FLEX-ERA5.1	0.357	2.794	4.682	1.676
	FLEX-WRF	0.217	2.510	2.935	1.169
OND	FLEX-ERA5.05	0.488	2.575	3.016	1.171
	FLEX-ERA5.1	0.457	3.577	4.494	1.256
	FLEX-WRF	0.276	2.661	2.853	1.072
ANNUAL	FLEX-ERA5.05	0.643	1.822	1.972	1.082
	FLEX-ERA5.1	0.553	2.540	3.372	1.327
	FLEX-WRF	0.501	1.894	1.806	0.954

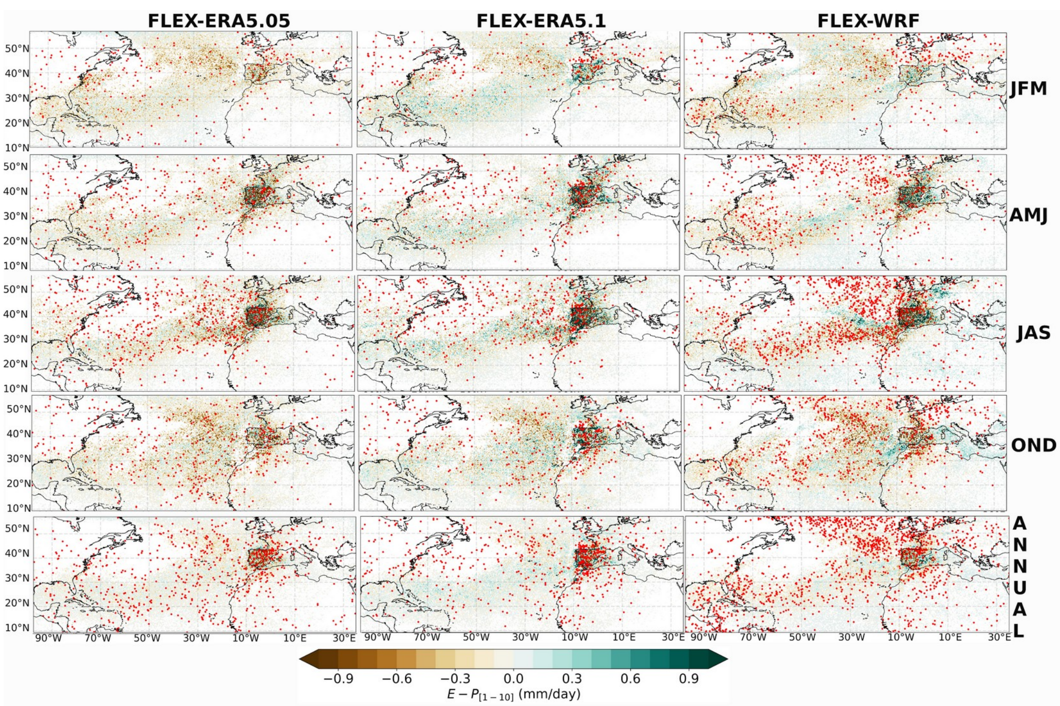

Figure S38. Differences of the E-P pattern corresponding to the IP target region with respect to the control experiment (FLEX-ERA-I.1) for the configurations: FLEX-ERA5.05, FLEX-ERA5.1 and FLEX-WRF. The red dots represent the regions with significant differences at 99% (significance level 0.01).

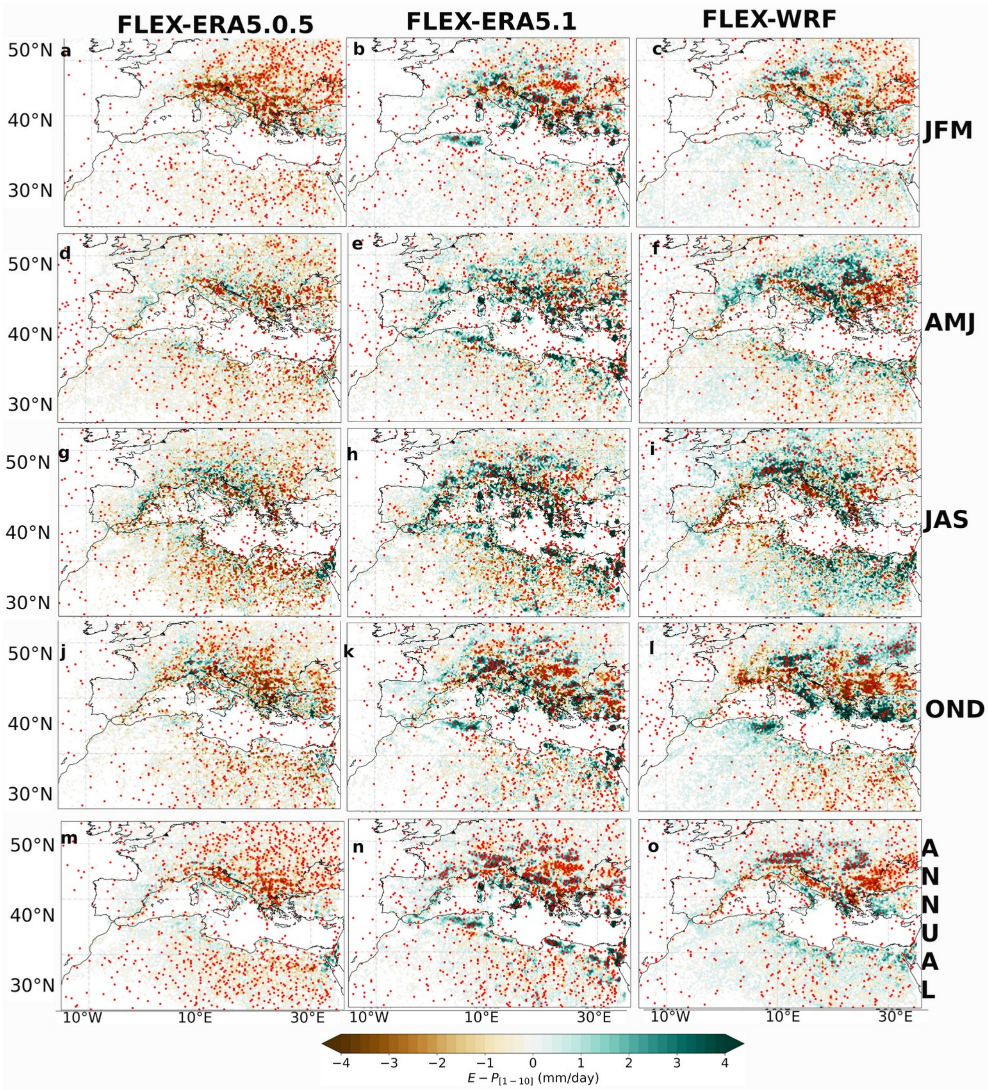

Figure 39. Differences of the E-P pattern corresponding to the MED target region with respect to the control experiment (FLEX-ERA-I.1) for the configurations: FLEX-ERA5.05, FLEX-ERA5.1 and FLEX-WRF. The red dots represent the regions with significant differences at 99% (significance level 0.01).

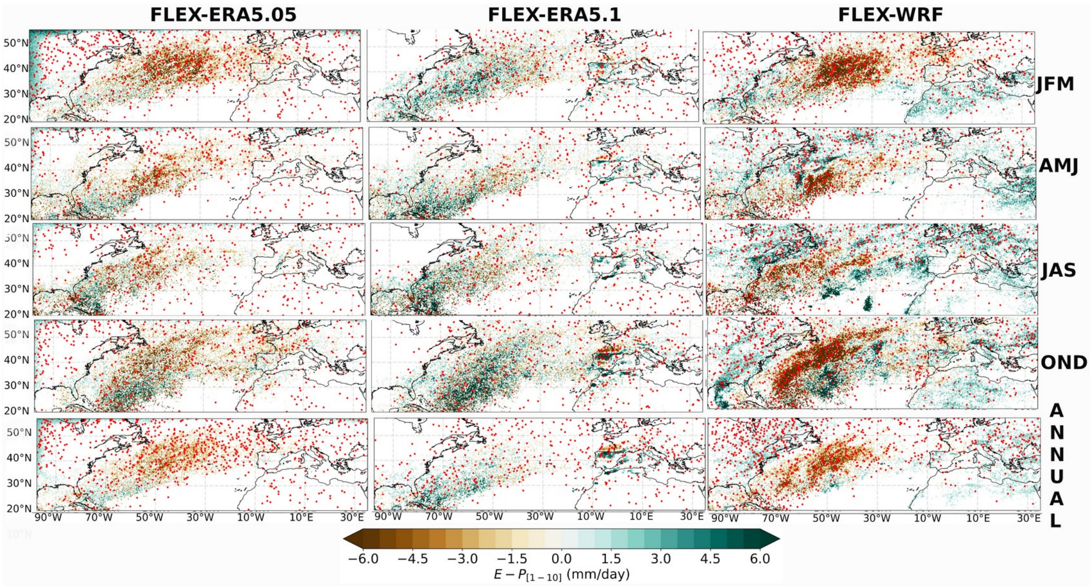

Figure S40. Differences of the E-P pattern corresponding to the NATL target region with respect to the control experiment (FLEX-ERA-I.1) for the configurations: FLEX-ERA5.05, FLEX-ERA5.1 and FLEX-WRF. The red dots represent the regions with significant differences at 99% (significance level 0.01).

Supplementary Information for

Projected changes in atmospheric moisture transport contributions associated with climate warming in the North Atlantic

José C. Fernández-Alvarez[1,2], Albenis Pérez-Alarcón[1,2], Jorge Eiras-Barca[1,3], Stefan Rahimi[4,5], Raquel Nieto[1], Luis Gimeno[1,*]

[1]Centro de Investigación Mariña, Universidade de Vigo, Environmental Physics Laboratory (EPhysLab), Campus As Lagoas s/n, Ourense, 32004, Spain

[2]Departamento de Meteorología, Instituto Superior de Tecnologías y Ciencias Aplicadas, Universidad de La Habana, La Habana, Cuba.

[3]Defense University Center at the Spanish Naval Academy, Group of Applied Mathematics for Defense, Plaza de España s/n 36920 Marín, Spain

[4]Department of Atmospheric Science, University of Wyoming

[5]Center for Climate Science, University of California Los Angeles

* Luis Gimeno

Section 1. Materials and Methodology

Section 1.1 Data description

To obtain the FLEXPART-WRF outputs for our experiments during the historical and future periods (under the SSP5-8.5 scenario), two sets of input data were used: dynamical downscaled data (using the Weather Research and Forecasting, WRF-ARW, model) from CESM2 outputs and from ERA5 reanalysis (WRF-CESM2 and WRF-ERA5, respectively).

The CESM2 (Community Earth System Model Version 2)[1] data were downloaded from the Earth System Grid Federation (ESGF2) and they were obtained for the native "gn" grid with a resolution of 0.9 x 1.25 (~1º) and presented as an output mesh with 288 × 192 longitude/latitude, 32 vertical levels (top level at 2.25 mb). To force the WRF-ARW model, all CESM2 climatic data were processed to create intermediate files (26 vertical levels) that were used as the initial and boundary conditions. The CESM2 data has been evaluated for representing jet streams and storm tracks, Northern Hemisphere (NH) stationary waves, global divergent circulation, annular modes, the North Atlantic Oscillation and NH winter blocking[2]. CESM2 ranks within the top 10% of CMIP class models with respect to many of these features[2]. CESM2 provides all the necessary variables to force WRF-ARW at a better resolution than other models that which have a resolution of approximately 250 km.

In addition, precipitation in CESM2-based subseasonal forecast systems has been shown to be similar to the one obtained with NOAA CFSv2 model, and slightly lower than the one provided by the ECMWF model[3]. Besides, the North Atlantic Oscilation (NAO) structure in winter and summer is relatively well represented in CESM2 with some minor biases that are quite similar to the rest of the CMIP6 climate models[2]. On the one hand, this implies an adequate representation of the associated precipitation anomalies over the Mediterranean[4]. According to these authors, many models present inadequacies in the representation, being the amplitude of the precipitation signal too weak, especially in the East. On the other hand, CESM2 has a remarkable representation of the velocity potential of the upper troposphere in both summer and winter. This element is closely related to tropical precipitation and represents a significant forcing of extratropical standing waves[2]. Moreover, it presents improvements in rainfall in regions of great global interest such as the Indian Ocean, East Asia, the tropical Atlantic and the Amazon[2]. Finally, CESM2 has been used to study the sea surface temperature effect increase on future changes in Atmospheric Rivers[5, 6].

The shared socioeconomic pathway (SSP) used in this research was SSP5-8.5[7,8]. SSP5-8.5 is a scenario (“worst-case scenario”) that represents emissions high enough to produce a radiative forcing of 8.5 W m^{-2} in 2100 under extreme conditions. This will amplify all signals detected in this analysis.

ERA5[9] is the most recent (5th generation) global atmospheric reanalysis of the European Centre for Medium-Range Weather Forecasts (ECMWF), and it was used to compare fields for the historical period of 1985–2014. WRF-ERA5 outputs were employed to force the FLEXPART-WRF model. These simulations corresponded to the control experiments for evaluating the configuration (see Section 1.4). The advantages of ERA5 are its high resolution (31 km horizontally and 137 vertical levels) and large number of assimilated historical observations. ERA5 significantly improves upon its predecessor, ERA-Interim reanalysis, particularly with respect to precipitation fields both over extratropical regions and tropical oceanic areas.

Section 1.2 Experimental setup for WRF and FLEXPART-WRF

The parameterisations employed in the WRF-ARW configuration were as follows: the WSM6 microphysics scheme[10], Yonsei University planetary boundary layer (PBL) scheme[11], revised MM5 surface layer scheme[12], United Noah Land Surface Model[13], shortwave and longwave RRTMG schemes[14] and the Kain-Fritsch cumulus scheme[15]. Spectral nudging of waves longer than approximately 1000 km was employed to avoid distortion of the large-scale circulation within the regional model domain due to the interaction between the model solution and lateral boundary conditions[16]. The outputs had 40 vertical layers from the surface to 50 hPa with a horizontal spacing of 20 km and they covered an area of 115.39–42.02°W and 19.41°S–59.51°N (see Fig. 1). The criteria used to select these parameterisation schemes were that they had been evaluated and employed in several previous investigations involving the WRF-ARW domain[17,18] (see Supplementary Fig. 1). For the WRF simulations, a 1-month spin-up was performed before each year to be simulated, and the restart mode was used when the WRF-ARW was stopped. Finally, the outputs of WRF-ARW had 40 vertical levels in sigma coordinates and 480 × 780 nodes in the output grid (~0.18°). The historical periods, mid-century and end of the century used were 1985-2014, 2036-2065 and 2071-2100, respectively.

For the FLEXPART-WRF[19] configuration, we used Hanna's[20] scheme for turbulence parameterisation with the convection scheme activated. This scheme is based on the boundary layer parameters PBL height, Monin–Obukhov length, convective velocity scale, roughness length and friction velocity[19]. We assumed skewed rather than Gaussian turbulence in the convective PBL. The FLEXPART-WRF has forty levels and 400 × 777 points, where in the output mesh where the particles are released. The outputs had spatial and temporal resolutions of 20 km and 6 h, respectively.

Section 1.3 Moisture sources and sinks used

The North Atlantic Ocean source (NATL; Sup. Fig. 1) is considered to be one of the main global oceanic sources that contributes moisture to continental precipitation[21]. This source contributes to several geographical areas, such as eastern North America, Central America, northern and central South America, Europe and northern Africa. Moreover, the NATL is an important oceanic contributor to the North and South American monsoon systems, as well as to the Atlantic Intertropical Convergence Zone (ITCZ)[22,23]. It shows marked seasonal behaviour; the moisture contribution increases during winter and decreases strongly in summer. Meanwhile, previous studies have not observed changes in its size and position[21].

The Mediterranean Sea (MED; Sup. Fig. 1) plays an important role in its surrounding areas in terms of the transport of atmospheric moisture for precipitation. During the boreal winter, it supplies moisture that generates precipitation in continental areas located over Europe to the northeast; during the summer, it provides moisture to its surroundings in all directions and extending into northern Europe, northeast Africa and the Middle East[21]. The moisture contribution from the MED is higher in summer and relatively lower in autumn and winter[21]. In particular, the western MED contributes directly to rainfall over the Alpine region and the eastern Iberian Peninsula, and it plays an important role in transporting moisture to northern Africa. Furthermore, the central MED has a substantial impact on rainfall over the Hellenic Peninsula and islands and in the central part of North Africa, and the eastern MED influences the Middle East and Egypt[24].

The Iberian Peninsula (IP; Sup. Fig. 1) is located in southwestern Europe and is surrounded by the Mediterranean Sea to the east and the Atlantic Ocean to the west. It is linked to the European continent in its northeastern corner. The precipitation regime north and west of the IP is strongly affected by the mean annual cycle of the Atlantic storm track and its variability, whereas in the interior and east of the IP, it is strongly affected by large-scale synoptic systems and convective precipitation[25]. The main moisture sources affecting the IP correspond to the tropical-subtropical region of North Atlantic Ocean and the Mediterranean Sea (a more local source).

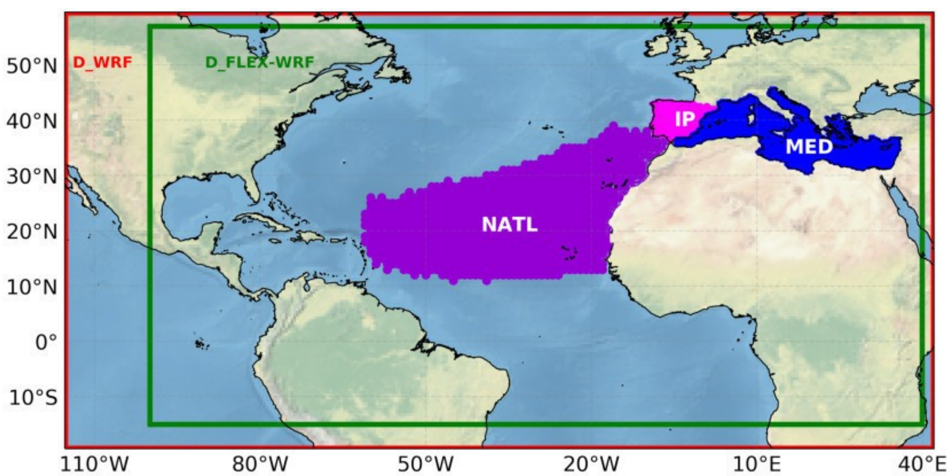

Supplementary Figure 1. Domains and target regions. Domain configuration for WRF-ARW (red) and FLEXPART-WRF (green) simulations. The moisture target regions are shown in blue (MED; Mediterranean Sea), pink (IP; Iberian Peninsula) and dark violet (NATL; North Atlantic moisture source).

Section 1.4 Evaluation of the used configurations

The evaluations were conducted for the reference period (1985–2014) for the boreal seasonal periods from January to March (JFM), April to June (AMJ), July to September (JAS) and October to December (OND), corresponding to winter, spring, summer and autumn, respectively[26], and for the annual scale. The selection of the JFM, AMJ, JAS and OND periods is mainly based on being able to use all the years simulated for the historical, mid- and end-century period. In addition, the consideration of these periods allows us to use the WRF-ARW and FLEXPAT-WRF configuration evaluated with ERA5 for the same study region and the same analyzed periods[27]. Finally, Gimeno et al.[26] used similar periods to study the moisture sources associated with IP, and therefore the ability to make a direct comparison between results is available.

First, the integrated water vapour transport (IVT) with the outputs of WRF-CESM2 and WRF-ERA5 (see Sup. Fig. 10) was evaluated using the following equations,

$$IVT=\sqrt{{u_q}^2+{v_q}^2}, \tag{1}$$

$$u_q=\frac{1}{g}\int_{ps}^{p} uqdp, \tag{2}$$

$$v_q=\frac{1}{g}\int_{ps}^{p} vqdp, \tag{3}$$

where g is gravitational acceleration, q is specific humidity, ps is surface pressure, p is pressure at the top, and u and v are the zonal and meridional winds, respectively[28, 29].

After verifying that the IVT field corresponded with the control experiments, the E-P fields for the moisture sources and sinks were evaluated (see Sup. Fig. 11, 12, 13). The statistics shown in Table 1 were used to evaluate the (E-P) patterns (see Sup. Fig. 14), where x_i and y_i are the simulated (FLEX-WRF) and control (FLEX-ERA5) values, respectively, n is the number of points and $\overline{x_i}$ and $\overline{y_i}$ are the mean values[30].

Supplementary Table 1. Equations for the used statigraphs

Statigraphs	**Equation**
Absolute error (MAE)	$MAE = \frac{\sum_{i=1}^{n} \lvert x_i - y_i \rvert}{n}$
Root mean square error (RMSE)	$RMSE = \sqrt{\frac{\sum_{i=1}^{n} (x_i - y_i)^2}{n}}$
Pearson's correlation (R)	$R = \frac{\sum_{i=1}^{n} (x_i - \overline{x})(y_i - \overline{y})}{\sqrt{\sum_{i=1}^{n} (x_i - \overline{x})^2 (y_i - \overline{y})^2}}$
Bias (B)	$B = \frac{\sum_{i=1}^{n} (x_i - y_i)}{n}$

Section 2. Supplementary figures

Supplementary figures for: Future projections for precipitation and geopotential height in the Noth Atlantic Ocean from the CESM2 model

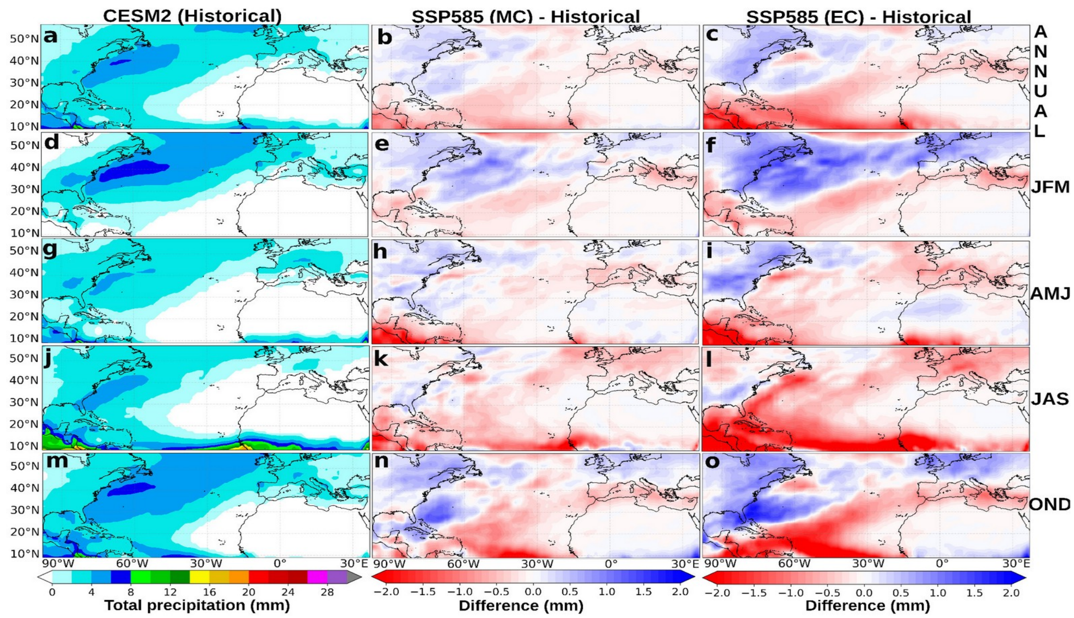

Supplementary Figure 2. Comparison of average seasonal precipitation field between historical period and SSP5-8.5 scenario for CESM2 model. | Precipitation (in mm day^{-1}) for the historical reference period (left column, 1985–2014) and differences with the SSP5-8.5 scenario for the mid- and end 21st century (central, MC, 2036–2065, and right, EC, 2071–2100, respectively).

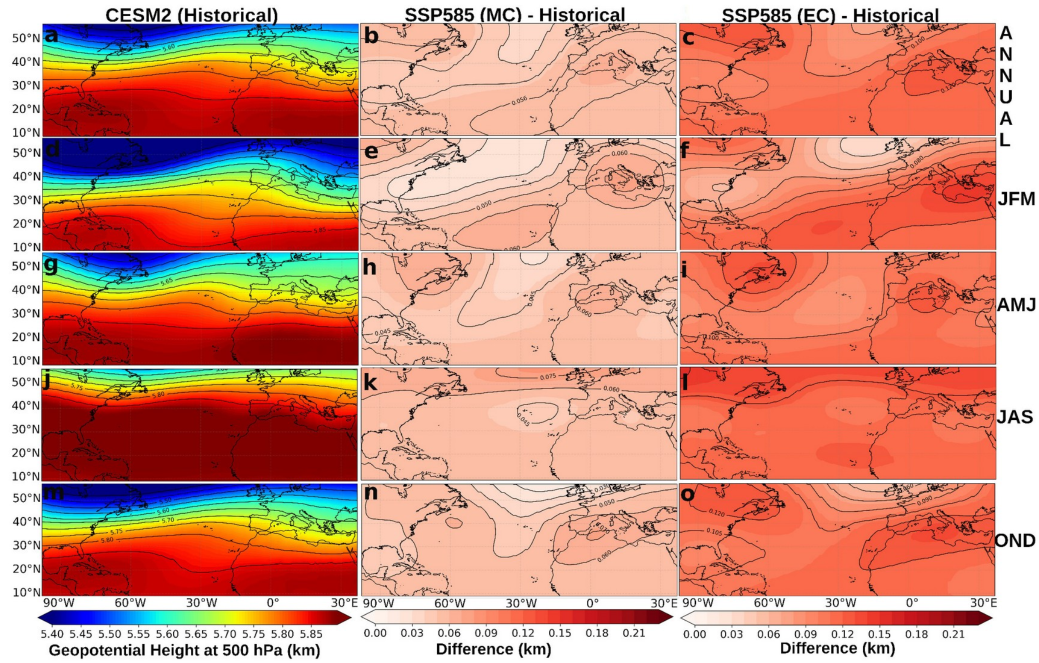

Supplementary Figure 3. Comparison of Geopotential height at 500 hPa field between historical period and SSP5-8.5 scenario for CESM2 model. | Same as Supplementary Figure 2 for geopotential height at 500 hPa (in km).

Supplementary figures and table for: Future projections for integrated water vapour transport (IVT) in the North Atlantic Ocean

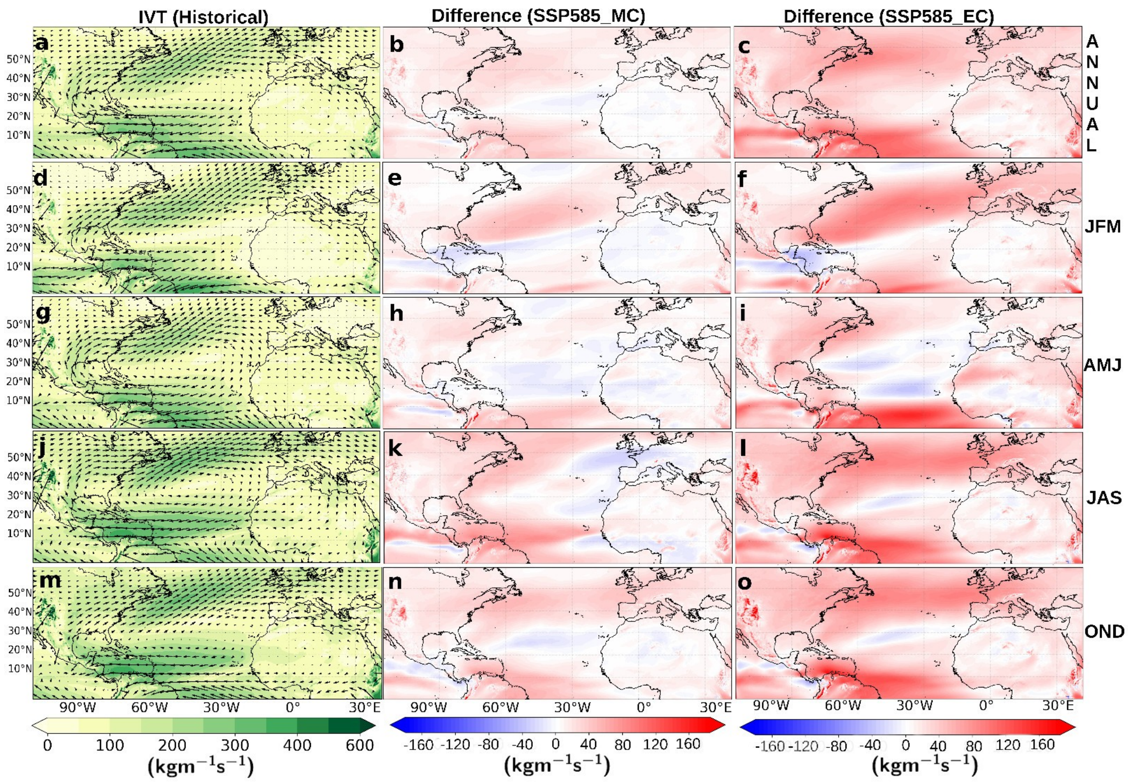

Supplementary Figure 4. Comparison of vertically integrated water vapour transport (IVT) field between historical period and SSP5-8.5 scenario | IVT module (coloured filled, in mm day^{-1}) and direction (arrows, in kg m^{-1} s^{-1}) for the historical reference period (left column, 1985–2014) and differences for the SSP5-8.5 scenario for the mid- and end 21st century (central, MC, 2036–2065, and right, EC, 2071–2100, respectively). The fields displayed from top to bottom correspond to annual, winter, spring, summer and autumn periods (ANNUAL, JFM, AMJ, JAS and OND).

Supplementary Table 2: Mean percentage differences (%) for vertically integrated water vapour transport (IVT) with respect to the historical period considering the SSP5-8.5 scenario | The periods analyzed correspond to the middle (2036–2065, MC) and end of the century (2071–2100, EC).

	Mid-century	End-century
Winter	10.5	24.1
Spring	9.2	21.9
Summer	10.9	27.6
Autumn	14.1	30.1
Annual	11.2	25.9

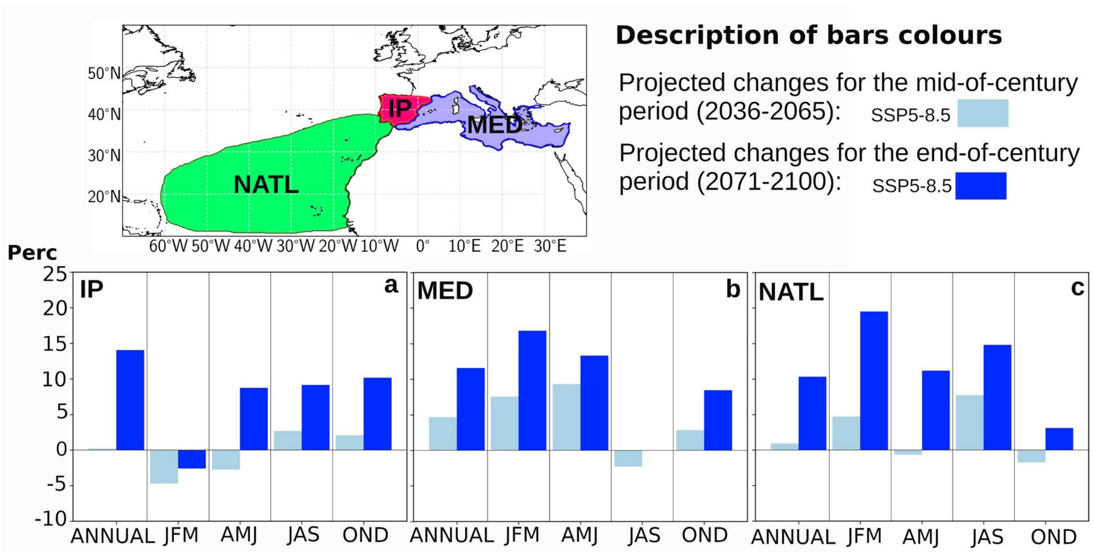

Supplementary Figure 5. Future changes in the yearly and seasonal variability for the relative contribution (in %) of the moisture sources to the Iberian Peninsula | Relative changes in the standard deviation of the time series are shown for Mediterranean Sea (MED), North Atlantic Ocean (NATL) and the precipitation recycling processes (PRPs) over the four seasons as well as in annual terms both for middle (2036–2065, MC) and end of the century (2071–2100, EC).

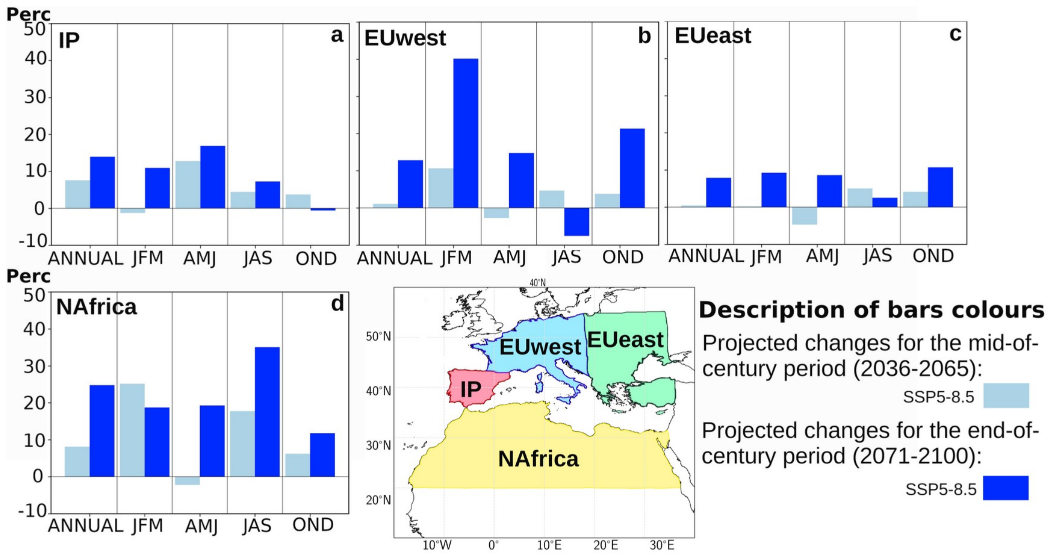

Supplementary Figure 6. Future changes in the yearly and seasonal variability for the relative contribution of precipitation (in %) to moisture sinks from the Mediterranean source | Relative changes in the standard deviation of the time series are shown for Western Europe (EUwest), Eastern Europe (EUeast) and North Africa (Nafrica) and Iberian Peninsula (IP) associated with the Mediterranean sea (MED) source.

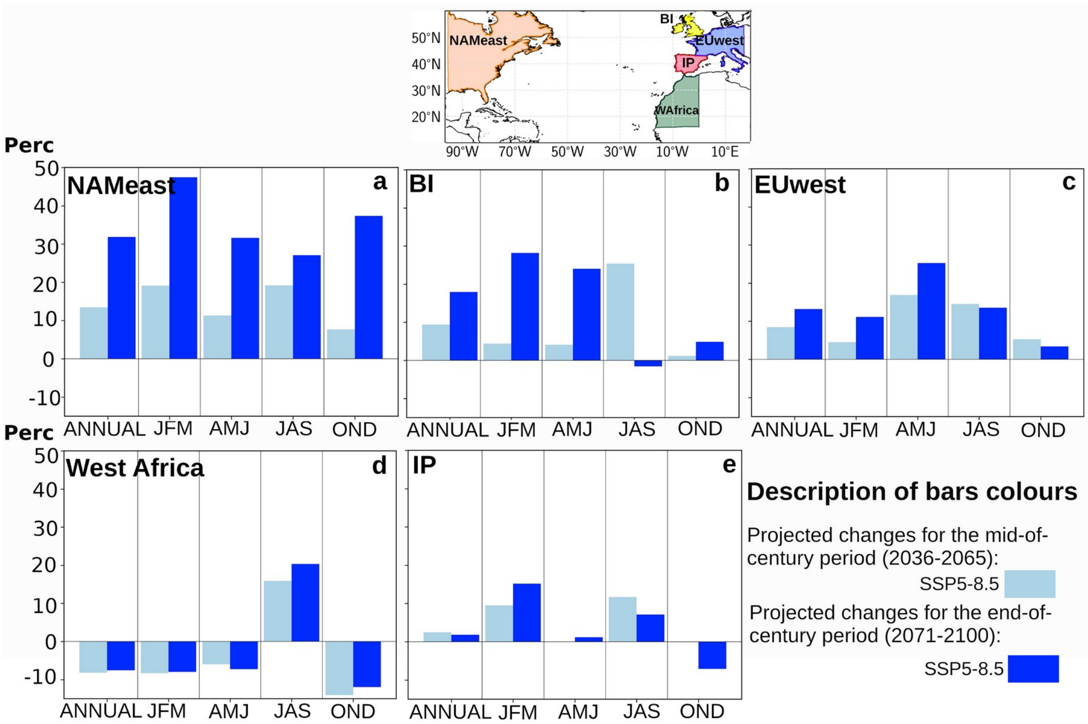

Supplementary Figure 7. Future changes in the yearly and seasonal variability for the the relative contribution of precipitation (in %) to moisture sinks from the North Atlantic source | Relative changes in the standard deviation of the time series are shown for British Isles (BI), European West Coast (EUwest), Iberian Peninsula (IP), West Africa (WAfrica) and the North American East Coast (NAMeast) associated with the North Atlantic Ocean (NATL) source.

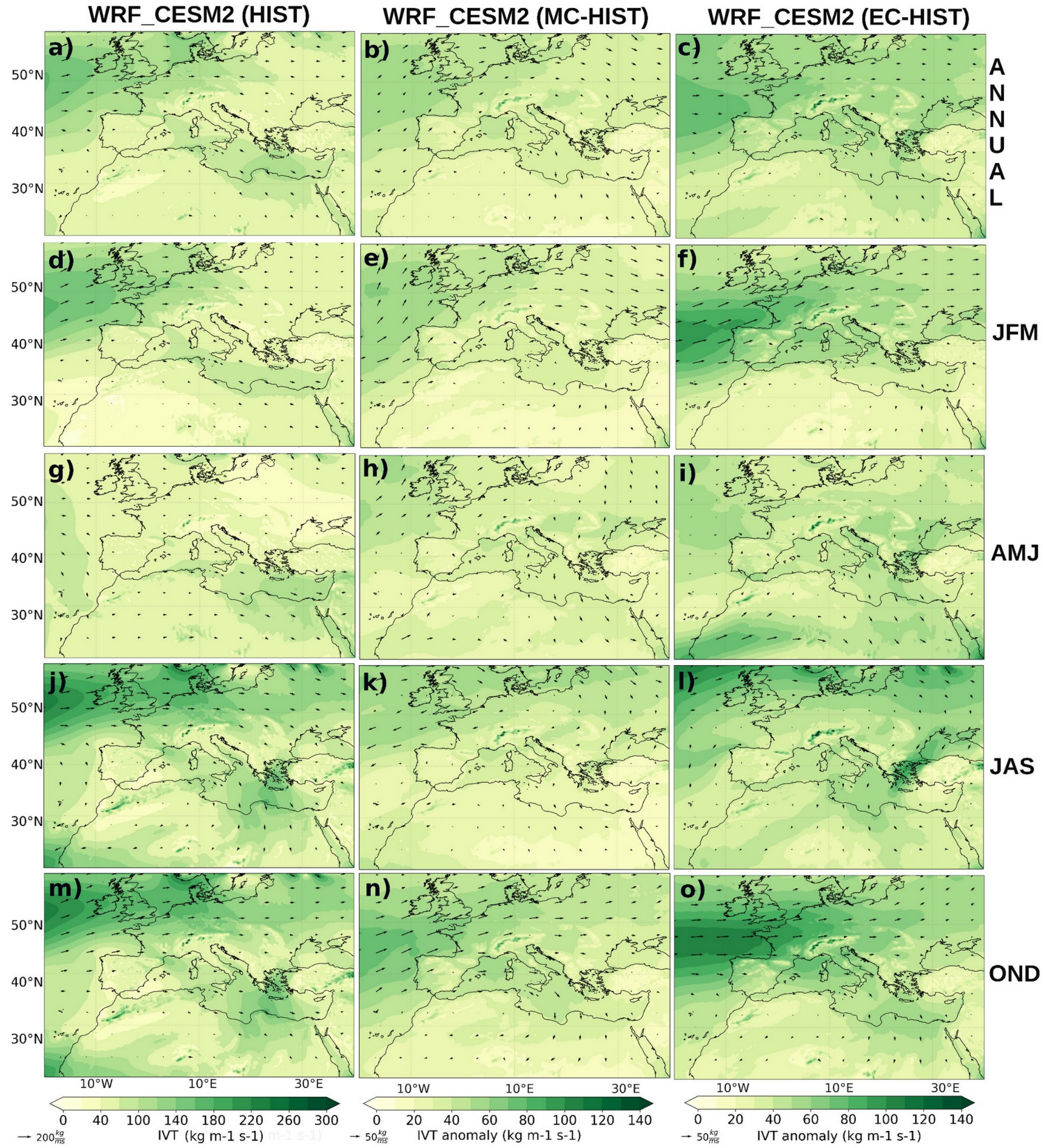

Supplementary Figure 8. Comparison of vertically integrated water vapour transport (IVT) field between historical period and its anomalies with scenario SSP5-8.5 for MC and EC focused on the Mediterranean sea (MED) | IVT module (coloured filled, in mm day^{-1}) and direction (arrows, in kg m^{-1} s^{-1}) for the historical reference period (left column, 1985–2014) and anomalies for the SSP5-8.5 scenario for the mid- and end 21st century (central, MC, 2036–2065, and right, EC, 2071–2100, respectively). The fields displayed from top to bottom correspond to annual, winter, spring, summer and autumn periods (ANNUAL, JFM, AMJ, JAS and OND).

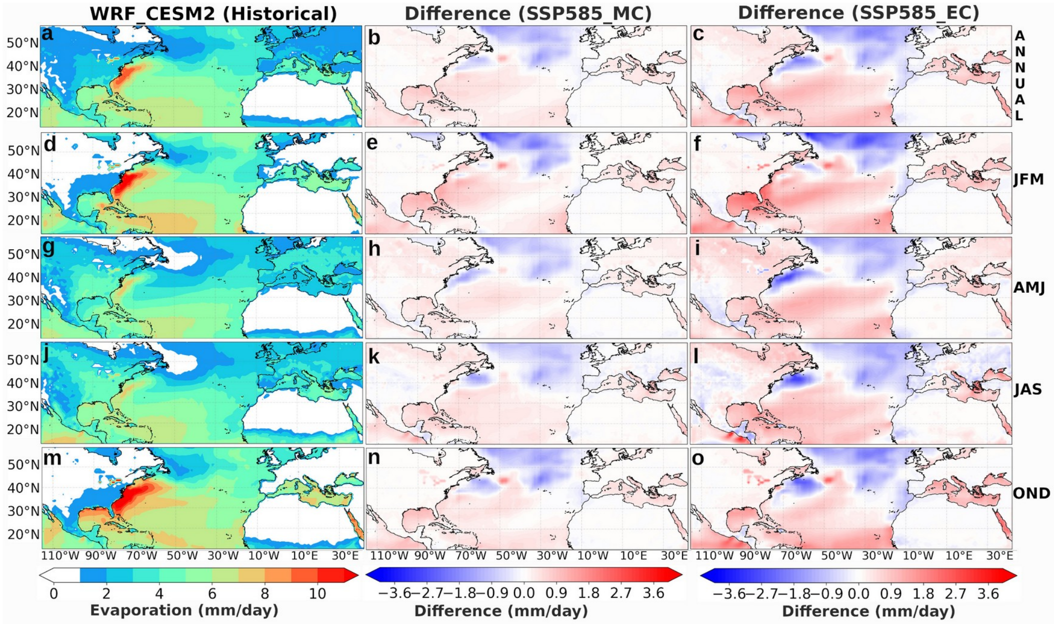

Supplementary Figure 9. Comparison of evaporation (E) field between historical period and SSP5-8.5 scenario focused on the North Atlantic and Mediterranean Sea | E field (coloured filled, in mm day^{-1}) for the historical reference period (left column, 1985–2014) and differences for the SSP5-8.5 scenario for the mid- and end 21st century (central, MC, 2036–2065, and right, EC, 2071–2100, respectively). The fields displayed from top to bottom correspond to annual, winter, spring, summer and autumn periods (ANNUAL, JFM, AMJ, JAS and OND).

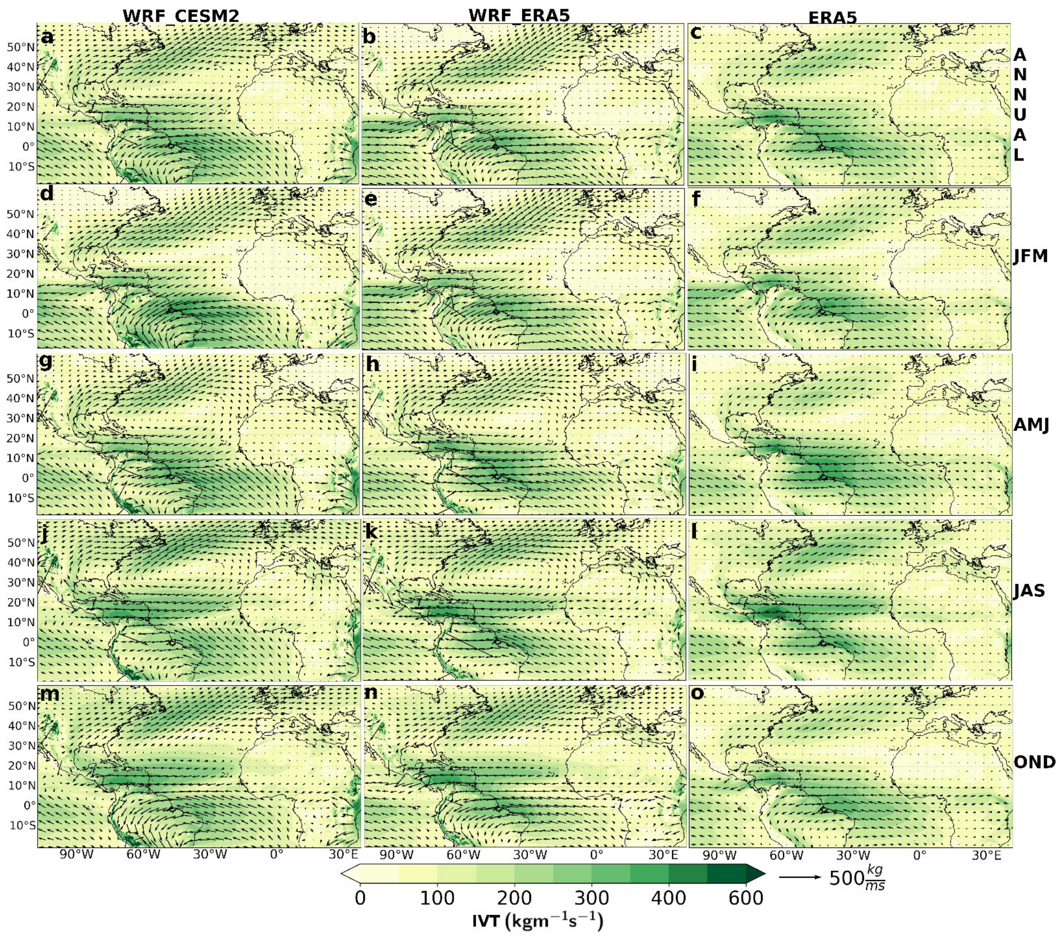

Supplementary Figure 10. Comparison of vertically integrated water vapour transport (IVT) field between WRF-CESM2 and WRF-ERA5 | IVT module (contours) and direction (arrows) for WRF-CESM2 (left column), WRF-ERA5 (central) and ERA5 (right) in the period 1985–2014 (kg m^{-1} s^{-1}). The fields displayed from top to bottom correspond to annual, winter, spring, summer and autumn periods (ANNUAL, JFM, AMJ, JAS and OND).

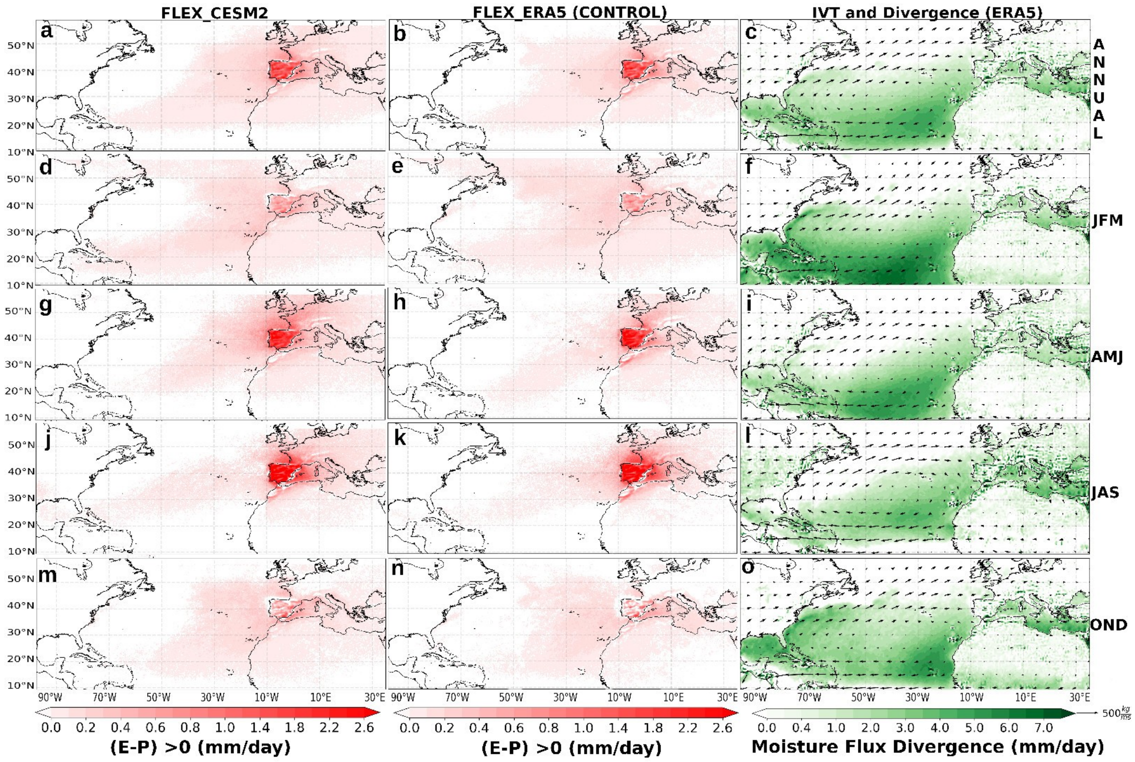

Supplementary Figure 11. Moisture source fields for the Iberian Peninsula in the historical period | Moisture sources fields for the Iberian Peninsula (in mm day^{-1}) for FLEX-CESM2 (left) and FLEX-ERA5 (right), and the vertically integrated water vapour transport (IVT) field and its divergence from ERA5 (right, vectors in vectors in kg m^{-1} s^{-1} and coloured field in mm day^{-1}, respectively) during the historical period (1985-2014). The fields displayed from top to bottom correspond to annual, winter, spring, summer and autumn periods (ANNUAL, JFM, AMJ, JAS and OND).

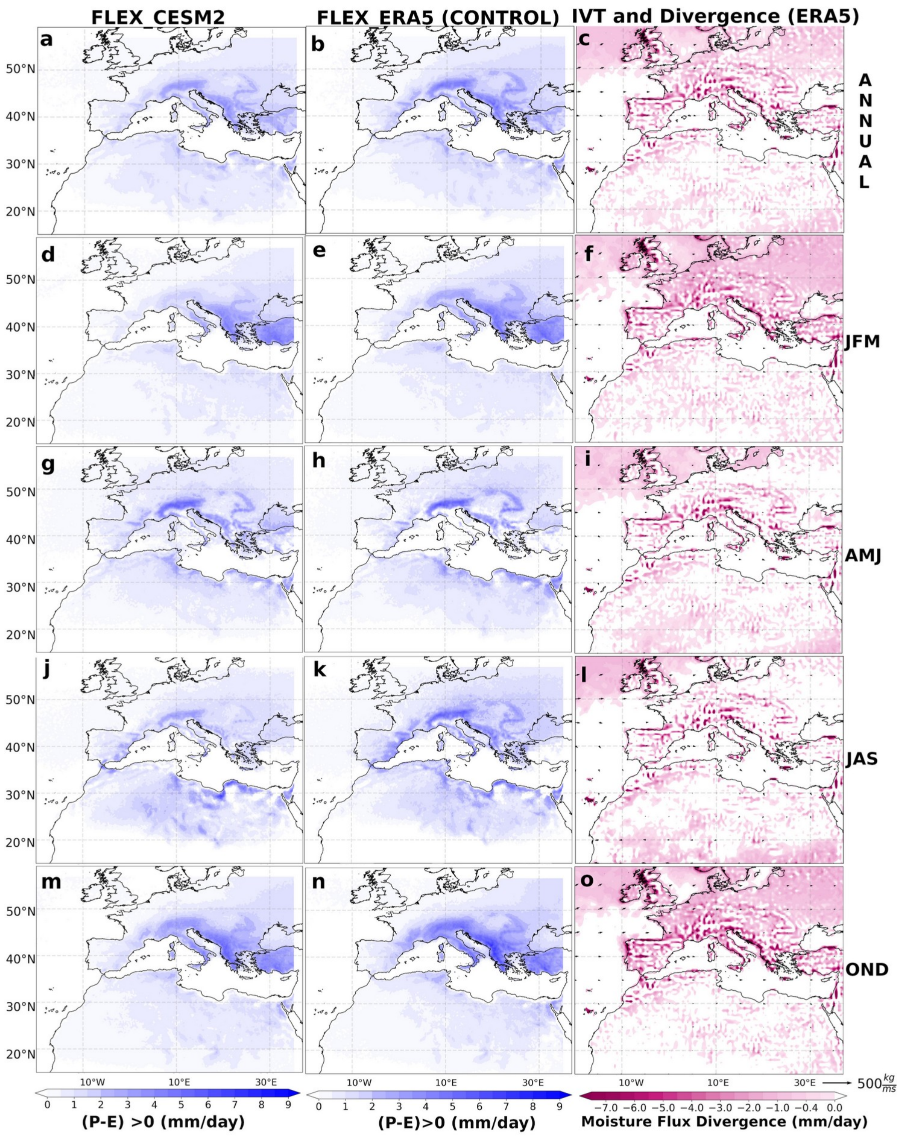

Supplementary Figure 12. Moisture sink fields for the Mediterranean source in the historical period | Moisture sink fields for the Mediterranean Sea (in mm day^{-1}) for FLEX-CESM2 (left) and FLEX-ERA5 (right), and the vertically integrated water vapour transport (IVT) field and its divergence from ERA5 (right, vectors in vectors in kg m^{-1} s^{-1} and coloured field in mm day^{-1}, respectively) during the historical period (1985-2014). The fields displayed from top to bottom correspond to annual, winter, spring, summer and autumn periods (ANNUAL, JFM, AMJ, JAS and OND).

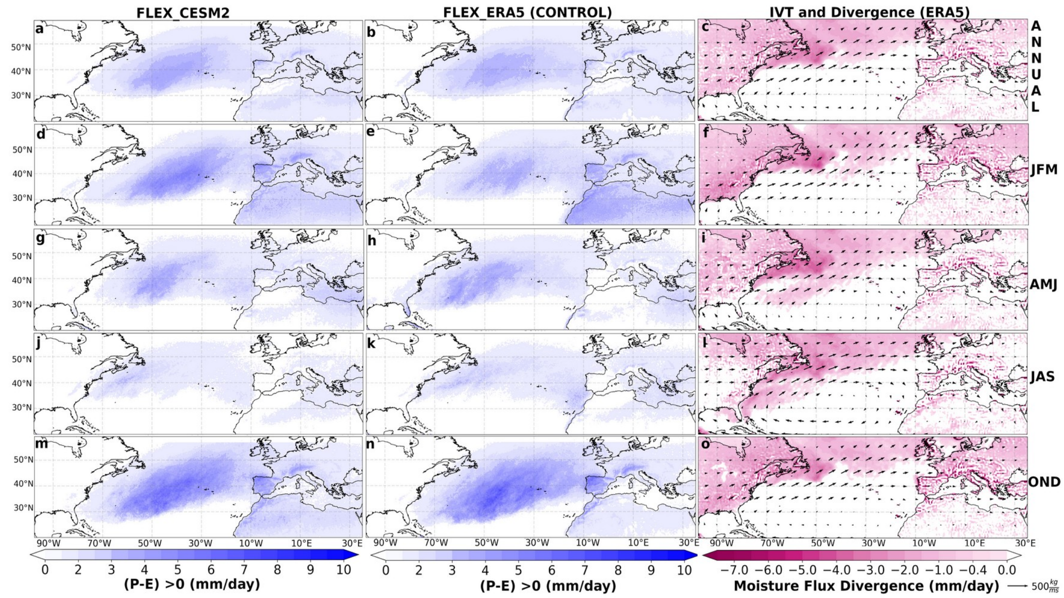

Supplementary Figure 13. Moisture sink fields for the North Atlantic source in the historical period. | Moisture sink fields for the North Atlantic (in mm day^{-1}) for FLEX-CESM2 (left) and FLEX-ERA5 (right), and the vertically integrated water vapour transport (IVT) field and its divergence from ERA5 (right, vectors in vectors in kg m^{-1} s^{-1} and coloured field in mm day^{-1}, respectively) during the historical period (1985-2014). The fields displayed from top to bottom correspond to annual, winter, spring, summer and autumn periods (ANNUAL, JFM, AMJ, JAS and OND).

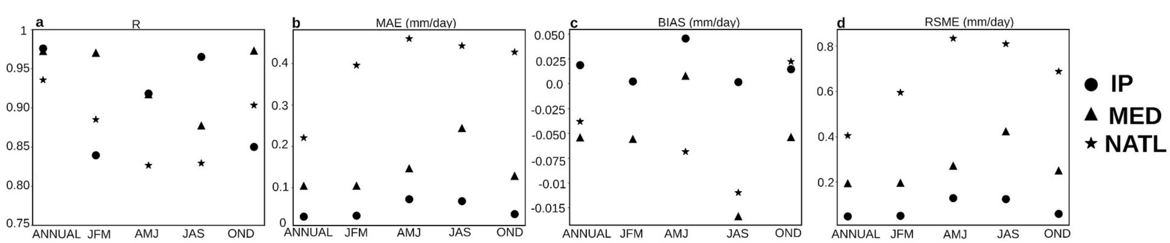

Supplementary Figure 14. Evaluation of FLEX-CESM2 configuration in the historical period. | Statigraphs used for evaluating moisture sources and sinks for target regions: Iberian Peninsula (IP), Mediterranean Sea (MED) and North Atlantic Ocean (NATL). The graphs shown correspond to: Pearson's correlation (R) (a), Absolute error (MAE) (b), Bias (BIAS) (c), and Root mean square error (RSME) (d). Period: 1985–2014.

Section 3. Comparison of results for WRF-CESM2 model vs Ensemble models database

The CESM2 model is considered warm since it reaches ~4ºC in the period 2060-2079 under the SSP5-8.5 scenario[31]. In order to identify if this behavior can influence the results, the main simulations in this manuscript are compared with those obtained using the outputs from the Bias-corrected CMIP6 global database[32] (WRF-ENS) as forcing data. For this comparison, we used a 5-year period (Historical: 2010-2014, MC: 2049-2053, EC: 2096-2100). These data are a bias-corrected global database based on 18 models from the CMIP6 and the European Center for Medium-Range Weather Forecasts Reanalysis 5 (ERA5) database. The bias-correction of these outputs is based on ERA5 mean climate and interannual variance, with a non-linear trend from the ensemble mean of the 18 CMIP6 models. The dataset spans the historical time period 1979–2014 and future scenarios for 2015–2100 with a horizontal grid spacing of (1.25° × 1.25°) at six-hourly intervals.

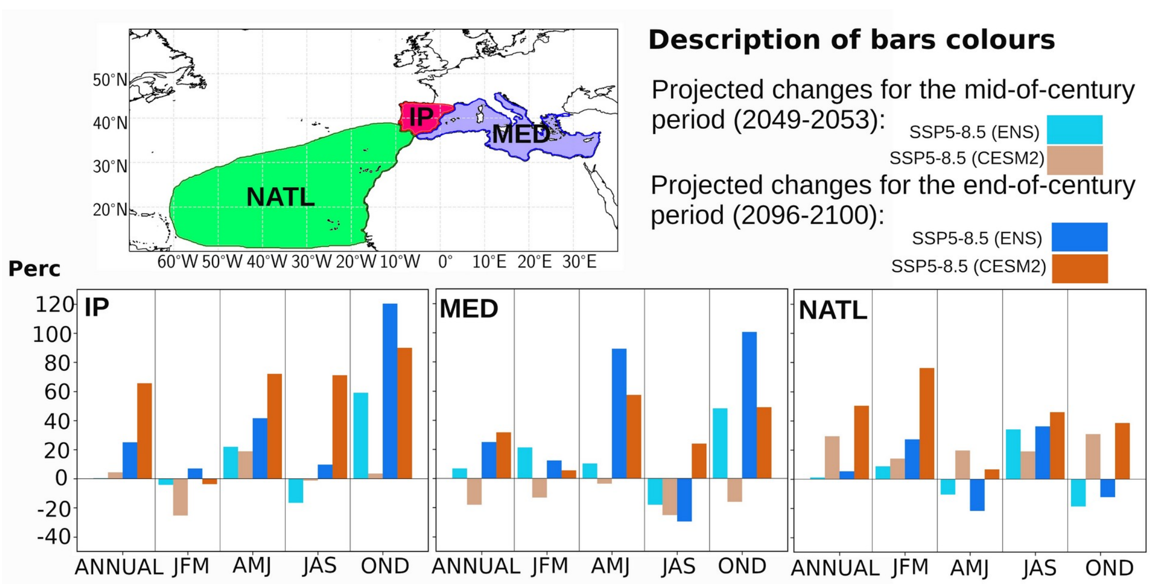

Supplementary Figure 15. Comparison of the future moisture contribution changes for the Iberian Peninsula for WRF-CESM2 vs WRF-ENS. Percentage values of future moisture contribution changes corresponding to the: berian Peninsula (IP), Mediterranean Sea (MED) and North Atlantic Ocean (NATL). The periods are annual, winter, spring, summer and autumn periods (ANNUAL, JFM, AMJ, JAS and OND) and the SSP5-8.5 scenario. Blue and red colours correspond to the WRF-ENS and WRF-CESM2, respectively.

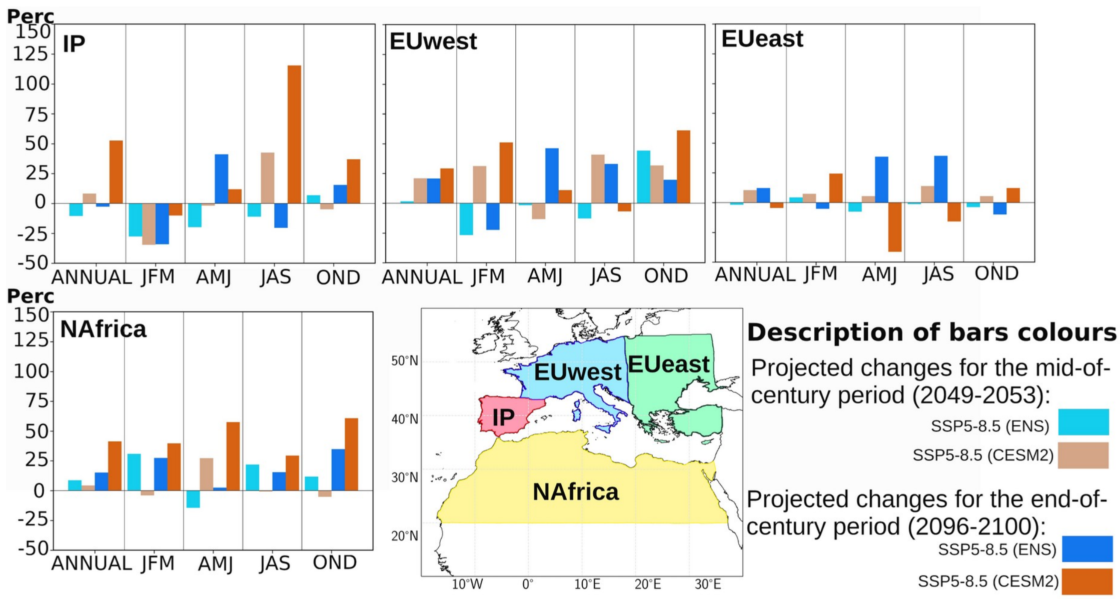

Supplementary Figure 16. Future changes in precipitation contribution associated with the Mediterranean source for WRF-CESM2 vs WRF-ENS. Percentage projected future changes in precipitation contribution over: Western Europe (EUwest), Eastern Europe (EUeast) and North Africa (Nafrica) and Iberian Peninsula (IP) associated with the Mediterranean sea (MED) source**.** The periods are annual, winter, spring, summer and autumn periods (ANNUAL, JFM, AMJ, JAS and OND) and the SSP5-8.5 scenario. Blue and red colours correspond to the WRF-ENS and WRF-CESM2, respectively.

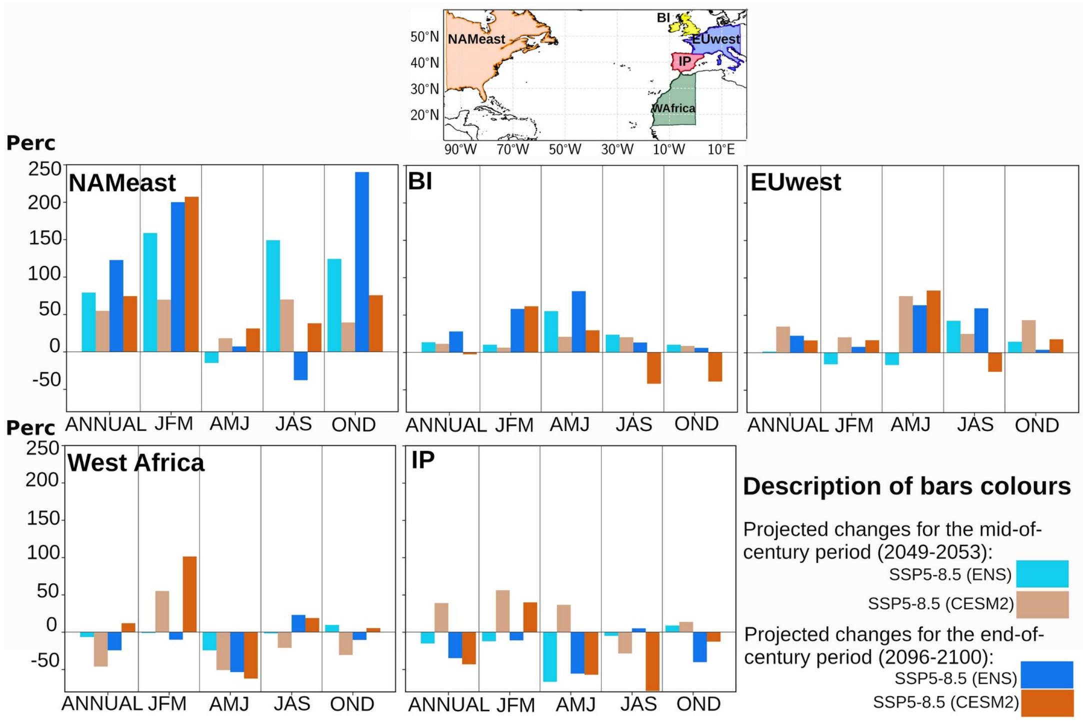

Supplementary Figure 17. Future changes in precipitation contributions from the North Atlantic source for WRF-CESM2 vs WRF-ENS. Percentage future changes in the precipitation contribution over: British Isles (BI), European West Coast (EUwest), Iberian Peninsula (IP), West Africa (WAfrica) and the North American East Coast (NAMeast) associated with the North Atlantic Ocean (NATL) source. The periods are annual, winter, spring, summer and autumn periods (ANNUAL, JFM, AMJ, JAS and OND) and the SSP5-8.5 scenario. Blue and red colours correspond to the WRF-ENS and WRF-CESM2, respectively.

Supplementary References

1- Danabasoglu, G., Lamarque, J.-F., Bacmeister, J., Bailey, D. A., DuVivier, A. K., Edwards, J., et al. The Community Earth System Model Version 2 (CESM2). *J. Adv. Model. Earth Syst.* **12,** e2019MS001916 (2020).

2- Simpson, I. R., Bacmeister, J., Neale, R. B., Hannay, C., Gettelman, A., Garcia, R. R., et al. An evaluation of the large-scale atmospheric circulation and its variability in CESM2 and other CMIP models. *J. Geophys. Res.* **125,** e2020JD032835 (2020).

3- Richter, J. H. et al. Subseasonal Earth system prediction with CESM2. *Weather Forecast.* **37**, 797-815 (2022).

4- Bladè, I., Fortuny, D., van Oldernborgh, G. J., Liebmann, B. The summer North Atlantic Oscillation in CMIP3 models and related uncertainties in projected summer drying in Europe. *J. Geophys. Res.* **117**, D166104 (2012).

5- McClenny, E. E., Ullrich, P. A. & Grotjahn, R. Sensitivity of atmospheric river vapor transport and precipitation to uniform sea surface temperature increases. *J. Geophys. Res. Atmos.* **125**, e2020JD033421 (2020).

6- McClenny, E. E. Using Simpler Models to Understand Atmospheric River Responses to Sea-Surface Temperature Increases (Doctoral dissertation, University of California, Davis) (2021).

7- O'Neill B. C. et al. The scenario model intercomparison project (ScenarioMIP) for CMIP6. *Geosci. Model Dev.* **9**, 3461–3482 (2016)

8- Riahi K. et al. The shared socioeconomic pathways and their energy, land use, and greenhouse gas emissions implications: an overview. *Glob. Environ. Change* **42**, 153-168 (2017).

9- Hersbach, H., Bell, B., Berrisford, P., Hirahara, S., Horányi, A., Muñoz-Sabater, J., et al. The ERA5 global reanalysis. *Q. J. R. Meteorol. Soc.* **146,** 1999–2049 (2020).

10- Hong, S. Y., & Lim, J. O. J. The WRF single-moment 6-class microphysics scheme (WSM6). *Journal of the Korean Meteorological Society* **42,** 129–151 (2006).

11- Hong, S. Y., Noh, Y., & Dudhia, J. A new vertical diffusion package with an explicit treatment of entrainment processes. *Mon. Weather Rev.* **134,** 2318–2341 (2006).

12- Jimenez, P. A., Dudhia, J., Gonzalez-Rouco, J. F., Navarro, J., Montavez, J. P., & Garcia–Bustamante, E. A revised scheme for the WRF surface layer formulation. *Mon. Weather Rev.* **140,** 898–918 (2012).

13- Tewari, M., Chen, F., Wang, W., Dudhia, J., LeMone, M., Mitchell, K., et al. Implementation and verification of the unified Noah land surface model in the WRF model, 20th Conference on Weather Analysis and Forecasting/16th Conference on Numerical Weather Prediction, Seattle, WA (2004).

14- Iacono, M. J., Delamere, J. S., Mlawer, E. J., Shephard, M. W., Clough, S. A., & Collins, W. D. Radiative forcing by long–lived greenhouse gases: Calculations with the AER radiative transfer models. *J. Geophys. Res.* **113**, D13103 (2008).

15- Kain, J. S. The Kain–Fritsch Convective Parameterization: An Update. *J. Appl. Meteorol.* **43,** 170-181 (2004).

16- Miguez-Macho, G., Stenchikov, G. L., & Robock, A. Spectral nudging to eliminate the effects of domain position and geometry in regional climate model simulations. *J. Geophys. Res. Atmos.* **109,** 1–15 (2004).

17- Insua-Castro, D. & Miguez-Macho, G. A new moisture tagging capability in the Weather Research and Forecasting model: formulation, validation and application to the 2014 Great Lake-effect snowstorm. *Earth. Syst. Dyn.* **9,** 167–185 (2018).

18- Insua-Castro, D., Miguez-Macho, G. & Llasat, M. C. Local and remote moisture sources for extreme precipitation: a study of the two catastrophic 1982 western Mediterranean episodes. *Hydrol. Earth Syst. Sci.* **23**, 3885–3900 (2019).

19- Brioude, J., et al. The Lagrangian particle dispersion model FLEXPART-WRF version 3.1. *Geosci. Model Dev.* **6,** 1889–1904 (2013).

20- Hanna, S. R. Applications in air pollution modeling, in: Atmospheric Turbulence and Air Pollution Modelling. Reidel Publishing Company, Dordrecht, Holland, 275–310 (1982).

21- Gimeno, L., Drumond, A., Nieto, R., Trigo, R. M. & Stohl, A. On the origin of continental precipitation. *Geophys. Res. Lett.* **37,** L13804 (2010).

22- Castillo, R., Nieto, R., Drumond, A. & Gimeno, L. Estimating the Temporal Domain when the Discount of the Net Evaporation Term Affects the Resulting Net Precipitation Pattern in the Moisture Budget Using a 3-D Lagrangian Approach. *PLoS ONE* **9,** e99046 (2014).

23- Drumond, A., Nieto, R., & Gimeno, L. On the contribution of the Tropical Western Hemisphere Warm Pool source of moisture to the Northern Hemisphere precipitation through a Lagrangian approach, *J. Geophys.* **116,** D00Q04 (2011).

24- Nieto, R., Gimeno, L., Drumond, A. & Hernandez, E. A Lagrangian identification of the main moisture sources and sinks affecting the Mediterranean area. *WSEAS Trans. Environ. Dev.* **6,** 365-374 (2010).

25- Trigo, I. F., Davies, T. D. & Bigg, G. R. Objective climatology of cyclones in the Mediterranean region. *J. Climate* **12,** 1685–1696 (1999).

26- Gimeno, L., Nieto, R., Trigo, R., Vicente-Serrano, S.M. & López-Moreno, J. I. Where does the Iberian Peninsula moisture comme from? An answer based on a Lagrangian approach. *J. Hydrometeorol.* **11,** 421-336 (2010).

27- Fernández-Alvarez, J. C., Vázquez M., Pérez-Alarcón A., Nieto R., Gimeno L. Comparison of moisture sources and sinks estimated with different versions of FLEXPART and FLEXPART-WRF models forced with ECMWF reanalysis data. *J. Hydrometeorol.* **24**, 221-239 (2022).

28- Lavers, D. A., Villarini, G., Allan, R. P., Wood, E. F., & Wade, A. J. The detection of atmospheric rivers in atmospheric reanalyses and their links to British winter floods and the large-scale climatic circulation. *J. Geophys. Res.* **117,** D20106 (2012).

29- Lavers, D. A., Villarini, G., Allan, R. P., Wood, E. F., & Wade, A. J. The detection of atmospheric rivers in atmospheric reanalyses and their links to British winter floods and the large-scale climatic circulation. *J. Geophys. Res.* **117**, D20106 (2012).

30- Brown B., Ebert E., Fowler T., Gilleland E., Kucera P., Wilson L. Verification methods for tropical cyclone forecasts. WMO Technical Document WWRP 2013-7, 7(November) (2013).

31- Seneviratne, S. I., Hauser, M. Regional Climate Sensitivity of Climate Extremes in CMIP6 Versus CMIP5 Multimodel Ensembles. *Earths Future* **8**, e2019EF001474 (2020).

32- Xu, Z., Han, Y., Tam, C. Y., Yang, Z. L., Fu, C. Bias-corrected CMIP6 global dataset for dynamical downscaling of the historical and future climate (1979–2100). *Sci. Data* **8**, 1-11 (2021).

JGR: Atmospheres

Supporting Information for

Changes in moisture sources of atmospheric rivers landfalling the Iberian Peninsula with WRF-Flexpart

José Carlos Fernández-Alvarez[1*], Albenis Pérez-Alarcón[1,2], Jorge Eiras-Barca[1,3], Alexandre M. Ramos[4], Stefan Rahimi-Esfarjani[5], Raquel Nieto[1], and Luis Gimeno[1]

[1] Centro de Investigación Mariña, Universidade de Vigo, Environmental Physics Laboratory (EPhysLab), Campus As Lagoas s/n, Ourense, 32004, Spain.

[2] Departamento de Meteorología, Instituto Superior de Tecnologías y Ciencias Aplicadas, Universidad de La Habana, La Habana, Cuba.

[3]Defense University Center, The Spanish Naval Academy, Marín, Spain.

[4]Instituto Dom Luiz (IDL), Facultade de Ciências, Universidade de Lisboa, Lisbon, Portugal.

[5]Department of Atmospheric and Oceanic Sciences, University of California, Los Angeles, United States.

Contents of this file

Figures S1-S8 and Tables S1-S3

Introduction

This file includes supplementary material regarding the domains of calculations used for the simulations of the meteorological conditions and the moisture transport corresponding to the released particles. In addition, a table with parameters used in the ARs detection method is presented.

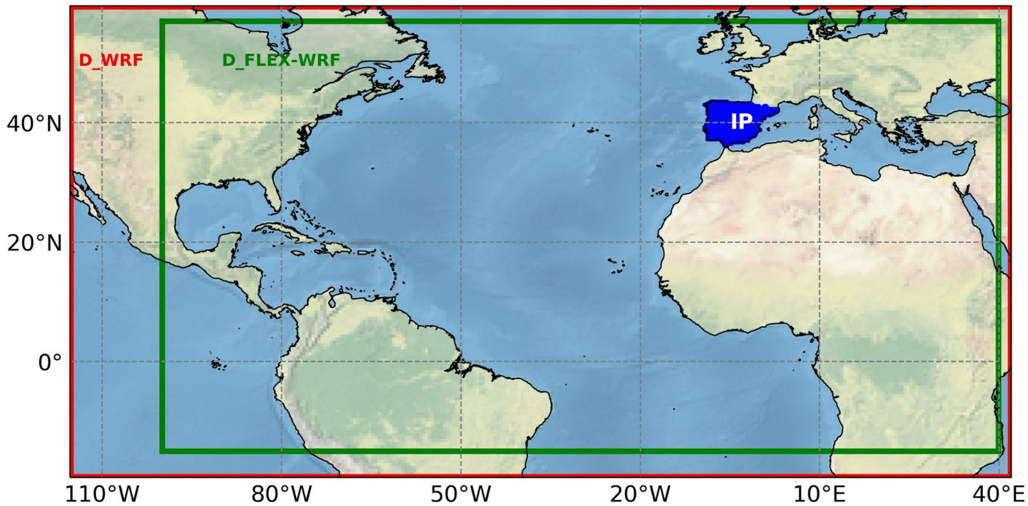

Figure S1. Calculation domains of the WRF-ARW (red) and FLEXPART-WRF (green). The target region is shown in blue (IP).

Table S1. Relevant parameters used in the IPART configuration for AR detection.

Parameters	**Value**
Minimum value for the IVT anomaly in the search for ARs (similar to IVT250 thresholding method)	1
Minimum value of area considered for ARs	$500*10^4$ km^2
Maximum value of area considered for ARs	$1800*10^4$ km^2
Minimal length/width ratio	2
Maximum latitude	80° N
Minimal latitude	20°N
Minimal length	2000 km
Minimal critical length to discard ARs	1500 km
Minimal proportion of flux component in a direction to total flux	0.4

Table S2. Annual mean detections of atmospheric river events considered in the analysis. **Bold** numbers correspond to the number of 6-hourly detections over the entire domain. The coordinates in (parentheses) refer to the mean position of the centroids and the numbers in *italics* refer to daily detections over the Iberian Peninsula.

Season	WRF-CESM2	WRF-ERA5	WRF-CESM2 (MC)	WRF-CESM2 (EC)
JFM	**789** (38.73 ºN, 40.65 ºW) *34*	**819** (38.60 ºN, 37.05 ºW) *30*	**769** (38.96 ºN, 39.22 ºW) *36*	**762** (38.96 ºN, 38.57 ºW) *43*
AMJ	**847** (39.93 ºN, 43.40 ºW) *20*	**889** (40.04 ºN, 42.12 ºW) *21*	**845** (40.08 ºN, 42.88 ºW) *20*	**879** (39.96 ºN, 41.49 ºW) *19*
JAS	**876** (42.83 ºN, 50.86 ºW) *14*	**928** (42.98 ºN, 47.84 ºW) *21*	**846** (43.82 ºN, 50.45 ºW) *12*	**751** (45.14 ºN, 50.81 ºW) *6*
OND	**852** (40.24 ºN, 42.31 ºW) *35*	**877** (40.22 ºN, 39.09 ºW) *38*	**825** (40.96 ºN, 42.17 ºW) *39*	**812** (41.58 ºN, 42.80 ºW) *37*
ANNUAL	**3364** (40.44 ºN, 44.30 ºW) *103*	**3513** (40.46 ºN, 41.52 ºW) *110*	**3285** (40.96 ºN, 43.68 ºW) *106*	**3204** (41.41 ºN, 43.41 ºW) *105*

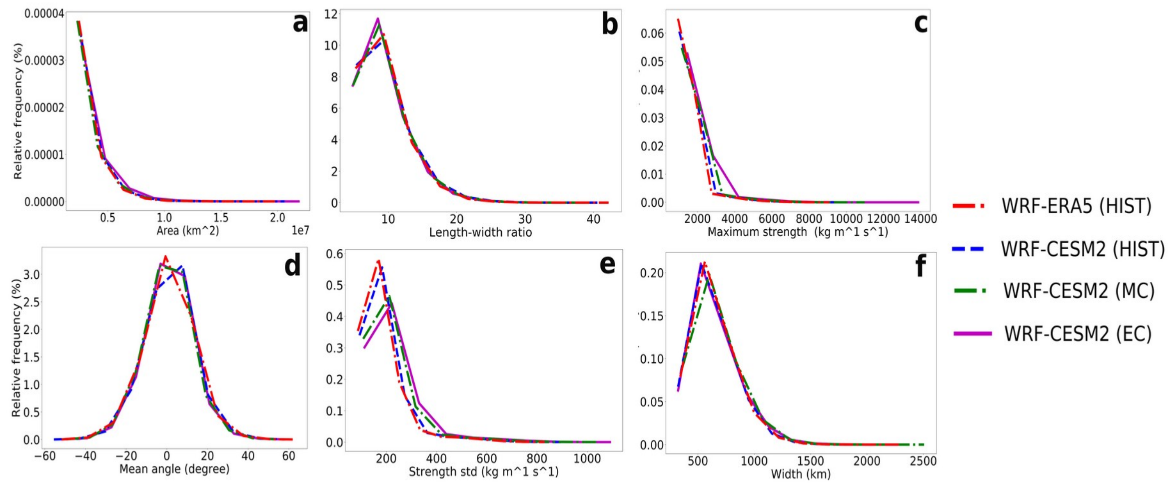

Figure S2. Probability density functions (PDFs) of WRF simulations considered in the analysis for different parameters of interest: a) AR mean area, (b) AR mean length-width ratio, c) AR Maximum strength, d) mean angle (AR moisture flux orientation), e) AR strength std and f) AR mean width. WRF-ERA5 (HIST) is shown in red dotted lines, WRF-CESM2 (HIST) is shown in blue dotted lines, WRF-CESM2 (MC) is shown in green dotted lines, and WRF-CESM2 (EC) shown in solid purple lines.

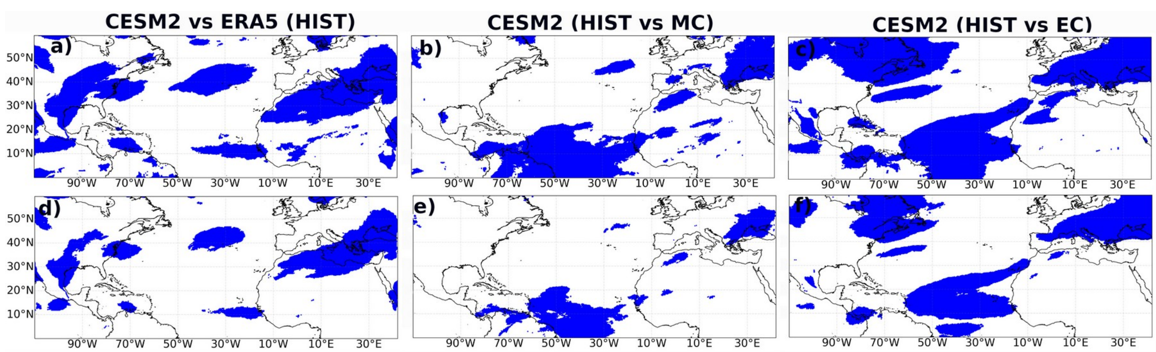

Figure S3. Highlighted in blue are the areas with statistically significant differences at 95% (a,b,c) and 99% (d,e,f) significance for: the daily HIST time series between the CESM2 and ERA5 (first column), CESM2 HIST and CESM2 MC (second column) and between the CESM2 HIST and CESM2 EC (third column).

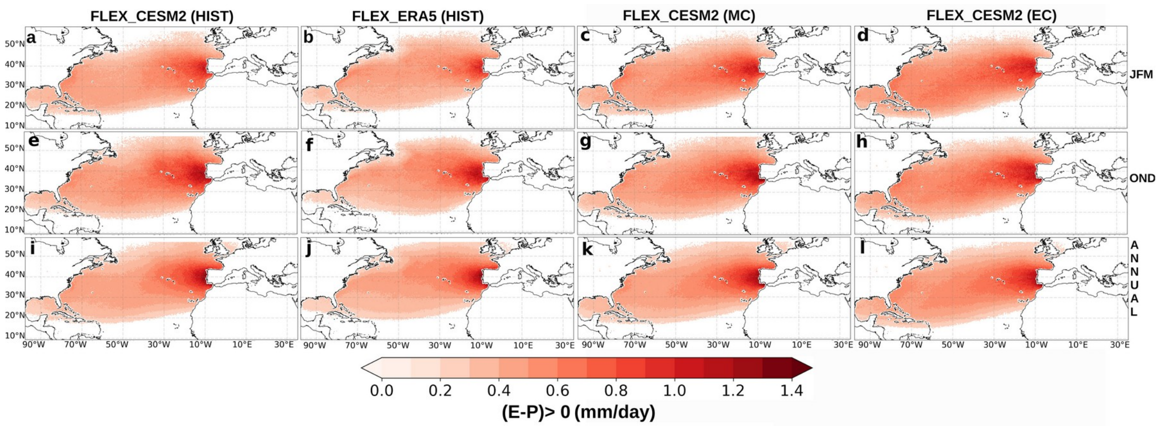

Figure S4. Patterns of moisture sources ((E-P) > 0 in mm day^{-1}) for the ARs landfalling over IP of the Lagrangian outputs of FLEX-CESM2 for the historical period (HIST), mid-century (MC) and end-century (EC), and FLEX- ERA5 for the historical period (HIST). The fields displayed from top to bottom correspond to JFM (a-d), OND (e-h), and ANNUAL (i-l).

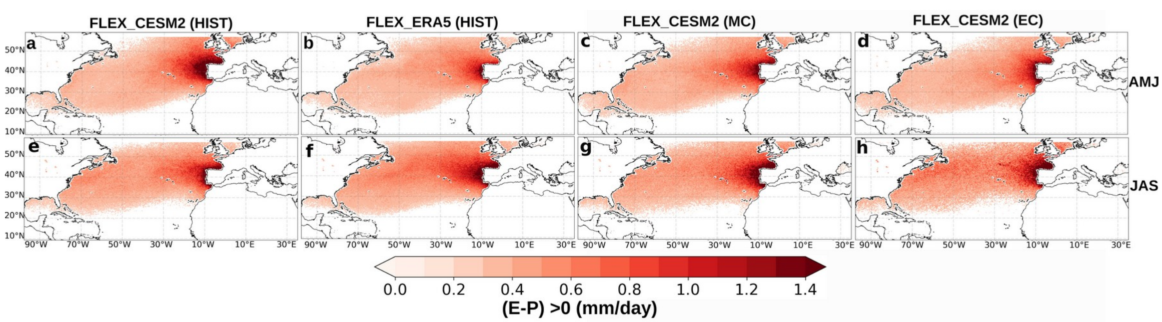

Figure S5. Patterns of moisture sources ((E-P) > 0 in mm day^{-1}) for the ARs landfalling over IP of the Lagrangian outputs of FLEX-CESM2 for the historical period (HIST), mid- (MC) and end-century (EC), and FLEX- ERA5 for the historical period (HIST). The fields displayed from top to bottom correspond to AMJ (a-d), and JAS (e-h).

Table S3. Statigraphs used in the evaluation of the AMU representation for FLEX-CESM2

Statigraphs	RSME (mm/day)	R	MAE (mm/day)	BIAS (mm/day)
JFM	0.05	0.96	0.04	0.01
AMJ	0.10	0.90	0.06	0.02
JAS	0.12	0.90	0.08	-0.03
OND	0.07	0.95	0.05	0.03
ANNUAL	0.05	0.97	0.04	0.01

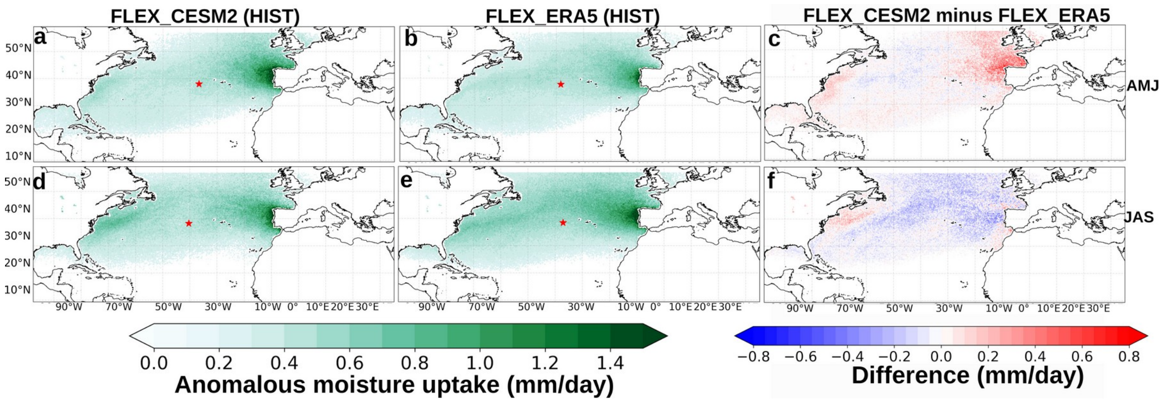

Figure S6. Anomalous moisture uptake (AMU) for FLEX CESM2 (HIST), FLEX ERA5 (HIST) and their differences in the first, second and third columns respectively. Results are shown for AMJ (a-c) and JAS (d-f) seasons, located in the different rows. Weighted centroids of the AMU patterns are labeled with a red star.

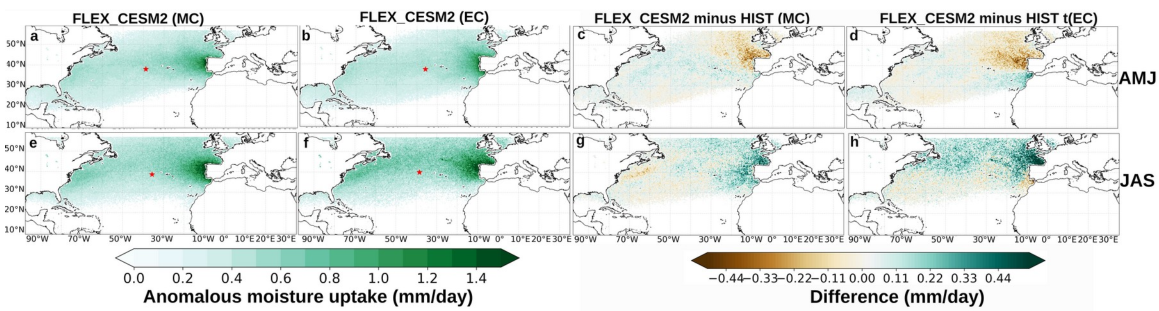

Figure S7. Anomalous moisture uptake (AMU) for FLEX CESM2 (mid-century (MC) and end-century (EC)) and their differences with regard to the historical simulation in the first, second, third and fourth columns respectively. Results are shown for AMJ (a-d) and JAS (e-h) seasons, located in the different rows. Weighted centroids of the AMU patterns are labeled with a red star.

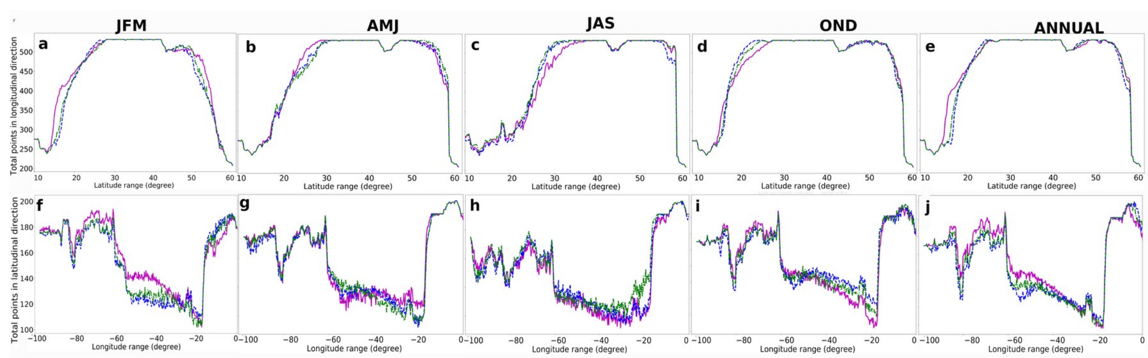

Figure S8. Latitudinal (a-e) and longitudinal (f-j) cross sections showing the number of grid points with AMU>0 for the mean pattern of each corresponding 30-year simulation. Blue, green and magenta colors belong to the historical data, middle and end of the century respectively.

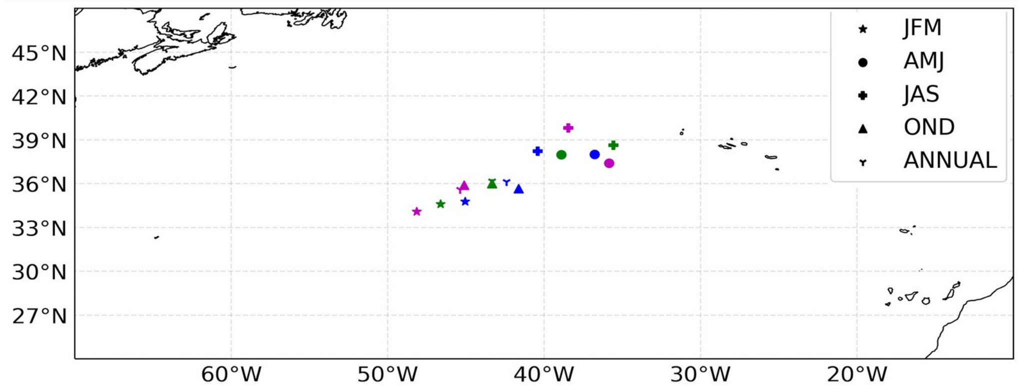

Figure S9. Weighted centroids for the AMU pattern corresponding to the historical periods, mid and end of the century. Blue, green and magenta colors belong to the historical data, middle and end of the century respectively.

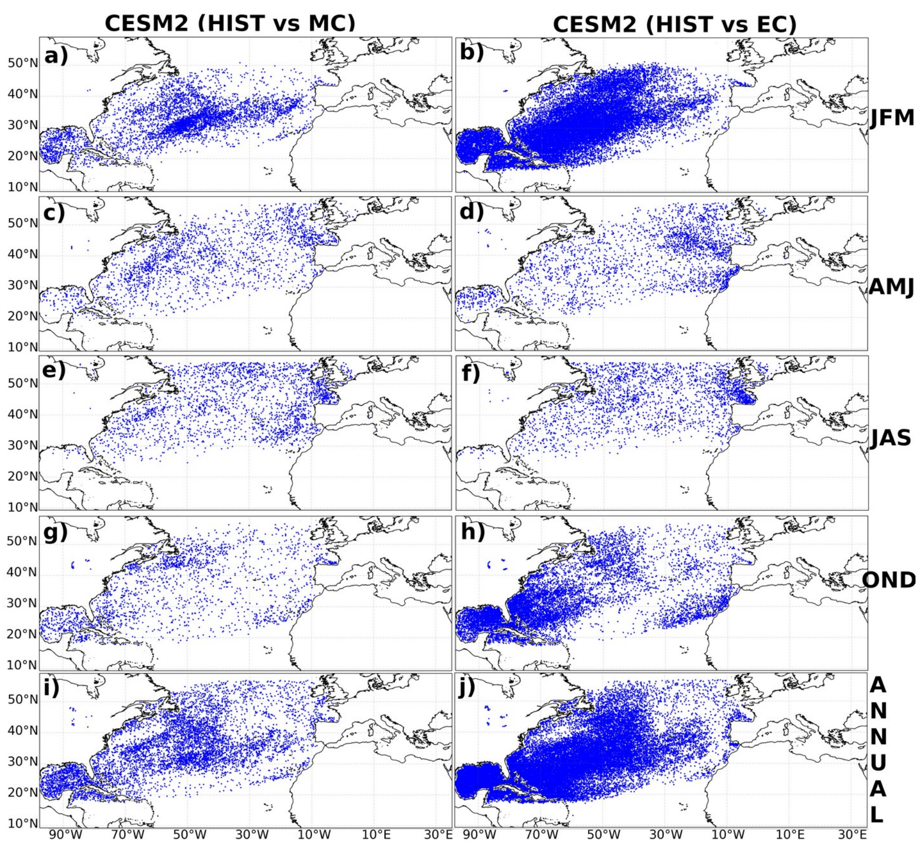

Figure S10. Highlighted in blue are the areas with t-test statistically significant differences (at 95%) in the anomalous moisture uptake (AMU) between the historical (HIST) and mid-century (MC) series of CESM2 (first column) and between the historical (HIST) and end-century (EC) series of CESM2 (second column).

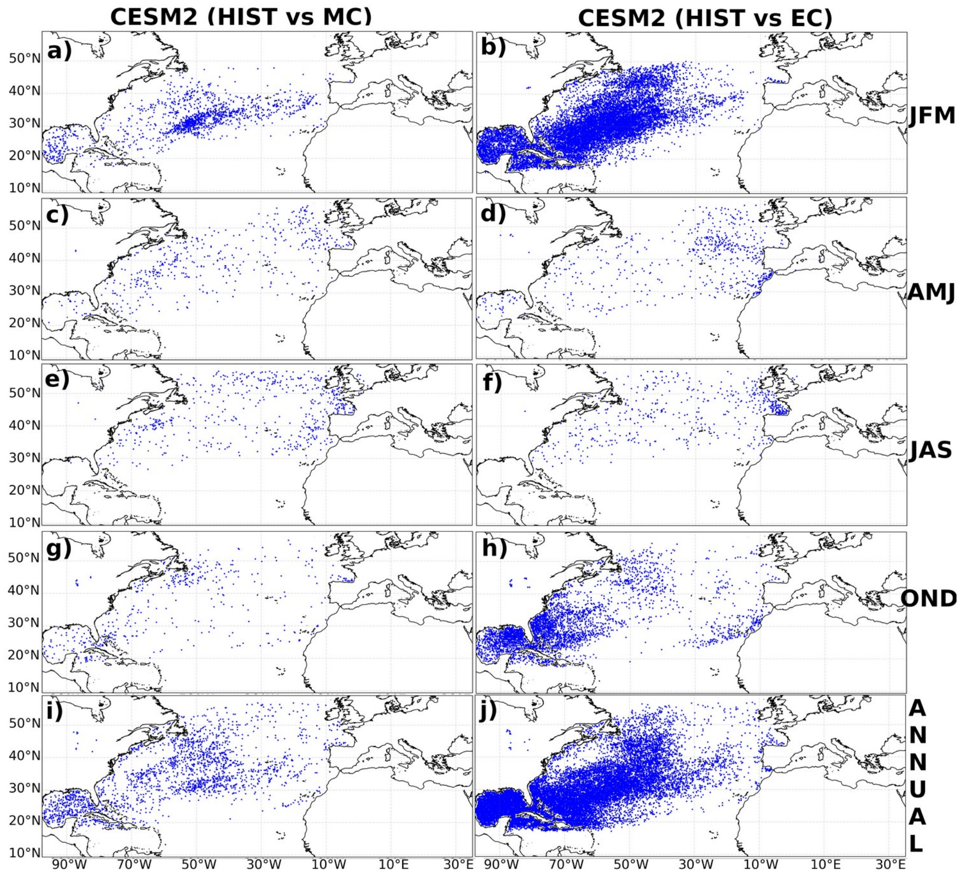

Figure S11. Highlighted in blue are the areas with t-test statistically significant differences (at 99%) in the anomalous moisture uptake (AMU) between the historical (HIST) and mid-century (MC) series of CESM2 (first column) and between the historical (HIST) and end-century (EC) series of CESM2 (second column).

Supplementary Information for

Dynamic downscaling of wind speed over the North Atlantic Ocean using CMIP6 projections: implications for offshore wind energy density

José C. Fernández-Alvarez[1,2*], Xurxo Costoya[1], Albenis Pérez-Alarcón[1,2], Stefan Rahimi-Esfarjani[3], Raquel Nieto[1], Luis Gimeno[1]

Corresponding author: José C. Fernández-Alvarez (jose.carlos.fernandez.alvarez@uvigo.es)

[1]Centro de Investigación Mariña, Universidade de Vigo, Environmental Physics Laboratory (EPhysLab), Campus As Lagoas s/n, Ourense, 32004, Spain
[2]Departamento de Meteorología, Instituto Superior de Tecnologías y Ciencias Aplicadas, Universidad de La Habana, La Habana, Cuba.
[3] Department of Atmospheric and Oceanic Sciences, University of California, Los Angeles, United States

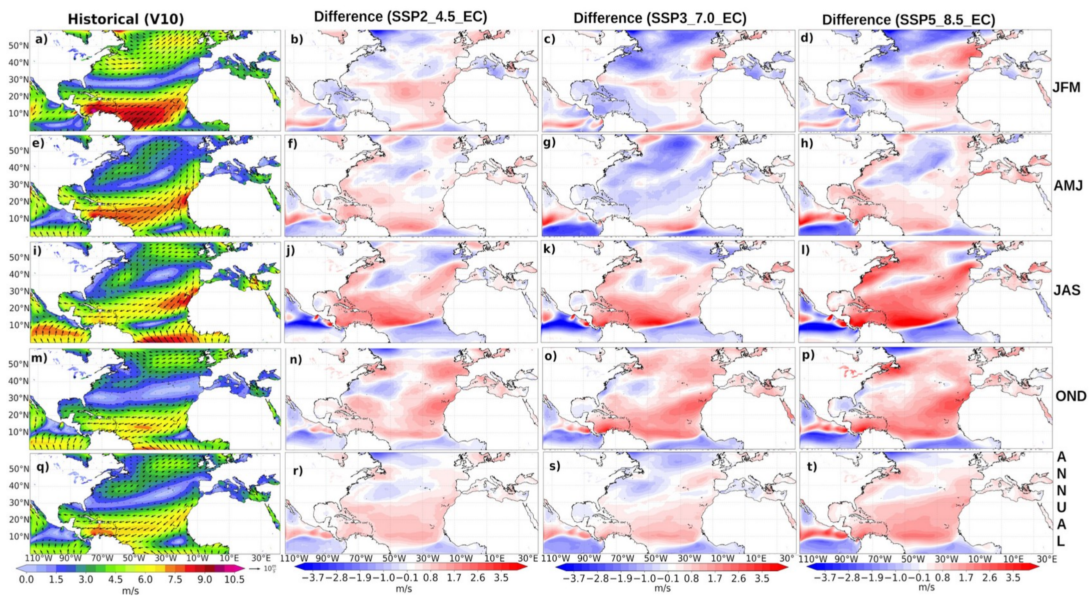

Figure S1. V10 for the historical period and the differences of the simulations of WRF- ARW for each SSPs with respect to this. The fields displayed from top to bottom correspond to JFM, AMJ, JAS, OND and ANNUAL. The modular value of V10 is represented by contours and the direction of V10 by arrows. Period: 2096-2100 (EC).

Bibliography

Akdağ, S. A. & Dinler, A. (2009). A new method to estimate weibull parameters for wind energy applications. *Energy conversion and management*, *50*(7), 1761–1766, https://doi.org/10.1016/j.enconman.2009.03.020.

Algarra, I., Eiras-Barca, J., Nieto, R., & Gimeno, L. (2019). Global climatology of nocturnal low-level jets and associated moisture sources and sinks. *Atmospheric Research*, *229*, 39–59, https://doi.org/10.1016/j.atmosres.2019.06.016.

Algarra, I., Nieto, R., Ramos, A., Eiras-Barca, J., Trigo, R., & Gimeno, L. (2020). Significant increase of global anomalous moisture uptake feeding landfalling atmospheric rivers. *Nature Communications*, *11*, 5082, https://doi.org/j.atmosres.2019.06.016.

Alizadeh-Choobari, O., Zawar-Reza, P., & Sturman, A. (2014). The "wind of 120 days" and dust storm activity over the sistan basin. *Atmospheric research*, *143*, 328–341, https://doi.org/j.atmosres.2014.02.001.

Allan, R. P., et al. (2020). Advances in understanding large-scale responses of the water cycle to climate change. *Annals of the New York Academy of Sciences*, *1472*(1), 49–75, https://doi.org/10.1111/nyas.14337.

AM (2023). Atmospheric moisture. https://www.nwcg.gov/publications/pms425-1/atmospheric-moisture#SAM. Accessed 08-09-2023.

AMS (2022). Atmospheric river. https://glossary.ametsoc.org/wiki/Atmospheric_river. Accessed 23-06-2023.

Araghi, A., Maghrebi, M., & Olesen, J. E. (2022). Effect of wind speed variation on rainfed wheat production evaluated by the ceres-wheat model. *International Journal of Biometeorology*, *66*(1), 225–233, https://doi.org/10.1007/s00484-021-02209-7.

ARIA (2023). Atmospheric rivers in australia (aria). https://climateextremes.org.au/atmospheric-rivers-in-australia/. Accessed 23-06-2023.

AROCT (2023). Atmospheric reanalysis: Overview comparison tables (aroct). https://climatedataguide.ucar.edu/climate-data/atmospheric-reanalysis-overview-comparison-tables. Accessed 23-06-2023.

Bao, J., Michelson, S., Neiman, P., Ralph, F., & Wilczak, J. (2006). Interpretation of enhanced integrated water vapor bands associated with extratropical cyclones: Their formation and connection to tropical moisture. *Monthly weather review*, *134*(4), 1063–1080, https://doi.org/10.1175/MWR3123.1.

Bao, J., Sherwood, S., Alexander, L., & Evans, J. (2017). Future increases in extreme precipitation exceed observed scaling rates. *Nature Climate Change*, *7*, 128–132, https://doi.org/10.1038/nclimate3201.

Bao, J. & Sherwood, S. C. (2019). The role of convective self-aggregation in extreme instantaneous versus daily precipitation. *Journal of Advances in Modeling Earth Systems*, *11*(1), 19–33, https://doi.org/10.1029/2018MS001503.

Binder, H., Boettcher, M., Joos, H., & Wernli, H. (2016). The role of warm conveyor belts for the intensification of extratropical cyclones in northern hemisphere winter. *Journal of the Atmospheric Sciences*, *73*(10), 3997–4020, https://doi.org/10.5194/wcd-4-19-2023.

Bladé, I., Fortuny, D., van Oldenborgh, G. J., & Liebmann, B. (2012). The summer north atlantic oscillation in cmip3 models and related uncertainties in projected summer drying in europe. *Journal of Geophysical Research: Atmospheres*, *117*(D16), https://doi.org/10.1029/2012JD017816.

Blamey, R., Ramos, A., Trigo, R., Tomé, R., & Reason, C. (2018). The influence of atmospheric rivers over the south atlantic on winter rainfall in south africa. *Journal of Hydrometeorology*, *19*(1), 127–142, https://doi.org/10.1175/JHM-D-17-0111.1.

Bony, S., Bellon, G., Klocke, D., Sherwood, S., Fermepin, S., & Denvil, S. (2013). Robust direct effect of carbon dioxide on tropical circulation and regional precipitation. *Nature Geoscience*, *6*(6), 447–451, https://doi.org/10.1038/ngeo1799.

Brioude, J., et al. (2013). The lagrangian particle dispersion model flexpart-wrf version 3.1. *Geoscientific Model Development*, *6*(6), 1889–1904, https://doi.org/10.5194/gmd-6-1889-2013.

Brown, B., Ebert, E., Fowler, T., Gilleland, E., Kucera, P., & Wilson, L. (2013). Verification methods for tropical cyclone forecasts. *WMO Technical Document WWRP 2013-7*, *7*(November).

Bruyère, C. L., Monaghan, A. J., Steinhoff, D. F., & Yates, D. (2015). Bias-corrected cmip5 cesm data in wrf/mpas intermediate file.

Carlson, T. N. (1990). *Mid-latitude weather systems*. London: HarperCollins Acad.

Carreno-Madinabeitia, S., Ibarra-Berastegi, G., Sáenz, J., & Ulazia, A. (2021). Long-term changes in offshore wind power density and wind turbine capacity factor in the iberian peninsula (1900–2010). *Energy*, *226*, 120364, https://doi.org/10.1016/j.energy.2021.120364.

Carvalho, D., Rocha, A., Gómez-Gesteira, M., & Santos, C. S. (2017). Potential impacts of climate change on european wind energy resource under the cmip5 future climate projections. *Renewable Energy*, *101*, 29–40, https://doi.org/10.1016/j.renene.2016.08.036.

Cavazos, T. & Rivas, D. (2004). Variability of extreme precipitation events in tijuana, mexico. *Climate Research*, *25*(3), 229–243.

Chen, G., Norris, J., Neelin, J. D., Lu, J., Leung, L. R., & Sakaguchi, K. (2019). Thermodynamic and dynamic mechanisms for hydrological cycle intensification over the full probability distribution of precipitation events. *Journal of the Atmospheric Sciences*, *76*(2), 497–516, https://doi.org/10.1175/JAS-D-18-0067.1.

Christensen, J. H., et al. (2013). Climate phenomena and their relevance for future regional climate change. In *Climate change 2013 the physical science basis: Working group I contribution to the fifth assessment report of the intergovernmental panel on climate change* (pp. 1217–1308). Cambridge University Press.

CI (2023). Climate information. https://climateinformation.org/data-production-and-tailoring/why-use-a-model-ensemble/. Accessed 23-06-2023.

Cohen, J., et al. (2014). Recent arctic amplification and extreme mid-latitude weather. *Nature geoscience*, *7*(9), 627–637, https://doi.org/10.1038/ngeo2234.

Collins, M., et al. (2013). *Long-term climate change: projections, commitments and irreversibility*. Cambridge University Press.

Collow, A. M., et al. (2022). An overview of artmip's tier 2 reanalysis intercomparison: Uncertainty in the detection of atmospheric rivers and their associated precipitation. *Journal of Geophysical Research: Atmospheres*, *127*(8), e2021JD036155, https://doi.org/10.1029/2021JD036155.

Cosgrove, W. J. & Loucks, D. P. (2015). Water management: Current and future challenges and research directions. *Water Resources Research*, *51*(6), 4823–4839, https://doi.org/10.1002/2014WR016869.

Costoya, X., DeCastro, M., Carvalho, D., & Gómez-Gesteira, M. (2020a). On the suitability of offshore wind energy resource in the united states of america for the 21st century. *Applied Energy*, *262*, 114537, https://doi.org/j.apenergy.2020.114537.

Costoya, X., Rocha, A., & Carvalho, D. (2020b). Using bias-correction to improve future projections of offshore wind energy resource: A case study on the iberian peninsula. *Applied Energy*, *262*, 114562, https://doi.org/j.apenergy.2020.114562.

Dai, A. & Song, M. (2020). Little influence of arctic amplification on mid-latitude climate. *Nature Climate Change*, *10*(3), 231–237, https://doi.org/10.1038/s41558-020-0694-3.

Danabasoglu, G., et al. (2020). The community earth system model version 2 (cesm2). *Journal of Advances in Modeling Earth Systems*, *12*(2), e2019MS001916, https://doi.org/10.1029/2019MS001916.

de Vrese, P., Hagemann, S., & Claussen, M. (2016). Asian irrigation, african rain: Remote impacts of irrigation. *Geophysical Research Letters*, *43*(8), 3737–3745, https://doi.org/10.1002/2016GL068146.

deCastro, M., Costoya, X., Salvador, S., Carvalho, D., Gómez-Gesteira, M., Sanz-Larruga, F. J., & Gimeno, L. (2019). An overview of offshore wind energy resources in europe under present and future climate. *Annals of the New York Academy of Sciences*, *1436*(1), 70–97, https://doi.org/10.1111/nyas.13924.

Dee, D. P., et al. (2011). The era-interim reanalysis: Configuration and performance of the data assimilation system. *Quarterly Journal of the royal meteorological society*, *137*(656), 553–597, https://doi.org/10.1002/qj.828.

Deser, C., Phillips, A., Bourdette, V., & Teng, H. (2012). Uncertainty in climate change projections: the role of internal variability. *Climate dynamics*, *38*, 527–546, https://doi.org/10.1007/s00382-010-0977-x.

Dettinger, M. D., Ralph, F. M., Das, T., Neiman, P. J., & Cayan, D. R. (2011). Atmospheric rivers, floods and the water resources of california. *Water*, *3*(2), 445–478, https://doi.org/10.3390/w3020445.

Dettinger, M. D., Ralph, F. M., & Lavers, D. A. (2015). Setting the stage for a global science of atmospheric rivers. *Eos, Earth and Space Science News*, *96*, https://doi.org/10.1029/2015EO038675.

Diffenbaugh, N. S. & Giorgi, F. (2012). Climate change hotspots in the cmip5 global climate model ensemble. *Climatic change*, *114*, 813–822, https://doi.org/10.1007/s10584-012-0570-x.

Diffenbaugh, N. S., Pal, J. S., Giorgi, F., & Gao, X. (2007). Heat stress intensification in the mediterranean climate change hotspot. *Geophysical Research Letters*, *34*(11), https://doi.org/10.1029/2007GL030000.

DiNezio, P. N., Tierney, J. E., Otto-Bliesner, B. L., Timmermann, A., Bhattacharya, T., Rosenbloom, N., & Brady, E. (2018). Glacial changes in tropical climate amplified by the indian ocean. *Science advances*, *4*(12), eaat9658, https://doi.org/https://doi.org/10.1126/sciadv.aat9658.

Dominguez, F., Kumar, P., & Vivoni, E. R. (2008). Precipitation recycling variability and ecoclimatological stability—a study using narr data. part ii: North american monsoon region. *Journal of Climate*, *21*(20), 5187–5203, https://doi.org/10.1175/2008JCLI1760.1.

Donat, M. G., Angélil, O., & Ukkola, A. M. (2019). Intensification of precipitation extremes in the world's humid and water-limited regions. *Environmental Research Letters*, *14*(6), 065003, https://doi.org/10.1088/1748-9326/ab1c8e.

Donat, M. G., Lowry, A. L., Alexander, L. V., O'Gorman, P. A., & Maher, N. (2016). More extreme precipitation in the world's dry and wet regions. *Nature Climate Change*, *6*(5), 508–513, https://doi.org/10.1038/nclimate2941.

Donohue, R. J., McVicar, T. R., & Roderick, M. L. (2010). Assessing the ability of potential evaporation formulations to capture the dynamics in evaporative demand within a changing climate. *Journal of Hydrology*, *386*(1-4), 186–197, https://doi.org/10.1016/j.jhydrol.2010.03.020.

Drumond, A., Stojanovic, M., Nieto, R., Vicente-Serrano, S. M., & Gimeno, L. (2019). Linking anomalous moisture transport and drought episodes in the ipcc reference regions. *Bulletin of the American Meteorological Society*, *100*(8), 1481–1498, https://doi.org/10.1175/BAMS-D-18-0111.1.

Dubois, O. et al. (2011). *The state of the world's land and water resources for food and agriculture: managing systems at risk.* Earthscan.

Eiras-Barca, J., Dominguez, F., Hu, H., Garaboa-Paz, D., & Miguez-Macho, G. (2017). Evaluation of the moisture sources in two extreme landfalling atmospheric river events using an eulerian wrf tracers tool. *Earth System Dynamics*, *8*(4), 1247–1261, https://doi.org/10.5194/esd-8-1247-2017.

Eiras-Barca, J., Lorenzo, N., Taboada, J., Robles, A., & Miguez-Macho, G. (2018). On the relationship between atmospheric rivers, weather types and floods in galicia (nw spain). *Natural hazards and earth system sciences*, *18*(6), 1633–1645, https://doi.org/10.5194/nhess-18-1633-2018.

Eiras-Barca, J., et al. (2021). European west coast atmospheric rivers: A scale to characterize strength and impacts. *Weather and Climate Extremes*, *31*, 100305, https://doi.org/10.1016/j.wace.2021.100305.

Emerton, R., Cloke, H., Stephens, E., Zsoter, E., Woolnough, S., & Pappenberger, F. (2017). Complex picture for likelihood of enso-driven flood hazard. *Nature communications*, *8*(1), 14796, https://doi.org/10.1038/ncomms14796.

Emori, S. & Brown, S. (2005). Dynamic and thermodynamic changes in mean and extreme precipitation under changed climate. *Geophysical Research Letters*, *32*(17), https://doi.org/10.1029/2005GL023272.

Endo, H., Kitoh, A., & Ueda, H. (2018). A unique feature of the asian summer monsoon response to global warming: The role of different land–sea thermal contrast change between the lower and upper troposphere. *Sola*, *14*, 57–63, https://doi.org/10.2151/sola.2018-010.

EPCC (2023). Extreme precipitation and climate change. https://www.c2es.org/content/extreme-precipitation-and-climate-change/. Accessed 23-06-2023.

Espinoza, V., Waliser, D. E., Guan, B., Lavers, D. A., & Ralph, F. M. (2018). Global analysis of climate change projection effects on atmospheric rivers. *Geophysical Research Letters*, *45*(9), 4299–4308, https://doi.org/10.1029/2017GL076968.

Eyring, V., Bony, S., Meehl, G. A., Senior, C. A., Stevens, B., Stouffer, R. J., & Taylor, K. E. (2016). Overview of the coupled model intercomparison project phase 6 (cmip6) experimental design and organization. *Geoscientific Model Development*, *9*(5), 1937–1958, https://doi.org/10.5194/gmd-9-1937-2016.

Falvey, M. & Garreaud, R. (2007). Wintertime precipitation episodes in central chile: Associated meteorological conditions and orographic influences. *Journal of Hydrometeorology*, *8*(2), 171–193, https://doi.org/10.1175/JHM562.1.

Fernández-Alvarez, J. C., Costoya, X., Pérez-Alarcón, A., Rahimi, S., Nieto, R., & Gimeno, L. (2023a). Dynamic downscaling of wind speed over the north atlantic ocean using cmip6 projections: implications for offshore wind power density. *Energy Reports*, *9*, 873–885, https://doi.org/10.1016/j.egyr.2022.12.036.

Fernández-Alvarez, J. C., Pérez-Alarcón, A., Eiras-Barca, J., Rahimi, S., Nieto, R., & Gimeno, L. (2023b). Projected changes in atmospheric moisture transport contributions associated with climate warming in the north atlantic. *Nature Communications*, *14*(1), 6476, https://doi.org/10.1038/s41467-023-41915-1.

Fernández-Alvarez, J. C., Pérez-Alarcón, A., Eiras-Barca, J., Ramos, A. M., Rahimi-Esfarjani, S., Nieto, R., & Gimeno, L. (2023c). Changes in moisture sources of atmospheric rivers landfalling the iberian peninsula with wrf-flexpart. *Journal of Geophysical Research: Atmospheres*, (pp. e2022JD037612)., https://doi.org/10.1029/2022JD037612.

Fernández-Alvarez, J. C., Pérez-Alarcón, A., Nieto, R., & Gimeno, L. (2022). Trova: Transport of water vapor. *SoftwareX*, *20*, 101228, https://doi.org/10.1016/j.softx.2022.101228.

Fernández-Alvarez, J. C., Vázquez, M., Pérez-Alarcón, A., Nieto, R., & Gimeno, L. (2023d). Comparison of moisture sources and sinks estimated with different versions of flexpart and flexpart-wrf models forced with ecmwf reanalysis data. *Journal of Hydrometeorology*, *24*(2), 221–239, https://doi.org/10.1175/JHM-D-22-0018.1.

Fischer, E. M. & Knutti, R. (2016). Observed heavy precipitation increase confirms theory and early models. *Nature Climate Change*, *6*(11), 986–991, https://doi.org/10.1038/nclimate3110.

García-Herrera, R., et al. (2019). The european 2016/17 drought. *Journal of Climate*, *32*(11), 3169–3187, https://doi.org/10.1175/JCLI-D-18-0331.1.

Gimeno, L. (2013). Grand challenges in atmospheric science. *Frontiers in Earth Science*, *1*, 1, https://doi.org/10.3389/feart.2013.00001.

Gimeno, L., et al. (2016). Major mechanisms of atmospheric moisture transport and their role in extreme precipitation events. *Annual Review of Environment and Resources*, *41*, 117–141, https://doi.org/10.1146/annurev-environ-110615-085558.

Gimeno, L., Drumond, A., Nieto, R., Trigo, R. M., & Stohl, A. (2010a). On the origin of continental precipitation. *Geophysical Research Letters*, *37*(13), https://doi.org/10.1029/2010GL043712.

Gimeno, L., et al. (2021). The residence time of water vapour in the atmosphere. *Nature Reviews Earth & Environment*, *2*(8), 558–569, https://doi.org/10.1038/s43017-021-00181-9.

Gimeno, L., Nieto, R., Trigo, R. M., Vicente-Serrano, S. M., & López-Moreno, J. I. (2010b). Where does the iberian peninsula moisture come from? an answer based on a lagrangian approach. *Journal of Hydrometeorology*, *11*(2), 421–436, https://doi.org/10.1175/2009JHM1182.1.

Gimeno, L., Nieto, R., Vázquez, M., & Lavers, D. A. (2014). Atmospheric rivers: A mini-review. *Frontiers in Earth Science*, *2*, 2, https://doi.org/10.3389/feart.2014.00002.

Gimeno, L., et al. (2012). Oceanic and terrestrial sources of continental precipitation. *Reviews of Geophysics*, *50*(4), https://doi.org/10.1029/2012RG000389.

Gimeno, L., et al. (2020). Recent progress on the sources of continental precipitation as revealed by moisture transport analysis. *Earth-Science Reviews*, *201*, 103070, https://doi.org/10.1016/j.earscirev.2019.103070.

Gimeno-Sotelo, L. & Gimeno, L. (2022). Concurrent extreme events of atmospheric moisture transport and continental precipitation: The role of landfalling atmospheric rivers. *Atmospheric Research*, *278*, 106356, https://doi.org/10.1016/j.atmosres.2022.106356.

Giorgi, F. (2006). Climate change hot-spots. *Geophysical research letters*, *33*(8), https://doi.org/10.1029/2006GL025734.

Giorgi, F. (2019). Thirty years of regional climate modeling: where are we and where are we going next? *Journal of Geophysical Research: Atmospheres*, *124*(11), 5696–5723, https://doi.org/10.1029/2018JD030094.

Grythe, H., et al. (2017). A new aerosol wet removal scheme for the lagrangian particle model flexpart v10. *Geoscientific Model Development*, *10*(4), 1447–1466, https://doi.org/10.5194/gmd-10-1447-2017.

Guan, B. & Waliser, D. E. (2015). Detection of atmospheric rivers: Evaluation and application of an algorithm for global studies. *Journal of Geophysical Research: Atmospheres*, *120*(24), 12514–12535, https://doi.org/10.1002/2015JD024257.

GWEC (2020). Global offshore wind report 2020. global wind energy council. https://gwec.net/global-offshore-wind-report-2021/. Accessed 23-06-2023.

GWEC, G. W. E. (2021). Gwec global wind report 2021. *Global Wind Energy Council: Brussels, Belgium*.

Hanna, S. (1982). Applications in air pollution modelling, atmospheric turbulence and air pollution modelling, ftm nieuwstadt and h. van dop eds.

Harrison, I. J., Brummett, R., & Stiassny, M. L. (2016). The congo river basin. *The wetland book*, *1*, 845, https://doi.org/10.1017/CBO9780511542091.006.

Hawcroft, M., Shaffrey, L., Hodges, K., & Dacre, H. (2012). How much northern hemisphere precipitation is associated with extratropical cyclones? *Geophysical Research Letters*, *39*(24), https://doi.org/10.1029/2012GL053866.

Hawkins, E. & Sutton, R. (2009). The potential to narrow uncertainty in regional climate predictions. *Bulletin of the American Meteorological Society*, *90*(8), 1095–1108, https://doi.org/10.1175/2009BAMS2607.1.

Hawkins, E. & Sutton, R. (2012). Time of emergence of climate signals. *Geophysical Research Letters*, *39*(1), https://doi.org/10.1029/2011GL050087.

He, Y., Monahan, A. H., Jones, C. G., Dai, A., Biner, S., Caya, D., & Winger, K. (2010). Probability distributions of land surface wind speeds over north america. *Journal of Geophysical Research: Atmospheres*, *115*(D4), https://doi.org/10.1029/2008JD010708.

He, Y., Wu, B., He, P., Gu, W., & Liu, B. (2021). Wind disasters adaptation in cities in a changing climate: A systematic review. *PloS one*, *16*(3), e0248503, https://doi.org/10.1371/journal.pone.0248503.

Held, I. M. & Soden, B. J. (2000). Water vapor feedback and global warming. *Annual review of energy and the environment*, *25*(1), 441–475, https://doi.org/10.1146/annurev.energy.25.1.441.

Held, I. M. & Soden, B. J. (2006). Robust responses of the hydrological cycle to global warming. *Journal of climate*, *19*(21), 5686–5699, https://doi.org/10.1175/JCLI3990.1.

Herrera-Estrada, J. E. & Diffenbaugh, N. S. (2020). Landfalling droughts: Global tracking of moisture deficits from the oceans onto land. *Water Resources Research*, *56*(9), e2019WR026877, https://doi.org/10.1029/2019WR026877.

Hersbach, H., et al. (2020). The era5 global reanalysis. *Quarterly Journal of the Royal Meteorological Society*, *146*(730), 1999–2049, https://doi.org/10.1002/qj.3803.

Hersbach, H. & D., D. (2016). Era5 reanalysis is in production. http://www.ecmwf.int/sites/default/files/elibrary/2016/16299-newsletter-no147-spring-2016.pdf. Accessed 23-06-2023.

Higgins, R., Shi, W., & Hain, C. (2004). Relationships between gulf of california moisture surges and precipitation in the southwestern united states. *Journal of Climate*, *17*(15), 2983–2997, https://doi.org/10.1175/1520-0442(2004)017%3C2983:RBGOCM%3E2.0.CO;2.

Huang, X., Swain, D. L., & Hall, A. D. (2020). Future precipitation increase from very high resolution ensemble downscaling of extreme atmospheric river storms in california. *Science advances*, *6*(29), eaba1323, https://doi.org/10.1126/sciadv.aba1323.

Huguenin, C. N., Serafin, K. A., & Waylen, P. R. (2023). A spatio-temporal analysis of the role of climatic drivers influencing extreme precipitation events in a costa rican basin. *Weather and Climate Extremes*, *42*, 100602, https://doi.org/10.1016/j.wace.2023.100602.

Hwang, Y.-T., Frierson, D. M., & Kang, S. M. (2013). Anthropogenic sulfate aerosol and the southward shift of tropical precipitation in the late 20th century. *Geophysical Research Letters*, *40*(11), 2845–2850, https://doi.org/10.1002/grl.50502.

Insua-Costa, D. & Miguez-Macho, G. (2018). A new moisture tagging capability in the weather research and forecasting model: formulation, validation and application to the 2014 great lake-effect snowstorm. *Earth System Dynamics*, *9*(1), 167–185, https://doi.org/10.5194/esd-9-167-2018.

Insua-Costa, D., Miguez-Macho, G., & Llasat, M. C. (2019). Local and remote moisture sources for extreme precipitation: a study of the two catastrophic 1982 western mediterranean episodes. *Hydrology and Earth System Sciences*, *23*(9), 3885–3900, https://doi.org/10.5194/hess-23-3885-2019.

IPCC (2021). *Climate Change 2021: The Physical Science Basis. Contribution of Working Group I to the Sixth Assessment Report of the Intergovernmental Panel on Climate Change.* Cambridge, UK: Cambridge University Press.

IREA (2019). International renewable energy agency (irea). future of wind. https://wwwirenaorg/-/media/Files/IRENA/Agency/Publication/2019/Oct/IRENA_Future_of_wind_2019.pdf. Accessed 23-06-2023.

Jacobson, M. Z. & Kaufman, Y. J. (2006). Wind reduction by aerosol particles. *Geophysical Research Letters*, *33*(24), https://doi.org/10.1029/2006GL027838.

Jeong, D. I., Cannon, A. J., & Morris, R. J. (2020). Projected changes to wind loads coinciding with rainfall for building design in canada based on an ensemble of canadian regional climate model simulations. *Climatic Change*, *162*, 821–835, https://doi.org/10.1007/s10584-020-02745-y.

Joos, H., Sprenger, M., Binder, H., Beyerle, U., & Wernli, H. (2023). Warm conveyor belts in present-day and future climate simulations-part 1: Climatology and impacts. *Weather and Climate Dynamics*, *4*(1), 133–155, https://doi.org/10.5194/wcd-4-133-2023.

Kamae, Y., Mei, W., & Xie, S.-P. (2019). Ocean warming pattern effects on future changes in east asian atmospheric rivers. *Environmental Research Letters*, *14*(5), 054019, https://doi.org/10.1088/1748-9326/ab128a.

Lavers, D. A., Allan, R. P., Villarini, G., Lloyd-Hughes, B., Brayshaw, D. J., & Wade, A. J. (2013). Future changes in atmospheric rivers and their implications for winter flooding in britain. *Environmental Research Letters*, *8*(3), 034010, https://doi.org/10.1088/1748-9326/8/3/034010.

Lavers, D. A. & Villarini, G. (2013). The nexus between atmospheric rivers and extreme precipitation across europe. *Geophysical Research Letters*, *40*(12), 3259–3264, https://doi.org/10.1002/grl.50636.

Lavers, D. A. & Villarini, G. (2015). The contribution of atmospheric rivers to precipitation in europe and the united states. *Journal of Hydrology*, *522*, 382–390, https://doi.org/10.1016/j.jhydrol.2014.12.010.

Lavers, D. A., Villarini, G., Allan, R. P., Wood, E. F., & Wade, A. J. (2012). The detection of atmospheric rivers in atmospheric reanalyses and their links to british winter floods and the large-scale climatic circulation. *Journal of Geophysical Research: Atmospheres*, *117*(D20), https://doi.org/10.1029/2012JD018027.

Li, J., Li, W., Shum, C., Li, F., Zhang, S., & Lei, J. (2023). Unraveling the contributions of atmospheric rivers on antarctica crustal deformation and its spatiotemporal distribution during the past decade. *Geophysical Journal International*, *235*(2), 1325–1338, https://doi.org/10.1093/gji/ggad306.

Liang, J., Tan, M. L., Catto, J. L., Hawcroft, M. K., Hodges, K. I., & Haywood, J. M. (2023). Projected near-term changes in monsoon precipitation over peninsular malaysia in the highresmip multi-model ensembles. *Climate Dynamics*, *60*(3-4), 1151–1171, https://doi.org/10.1007/s00382-022-06363-5.

Liu, B., Tan, X., Gan, T. Y., Chen, X., Lin, K., Lu, M., & Liu, Z. (2020). Global atmospheric moisture transport associated with precipitation extremes: Mechanisms and climate change impacts. *Wiley Interdisciplinary Reviews: Water*, *7*(2), e1412, https://doi.org/10.1002/wat2.1412.

Liu, X., Zhang, X.-J., Tang, Q., & Zhang, X.-Z. (2014). Effects of surface wind speed decline on modeled hydrological conditions in china. *Hydrology and Earth System Sciences*, *18*(8), 2803–2813, https://doi.org/10.5194/hess-18-2803-2014.

Maclennan, M. L., et al. (2023). Climatology and surface impacts of atmospheric rivers on west antarctica. *The Cryosphere*, *17*(2), 865–881, https://doi.org/10.5194/tc-17-865-2023.

Madakumbura, G. D., et al. (2019). Event-to-event intensification of the hydrologic cycle from 1.5 c to a 2 c warmer world. *Scientific Reports*, *9*(1), 3483, https://doi.org/10.1038/s41598-019-39936-2.

Madonna, E., Wernli, H., Joos, H., & Martius, O. (2014). Warm conveyor belts in the era-interim dataset (1979–2010). part i: Climatology and potential vorticity evolution. *Journal of climate*, *27*(1), 3–26, https://doi.org/10.1175/JCLI-D-12-00720.1.

Marengo, J. A., Soares, W. R., Saulo, C., & Nicolini, M. (2004). Climatology of the low-level jet east of the andes as derived from the ncep–ncar reanalyses: Characteristics and temporal variability. *Journal of climate*, *17*(12), 2261–2280, https://doi.org/10.1175/1520-0442(2004)017%3C2261:COTLJE%3E2.0.CO;2.

Masson-Delmotte, V., Zhai, P., Pörtner, H.-O., Roberts, D., Skea, J., Shukla, P. R., et al. (2022). *Global Warming of 1.5 C: IPCC special report on impacts of global warming of 1.5 C above pre-industrial levels in context of strengthening response to climate change, sustainable development, and efforts to eradicate poverty.* Cambridge University Press.

Matrosov, S. Y. (2013). Characteristics of landfalling atmospheric rivers inferred from satellite observations over the eastern north pacific ocean. *Monthly Weather Review*, *141*(11), 3757–3768, https://doi.org/10.1175/MWR-D-12-00324.1.

McClenny, E. E. (2021). *Using Simpler Models to Understand Atmospheric River Responses to Sea-Surface Temperature Increases.* University of California, Davis.

McClenny, E. E., Ullrich, P. A., & Grotjahn, R. (2020). Sensitivity of atmospheric river vapor transport and precipitation to uniform sea surface temperature increases. *Journal of Geophysical Research: Atmospheres*, *125*(21), e2020JD033421, https://doi.org/10.1029/2020JD033421.

McMahon, T., Peel, M., Lowe, L., Srikanthan, R., & McVicar, T. (2013). Estimating actual, potential, reference crop and pan evaporation using standard meteorological data: a pragmatic synthesis. *Hydrology and Earth System Sciences*, *17*(4), 1331–1363, https://doi.org/10.5194/hess-17-1331-2013.

McVicar, T. R., et al. (2012). Global review and synthesis of trends in observed terrestrial near-surface wind speeds: Implications for evaporation. *Journal of Hydrology*, *416*, 182–205, https://doi.org/10.1016/j.jhydrol.2011.10.024.

Melgarejo, A. E., Ordoñez, P., Nieto, R., Peña-Ortiz, C., García-Herrera, R., & Gimeno, L. (2021). Mechanisms for severe drought occurrence in the balsas river basin (mexico). *Atmosphere*, *12*(3), 368, https://doi.org/10.3390/atmos12030368.

Min, S.-K., Zhang, X., Zwiers, F. W., & Hegerl, G. C. (2011). Human contribution to more-intense precipitation extremes. *Nature*, *470*(7334), 378–381, https://doi.org/10.1038/nature09763.

Murcia, J. P., Réthoré, P.-E., Hansen, K. S., Natarajan, A., & Sørensen, J. D. (2015). A new method to estimate the uncertainty of aep of offshore wind power plants applied to horns rev 1. *Proc. EWEA*, *20*.

Neelin, J. D., Sahany, S., Stechmann, S. N., & Bernstein, D. N. (2017). Global warming precipitation accumulation increases above the current-climate cutoff scale. *Proceedings of the National Academy of Sciences*, *114*(6), 1258–1263, https://doi.org/10.1073/pnas.1615333114.

Nie, J., Sobel, A. H., Shaevitz, D. A., & Wang, S. (2018). Dynamic amplification of extreme precipitation sensitivity. *Proceedings of the National Academy of Sciences*, *115*(38), 9467–9472, https://doi.org/10.1073/pnas.1800357115.

Nieto, R., Castillo, R., Drumond, A., & Gimeno, L. (2014). A catalog of moisture sources for continental climatic regions. *Water Resources Research*, *50*(6), 5322–5328, https://doi.org/10.1002/2013WR013901.

Nieto, R., Ciric, D., Vázquez, M., Liberato, M. L., & Gimeno, L. (2019). Contribution of the main moisture sources to precipitation during extreme peak precipitation months. *Advances in Water Resources*, *131*, 103385, https://doi.org/10.1016/j.advwatres.2019.103385.

Nieto, R., Gimeno, L., Drumond, A., & Hernandez, E. (2010). A lagrangian identification of the main moisture sources and sinks affecting the mediterranean area. *WSEAS Trans. Environ. Dev*, *6*(5), 365–374.

Nishikawa, H. (2020). A face-area-weighted 'centroid'formula for finite-volume method that improves skewness and convergence on triangular grids. *Journal of Computational Physics*, *401*, 109001, https://doi.org/10.1016/j.jcp.2019.109001.

Niyogi, D., et al. (2011). Urban modification of thunderstorms: An observational storm climatology and model case study for the indianapolis urban region. *Journal of Applied Meteorology and Climatology*, *50*(5), 1129–1144, https://doi.org/10.1175/2010JAMC1836.1.

Numaguti, A. (1999). Origin and recycling processes of precipitating water over the eurasian continent: Experiments using an atmospheric general circulation model. *Journal of Geophysical Research: Atmospheres*, *104*(D2), 1957–1972, https://doi.org/10.1029/1998JD200026.

O'Neill, B. C., et al. (2016). The scenario model intercomparison project (scenariomip) for cmip6. *Geoscientific Model Development*, *9*(9), 3461–3482, https://doi.org/10.5194/gmd-9-3461-2016.

Orme, L. C., et al. (2017). Past changes in the north atlantic storm track driven by insolation and sea-ice forcing. *Geology*, *45*(4), 335–338, https://doi.org/10.1130/G38521.1.

O'Brien, T. A., et al. (2022). Increases in future ar count and size: Overview of the artmip tier 2 cmip5/6 experiment. *Journal of Geophysical Research: Atmospheres*, *127*(6), e2021JD036013, https://doi.org/10.1029/2021JD036013.

O'Gorman, P. & Muller, C. J. (2010). How closely do changes in surface and column water vapor follow clausius–clapeyron scaling in climate change simulations? *Environmental Research Letters*, *5*(2), 025207, https://doi.org/10.1088/1748-9326/5/2/025207.

O'Gorman, P. A. (2015). Precipitation extremes under climate change. *Current climate change reports*, *1*, 49–59, https://doi.org/10.1007/s40641-015-0009-3.

O'Neill, B. C., et al. (2017). The roads ahead: Narratives for shared socioeconomic pathways describing world futures in the 21st century. *Global environmental change*, *42*, 169–180, https://doi.org/10.1016/j.gloenvcha.2015.01.004.

Palazzi, E. & Provenzale, A. (2016). Water in the climate system. In *The Fluid Dynamics of Climate* (pp. 161–182). Springer.

Pall, P., et al. (2011). Anthropogenic greenhouse gas contribution to flood risk in england and wales in autumn 2000. *Nature*, *470*(7334), 382–385, https://doi.org/10.1038/nature09762.

Papritz, L., Aemisegger, F., & Wernli, H. (2021). Sources and transport pathways of precipitating waters in cold-season deep north atlantic cyclones. *Journal of the Atmospheric Sciences*, *78*(10), 3349–3368, https://doi.org/10.1175/JAS-D-21-0105.1.

Papritz, L., Pfahl, S., Rudeva, I., Simmonds, I., Sodemann, H., & Wernli, H. (2014). The role of extratropical cyclones and fronts for southern ocean freshwater fluxes. *Journal of Climate*, *27*(16), 6205–6224, https://doi.org/10.1175/JCLI-D-13-00409.1.

Payne, A. E., et al. (2020). Responses and impacts of atmospheric rivers to climate change. *Nature Reviews Earth & Environment*, *1*(3), 143–157, https://doi.org/10.1038/s43017-020-0030-5.

Peixoto, J. P. & Oort, A. H. (1992). *Physics of climate.* New York, NY (United States); American Institute of Physics.

Pendergrass, A. G. (2018). What precipitation is extreme? *Science*, *360*(6393), 1072–1073, https://doi.org/10.1126/science.aat1871.

Pendergrass, A. G., Reed, K. A., & Medeiros, B. (2016). The link between extreme precipitation and convective organization in a warming climate: Global radiative-convective equilibrium simulations. *Geophysical Research Letters*, *43*(21), 11–445, https://doi.org/10.1002/2016GL071285.

Pérez-Alarcón, A., Fernández-Alvarez, J. C., Sorí, R., Nieto, R., & Gimeno, L. (2023). Moisture source identification for precipitation associated with tropical cyclone development over the indian ocean: a lagrangian approach. *Climate Dynamics*, *60*(9-10), 2735–2758, https://doi.org/10.1007/s00382-022-06429-4.

Pérez-Alarcón, A., Sorí, R., Fernández-Alvarez, J. C., Nieto, R., & Gimeno, L. (2022). Where does the moisture for north atlantic tropical cyclones come from? *Journal of Hydrometeorology*, *23*(3), 457–472, https://doi.org/10.1175/JHM-D-21-0117.1.

Pfahl, S., O'Gorman, P. A., & Fischer, E. M. (2017). Understanding the regional pattern of projected future changes in extreme precipitation. *Nature Climate Change*, *7*(6), 423–427, https://doi.org/10.1038/nclimate3287.

Pisso, I., et al. (2019). The lagrangian particle dispersion model flexpart version 10.4. *Geoscientific Model Development*, *12*(12), 4955–4997, https://doi.org/10.5194/gmd-12-4955-2019.

Pope, M., Jakob, C., & Reeder, M. J. (2009). Regimes of the north australian wet season. *Journal of Climate*, *22*(24), 6699–6715, https://doi.org/10.1175/2009JCLI3057.1.

Prein, A. F., Liu, C., Ikeda, K., Trier, S. B., Rasmussen, R. M., Holland, G. J., & Clark, M. P. (2017). Increased rainfall volume from future convective storms in the us. *Nature Climate Change*, *7*(12), 880–884, https://doi.org/10.1038/s41558-017-0007-7.

Priestley, M. D. & Catto, J. L. (2022). Future changes in the extratropical storm tracks and cyclone intensity, wind speed, and structure. *Weather and Climate Dynamics*, *3*(1), 337–360, https://doi.org/10.5194/wcd-3-337-2022.

Pryor, S., Barthelmie, R., & Kjellström, E. (2005). Potential climate change impact on wind energy resources in northern europe: analyses using a regional climate model. *Climate Dynamics*, *25*, 815–835, https://doi.org/10.1007/s00382-005-0072-x.

Pryor, S., Schoof, J. T., & Barthelmie, R. (2006). Winds of change?: Projections of near-surface winds under climate change scenarios. *Geophysical research letters*, *33*(11), https://doi.org/10.1029/2006GL026000.

Qi, L., Leslie, L., & Zhao, S. (1999). Cut-off low pressure systems over southern australia: climatology and case study. *International Journal of Climatology: A Journal of the Royal Meteorological Society*, *19*(15), 1633–1649, https://doi.org/10.1002/(SICI)1097-0088(199912)19:15%3C1633::AID-JOC445%3E3.0.CO;2-0.

Quante, M. & Matthias, V. (2006). Water in the earth's atmosphere. In *Journal de Physique IV (Proceedings)*, volume 139 (pp. 37–61).: EDP sciences.

Rahmstorf, S., Box, J. E., Feulner, G., Mann, M. E., Robinson, A., Rutherford, S., & Schaffernicht, E. J. (2015). Exceptional twentieth-century slowdown in atlantic ocean overturning circulation. *Nature climate change*, *5*(5), 475–480, https://doi.org/10.1038/nclimate2554.

Ralph, F., Coleman, T., Neiman, P., Zamora, R., & Dettinger, M. (2013a). Observed impacts of duration and seasonality of atmospheric-river landfalls on soil moisture and runoff in coastal northern california. *Journal of Hydrometeorology*, *14*(2), 443–459, https://doi.org/10.1175/JHM-D-12-076.1.

Ralph, F. M., et al. (2017). Atmospheric rivers emerge as a global science and applications focus. *Bulletin of the American Meteorological Society*, *98*(9), 1969–1973, https://doi.org/10.1175/BAMS-D-16-0262.1.

Ralph, F. M., Dettinger, M. D., Cairns, M. M., Galarneau, T. J., & Eylander, J. (2018). Defining "atmospheric river": How the glossary of meteorology helped resolve a debate. *Bulletin of the American Meteorological Society*, *99*(4), 837–839, https://doi.org/10.1175/BAMS-D-17-0157.1.

Ralph, F. M., et al. (2013b). The emergence of weather-related test beds linking research and forecasting operations. *Bulletin of the American Meteorological Society*, *94*(8), 1187–1211, https://doi.org/10.1175/BAMS-D-12-00080.1.

Ralph, F. M., Neiman, P. J., & Rotunno, R. (2005). Dropsonde observations in low-level jets over the northeastern pacific ocean from caljet-1998 and pacjet-2001: Mean vertical-profile and atmospheric-river characteristics. *Monthly weather review*, *133*(4), 889–910, https://doi.org/10.1175/MWR2896.1.

Ralph, F. M., Neiman, P. J., & Wick, G. A. (2004). Satellite and caljet aircraft observations of atmospheric rivers over the eastern north pacific ocean during the winter of 1997/98. *Monthly weather review*, *132*(7), 1721–1745, https://doi.org/10.1175/1520-0493(2004)132%3C1721:SACAOO%3E2.0.CO;2.

Ralph, F. M., et al. (2019). A scale to characterize the strength and impacts of atmospheric rivers. *Bulletin of the American Meteorological Society*, *100*(2), 269–289, https://doi.org/10.1175/BAMS-D-18-0023.1.

Ramanathan, V. & Feng, Y. (2008). On avoiding dangerous anthropogenic interference with the climate system: Formidable challenges ahead. *Proceedings of the National Academy of Sciences*, *105*(38), 14245–14250, https://doi.org/10.1073/pnas.0803838105.

Ramos, A., Trigo, R., Blamey, R., Tome, R., & Reason, C. (2017). The influence of atmospheric rivers over the south atlantic on rainfall in south africa. In *AGU Fall Meeting Abstracts*, volume 2017 (pp. A33H–2479).

Ramos, A. M., Martins, M. J., Tomé, R., & Trigo, R. M. (2018). Extreme precipitation events in summer in the iberian peninsula and its relationship with atmospheric rivers. *Frontiers in Earth Science*, *6*, 110, https://doi.org/10.3389/feart.2018.00110.

Ramos, A. M., Tomé, R., Trigo, R. M., Liberato, M. L., & Pinto, J. G. (2016). Projected changes in atmospheric rivers affecting europe in cmip5 models. *Geophysical Research Letters*, *43*(17), 9315–9323, https://doi.org/10.1002/2016GL070634.

Renault, L., McWilliams, J. C., & Masson, S. (2017). Satellite observations of imprint of oceanic current on wind stress by air-sea coupling. *Scientific reports*, *7*(1), 17747, https://doi.org/10.1038/s41598-017-17939-1.

Riahi, K., et al. (2017). The shared socioeconomic pathways and their energy, land use, and greenhouse gas emissions implications: An overview. *Global environmental change*, *42*, 153–168, https://doi.org/10.1016/j.gloenvcha.2016.05.009.

Richardson, T. B., Forster, P. M., Andrews, T., & Parker, D. J. (2016). Understanding the rapid precipitation response to co2 and aerosol forcing on a regional scale. *Journal of Climate*, *29*(2), 583–594, https://doi.org/10.1175/JCLI-D-15-0174.1.

Richter, J. H., et al. (2022). Subseasonal earth system prediction with cesm2. *Weather and Forecasting*, *37*(6), 797–815, https://doi.org/10.1175/WAF-D-21-0163.1.

Rios-Entenza, A. & Miguez-Macho, G. (2014). Moisture recycling and the maximum of precipitation in spring in the iberian peninsula. *Climate dynamics*, *42*, 3207–3231, https://doi.org/10.1007/s00382-013-1971-x.

Rios-Entenza, A., Soares, P. M., Trigo, R. M., Cardoso, R. M., & Miguez-Macho, G. (2014). Moisture recycling in the iberian peninsula from a regional climate simulation: Spatiotemporal analysis and impact on the precipitation regime. *Journal of Geophysical Research: Atmospheres*, *119*(10), 5895–5912, https://doi.org/10.1002/2013JD021274.

Ritchie, H. & Roser, M. (2019). Our world in data: Co2 and greenhouse gas emissions.

Rivera, E. R., Dominguez, F., & Castro, C. L. (2014). Atmospheric rivers and cool season extreme precipitation events in the verde river basin of arizona. *Journal of Hydrometeorology*, *15*(2), 813–829, https://doi.org/10.1175/JHM-D-12-0189.1.

Roberts, M. J., et al. (2020). Projected future changes in tropical cyclones using the cmip6 highresmip multimodel ensemble. *Geophysical research letters*, *47*(14), e2020GL088662, https://doi.org/10.1029/2020GL088662.

Roberts, N., et al. (2012). Palaeolimnological evidence for an east–west climate see-saw in the mediterranean since ad 900. *Global and Planetary Change*, *84*, 23–34, https://doi.org/10.1016/j.gloplacha.2011.11.002.

Robson, J., et al. (2018). Recent multivariate changes in the north atlantic climate system, with a focus on 2005–2016. *International Journal of Climatology*, *38*(14), 5050–5076, https://doi.org/10.1002/joc.5815.

Roderick, M. L., Rotstayn, L. D., Farquhar, G. D., & Hobbins, M. T. (2007). On the attribution of changing pan evaporation. *Geophysical research letters*, *34*(17), https://doi.org/10.1029/2007GL031166.

Rousi, E., Selten, F., Rahmstorf, S., & Coumou, D. (2021). Changes in north atlantic atmospheric circulation in a warmer climate favor winter flooding and summer drought over europe. *Journal of Climate*, *34*(6), 2277–2295, https://doi.org/10.1175/JCLI-D-20-0311.1.

Rutz, J. J., Steenburgh, W. J., & Ralph, F. M. (2014). Climatological characteristics of atmospheric rivers and their inland penetration over the western united states. *Monthly Weather Review*, *142*(2), 905–921, https://doi.org/10.1175/MWR-D-13-00168.1.

Salvador, S., Costoya, X., Sanz-Larruga, F. J., & Gimeno, L. (2018). Development of offshore wind power: Contrasting optimal wind sites with legal restrictions in galicia, spain. *Energies*, *11*(4), 731, https://doi.org/10.3390/en11040731.

Samset, B., et al. (2016). Fast and slow precipitation responses to individual climate forcers: A pdrmip multimodel study. *Geophysical research letters*, *43*(6), 2782–2791, https://doi.org/10.1002/2016GL068064.

Samset, B. H., et al. (2018). Weak hydrological sensitivity to temperature change over land, independent of climate forcing. *npj Climate and Atmospheric Science*, *1*(1), 20173, https://doi.org/10.1038/s41612-017-0005-5.

Sandvik, M. I., Sorteberg, A., & Rasmussen, R. (2018). Sensitivity of historical orographically enhanced extreme precipitation events to idealized temperature perturbations. *Climate dynamics*, *50*, 143–157, https://doi.org/10.1007/s00382-017-3593-1.

Santos, F., Gómez-Gesteira, M., DeCastro, M., Añel, J., Carvalho, D., Costoya, X., & Dias, J. (2018). On the accuracy of cordex rcms to project future winds over the iberian peninsula and surrounding ocean. *Applied Energy*, *228*, 289–300, https://doi.org/10.1016/j.apenergy.2018.06.086.

Schneider, T., Bischoff, T., & Haug, G. H. (2014). Migrations and dynamics of the intertropical convergence zone. *Nature*, *513*(7516), 45–53, https://doi.org/10.1038/nature13636.

Seidel, D. J. (2002). Water vapor: distribution and trends, encyclopedia of global environmental change.

Seneviratne, S. I. & Hauser, M. (2020). Regional climate sensitivity of climate extremes in cmip6 versus cmip5 multimodel ensembles. *Earth's future*, *8*(9), e2019EF001474, https://doi.org/10.1029/2019EF001474.

Shen, C., Zha, J., Li, Z., Azorin-Molina, C., Deng, K., Minola, L., & Chen, D. (2022). Evaluation of global terrestrial near-surface wind speed simulated by cmip6 models and their future projections. *Annals of the New York Academy of Sciences*, *1518*(1), 249–263, https://doi.org/10.1111/nyas.14910.

Simpson, I. R., et al. (2020). An evaluation of the large-scale atmospheric circulation and its variability in cesm2 and other cmip models. *Journal of Geophysical Research: Atmospheres*, *125*(13), e2020JD032835, https://doi.org/10.1029/2020JD032835.

Sinclair, M. R. (1993). A diagnostic study of the extratropical precipitation resulting from tropical cyclone bola. *Monthly weather review*, *121*(10), 2690–2707, https://doi.org/10.1175/1520-0493(1993)121%3C2690:ADSOTE%3E2.0.CO;2.

Singh, M. S. & O'Gorman, P. A. (2014). Influence of microphysics on the scaling of precipitation extremes with temperature. *Geophysical Research Letters*, *41*(16), 6037–6044, https://doi.org/10.1002/2014GL061222.

Skamarock, W. C., et al. (2008). A description of the advanced research wrf version 3. *NCAR technical note*, *475*, 113, https://doi.org/10.5065/D68S4MVH.

Smith, I., Wilson, L., & Suppiah, R. (2008). Characteristics of the northern australian rainy season. *Journal of Climate*, *21*(17), 4298–4311, https://doi.org/10.1175/2008JCLI2109.1.

Sohn, B., Yeh, S.-W., Schmetz, J., & Song, H.-J. (2013). Observational evidences of walker circulation change over the last 30 years contrasting with gcm results. *Climate Dynamics*, *40*, 1721–1732, https://doi.org/10.1007/s00382-012-1484-z.

Sorí, R., Vázquez, M., Stojanovic, M., Nieto, R., Liberato, M. L., & Gimeno, L. (2020). Hydrometeorological droughts in the miño–limia–sil hydrographic demarcation (northwestern iberian peninsula): the role of atmospheric drivers. *Natural Hazards and Earth System Sciences*, *20*(6), 1805–1832, https://doi.org/10.5194/nhess-20-1805-2020.

Sousa, P. M., Ramos, A. M., Raible, C. C., Messmer, M., Tomé, R., Pinto, J. G., & Trigo, R. M. (2020). North atlantic integrated water vapor transport—from 850 to 2100 ce: Impacts on western european rainfall. *Journal of Climate*, *33*(1), 263–279, https://doi.org/10.1175/JCLI-D-19-0348.1.

Steffen, W., et al. (2018). Trajectories of the earth system in the anthropocene. *Proceedings of the National Academy of Sciences*, *115*(33), 8252–8259, https://doi.org/10.1073/pnas.1810141115.

Stensrud, D. J. (1996). Importance of low-level jets to climate: A review. *Journal of Climate*, (pp. 1698–1711)., https://doi.org/10.1175/1520-0442(1996)009%3C1698:IOLLJT%3E2.0.CO;2.

Stephens, E., Day, J. J., Pappenberger, F., & Cloke, H. (2015). Precipitation and floodiness. *Geophysical Research Letters*, *42*(23), 10–316, https://doi.org/10.1002/2015GL066779.

Stocker, T. F. e. a. (2013). *IPCC AR5: Climate Change: The Physical Science Basis*. Cambridge; New York, NY: Cambridge University Press.

Stohl, A. (1998). Computation, accuracy and applications of trajectories—a review and bibliography. *Atmospheric Environment*, *32*(6), 947–966, https://doi.org/10.1016/S1352-2310(97)00457-3.

Stohl, A. & James, P. (2004). A lagrangian analysis of the atmospheric branch of the global water cycle. part i: Method description, validation, and demonstration for the august 2002 flooding in central europe. *Journal of Hydrometeorology*, *5*(4), 656–678, https://doi.org/10.1175/1525-7541(2004)005%3C0656:ALAOTA%3E2.0.CO;2.

Stohl, A. & James, P. (2005). A lagrangian analysis of the atmospheric branch of the global water cycle. part ii: Moisture transports between earth's ocean basins and river catchments. *Journal of Hydrometeorology*, *6*(6), 961–984, https://doi.org/10.1175/JHM470.1.

Stohl, A. & Thomson, D. J. (1999). A density correction for lagrangian particle dispersion models. *Boundary-Layer Meteorology*, *90*, 155–167, https://doi.org/10.1023/A:1001741110696.

Stojanovic, M., Drumond, A., Nieto, R., & Gimeno, L. (2018). Anomalies in moisture supply during the 2003 drought event in europe: A lagrangian analysis. *Water*, *10*(4), 467, https://doi.org/10.3390/w10040467.

Swart, R.; Coppens, C. G. H. P. M. R. P. S. J. S. P. H. M. P. M. d. V. E. e. a. (2009). *Europe's onshore and offshore wind energy potential: an assessment of environmental and economic constraints (No. 6/2009)*. Publications Office.

Tabari, H. & Willems, P. (2018). Lagged influence of atlantic and pacific climate patterns on european extreme precipitation. *Scientific reports*, *8*(1), 5748, https://doi.org/10.1038/s41598-018-24069-9.

Torres-Alavez, J. A., et al. (2021). Future projections in the climatology of global low-level jets from cordex-core simulations. *Climate Dynamics*, (pp. 1–19)., https://doi.org/10.1007/s00382-021-05671-6.

Trenberth, K. E. (1998). Atmospheric moisture residence times and cycling: Implications for rainfall rates and climate change. *Climatic change*, *39*, 667–694, https://doi.org/10.1023/A:1005319109110.

Trenberth, K. E. & Dai, A. (2007). Effects of mount pinatubo volcanic eruption on the hydrological cycle as an analog of geoengineering. *Geophysical Research Letters*, *34*(15), https://doi.org/10.1029/2007GL030524.

Trenberth, K. E., Dai, A., Rasmussen, R. M., & Parsons, D. B. (2003). The changing character of precipitation. *Bulletin of the American Meteorological Society*, *84*(9), 1205–1218, https://doi.org/10.1175/BAMS-84-9-1205.

Trenberth, K. E. & Guillemot, C. J. (1998). Evaluation of the atmospheric moisture and hydrological cycle in the ncep/ncar reanalyses. *Climate Dynamics*, *14*, 213–231, https://doi.org/10.1007/s003820050219.

Trenberth, K. E. & Smith, L. (2005). The mass of the atmosphere: A constraint on global analyses. *Journal of Climate*, *18*(6), 864–875, https://doi.org/10.1175/JCLI-3299.1.

Ulazia, A., Nafarrate, A., Ibarra-Berastegi, G., Sáenz, J., & Carreno-Madinabeitia, S. (2019). The consequences of air density variations over northeastern scotland for offshore wind energy potential. *Energies*, *12*(13), 2635, https://doi.org/10.3390/en12132635.

Ulbrich, U., Pinto, J. G., Kupfer, H., Leckebusch, G., Spangehl, T., & Reyers, M. (2008). Changing northern hemisphere storm tracks in an ensemble of ipcc climate change simulations. *Journal of Climate*, *21*(8), 1669–1679, https://doi.org/10.1175/2007JCLI1992.1.

Undorf, S., Polson, D., Bollasina, M., Ming, Y., Schurer, A., & Hegerl, G. (2018). Detectable impact of local and remote anthropogenic aerosols on the 20th century changes of west african and south asian monsoon precipitation. *Journal of Geophysical Research: Atmospheres*, *123*(10), 4871–4889, https://doi.org/10.1029/2017JD027711.

Van der Ent, R. & Savenije, H. (2011). Length and time scales of atmospheric moisture recycling. *Atmospheric Chemistry and Physics*, *11*(5), 1853–1863, https://doi.org/10.5194/acp-11-1853-2011.

Van Der Ent, R. J. & Tuinenburg, O. A. (2017). The residence time of water in the atmosphere revisited. *Hydrology and Earth System Sciences*, *21*(2), 779–790, https://doi.org/10.5194/hess-21-779-2017.

Vázquez, M., Algarra, I., Eiras-Barca, J., Ramos, A. M., Nieto, R., & Gimeno, L. (2018). Atmospheric rivers over the arctic: Lagrangian characterisation of their moisture sources. *Water*, *11*(1), 41, https://doi.org/10.3390/w11010041.

Vazquez, M., Nieto, R., Liberato, M. L., & Gimeno, L. (2020). Atmospheric moisture sources associated with extreme precipitation during the peak precipitation month. *Weather and Climate Extremes*, *30*, 100289, https://doi.org/10.1016/j.wace.2020.100289.

Viale, M. & Nuñez, M. N. (2011). Climatology of winter orographic precipitation over the subtropical central andes and associated synoptic and regional characteristics. *Journal of Hydrometeorology*, *12*(4), 481–507, https://doi.org/10.1175/2010JHM1284.1.

Vincent, L. (1993). Morphological grayscale reconstruction in image analysis: applications and efficient algorithms. *IEEE transactions on image processing*, *2*(2), 176–201, https://doi.org/10.1109/83.217222.

Waliser, D. E. & Graham, N. E. (1993). Convective cloud systems and warm-pool sea surface temperatures: Coupled interactions and self-regulation. *Journal of Geophysical Research: Atmospheres*, *98*(D7), 12881–12893, https://doi.org/10.1029/93JD00872.

Waliser, D. E., et al. (2012). The "year" of tropical convection (may 2008–april 2010): Climate variability and weather highlights. *Bulletin of the American Meteorological Society*, *93*(8), 1189–1218, https://doi.org/10.1175/2011BAMS3095.1.

Wallace, J. M. & Hobbs, P. V. (2006). *Atmospheric science: an introductory survey*, volume 92. Elsevier.

Wandel, J., Quinting, J. F., & Grams, C. M. (2021). Toward a systematic evaluation of warm conveyor belts in numerical weather prediction and climate models. part ii: Verification of operational reforecasts. *Journal of the Atmospheric Sciences*, *78*(12), 3965–3982, https://doi.org/10.1175/JAS-D-20-0385.1.

Wang, R., et al. (2017). Variation of strong dust storm events in northern china during 1978–2007. *Atmospheric Research*, *183*, 166–172, https://doi.org/10.1016/j.atmosres.2016.09.002.

Wang-Erlandsson, L., Fetzer, I., Keys, P. W., Van Der Ent, R. J., Savenije, H. H., & Gordon, L. J. (2018). Remote land use impacts on river flows through atmospheric teleconnections. *Hydrology and Earth System Sciences*, *22*(8), 4311–4328, https://doi.org/10.5194/hess-22-4311-2018.

Wentz, F. J. & Schabel, M. (2000). Precise climate monitoring using complementary satellite data sets. *Nature*, *403*(6768), 414–416, https://doi.org/10.1038/35000184.

Wey, H.-W., Lo, M.-H., Lee, S.-Y., Yu, J.-Y., & Hsu, H.-H. (2015). Potential impacts of wintertime soil moisture anomalies from agricultural irrigation at low latitudes on regional and global climates. *Geophysical Research Letters*, *42*(20), 8605–8614, https://doi.org/10.1002/2015GL065883.

Wilson, A. M., et al. (2022). Atmospheric river reconnaissance workshop promotes research and operations partnership. *Bulletin of the American Meteorological Society*, *103*(3), E810–E816, https://doi.org/10.1175/BAMS-D-21-0259.1.

Winschall, A., Pfahl, S., Sodemann, H., & Wernli, H. (2014). Comparison of eulerian and lagrangian moisture source diagnostics–the flood event in eastern europe in may 2010. *Atmospheric Chemistry and Physics*, *14*(13), 6605–6619, https://doi.org/10.5194/acp-14-6605-2014.

Woollings, T., Hannachi, A., & Hoskins, B. (2010). Variability of the north atlantic eddy-driven jet stream. *Quarterly Journal of the Royal Meteorological Society*, *136*(649), 856–868, https://doi.org/10.1002/qj.625.

Wu, J., Shi, Y., & Xu, Y. (2020). Evaluation and projection of surface wind speed over china based on cmip6 gcms. *Journal of Geophysical Research: Atmospheres*, *125*(22), e2020JD033611, https://doi.org/10.1029/2020JD033611.

Xu, G., Ma, X., Chang, P., & Wang, L. (2020). Image-processing-based atmospheric river tracking method version 1 (ipart-1). *Geoscientific Model Development*, *13*(10), 4639–4662, https://doi.org/10.5194/gmd-13-4639-2020.

Xu, Y. & Ramanathan, V. (2017). Well below 2 c: Mitigation strategies for avoiding dangerous to catastrophic climate changes. *Proceedings of the National Academy of Sciences*, *114*(39), 10315–10323, https://doi.org/10.1073/pnas.1618481114.

Xu, Z., Han, Y., Tam, C.-Y., Yang, Z.-L., & Fu, C. (2021). Bias-corrected cmip6 global dataset for dynamical downscaling of the historical and future climate (1979–2100). *Scientific Data*, *8*(1), 293, https://doi.org/10.1038/s41597-021-01079-3.

Yamada, T. & Mellor, G. (1975). A simulation of the wangara atmospheric boundary layer data. *Journal of Atmospheric Sciences*, *32*(12), 2309–2329, https://doi.org/10.1175/1520-0469(1975)032%3C2309:ASOTWA%3E2.0.CO;2.

Yu, L. (2007). Global variations in oceanic evaporation (1958–2005): The role of the changing wind speed. *Journal of climate*, *20*(21), 5376–5390, https://doi.org/10.1175/2007JCLI1714.1.

Zhang, Z., Ralph, F. M., & Zheng, M. (2019). The relationship between extratropical cyclone strength and atmospheric river intensity and position. *Geophysical Research Letters*, *46*(3), 1814–1823, https://doi.org/10.1029/2018GL079071.

Zhu, Y. & Newell, R. E. (1998). A proposed algorithm for moisture fluxes from atmospheric rivers. *Monthly weather review*, *126*(3), 725–735, https://doi.org/10.1175/1520-0493(1998)126%3C0725:APAFMF%3E2.0.CO;2.

Universidade Vigo

Universidade Vigo